University of Nottingham
UK | CHINA | MALAYSIA

Design and evaluation of icephobic coatings for efficient thermal de-icing

Jack Brierley

Thesis submitted to the University of Nottingham for the degree of Doctor of Philosophy

September 2024

Abstract

Ice accretion on engineering structures is a significant safety concern, and the current in-use mitigation strategy of electro-thermal de-icing systems is energy-intensive. Icephobic coatings have been identified as a potential zero-energy solution, passively de-icing the surface or altering the accretion formation. Numerous approaches are being studied, and progress is being made towards this goal. However, coating durability remains a significant hurdle.

This work is primarily motivated by the extreme use case of ice accretion on a helicopter blade. The leading edge, where ice typically forms, experiences abrasive wear through sea spray and particulate erosion so severe that damage to the titanium erosion shield can be a life-limiting issue. Icephobic coatings may never have a sufficient lifespan to be applied as a stand-alone passive solution to solve this particular problem.

We consider a hybrid approach, with the coating considered a sacrificial barrier, extending the life of the erosion shield with the additional benefit of icephobic properties, leading to a reduction in the electro-thermal energy required to de-ice the leading edge. The goal of this coating would be to minimise cumulative energy costs by reducing the frequency and severity of icing incidents, the energy cost per de-icing cycle, or both.

While the need for a hybrid solution may only be suitable for niche or low-volume applications, many others where a passive solution would be appropriate will have that passive solution retroactively applied. Testing such coatings alongside an electro-thermal de-icing system would not be necessary to improve function. Still, it would provide confidence in early candidates. If the coating failed to passively de-ice due to unexpected performance outcomes or incurred damage inhibiting its capabilities, the active system would remain effective as a secondary safety system. In comparison, a hybrid coating system would be an electro-thermal de-icing system that is enhanced by an icephobic coating and not replaced by one.

This thesis addresses the new considerations required of a hybrid icephobic coating deployed alongside an electro-thermal de-icing system. We show that altering a coating's properties to optimise the performance of an electro-thermal de-icing system produces detrimental changes to its performance in passive icephobic metrics. An example of such a modification would be the addition of fillers to increase the thermal conductivity for use as part of an active system, but which also increases the frequency and growth rate of ice accretions and also increases the Young's modulus of the elastomer matrix material, increasing the

ice adhesion strength. Every factor that can be manipulated to improve one performance metric is often a detriment to another, meaning any potential success would be application-specific, with carefully delineated optimisation requirements.

Polydimethylsiloxane (PDMS) was chosen as a matrix material following accepted best practices from icephobic literature. It was tested through a range of thicknesses and with the addition of filler material. A static electro-thermal de-icing experiment was produced that was capable of characterising the energy cost associated with a coating's surface properties and bulk materials properties. The energy required to de-ice the surface increases linearly with coating thickness. PDMS containing 8.3 wt% of SiC submicron fibres reduced the per-thickness energy cost by 59% compared to PDMS alone. Dynamic electro-thermal de-icing was tested by attaching an iced sample atop an electro-thermal de-icing system at the end of a rotating arm. Spinning the arm at a fixed speed applied shear stress to the surface-ice interface subject to electro-thermal de-icing.

When the rotational speed was sufficiently high, airflow over the rotor increased the heat lost to the environment, significantly increasing the energy cost to de-ice. The linear relationship between coating thickness and energy cost was lost, with some samples failing to de-ice with sufficiently thick coatings. This highlights a key safety concern if an early passive coating fails.

Adding thermally conductive fillers to a coating will also change the accretion process as the transfer of latent heat of freezing will be higher for a more thermally conductive coating. Altering the coating could therefore alter the accretion formation process for a given environment. If a coating changes the accretion structure to one that has not been optimised to de-ice, then an iterative design would be necessary.

A cloud was simulated with a nebuliser in a freezing environment to form ice on the leading edge of spinning turbine blades. Properties of the cloud, flow conditions relative to the blades' motion and environmental temperature were successfully used to analyse a wide range of ice accretion structures and to understand how they form. This experiment has shown that it could provide a basis for modelling techniques to predict ice accretions and show how implementing a coating could alter the accretion. A second icing experiment forming accretions on a spinning disc shows promise as a preliminary icing test for candidate coatings. The results can inform how the coating will alter the accretions formed in the blade icing experiment.

Acknowledgements

To me, a PhD is possibly the one true opportunity I may get in my life to have the freedom to just think.

I truly love learning, and I am sincerely grateful to the people around me that have enabled me to do so. When I began, I knew that I was dyslexic and I was prepared to struggle through. It became apparent to me that my difficulty with writing was a significant barrier. The hiccups of a pandemic and lab fire halting my work were dwarfed by what I identified as apathy that I couldn't shake. With roughly five months left in the lab I was diagnosed with ADHD, and I lost all understanding of myself and who I was. I spent over a year struggling with medication to find something that worked.

The unwavering support and belief of my family allowed me to get diagnosed in the first place and deal with the trials that came with it. Without their help, my supervisors and the accommodations provided by the university I would not have a single chapter to my name. I have several friends whom I also deeply appreciate, Merryn would be the most disappointed in not being mentioned, so there.

I have had the pleasure of working with four supervisors over my PhD whom I would also like to thank. Dr Xianghui Hou was my supervisor for my final year project in my undergraduate degree and asked me to apply for this project. His depth of knowledge and respect for my ideas was exemplary of what a good supervisor should be. I would like to thank Professor Wei Sun for his help during the early stages of this project and his infectious optimism was always welcome, and Professor David Grant for helping push me over the finish line as a late arrival to my project.

I would like to thank Dr Barbara Turnbull, who has the stamina to be the only original supervisor still standing and who has supported me through turbulence in and out of the lab.

I have made great use of Sam Cook's technical support over the years and he has been exceptionally helpful. There have been several colleagues and research support staff at the University that have contributed in one way or another.

I would like to thank the final-year undergraduate students I have worked with over the years, who have made data collection more interactive.

I would like to thank Chris Hawkins and Richard Markiewicz from DSTL for providing such an interesting project and their technical support, funded under Contract No. DSTLX-1000129163.

Contents

List of figures

List of tables

List of abbreviations

Symbol	***Parameter***
α	*Thermal diffusivity*
$\bar{\lambda}$	*Average wavelength*
$\bar{h}$	*Average amplitude*
$\Delta\phi$	*Change in angle*
$\Delta\, G_{fv}$	*Gibbs free energy between the ice and the water*
$\Delta\, T$	*Temperature difference*
Γ	*Interfacial toughness*
γ_{LV}	*Surface tension at the liquid-vapour boundary*
γ_{SL}	*Surface tension at the solid-liquid boundary*
γ_{SV}	*Surface tension at the solid vapour boundary*
μ	*Dynamic viscosity*
μ_g	*Dynamic viscosity of the fluid*
ω	*Angular velocity*
Ω	*Motor speed (rpm)*
φ_{glaze}	*Glaze angle*
ρ	*Density*
ρ_p	*Particle density*
ρ_s	*Density solid phase*
σ	*Surface tension*
σ_{sl}	*interfacial tension between the ice and surrounding water*
σ_Y	*Yield strength*
τ	*Shear stress*
τ_{ice}	*Ice adhesion strength*
θ	*Angle*
θ_a	*Advancing angle*
θ_r	*Receding angle*
θ_{tilt}	*Angle of tilt*
$+-$	*Standard error of the mean*
$2D$	*Two dimensional*
$3D$	*Three dimensional*
A	*Area*
a	*acceleration*
A_{shard}	*Area of the shard*
A_{tip}	*Area of the tip*
$AERTS$	*Adverse Environment Rotor Test Stand*
Al	*Aluminium*
C_D	*Drag coefficient*
C_l	*Chord length*
$C_{l,x}$	*Chord length at position x*
c_p	*Specific heat capacity*
CAH	*Contact angle hysteresis*
CAT	*Centrifuge adhesion test*

CC	*Carbon coated*
CNT	*Carbon nanotubes*
d_p	*Particle*
E	*Young's modulus*
$E_{coating}$	*Young's modulus of the coating*
E_{ice}	*Young's modulus of ice*
$ESEM$	*Environmental scanning electron microscope*
F	*Force*
FEA	*Finite element analysis*
ft	*foot*
G	*Shear modulus*
h	*Ice thickness*
I	*Inertia*
k	*Thermal conductivity*
L	*Characteristic length*
ℓ	*Radius of the solid-liquid interface*
l_0	*Characteristic length of the particle*
L_{am}	*Angular momentum*
L_c	*Critical length*
l_{edge}	*Edge length*
L_{ml}	*Melt layer depth*
l_{shard}	*Length of the shard*
$L_{solidification}$	*Latent heat of solidification*
LIT	*Low interfacial toughness*
LWC	*Liquid water content*
m	*Mass*
$m_{expected}$	*Expected mass*
$MMAD$	*Mass median average diameter*
MVD	*Median volumetric diameter*
$MWCNT$	*Multi-walled carbon nanotubes*
NaF	*Sodium fluoride*
$PDMS$	*Polydimethylsiloxane*
PLA	*polylactic acid*
$POTS$	*1H,1H,2H,2H-perfluorooctyltriethoxysilane*
q_l	*Vector of local heat flux for the liquid*
q_s	*Vector of local heat flux for the solid*
r	*Radius*
R	*Length of the leading edge*
r^*	*Critical radius for nucleation*
r_{tip}	*Radius of the blade tip*
R_v	*Maximum profile valley depth*
Re	*Reynolds number*
Re_{tip}	*Reynolds number at the tip*
$Re_{transition}$	*Reynolds number at the transition point*
rpm	*Revolutions per minute*
S	*Stefan number*
S_a	*Surface arithmetical mean height*

S_{dq}	*Root Mean Square Gradient*
S_{dr}	*Developed Interfacial Area Ratio*
S_{td}	*Texture direction*
SAM	*Self-assembling monolayer*
SEM	*Scanning electron microscope*
SiC	*Silicon carbide*
$SLIPS$	*Slippery liquid infused polymer surface*
St	*Stokes number*
t	*Coating thickness*
t_0	*Particle relaxation time*
T_b	*Boundary temperature*
T_m	*Equilibrium freezing temperature*
u	*Local flow velocity*
u_0	*Local flow velocity*
v	*velocity*
V	*Volume*
V_{drop}	*Droplet volume*
V_n	*Local rate of solidification*
v_{pn}	*Poisson's ratio*
WCA	*Water contact angle*
We	*Weber number*
$wt\%$	*Percent by weight*
$x/R_{leading\ edge}$	*Relative position along the leading edge*

Chapter 1: Introduction

Ice accretion causes many problems in the modern world, whether simple or more noticeable, like a car's windshield and the roads they drive on. To less apparent but more complicated problems to solve, like the leading edge of an aerofoil on a fixed-wing aircraft, rotorcraft [1][2], or wind turbine blades [3][4]. Current ice mitigation solutions utilise electro-thermal de-icing to shed ice on aircraft or cease the operation of wind turbines [5][6][7].

Although this project may have carryover to this issue of the power grid and fixed-wing aircraft, the primary focus was targeting the leading edge of helicopter and wind turbine blades. Ice accretion on wind turbines is a cause for stopped operation due to the risk of shedding during operation [8], which could be lethal to the recipient of the ice on the ground. Ceased operation due to ice causes losses of over 10% [8] in Swedish wind farms, and iced turbines suffer significant aerodynamic losses [3][9]. Icephobic coatings could provide an efficient solution to reduce this downtime and, in unison with electro-thermal de-icing systems, further reduce this downtime. Efficient use of heating systems to shed ice quicker before it becomes dangerous could allow safe operation in weather not ordinarily acceptable to do so. With this application, the energy required to de-ice must be smaller than what is produced during the additional operation time of the turbine so that it can reach a position of consideration as a possible mitigation strategy. Operation in severe weather conditions is particularly relevant as a given turbine's performance depends on the airspeed and density. The density of air changes significantly with temperature, causing cold and windy places to be the best locations for power output [9]. Being in a colder environment increases the risk of ice accretion, which, as well as creating the issues above, can cause structural damage due to fatigue on load-bearing features due to the ice adding weight and increasing vibrations due to uneven and added loading on the blade [10].

In aerospace, the areas where ice causes the most significant issues are the aerofoil's leading edge and the nacelle's leading edge, surrounding the engine [6]. Ice forms most prevalently here because the surfaces are close to perpendicular to the direction of travel, meaning any impacting water has the highest dwell times here as the relative velocity is the lowest after impact at the stagnation point. The more time a droplet is in contact with these surfaces, the greater the opportunity for latent heat to be transferred to the surface and begin freezing [11]. This window ends when the airflow shears the water from the surface. If it does not shed, runback ice can form, most commonly after thermally de-icing the leading edge [12] [13]. If the ice forms further down the wing's chord, it is less of an issue as it affects the aerodynamics far less. If it causes the airflow to separate

from the aerofoil, it will happen further down the chord length. The risk associated with this ice is initially smaller but cannot be mitigated by the de-icing system located within the leading edge. Another area at risk of icing is the leading edge of the nacelle of an engine intake; ice buildup poses a risk of shedding large pieces into the engine and damaging it.

Another significant issue is the rotor blades on helicopters. A small buildup on the leading edge can alter the flight characteristics enough to destabilise the aircraft, similar to fixed-wing aircraft. The ice alters the geometry of the aerofoil, reducing lift, increasing drag, and reducing the stall angle, making the aircraft less efficient and more challenging to control and fly safely. If left, the ice can cause fatal crashes.

Rotational applications such as rotorcraft and wind turbines add more complexity to the problem than fixed-wing aircraft. Whilst both cases are affected by environmental conditions such as cloud conditions, temperature, wind speed and operational speed, rotating applications have several factors that vary along the leading edge, such as local air velocity, within that identical climate by virtue of the rotation. Considering how this impacts the ice formation process along the leading edge and the mechanical loading present, it has the potential to allow more specificity when providing a solution. Utilising different mechanisms and tailoring a coating's properties for the location on a blade might provide a solution more readily than attempting to produce a uniform coating. Tailoring the solution would potentially mitigate any one coating's shortfalls, which is required to be reliable in various operational environments and local conditions along the blade.

Icephobic coatings have been identified as a passive solution capable of mitigating the dangers caused by icing and making electro-thermal de-icing systems redundant, producing a significant energy saving. As passive icephobic coatings often lack durability and research often focuses on improving one metric of performance, a viable solution may remain out of reach in the near future. Little consideration has been applied to designing an icephobic coating with the goal of enhancing electro-thermal de-icing systems rather than replacing them. This could provide a meaningful improvement to many applications, and if a passive solution is possible, it could provide a wider understanding and inform further research.

Helicopter blades may be the most extreme potential application, so a passive solution may never be possible. Targeting this application ensures that research in this direction is much more meaningful. A less demanding application would likely find a suitable passive solution readily, making researching a hybrid solution redundant. As the titanium erosion shield on the leading edge of a

helicopter's rotor blade is a lifespan-limiting part when operating in a high erosion environment where abrasive wear is extreme, it is reasonable to assume that any icephobic coating will not be more durable and, therefore, the active system must remain. Other applications, such as commercial fixed-wing aircraft, would likely have passive solutions retroactively applied due to the vehicle's lifespan. Additionally, confidence in the passive solution will require flight testing and its impact on the efficacy of the active system must be known if the coating fails to de-ice during the test flight.

This provides a window for icephobic research to produce testing methods and coatings with very different goals to those for a passive solution without necessarily detracting resources from that goal. This leads to potentially achieving a passive solution sooner with the additional understanding obtained and proven efficacy within the field, driving demand for further research.

Chapter 2: Literature review

2.1 Different types of ice structure

There are two main categories of ice, glaze and rime, that have very different properties and formation conditions [14]. Glaze ice is clear and sometimes referred to as wet ice as it is not entirely frozen as it forms with a wet growth regime [15]. The freezing front moves slowly enough to not wholly solidify the liquid film before additional droplets impinge the surface. It is the densest form of ice with little to no porosity [14]. It forms when the freezing rate is slower at warmer temperatures, because it is a Stefan-type boundary condition [15]. From precipitation, this ice occurs from large droplets as freezing rain between 0 and -10°C [14]. It is much more difficult to remove from surfaces because it is far less likely to fail cohesively, and more of the interface is ice than air pockets due to its higher density. Increasing the porosity at the interface reduces the fraction of the surface area experiencing surface-ice adhesion [14]. A consistent interface minimises stress concentrations and risks mechanical interlocking with topographical features if the surface is fully wetted before solidification. It often forms when there is poor heat transfer between the supercooled water and the surface, limiting the release of latent heat [6]. As it is more difficult to shed it is typically used for testing ice adhesion strength. A lack of porosity of the adhered ice provides more consistency in testing due to its uniformity and its transparency allows quality control of the interface.

Rime ice is the other primary category of ice, and there are soft rime and hard rime ice, and both are in a completely frozen state [14][15]. These form rapidly after a supercooled droplet hits a solid surface and the latent heat is quickly diffused [6][15]. This causes a more discrete freezing process where droplets freeze fast enough that solidification occurs before the addition of more water to the surface. So, the freezing process outpaces the rate of water impingement, unlike glaze ice produced by wet growth. Alternatively, mixed icing occurs where a higher density glaze ice increases latent heat transfer by having a higher thermal conductivity than rime so that denser glaze ice accelerates the freezing of additional droplets, which form rime, which slows further growth, inducing denser ice on the rime [15].

The rate of latent heat transfer in relation to the sensible heat boundary conditions, described by the Stefan number, dictates the growth rate and, by extension, the type of ice formed for a given cloud condition. Rime ice forms at lower temperatures as the more supercooled water/surface induces faster freezing and smaller droplet diameter — the lower the temperature and wind

speed, the lower the density of the rime. Smaller droplets in clouds form soft rime rather than hard rime or glaze ice [14], where the Stefan number can be used to describe the growth rate present. The higher the water content in the cloud, the denser the ice that forms. For precipitation icing, wet snow is initially easy to remove but can prove difficult after complete freezing. Wet snow is formed between 0 and 3°C and is slightly liquid with a similar density to soft rime ice [14]. Glaze ice can span further along the chord length as the water can travel further as it is freezing, whereas rime forms a wedge on the leading edge [16].

Suppressing ice nuclei formation and suppressing crystal growth are the two primary functions an anti-icing surface must have to succeed. The surfaces most equipped for this are superhydrophobic. These utilise a low surface energy and a high roughness topography to trap air and produce a high water contact angle (WCA) [17][18], limiting heat transfer to the surface [19] and reducing friction between the droplet and the surface by reducing the contact area. In certain conditions, ice can form between asperities of superhydrophobic surfaces, causing mechanical interlocking, which increases the adhesion strength compared to when no interlocking occurs [12]. For example, tiny droplets could condense within the roughness and freeze before coalescing into larger droplets that would be forced above the air pockets by their surface tension. High-speed supercooled droplets could overcome their capillary pressure and displace the air to fully or partially wet the surface before freezing [20]. This limits the applicability of high-roughness hydrophobic surfaces in icephobic research [21][22].

2.2 Existing de-icing systems used in aerospace

If an aircraft does not have a functioning de-icing system, the only option is to move to low-risk air, typically losing altitude to warmer air and out of clouds. This procedure is not very useful, relies heavily on warning systems, and is a high-risk mitigation strategy without a guarantee of success as the aircraft may not be near safer air. If there is a risk of ice forming pre-flight on the ground, glycol-based sprays are often employed in airports to de-ice fixed-wing aircraft [23]. This method does not require energy supplied by the aircraft and is very effective for stationary craft. Unexpected use causes delays that could cause missed changeovers and logistical attention within the airport. The sprays vary but typically contain ethylene glycol or propylene glycol that have a high biochemical oxygen demand [24], meaning they can negatively affect aquatic life as microbial life uses oxygen in the water to breakdown both ethylene glycol and propylene glycol, the two most common constituents. In some cases, the liquid must be

heated before being sprayed [23], increasing the system's energy consumption. The liquid often wets the wing during take-off before the airflow is fast enough to shear the fluid from the surface, making it susceptible to further ice accretion. The take-off is the cause of most accidents as pilots pay more attention to the vertical speed than the horizontal, and the effect of the ice seems less noticeable [6].

Smaller aircraft without the ability to carry significant power systems use pneumatic rubber boots that inflate on the wing [25]. Once solid ice forms, it can be inflated to cause a crack at the interface and the ice to detach. The issues with this method are that the system requires regular maintenance and repair, and the flight characteristics are altered for the brief period the boots are inflated. If they are inflated too soon, they can cause ice formations that the system can no longer shed. This issue arises because if they are inflated before a solid layer has formed, the ice can crack and refreeze in the geometry of the inflated boot that remains fixed when the boots deflate, increasing the negative impact of the ice and making it more difficult to remove [25].

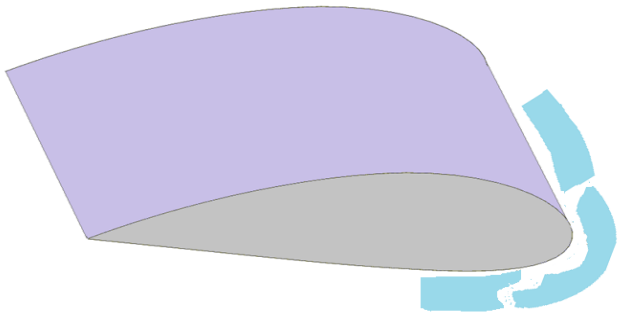

Figure 2.1 Diagram illustrating the target area electro-thermal de-icing systems in aerospace to remove the ice from the leading edge of the aerofoil.

In the World War Two era plane, Avro Shackleton WR90, the leading edge Figure 2.1, contained plywood which, during icing conditions, would be soaked with methylated spirits by a pump activated by the pilot. This method was somewhat unreliable due to the delay in thoroughly soaking the wood in the system. Figure 2.2 shows the piping used to pump the methylated spirits.

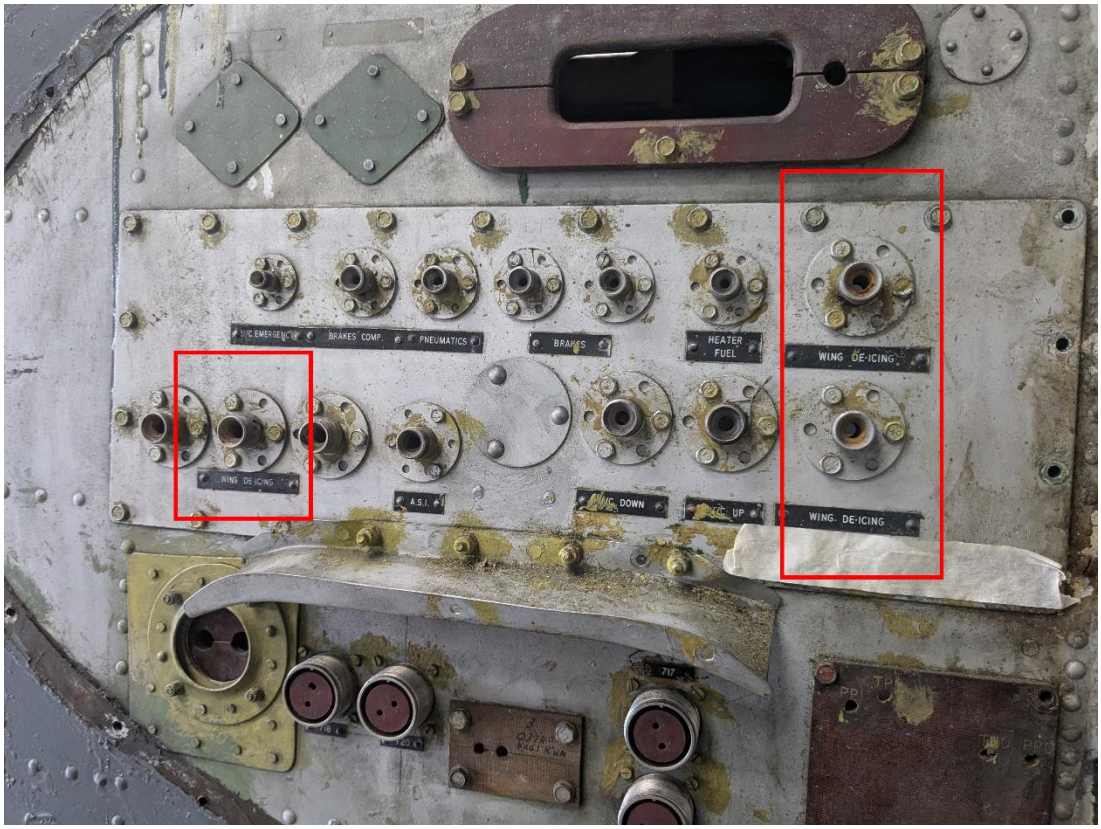

Figure 2.2 Piping outlets from the fuselage to the wing of an Avro Shackleton with the de-icing pipes for methylated spirits highlighted. Image taken by the author at the Avro Heritage Museum.

Until over a decade ago, the typical method for commercial aircraft was to bleed hot air from the compressor stage of the jet engine. This hot air was then piped through the wing's leading edge, shown on the right in Figure 2.1, and around the nacelle to melt the ice. This significantly reduced the efficiency of the engine and required a heavy piping system. The Boeing 787 Dreamliner bucked the trend, having sprayed metal mats in the composite layers of the wing to form an electro-thermal de-icing system [26]. This is three to four times more efficient than the air bleed systems and does not impact the performance of the engine as significantly.

The aerospace industry aims to have fully electric aircraft by ~2050; modern aircraft use multiple power sources. Using many systems such as pneumatic, electrical and mechanical means added weight for the separate systems and unifying the power systems would improve efficiency and move away from the use of fossil fuels. So, the industry is driving to embrace electrical systems and improve efficiency in power-hungry applications such as de-icing [26]. One part of the icing in aerospace problem is the response time of the heaters and the effective use of the heat produced. As the heaters do not need to be continuously

operated, they have a delay where the energy input is used to heat the heating element itself and the material between it and the surface that may have a high volumetric heat capacity. Ideally, using a lightweight heater that can be easily incorporated into current structures that efficiently dissipates electrical to thermal energy to the surface only, with a low specific heat capacity to improve the response time when heating the surface. This has been achieved with a superhydrophobic surface [27].

The focus of this project is, in part, how the surface affects ice formation while focusing on its removal and efficient use of electro-thermal de-icing systems already in place. It aims to produce a coating that enhances the electro-thermal de-icing system's performance, utilising it and the forces applied to the ice via airflow and any cyclic loading from any present vibrations to provide a low-energy solution. Whilst it must be durable enough to have an economically viable lifespan on an aircraft or wind turbine, which could potentially operate in a very harsh condition such as a helicopter taking off in a dusty environment, the coating could also provide a sacrificial layer protecting the structural components, extending the lifespan of the blades, providing significant savings in repair and maintenance costs. This in turn will produce trickle-down savings by reducing aircraft downtime, saving human resources, the space it requires, or making operations like mountain rescue and air ambulance more widely available for the same capital.

Helicopters suffer more from icing than other similar-sized vehicles due to their operation altitudes and the importance of mass distribution due to the high rotation speeds of the rotor blades [28].

2.3 The mechanisms of hydrophobicity and its contribution to icephobicity

As the aerospace industry moves towards more electric aircraft to improve efficiency and move away from the reliance on fossil fuels, electro-thermal de-icing systems are preferable. A way to improve the efficiency of any de-icing system is to minimise the time required to be operational. A simple way of doing this is delaying ice formation. For this reason, hydrophobic surfaces were of initial interest to the field, defined as having little to no affinity with water. The water contact angle (WCA) shown in Figure 2.3 is used as an experimental measurement [29]. Merely viewing a sessile droplet smaller than the capillary length for the surface, millimetric in length, and measuring the tangential angle of the droplet at the interface relative to the interface. If the droplet is larger than

the capillary length, the drop becomes flattened as weight exceeds the surface tension, altering the shape of the minimum energy state. This occurs because the gravitational energy scales with a higher order of the radius of a spherical droplet compared to the surface tension [30] due to them being proportional to volume and surface area, respectively.

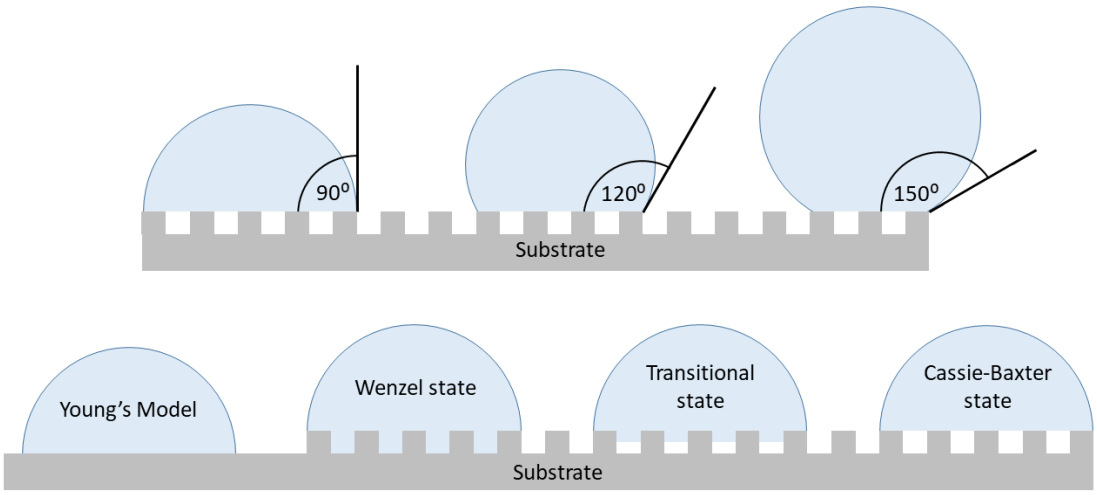

Figure 2.3 Visual representations of different water contact angles and wetting states.

If this angle is >90^0, then it is hydrophobic and superhydrophobic if it exceeds 150^0 and the contact angle hysteresis is less than 5^0 [29]. Many factors determine this angle. First, we will consider a homogeneous surface (Young's model). The droplet has two interfaces: a solid-liquid surface area and a liquid-vapour surface area, with a third surface of the solid-vapour interface. The shape of the droplet, therefore the WCA, is determined by the ratio of these surface energies at the three-phase boundary. The droplet forms in the lowest energy state possible by balancing the surface tension of these two interfaces in the environment, typically air (1) [29] [30].

$$cos\theta = \frac{\gamma_{SV} - \gamma_{SL}}{\gamma_{LV}} \qquad (1)$$

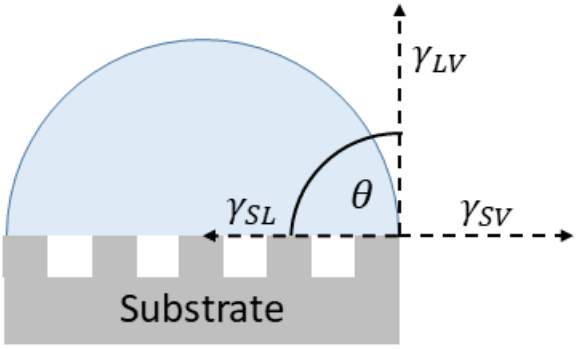

Figure 2.4 Visualisation of the effect of surface energies on the water contact angle.

where γ_{XY} is the surface tension between surface *X* and surface *Y. S, L,* and *V* denote solid, liquid and vapour, respectively. The system is in equilibrium when the energy is at the minimum, which can be derived by altering the solid-liquid contact area's radius and calculating the surface energy's variation.

If the solid-vapour surface tension is larger than the solid-liquid plus the liquid-vapour surface tension, then the lowest energy system is when the liquid completely wets the solid, so the least amount of the solid is in contact with the vapour as possible. This occurs with low surface energy substrates such as noble metals and glass without any pollutants on the surface and with liquids with extremely low surface tension, such as silicone oils [30].

If $(\gamma_{SL} - \gamma_{SV}) > \gamma_{LV}$, $\theta = 180°$, shown by inversing a complete wetting situation, such as blowing a bubble of air into a box of silicon oil, where the bubble rests at the ceiling with a contact angle of 180^0. This is impossible for water on a surface surrounded by air. The limit for homogenous surfaces seems to be in the region of 120^0 [29], achieved by waxes and fluorinated materials with a low surface energy on polished silicon. Surface energy is defined as the energy per unit area required to make a new surface. For example, it can be derived from the energy to increase the length of a crack in the material. It is easier to work with surface tension than surface energy for liquids. In the case of water, the surface tension increases the lower its temperature.

Most solids are heterogeneous and rough, possibly not to the naked eye, but with micro or nanoscale roughness. This affects the contact angle as a millimetric droplet will encounter many such defects and can fix the water surface at the edge of a roughness feature. The energy to bridge the air gap to the next is too significant to make the result of wetting the surface further a lower energy state. The scale of the droplet is possibly several orders of magnitude larger than that of the surface features. The measured contact angle can vary across the surface

as the interaction will vary slightly depending on the droplet's location relative to the location of the asperities on the surface. Considering a droplet with a stable contact angle and slowly increasing its volume on a surface with roughness, the contact area will not change until the threshold WCA is reached. After this, the radius of the contact area increases as the edge of the water moves as the surface tension is overcome, as shown in Figure 2.5. This maximum WCA is known as the advancing contact angle or θ_a. Using a syringe to remove the water allows the opposite to be viewed, *receding contact angle* or θ_r both shown in Figure 5. $\theta_a - \theta_r$ is known as the contact angle hysteresis [30], which is commonly used as a predictor of icephobicity [31].

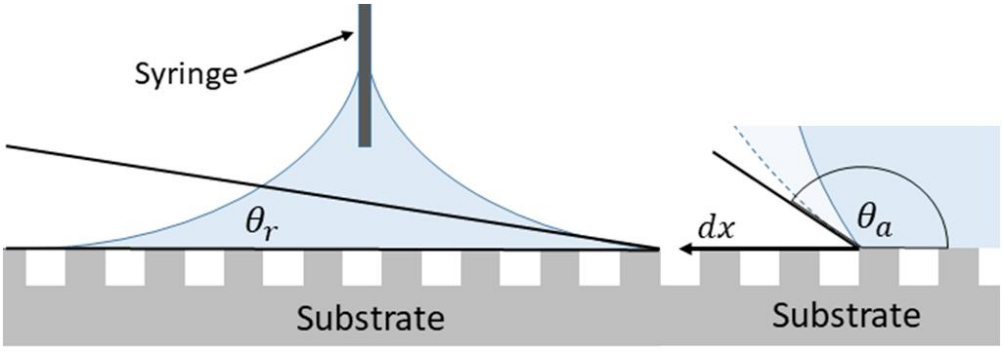

Figure 2.5 Visual description of the receding and advancing contact angles, respectively.

Hydrophobic properties are helpful because the water can be removed more easily from the surface for applications like self-cleaning glass. One measure of this is the roll-off angle, where the surface is inclined until the droplet rolls down the surface [32]. Immediately before this, the most downhill point has a WCA of θ_a (advancing angle) and the most uphill point, θ_r (receding angle) a schematic describing what both angles represent is illustrated in Figure 2.5 and Figure 2.6, where tilting the surface any steeper would cause the droplet to become unstuck. If the contact angle hysteresis is small, the roll-off angle will be low as there is only a small window of movement for the centre of mass before overcoming the adhesion strength due to the electrostatic attraction between the surface and the water and moving it past the boundary of the contact area on the surface. Whether the droplet remains stuck depends on the limit (2) [30].

$$\pi \ell \gamma_{LV} (cos\theta_r - cos\theta_a) \geq \rho g V_{drop} sin\alpha \qquad (2)$$

Where ℓ is the radius of the solid-liquid interface, V_{drop} is the droplet volume, and α is the angle of tilt.

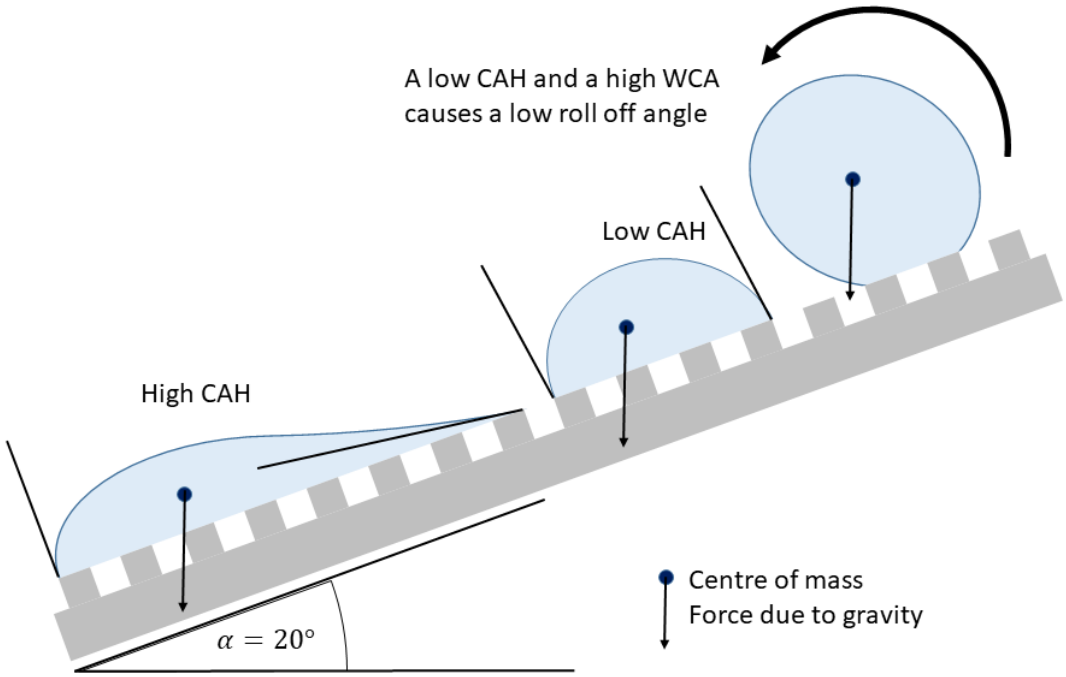

Figure 2.6 The effect of a high contact angle and contact angle hysteresis on the roll-off angle of a sessile droplet.

A low contact angle hysteresis and roll-off angle requires a very high WCA, higher than a flat surface can achieve. Many naturally occurring surfaces, such as the lotus leaf or rose petal, exhibit superhydrophobicity. These surfaces have hierarchical roughness features coated in a low surface energy material, a film of wax [10] [34] [33]. The hierarchical roughness is typically an ordered structure of $\sim 10\ \mu m$ features covered in $\sim 1\ \mu m$ features of a different morphology. Some animals are superhydrophobic, with features ranging as small as $100nm$ to micrometres. Manmade superhydrophobic structures often contain roughness features of a wide range of scale with sharp angular drop offs from the uppermost point, like narrow square posts [35].

Roughness enhances the surface properties regarding WCA [18], Figure 2.7, making high surface energy materials more hydrophilic and low surface energy materials more hydrophobic. Another reasoning for this depends on how the substrate wets. If, for example, the roughness is in the form of pillars and the water doesn't completely wet the structures there is a significant proportion of the solid-liquid interface that contains pockets of air [11] [19] [36], meaning the

surface area in contact with the water is significantly lower than apparent from a millimetric view, despite the increased surface area of the substrate. Altering the equation for the energy change to have a roughness factor, R_f, which is the actual surface area divided by the flat area. A surface roughness parameter describing this is S_{dr} which is expressed as a percentage of the increase in surface area due to the topography from the projected area being measured.

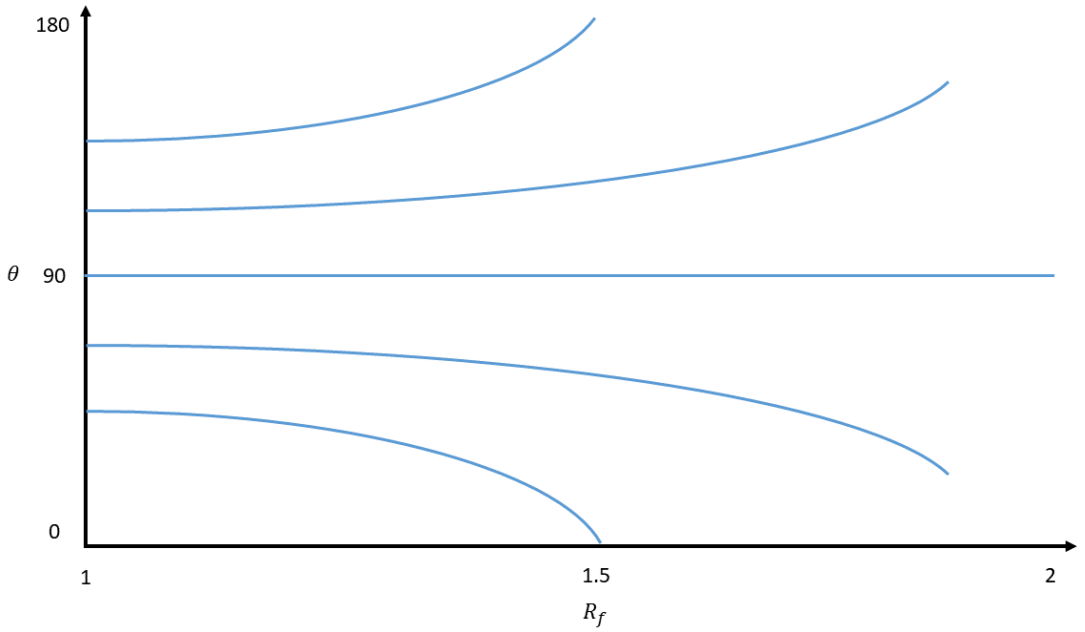

Figure 2.7 General trend between water contact angle and a surface's roughness factor. Trends taken from [18], describe how increasing the surface roughness of a hydrophobic material will make it more hydrophobic and hydrophilic material more hydrophilic.

Wenzel's model works by calculating the change in surface energy with a small displacement of the contact line; however, on a rough surface that is wholly wetted, where θ is Young's angle that is for a flat surface, this relationship has been shown to be qualitative but not quantitative. It also suggests that a $\theta_a = 180°$ can be achieved, which is not the case [30]. In the Wenzel state, the droplet completely wets the surface, leaving some liquid behind in the cavities, decreasing θ_r. This can cause some hydrophobic surfaces to have a more hydrophilic θ_r as the roughness increases before increasing the WCA as the surface becomes superhydrophobic. As such, increasing the roughness is not always an improvement if the geometry causes undesirable wetting states.

Superhydrophobic structures are not directly crucial for icephobic coatings, as explained in the following section and have been described as not being a viable

solution [21]. However, once the surface has experienced wear, the surface roughness will change, and how it does so may dramatically improve the anti-icing properties but will hinder de-icing performance in certain wetting conditions. Knowledge of hydrophobicity is essential to understanding the surface's response to wear and how this will affect long-term performance in harsh operating conditions.

2.4 Icephobic surfaces and their mechanisms of function

2.4.1 Anti-icing properties

Superhydrophobic properties possess great potential for delaying ice formation, and a wide range of surface designs have been successfully used to produce these properties [29]. If water strikes a superhydrophobic surface, it can rebound, easily roll off or be shed by shear flow. Reducing contact with the surface reduces the potential for ice to form. Ice formation requires the transfer of latent heat from the water to form ice. The rate of which is affected by a multitude of factors. The most obvious is the temperature of the droplet and surface, mainly if they are supercooled and by how much [6]. The thermal conductivity of the surface material is similarly important. If the surface allows fast thermal transport, the water can freeze quicker as the latent heat passes to the surface more readily over the same contact period [37]. Assuming that the substrate is large enough that no droplet meaningfully changes its temperature, thermal conductivity is most appropriate. If the substrate temperature changes noticeably, thermal diffusivity is more appropriate as the boundary conditions are not in equilibrium. A higher WCA is relevant because freezing will be much slower if the solid-liquid interface is small relative to the droplet size. On a homogeneous surface, the material's surface energy determines this [38][39]. The wetting state of the droplet also affects the heat transfer. If the water contact angle is high, the footprint of the droplet on the surface is small. However, 90% of that footprint may be air pockets as it acts as a composite interface with the water of trapped air and the surface [18]. Further limiting thermal transport and delaying freezing. However, if the droplet is in a Wenzel state, as opposed to a droplet in the Cassie-Baxter state, then the actual surface area in contact will be higher rather than lower due to the roughness factor [17]. The droplet having a low CAH improves the ability for shear air flow to remove the droplet as well as

the roll-off angle when coupled with a high WCA, limiting the contact time of the water [40].

On surfaces employing a hierarchical structure to make a superhydrophobic surface, it may exhibit a jumping droplet phenomenon where small droplets condense of the surface until they grow and join [41]. Once they coalesce, they can jump out of plane due to a release of surface energy as the water forms a lower energy state, and the excess is transformed to kinetic energy that is significant enough to remove the droplet on a high WCA and low CAH surface, which increases the delay for frost formation of the surface [39][41]. Having nanostructures makes the surface far more susceptible to mechanical wear and, therefore, degradation in performance, as an abrasive impact damages the structure. If there is not a hierarchical structure, only microscale, then the surface is vulnerable to condensation within the structure in particular environmental conditions. Eventually, the surface will be fully wetted in the Wenzel state. If this then freezes and is removed mechanically without any melting, one freezing cycle could destroy the structures [29].

The interface is the most important as, in almost all cases, heterogeneous freezing is dominant; homogeneous freezing will occur eventually, with the latent heat being transferred to the air instead, especially if the airflow is significant but not enough to shear the droplet from the surface. Meaning that ice formation is inevitable despite how well a surface may delay formation at the surface [39].

Some porous surfaces are wholly wetted with a liquid to improve their icephobic properties. One such example would be a liquid that lowers the freezing point of water it is in contact with, increasing its supercooling ability compared to superhydrophobic surfaces due to a lack of nucleation sites [39]. These are called liquid-infused surfaces, also known as SLIPS, which do not have any air pockets, allowing high performance to be maintained under frosting conditions [42]. These surfaces can lose their lubricant layer through high shear flow, gravity, or by wetting other solid or liquid interfaces. This and possible pollution of the liquid leads to a deterioration of function [11]. To prevent this, nanostructures on the surface are imperative to increase the Laplace pressure, and larger asperities can be exposed and be the edge that pins the water droplet, causing a high WCA. These surfaces can rival many superhydrophobic surfaces but require further design optimisation to provide a practical lifespan.

Most anti-icing testing is qualitative rather than quantitative, such as the mass of accretion per unit area, which has far more practical significance [11]; however, it is far more complex and costly to simulate realistic icing conditions. Some methods include using wind tunnels [42] and then comparing the change in mass. Superhydrophobic surfaces perform better in this test as the droplets can

bounce or roll off before freezing. Some work has been done with this experiment where a hydrophilic filter paper impregnated with a hydrophilic lubricant outperforms generic materials like aluminium and copper and filter paper with a hydrophobic oil [42]. This phenomenon shows that wettability and surface energy do not dictate ice accretion and that anti-icing surfaces cannot consistently maintain their properties. The first frost layer alters the surface from hydrophobic coating to hydrophilic ice. This is especially important when considering the possible application of the coating. If the coating design choices favour anti-icing properties too heavily, the ice accretions may be less frequent but more severe due to the coating's lack-lustre de-icing performance.

2.4.2 De-icing properties

A significant portion of the work on icephobic coatings has been developing highly elastic, low surface energy materials [12]. This is because one of the main factors in ice adhesion strength is the ability of a material to initiate a crack between the surface and the ice. This mechanism is known as interfacial cavitation and occurs due to large stress distribution at the interface caused by a significant relative difference in the elastic modulus of the ice and the coating [40]. A cavity forms as an energy release mechanism due to a buildup of elastic instability withing the coating. Ice has a Young's modulus ranging up to around 8.5 GPa [43], which is lower for lower-density accretions. The most effective materials utilising this mechanism are soft polymers with a low surface energy and a low elastic modulus, such as fluorinated PDMS. As a force is applied to the ice, the coating elongates and compresses due to the load at a far higher rate than the ice. In every case, the loading is not in pure shear and has a peel stress element perpendicular to the interface[44][45]. Depending on how far away from the surface, the force acts as a moment is applied about the surface. For many testing methods of ice adhesion, this force acts around the centre of the body of ice or at least its height. Either the mechanical force acts across a whole face, or the centre of mass is the location in centrifuge adhesion test (CAT) for example [45].

Low surface energy is vital as the electrostatic forces between the ice and the surface are the driving forces keeping them adhered to one another. This is determined by the chemistry of the coating, which is where much of the research in this field has been done. It also determines the WCA of an atomically flat surface [46]. The surface chemistry is an essential component for ice adhesion as, for example, functional groups such as a hydroxyl group can form hydrogen bonding with the ice and increase the adhesion strength, while fluorinated

compounds have very little electrostatic interaction and a high water contact angle [32].

Electro-thermal de-icing systems are becoming more common in aerospace [12], meaning thermally conductive coatings are necessary for a low-energy solution to ice accretion. This has the caveat of faster ice accretion due to latent heat transfer through the surface, reducing its anti-icing properties [47]. A lower thermal conductivity would induce a higher proportion of both runback ice, which is less problematic but would produce more glaze ice or mixed icing which has a higher adhesion strength than rime ice.

A low roughness has been found to reduce ice adhesion strength by mitigating any mechanical interlocking between the ice and the surface [21][48][49]. This poses a significant issue as superhydrophobic surfaces are incredibly rough. If the ice forms in the Cassie-Baxter state, the adhesion strength is low as the interface surface area is very small and has several contact points that cause stress concentrations for crack initiation, so a low ice adhesion strength. However, ice does not always form in this state. Large, high-velocity, supercooled droplets can partially or fully wet the surface and freeze before rebounding or remaining fully wetted, having displaced the air between the asperities. Small, supercooled droplets or vapour form within the roughness structure and freeze before they grow large enough that the lowest surface energy state rests on top of the asperities [11]. This mechanical interlocking poses two issues: the larger surface area in contact with the ice and the interlocking increases the adhesion strength; when the ice is removed, the interlocking causes severe damage to the surface structure by the cohesive failure of the coating [21]. Cohesive failure of the ice can also occur, which is not ideal as some ice will be left behind, providing a site for rapid nucleation of supercooled droplets impacting the surface. The damage to the superhydrophobic structure will reduce the surface's anti-icing capabilities, meaning the durability and lifespan of the surface is very low without considering abrasive wear or the impact of airborne particles. Considering this, low-roughness coatings are ideal for low ice adhesion strength despite the lowered WCA and related anti-icing properties due to high-roughness surfaces. This is a significant reason why superhydrophobic surfaces are not suitable for de-icing [21].

Another factor in de-icing is crack initiation [50]. Once the ice begins to separate from the surface, the energy required to propagate the crack is typically much lower than the energy threshold required to create one. As the area of the interface reduces due to the growth of the crack, the stress increases, mainly local to the crack edge, causing fast propagation and failure. It has been proposed that in order to reach low ice adhesion strengths on non-slippery surfaces, multi-scale crack initiation features must be present [50].

Superhydrophobic surfaces with a simple post structure have shown a lower adhesion strength compared to a similar surface with a higher density of identical posts; the increase in edges for crack initiation has been attributed to this improvement [42]. This result is surprising as the solid fraction of the interface with the ice is higher, so a higher ice adhesion strength would be expected to scale with it due to lower stress per post for the same force applied to the ice. One coating has been synthesised using an icephobic polymer matrix and microparticles of highly elastic gel. The discrepancy in elastic modulus between these pockets of gel and the surrounding material caused stress fields under shear loading, causing cracks to form above these particles reducing the adhesion strength of the material. Having these particles evenly dispersed in the matrix allows this mechanism to function after the top surface is removed or worn away. This is extremely promising as a method to reduce the adhesion strength of flat materials; however, this coating's durability was not sufficient for practical use [51].

Ice adhesion strength is ineffective for holistically determining a coating's de-icing performance [52]. Measuring a surface's interfacial toughness, the ability for a crack to propagate, has been identified as a more desirable method of designing coatings for larger de-icing applications. Where ice adhesion strength scales with the area of adhesion, low interfacial toughness (LIT) coatings reach a limit in the length scale of adhered ice where the force required for detachment does not increase with any further increase of the adhered area [52][53][54]. These surfaces are limited by the force required to initiate a crack and once produce it propagates freely, so the measured ice adhesion strength decreases for length scales past the critical length. These coatings are often not elastomeric and perform better with a thinner coating, unlike elastomeric coatings, which better utilise interfacial cavitation with a thicker coating. This mechanism is extremely promising for producing a passive icephobic solution.

Little research was available considering the employment of icephobic coatings alongside active systems at the start of this project, and its potential has been considered more readily since with the testing of coatings alongside thermal de-icing systems [12][55][56][57][58]. A clear negative of this approach is that the successes may largely be made redundant when passive solutions become viable. As coatings are most likely to be retroactively applied to structures currently using a thermal de-icing system, testing alongside them could provide an early avenue for success. Or form the basis of safety testing to predict the coating's impact on the efficacy of the active system and prevent unforeseen circumstances when testing passive solutions. Delaying an active system's ability to de-ice before catastrophic failure occurs would be a significant concern. As the coating properties that would aid thermal de-icing are not

necessarily conducive to a successful passive icephobic solution, investigating how different properties affect the thermal de-icing performance and the relative sensitivity between them was identified as a means to provide clarity as to the potential successes or safety concerns. For example, reducing a coating's thermal conductivity effectively delays nucleation [11]. This would inhibit an active system. A thicker coating would benefit elastomeric icephobic coatings [59] by reducing ice adhesion strength but increasing interfacial toughness [52].

This research considered this approach the most viable for de-icing helicopter blades where the harsh environment will limit any coating's lifespan. The titanium erosion shield is a concern for operation in dusty environments where abrasive erosion is extreme [1]. If applied to these blades, it is reasonable to assume that providing a sacrificial coating with icephobic properties would be easier to achieve than a coating more durable than the erosion shield that is also sufficiently icephobic to phase out the use of the active system. Producing a coating that can be easily reapplied, perhaps in the form of a tape, would be versatile, extend the lifespan of the blade, and, if successful, improve the blade's icephobicity. The flexibility of elastomers would lend themselves to be used in this way and allow curing to be completed on a flat surface, reducing inconsistencies or complexities of the manufacturing process.

2.4.3 How the surface affects ice nucleation and growth

The formation of ice is a complex system and can occur in three main ways: vapour-solid deposition or frosting, vapour-liquid-solid freeze, and liquid-solid freeze. The nucleation and growth of ice are linked to the phase changes[11]. The cloud conditions influence the structure produced by means of dwell time, regularity of features and growth rate. The growth rate is determined by the Stefan number, (3) [60], which relates the release of the latent heat of solidification to sensible heat, where $L_{solidification}$ is the latent heat of solidification, c_p the specific heat capacity, T_m the equilibrium freezing temperature and T_b the boundary temperature. In calculations within this work, the boundary temperature is assumed to be the environmental temperature.

$$S = \frac{L_{solidification}}{c_p(T_m - T_b)} \tag{3}$$

The Reynolds number describes the flow conditions over the aerofoil (4) [61]. This helps predict fluid flow by relating inertial forces present in the flow to the viscous forces of that fluid, where ρ is the density of the fluid, u is the local flow velocity,

L is the characteristic length of the object in the flow, and μ is the fluid's dynamic viscosity.

$$Re = \frac{\rho u L}{\mu} \tag{4}$$

The Stokes number describes whether a droplet's change in velocity is inertia or flow dominant, (5) [61]. When combined with the Reynolds number, this can be used to predict particle flow within a fluid flow. With u_0 representing the local flow velocity, l_0 the characteristic length of the particle and t_0 the particle relaxation time (6), where ρ_p is the density of the particle, d_p is the diameter of the particle and μ_g is the dynamic viscosity of the fluid.

$$St = \frac{t_0 u_0}{l_0} \tag{5}$$

$$t_0 = \frac{\rho_p d_p^2}{18\mu_g} \tag{6}$$

Homogenous freezing occurs due to the spontaneous formation of hydrogen bonds that form an ice nucleus until it reaches a threshold Gibbs free energy [11]. More ordered hydrogen bonds form at this point, and the growth accelerates. If this energy is not met, then the water becomes supercooled. Once the threshold is met by supercooled water, the latent heat can be rapidly released, causing fast expansion of the freezing front and raising the temperature of the water to t_m. The growth of the nuclei increases the surface energy at the liquid interface. However, the formation of these nuclei reduces the system's free energy (7).

$$r^* = \frac{2\sigma_{SL}}{\Delta G_{fv}} \tag{7}$$

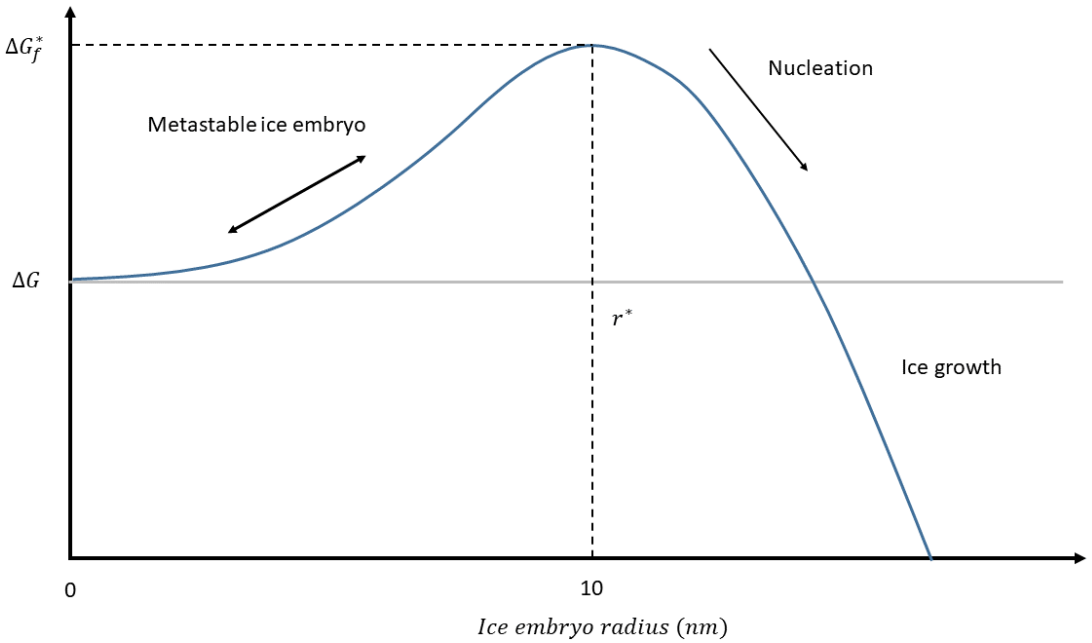

Figure 2.8 The relationship between Gibb's free energy and the ice's radius, illustrating the critical energy boundary required for freezing to propagate. Relationship taken from [11][39].

Water forms ice when the ratio of the two parameters in (7) equates to roughly 5 nm and $r^* \cong 10\ \mathrm{nm}$ for bulk water, Figure 2.8, where supercooled water is in an unstable state, ice embryos form and destabilise before growing to the critical radius, r^*, and the temperature of the water can fall below 0°C without solidifying.

The surface can influence this initial accretion by reducing the probability of ice nucleation and reducing the initial rate of growth if it does if nucleation does occur. If an unstable embryo contacts a surface, it can aid in exceeding r^* and If that surface readily absorbs the latent heat, the growth rate can accelerate until equilibrium is achieved.

2.5 Targeted surface and material properties

Icephobic and hydrophobic coatings often have a deficit of durability as they often rely on delicate surface topography or highly elastic material [62]. Depending on the targeted de-icing method, a high thermal conductivity or thermal diffusivity can be very influential, with a more thermally conductive material more appropriate for working alongside a thermal de-icing system but more susceptible to ice nucleation and faster accretion growth [11]. A rougher surface has been linked to higher ice adhesion strength [21] and a higher

interfacial toughness [53] by causing adhered ice to interlock with asperities and inhibit crack propagation mechanically. Providing a greater resistance to shear forces and a higher surface area for Van der Waals forces to act while increasing the distance a crack must propagate. A low surface energy reduces the Van der Waals forces between the surface and either water or ice [22] [46]. This increases WCA, and reduces CAH and ice adhesion strength [22][32]. A low ice adhesion strength is ideal for limiting the maximum size an accretion can grow to before being shed. A low interfacial toughness provides an effective method for de-icing large surfaces as the force required to initiate the crack becomes the dominating factor past the critical length [52][53].

When considering ice adhesion, strength is defined as the shear stress to remove ice the required force scales with the area. Most structures with ice accretion issues have a substantial surface area, such as an aeroplane wing. This means a potentially huge force is still required to de-ice an entire wing despite small pieces of ice can be easily shed. Another perspective is to look at the adhesion strength as the bonding energy at the interface, so the interfacial toughness. Analytical models have shown that when the ice surface is small, the adhesion strength model is predominant, which is modelled as instantaneous removal, where $\tau_{ice} = \tau$, where τ is ice adhesion strength and τ_{ice} the apparent adhesion strength. However, over large areas, the interfacial toughness is predominant as the propagation of a crack is dominant, not its instigation. The critical length at which the interfacial toughness of a material becomes the overriding factor is described in (8) [52].

$$L_c = \sqrt{\frac{2E_{ice}\Gamma h}{\tau_{ice}^2}} \tag{8}$$

The modulus for ice $(E_{ice}) \cong 8.5GPa$ and the thickness of the ice is h and the ice behaves in a brittle manner and is treated as an elastic solid. If: $\frac{2E_{ice}\Gamma}{\sigma_Y^2} < h < L$ with σ_Y being the yield strength of ice and $L > L_c$, where L is the length scale, L_c the critical length, τ_{ice} the ice adhesion strength and Γ the interfacial toughness. The force necessary to remove the ice is constant, meaning there is also a critical area for a fixed thickness of ice, past which the weight alone will be enough to remove the ice. This model represents the energy to create a crack that reaches a critical separation height between the ice and the surface [52]. The applicability of a surface to function using this mechanism will vary on the effect of ice

thickness on the function of the surface. For example, a few millimetres could impact the functionality of an aerofoil significantly.

This means that the ideal surface would have a low ice adhesion strength and a short critical length for the interfacial toughness to be the dominant factor in ice removal. Many coatings with low ice adhesion have a critical length large enough for large surface areas. They perform worse when compared to common polymers with a much higher adhesion strength but smaller critical length, Figure 2.9, Figure 2.10.

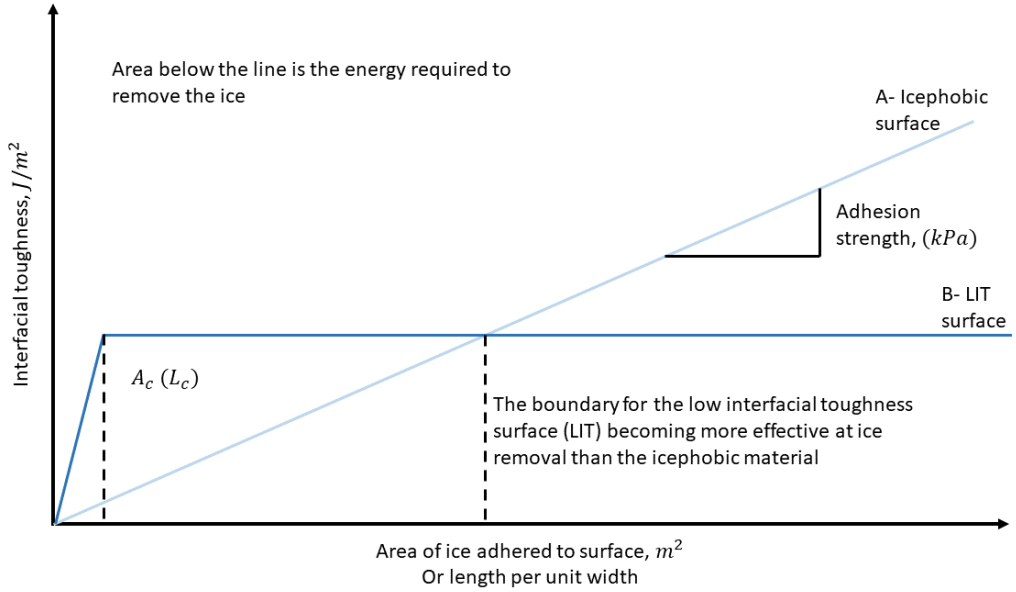

Figure 2.9 How the peak force at failure changes with the size of ice accretion for low interfacial toughness materials and icephobic materials, illustrating a limit that is reached due to the mechanism of failure. Trends taken from [52].

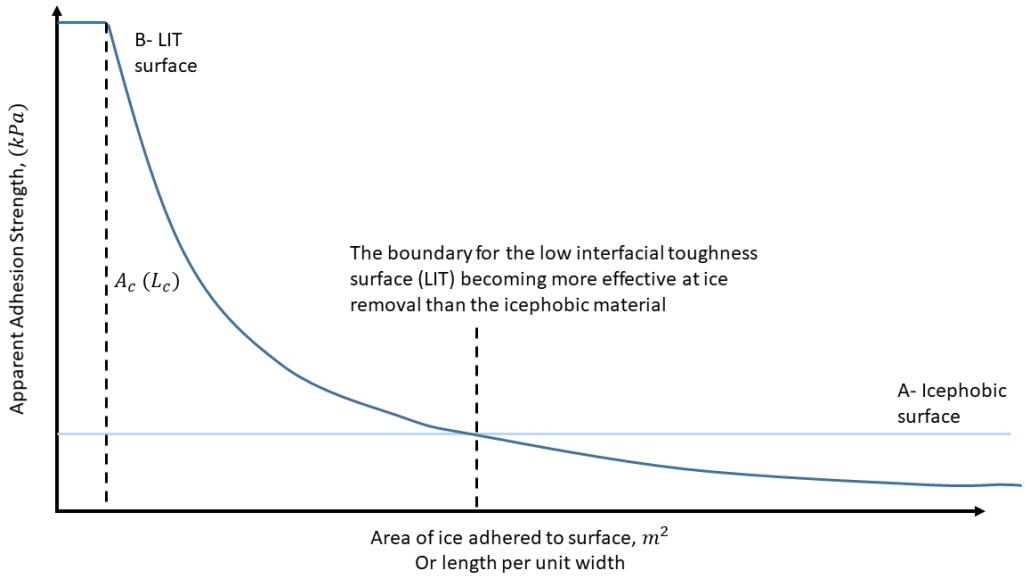

Figure 2.10 Comparing the force applied and the area of ice removed to determine the adhesion strength (F/A) as shear stress. This shows that the larger the surface, the more critical the interfacial toughness is. Trends taken from [52].

If both the adhesion strength and interfacial toughness are low, the coating will be effective at passively removing ice accretions of all scales. Prompting crack initiation may help bring down the critical length for the interface for polymers with a large L_c and low τ_{ice} or, more likely, just reduce the adhesion strength while maintaining the critical length. Keeping the interfacial toughness down can mean that over large areas of ice, the ice adhesion strength is lower than that of a low adhesion strength polymer that has a large critical length.

This critical length is for a fixed width, meaning the result of the toughness is in J/m^2 [52]. On an infinite 2D, vertical plane, there is also a critical thickness of ice that cannot be surpassed, and the weight of the ice will overcome τ_{ice}, the critical length does increase with the ice thickness however. Ideally, a surface would have a critical ice thickness for all forms of ice lower than a threshold to cause severe risk if the de-icing system fails.

These two aspects of measuring de-icing capability pose an interesting question as to how thick a coating should be. For low ice adhesion strength materials, the thicker the highly elastic coating, the better it performs as the range of motion from the same strain is much larger, increasing the rate of interfacial cavitation due to the difference of elastic modulus at the interface, $\tau_{ice} \propto 1/t^{\frac{1}{2}}$ [59]. This improvement due to increased thickness will have a limit caused by the adhesion strength of the coating to the surface or the shear failure of the coating. A larger force will be required to achieve the same strain as a thinner coating but with lower stress.

However, work on the interfacial toughness suggests that thinner coating performs better [52] when causing failure by this mechanism. This means that the thickness of a coating could be tailored to the size of the application. Larger surfaces that are at risk from large sheets of ice should have thinner coatings than those more sensitive to ice. However, many largescale applications of icephobic surfaces require durability from weathering and possible high levels of erosion, such as helicopter blades that have to take off and land in dusty environments but fly in icing conditions. Simply put, if the coating is extremely thin, then wearing through it will take far less time. Once a hole has formed, there is a risk of water going underneath the coating and causing it to peel if poorly bonded, causing a rapid deterioration in performance. A thinner coating is also more energy efficient when coupled with an electro-thermal de-icing system as there is simply less material to heat and a shorter distance the heat must transfer across. However, this will increase the adhesion strength for small ice accretions and reduce the coating's life span. The result used to display this compares a coating $2\ \mu\mathrm{m}$ thick and $150\ \mu\mathrm{m}$ thick. Having an interfacial toughness of roughly $2\ \mathrm{J/m^2}$ and $3\ \mathrm{J/m^2}$ respectively [52]. This energy difference has been attributed to the strain energy of the coating. This comparison shows a significant reduction; however, possibly a severe compromise in the lifespan of the coating. This is what these coatings excel at, particularly when considering the precision required to apply it to a large surface area, which will likely not be flat and may have difficulty navigating geometry. Increasing the thickness does have the obvious negative of more material costs per unit area, which could mean the cost is multiple times larger. However, if the coating is repairable by local reapplication and requires total reapplication less frequently, this may reduce the lifetime cost and downtime for any aircraft.

Circling back to the interfacial toughness, the equations provided in this paper can be adjusted as follows to make predictions about a coating's large-scale performance (9) [52].

$$\Gamma \approx \frac{\tau^2 t}{2G} \tag{9}$$

Where τ is the adhesion strength, t the coating's thickness, and G is the shear modulus of the coating. The ideal material for a low interface toughness should have a high shear modulus, low thickness and low adhesion strength.

To achieve a low adhesion strength, except in the case of lubricated coatings, a low elastic modulus is necessary to facilitate failure by interfacial cavitation.

Shear modulus is the ratio of shear stress and shear strain but can also be represented in relation to the Young's modulus, E,(10).

$$2G\left(1 + v_{pn}\right) = E \tag{10}$$

Where v_{pn} is the material's Poisson's ratio, we can relate (9) from [44] and (10) to assume the following two new relationships to help design coatings in this project, the first being (11).

$$\Gamma \approx \frac{\tau_{ice}^2 t(1 + v_{pn})}{E_{coating}} \tag{11}$$

Relating the critical length to the elastic modulus provides (12).

$$L_c \approx \sqrt{\frac{E_{ice}}{E_{coating}} 2ht(1 + v_{pn})} \tag{12}$$

Suggesting the ideal material would have a low ice adhesion strength but a high elastic modulus to minimise $E_{ice}/E_{coating}$, this is contrary to much of the non-lubricated icephobic work [12]. The work in this research project used the PDMS due to its reasonable durability for an elastomer and low elastic modulus. However, (12) suggests that the critical length for this material will be substantial because of its elastic modulus. A new study has shown that a low interfacial toughness can be achieved with PDMS [63].

The critical length does not depend on the ice adhesion strength of the material in (12). This seems to be the case as when comparing the effectiveness of a polymer and the same polymer plasticised with oil, the oil noticeably improved the apparent adhesion strength with only a slight increase in the critical length — providing a significant improvement to the interfacial toughness as the interfacial toughness scales slower and flattens off at the same length [52].

One issue is potentially the Poisson's ratio of the material, which could be in the region of 0.5, which is typical for PDMS and rubbers [64]. Looking at (11), this could drastically increase the interfacial toughness compared to a material with a low Poisson's ratio, for example, 36% more than an identical material with a Poisson's ratio of 0.1. This suggests that the best material for a matrix would be stiff and have a low Poisson's ratio with hydrophobic properties. That has the

lowest adhesion strength possible for a material that does not utilise interfacial cavitation, so adhesion will likely be dominated by a low surface energy.

This could present an opportunity to utilise auxetic materials. Having a negative Poisson's ratio could cause significant stress at the interface, aiding crack initiation. This may produce a surface that performs well in both failure methods: interfacial cavitation and interfacial toughness. As interfacial cavitation is caused by stress at the interface due to a significant difference in the elastic modulus of the surface and the ice, as the leading face of the ice stretches the material away from the trailing edge. If the surface has a negative Poisson's ratio, the material will also stretch away from the perpendicular edges. After contacting the author of the LIT research, auxetic materials had been explored with little success, so they were not pursued within this body of work.

2.6 Testing methods for icephobic performance

2.6.1 General challenges when testing ice adhesion strength

In standard adhesive testing methods such as a lap shear tests, the adherend is required to be stiffer than the adhesive, which is the means of force transfer from one adherend to the other Figure 2.11. This ensures that the failure will occur due to the adhesive. In many ice adhesion tests, the ice is both an adherend and an adhesive, which can be considered an interfacial zone of similar magnitude to the surface roughness. This often results in cohesive failures of the ice and not an interfacial adhesion failure. Lap shear tests can be performed with ice; however, forming a strong bond can be difficult, and due to the geometry impacting the formation process of the ice, it cannot be used effectively [65].

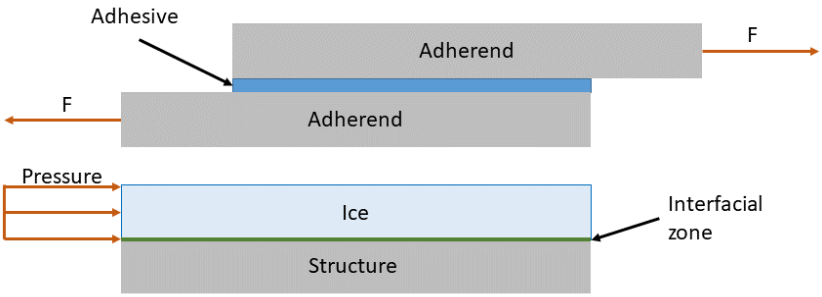

Figure 2.11 How a lap shear test varies from other ice adhesion tests.

Mechanical ice protection systems seek failure by applying forces to the underlying structure. The aim is to cause delamination of the ice from the surface. This happens due to the adherend deforming, causing the ice to deform, delaminating or failing cohesively. Adhesive ice failure tends to happen because peel stress causes interfacial cavitation, where the ice delaminates from the surface and is typically initiated away from the edges where shear stress dominates. This is in the form of pneumatic rubber boots or ultrasonic de-icing systems [66].

Ice adhesion strength is measured as the shear stress required to remove ice from the surface. The main issue with this concept is the lack of pure shear testing methods [65]. This would require the force to be applied in the same plane as the interface with no strain on the ice or surface. This brings to question the accuracy of the results measured and the reliability of the surface's performance between different testing methods and equipment for the same method. Even when considering a lap shear test using a thin ice sample, a simple arrangement will lead to flexion of the adherend beams and stress concentrations at the corners [45]. This method is also very prone to cohesive failure if any cracks are present in the ice, which will be challenging to check for before testing due to the geometry of the equipment. There are many methods of testing ice adhesion strength, and variations of the two most common methods were used in this project, which will be explored further in this section.

The temperature at which the testing occurs is critical as the adhesion strength varies with it [46][55]. The colder the temperature, the stronger the adhesion. However, the rate of change is different for different materials and can depend on the temperature range; a defined relationship has not been researched [65]. The temperature could also affect elastic materials as they may reach a temperature where they become much less pliable, reducing their effectiveness at utilising interfacial cavitation[40]. The standard deviation also varies with temperature, typically quite high when approaching zero and more consistent at

colder temperatures [65]. Standard deviation is a significant problem when testing ice adhesion due to many factors, such as heat input from the user or non-uniformity of temperature in the substrate, strain rate and stress concentrations being present [65].

The most significant issue, particularly between different studies, is stress concentrations, as all tests assume an even distribution of force when this is not the case. In the example of an ice cube, shear stress will concentrate at the corners and dominate at the edges, mainly the two corners in the leading direction of the force. However, at the back, the peel stress will be higher than at the front, as any moment will cause the front to nosedive and the back to lift, and the ice rotates about the front edge of the interface. These are rarely considered and will vary significantly with ice geometry, with tests often using simplified geometry, which is more reliable to test but far from what forms on aircraft. The ice will vary across the surface, and features like horns and runback ice will alter how the stress is distributed [65].

The strain rate can also affect the adhesion strength by an order of magnitude; this can be difficult to control in centrifuge tests, the effect of which may vary for different material's failure mechanisms. Notably, as low adhesion materials will fail at lower speeds and experience a different strain rate than high adhesion strength materials, the larger the difference in the adhesion strength, the greater the disparity in strain rate at failure. Lap shear tests have the lowest standard deviation, but controlling the ice is a problem, particularly if you want to test impact icing [65].

The presence of peel stress in testing methods affects the relative performance between material and coating categories. A low elastic modulus coating becomes more effective at shedding ice with additional peel stress, and a greater strain perpendicular to the interface causes a cavity or crack that can then propagate along the interface, as shown in Figure 2.12.

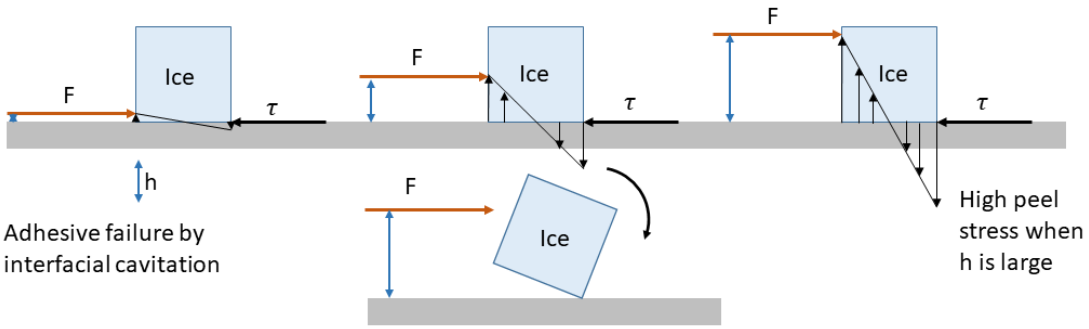

Figure 2.12 The effect of where the force is applied and peel stress, which is rarely accounted for in ice adhesion testing.

Discrepancies between different publications can also be attributed to unreported roughness of the substrates or only undetailed parameters such as r_a; this will significantly affect the results and their standard deviation.

There are numerous issues, and as a result, the adhesion strength is often referred to as an ARF or adhesion reduction factor, typically using aluminium as a reference material. This then has the issue of what alloy, roughness, and exposure to water before looking at how the ice is formed, the geometry of the ice and the way it is tested [65]. A significant amount of contextual information is often lacking, which will impact the results and reduce repeatability between laboratories. Standardisation is a massive problem in this field. It can somewhat be mitigated if adequate context is listed with the methodologies used.

Several methodologies test glaze ice due to its imperfection-free interface, transparency and high adhesion strength. As this ice forms from a slow, wet growth regime, it may pose a source of error if the freezing time is insufficient for it to be reliably solid throughout.

2.6.2 Centrifuge ice adhesion test (CAT)

In these tests, the motion of the ice is used to induce a shear force on the interface of the ice and the surface it is adhered to rather than applied directly to the ice mechanically [67]. A known mass of ice is spun faster and faster until it separates from the surface to which it is adhered. Using the rotational speed at the instance of separation ω, the radius of the ice was spun at r, the adhered area A and the mass of the ice m, to infer the adhesion strength τ_{ice} (13).

$$\tau_{ice} = \frac{mr\omega^2}{A} \quad (13)$$

There are a variety of centrifuge tests, and the first was used in 2005 [67], the centrifuge adhesion test (CAT) is in the Anti-icing Materials International Laboratory. This system uses a counterweight to minimise any vibration that would apply cyclic loading to any stress concentrations that are not accounted for directly. Shear stress is predominant at the edges, with peel stress dominating under the main body of the ice [45]. As the shear strength of the ice adhesion is assumed to be uniform across the surface, it can only be used as a qualitative result. As such, the result is reported as the adhesion reduction factor (ARF) ratio, which is the comparative ratio of the adhesion strength of an uncoated sample to a coated sample. The higher the ratio, the better the performance of the coating, the reduction factor being the adhesion strength of aluminium divided by the adhesion strength of the coating in question [45][67]. Comparing the base aluminium value with other literature can be difficult as many other variables affect the adhesion strength, which does not remain constant across the literature, mainly due to its oxidation layer and potential to react with water over time.

Many samples for the CAT are formed at once, ensuring identical conditions to minimise discrepancies in the ice within repeats from each batch. In each batch, there are three uncoated reference samples, three with the potential icephobic coating and one sample to measure the ice density. All are measured before and after to determine the mass of the ice on each beam. While this method of sample production is consistently repeatable, some features are not. As the samples are made from low-impact spray, the edges have non-uniform geometry, which affects the stress distribution [67].

The beams with ice adhered to them are then accelerated at a constant rate, with the speed at which the centrifuge was spinning being inferred from the impact of the ice onto the surrounding wall, which contains the centrifuge rig (destroying the ice sample), the impact is registered by piezoelectric cells within the wall itself. Cohesive failures can be easily disregarded as the first impact of ice on the wall stops the test. Once the beam has stopped spinning, any ice that is still adhered can be easily identified, and the result is marked down as an invalid data point and removed. Another method is using the sound of the impact to record the time taken from when the motor begins spinning. The speed can be inferred from the constant angular acceleration applied to the arm [49] [67].

The centrifuge method is the most commonly used method of ice adhesion testing [46] [49], and FEA has shown that the stress distribution is predominantly

shear and relatively even [37]. A straightforward issue with repeatability is the ice used. Like with all testing methods, a layer of transparent glaze ice is desirable at the interface unless testing impact ice is required. This assures a lack of porosity and the most reliable and strongest adhered ice for that temperature. It also eliminates risks of cracks, causing stress concentrations that initiate adhesive or cohesive failure, which could lower the apparent adhesion strength measured, so the surface appears to perform better than it should. Peel stress also has this effect as it is a product of the moment about the interface from the centre of the applied force [45][65]. In the example of the centrifuge test, the position of the centre of mass. If the ice is not symmetrical, this will lead to uneven force distribution. If the centre of mass is high, then there will be more peel stress than if it was close to the interface. A drawback of having a flatter geometry of ice is that it will have less mass for the same area of the interface. This could make surfaces with a high adhesion strength untestable in the equipment being used if a high enough rotational speed cannot be attained. However, the result will be more sensitive for low-adhesion materials as the mass determines the force applied to the interface at a given speed.

Altering the geometry of the adhered ice while maintaining the total volume would present higher or lower peel stresses by changing the position of the ice's centre of mass relative to the surface. If the tested coating relies on a mechanism to produce a low ice adhesion strength that disproportionally benefits from the presence of peel stress, also referred to as normal stress, this will affect the result [51][68]. A taller ice accretion will produce a higher peel stress from the applied rotation, and the change in its surface area and drag coefficient could further compound this discrepancy. As such, the methodology of a CAT could be tuned to produce more favourable results for certain categories of coatings or suggest that altering certain properties of these coatings appears more effective without this appropriate contextual information. Elastomeric coatings are a prime example of this as peel stress is very beneficial for interfacial cavitation as the coatings ability to experience greater strain than the adhered ice, pushing on the ice that is adhered forces the far edge of the adhered area into the surface and the near edge up, any cavity that forms will more readily expand if there is greater stress normal to the interface. Thicker elastomeric coatings have a lower ice adhesion strength [59], with the mechanism more accurately defined by sliding a rigid slab across a PDMS film [68].

If the geometry of the ice changes from a hemisphere to a cube, the height above the surfaces that the resulting centre of mass changes from 3/8× r to 0.5× l_{edge}, with r the height or radius of the hemisphere and l_{edge} the side length of the cube. For a hemisphere of radius 1 cm, the centre of mass is 0.375 cm above the surface, the centre of a cube with the same volume would be 0.64 cm above the

surface. As the peel stress increases as the applied force increases, the impact of this discrepancy compounds as the measured ice adhesion strength increases. This would go some way to explain the difference in obtained values between laboratories all testing aluminium, for example, and the trends produced within each equipment's data [12][46][49][51][62][69][70]. This hypothetical change will also affect the drag coefficient as the shape changes and the surface area drag acts on. Increasing the applied peel stress in the plane perpendicular to the rotor arm means the geometry of ice used provides a significant reason for discrepancy depending on the equipment.

Considering drag further, the stress force applied at detachment is measured based on the angular velocity at the point of shedding and the mass. A higher mass of ice will shed while experiencing a lower relative air velocity for a given area of adhesion. This means that the influence of drag is a further source of error between methodologies that is dependent on the geometry of ice and velocity at adhesion failure. Additionally, if the shedding occurs at a lower speed, any cooling from the airflow would be less significant unless the test is sufficiently long. As ice adhesion strength varies with the environmental temperature [46], knowing this variable would be useful context for comparative or replication studies. Dynamic methods such as the CAT also have the drawback of potential vibrations weakening the interface, which will vary across equipment. Both from the structural design and the induced airflow creating turbulence.

2.6.3 Mechanical push tests

How the force is applied is also crucial for mechanical push-pull tests, where a force is mechanically applied to the stationary ice. Assuming an even force distribution from the pushing face, it can be assumed that a point force is applied at the centre of the surface in contact with the ice. Typically, with this kind of test, the mechanical pusher, or harness pulling, is either a flat surface or that is in contact with the entirety of one side face of the adhered ice or a force probe. It can be assumed to be applied at half the height of the ice cube if the entire surface is pushed against or the centre of the force probe face. Altering how the load is applied will alter the stress on the interface. Models of these tests indicate that more peel stress can be present and produce less uniform results than centrifuge tests but can be carried out in a smaller cold chamber or Peltier stage with fewer safety risks due to high-speed parts [45][65].

2.6.4 Durability testing of coatings and surfaces

Most icephobic surfaces lack durability, and this has been tested using abrasion and erosion by spraying an abrasive suspension [71][72], for example of, silicon carbide powder at high pressure to simulate in-flight wear. Water impinging tests with no abrasive and separate teste with an abrasive surface [73] Many surfaces in the literature do not test this extensively, and many superhydrophobic surfaces have their durability measured in freezing and de-icing cycles [40][51]. The structural damage caused by the forceful removal of ice limits the application of many coatings. Coatings relying on surface structures are sometimes tested with scratch tests [74]. It is often worth testing coatings for durability after exposure to extended periods of humidity or ultraviolet radiation, which can significantly degrade polymers [75][76]. For these tests to be meaningful, they must be application-specific and not some erroneous attempt to display durability. If a category of surface struggles to survive freezing cycles or a less destructive test category that is not application-specific, it is largely not worthwhile to complete. If the study is novel, it may well be worthwhile, but not under the guise of producing or researching coatings targeting an appropriate application for that durability test to be comparable to operational conditions. Non-applicable durability tests can provide a useful addendum where less progress in durability is more easily quantified, suggest a wider range of possible applications, or identify progress that has been made.

2.6.5 Low interfacial toughness (LIT) testing

Low interfacial toughness testing measures the change in ice adhesion strength with the length scale of the ice being tested, where past a critical length for the adhered, the force required to delaminate the ice from the adherend no longer increases as the length scale increases. These tests use a force probe with a typical velocity of <100 $\mu m/s$ to allow for a more precise measurement of the point of adhesion failure [52][53][63]. Elastomeric coatings have been found to have a critical speed where an elastic solid pushed over its surface produces cavities as an energy-releasing mechanism for elastic instability in the coating [68]. The size of the cavity relates to the size of the object and the speed at which it is pushed over the surface. Past a certain velocity, the object becomes unstable due to the size of the cavity produced [68]. Testing elastomeric coatings below this velocity showed that a large cavity could form, initiating a crack, but the force applied was not sufficient to reach the critical velocity where the crack would propagate and sudden de-bonding would occur [53]. While testing for interfacial toughness is extremely valuable as knowing this property of a coating is clearly

useful, testing at lower velocities may inherently favour LIT coatings where a dynamic application such as a helicopter blade may be inherently unstable enough such that an induced cavity will more readily propagate a crack in a non-confined system.

LIT coatings on a curved surface have been tested for ice adhesion strength in a wind tunnel, where ice was accreted in 80 m/s air flow for 10 minutes and then detached in situ with the centrifuge method and successfully achieved a low ice adhesion strength [54]. This is an excellent example of an application-specific testing methodology that lacks some contextual information, like the thickness of the accretion and estimations of the Reynolds and Stokes number using the cloud properties and air speed provided with the geometry of the equipment. These values with images of the ice would help infer its applicability. With the information provided enough to show the applicable conditions, these details would allow for better comparative analysis or replication.

2.6.6 Enhancing thermal de-icing systems

The literature lacks testing of surfaces in parallel with heating systems or the improvement of heating systems, but examples are becoming more frequent [27][55][57][58][69][75][77]. This is fundamental to their performance in many de-icing applications until reliable, durable, passive solutions are accessible. This is incredibly important as an icephobic polymer coating with a low thermal conductivity may reduce the efficacy of an electro-thermal de-icing system, rendering it a hindrance once the ice accretion has formed, which is inevitable in prolonged icing conditions and can only be delayed [17]. Once the ice has formed over the surface, the surface has a limited impact on the growth rate of further accretions. A publication testing a SLIPS with heating showed it provided a 53% energy saving [78]. Another method is using a black cermet layer that absorbs almost all of the light that hits it, a thin aluminium layer, and then insulation below it, forming an energy-free system that relies on sunlight to efficiently heat the entire surface of the aerofoil [79]. It is effective in low-light conditions. However, it obviously will not work at night. This leaves it nearly useless in regions where extended night times are normal for a significant portion of the year, such as the Arctic Circle, and it would not be applicable for long-haul flights [79]. LIT coatings have been shown to be effectively enhanced with an active de-icing system by raising the temperature of the coating without melting the ice to promote effective shedding at colder environmental temperatures [55].

2.6.7 Ice accretion methods

Adverse Environment Rotor Test Stand (AERTS) is a large-scale rotational ice accretion testing method where a section of an aerofoil [7][80][81], referred to as a coupon, is attached to 9 ft diameter rotor arm with an overhead spray system producing icing conditions that has been used to test coating's shedding properties on a helicopter blade [7]. This is an incredible piece of testing equipment that allows for the high-quality analysis of ice accretion. However, requiring a 6 m × 6 m × 3.5m cold chamber, large blade system, 89.5 kW motor, 24 signal and power channel slip ring, 6-axis load cell in the bell housing, and an array of overhead icing spray nozzles, the accessibility for testing of this kind is low. Wind tunnels are more common and have been used to test icephobic coatings for anti-icing capabilities [82] or the importance of thermal conductivity of the surface [47], ice accretion structures [83], electrically heated coating with a superhydrophobic surface [27] in some cases forming ice to test ice adhesion strength with impact icing formed in cloud conditions [54]. Analysing the freezing process of sessile droplets is also utilised as a small-scale method to precisely test a coating's ant-icing capability [39][17][84]. Most icing analyses for rotary applications are limited to numerical analysis [85][86][15], likely due to the high capital required to produce adequate icing conditions for experimental study and the more complex geometry of turbine blades. A very recent study analysed the formation of runback ice behind a thermal ice protection system within the leading edge of an aerofoil in a wind tunnel [13]. This kind of experimentation and analysis is terrific to see and helps piece together every stage of the freezing and de-icing process to produce a more efficacious solution and approach to a solution.

2.7 Summary

The potential applications for icephobic coatings are varied and complex, and specificity must be at the forefront of icephobic coating design to find solutions and accelerate research progress. The leading edge of a helicopter's rotor blades is arguably the most challenging use case for icephobic coatings. Typical research aims of producing a passive de-icing solution are well out of reach for this application using current techniques. Adjusting the goals of a potential solution to improve lifespan de-icing outcomes rather than solve de-icing opens a broader range of possible research angles and creative design opportunities.

Designing a coating that can provide some of the typical passive benefits of an icephobic coating, such as a low ice adhesion strength and hydrophobicity, while synergising with an electro-thermal de-icing system could be of great use. This is a worthwhile pursuit as it is reasonable to assume any early candidates for a

passive solution will be retroactively applied to a structure containing an electro-thermal de-icing system. It is reasonable to assume that to ensure confidence in its initial application, some testing, or at least consideration, will be necessary to ensure that if the coating fails to perform as anticipated or through damage, it does not also insulate the electro-thermal de-icing system, causing it to fail to function effectively.

Testing icephobic coatings alongside an active system is occasionally performed as an addendum but is rarely the focus of performance or design. An apparent gap in icephobic research is a testing methodology for electro-thermal de-icing that can account for the coating's surface, material and geometric properties. If any aspect is missing, the results will be much less informative and accurate performance comparisons will not be possible. This approach can be applied to passive testing methods for properties such as ice adhesion strength, where increasing the thickness reduces an elastomeric coating's ice adhesion strength, it is reasonable to assume it will increase the energy an electro-thermal de-icing system will require to operate. Adding thermally conductive fillers will diminish the increased energy cost and could be utilised to improve the coating's durability. However, this would have a penalty, likely increasing the coating's stiffness and its ice adhesion strength. Furthermore, increasing the coating's thermal conductivity will more readily induce ice nucleation on the coating.

Such an approach to designing icephobic coatings will not be suitable for many applications. For some, it may be the only viable solution at present. To fully comprehend the additional complexity of designing a hybrid solution which uses the passive benefits of icephobicity alongside an active de-icing system, wider testing methods are necessary. Testing a hybrid solution in a hybrid operational scenario, where a shear load is applied to an ice accretion as an electro-thermal de-icing system operates, may highlight a window of opportunity for success—allowing a tailored solution to balance a coating's properties to provide a benefit. Considering the potential benefit of a sacrificial coating on the lifespan of a rotor blade and any changes to the frequency of icing events, severity of icing events, and energy cost to electro-thermally de-ice the surface, a cost-effective improvement may be found.

As the operational environment of helicopters is broad and the local environment along a blade also has significant variation in conditions, understanding how complex ice accretion structures form could also be profoundly informative on icephobic coating design. Adjusting the surface properties changes the fluid mechanics of impinging droplets, and the thermal properties can alter the solidification regimes, changing the type and form of ice accretions in an identical scenario. Analysis of the ice accretion process and understanding the impact of the coating on it and the ability to remove the resulting accretion can inform modelling techniques and accelerate the process by reducing the need for iterative testing.

Chapter 3: Project aims and objectives

This PhD project aims to highlight the need for specificity in icephobic coating design and expand what could be considered a successful solution by applying icephobic research to a modified use case that aims to improve an electro-thermal de-icing system and not replace it, with the explicit purpose that an imperfect solution could still be economically viable. This project must approach this problem with a complete understanding of how an icephobic coating designed to work passively may also hinder an active system. As an icephobic coating also changes the ice accretion process, understanding this process more precisely can inform modelling and iterative coating design to optimise for a specific application. A simple parameter, such as the thickness of a coating, can have a meaningful impact on a passive coating's performance and its durability. Adding performance requirements associated with working alongside an active system adds metrics that are also impacted by the thickness. This applies to heat transfer properties, which could be tuned to improve de-icing efficiency by adding thermally conductive fillers or reducing the delay in ice accretion.

Adding additional performance metrics is a double-edged sword as it adds more metrics to consider but reduces the critical reliance on any to be successful. A coating incapable of functioning passively may be suitable for a hybrid solution, potentially bearing fruit sooner than research limited to a passive-only solution.

The objectives of this project are as follows:

- Produce robust testing methods to characterise an icephobic coating's performance when used in tandem with an electro-thermal de-icing system. Allowing meaningful comparisons between laboratories to compare coatings and accurately identify causes of improvement.
- Identify key properties that require consideration when designing a coating to work alongside active ice protection systems. Then, extrapolate how altering each will impact the passive performance metrics, allowing other researchers to tailor every aspect of their coating with specific performance goals in mind.
- Simulate the ice accretion process on an aerofoil, considering how the surface and environmental conditions alter its structure and formation process.
- Produce an elastomeric icephobic coating to form the basis of testing and improve its electro-thermal de-icing capabilities with thermally conductive filler materials.

Chapter 4: Research methodologies

This work develops a portfolio of experimental methods to elucidate how the properties of icephobic coatings and surfaces effect electro-thermal energy consumption in a hybrid de-icing system. PDMS coatings were made varying the thermally conductive filler material and through a range of coating thicknesses and with different surface properties. Changes to ice accretion formation was also considered, since this a key parameter in evaluating the energy consumption per de-icing cycle.

The goal was to define how and if a coating could be designed for a specific application to maximise its benefits over its lifetime, specific periods of operation and individual icing events. The surfaces were characterised by static wettability and roughness, the material's thermal diffusivity was investigated, and icephobic performance was tested in a range of de-icing scenarios using mechanical loading, thermal de-icing and a combination of the two. The structure of ice accretions on a rotating body through a range of environmental conditions was observed to understand how the application of an icephobic coating could impact how ice accretion's structure and formation process may change for that operational environment. This section describes the methodologies used in sample preparation, characterisation, and testing protocols. All error bars in this document represent the standard error of the mean.

4.1 Substrate preparation

All substrates for samples used were 1.2 mm thick aluminium 1050 sheet cut to 50 mm by 20 mm with two 4 mm holes to allow the samples to be bolted down where necessary.

Each substrate was cut to size using a waterjet cutter, often made in large batches, to minimise any influence caused by any potential variation in the material and machining from batch to batch. A grit blaster was used to increase the surface roughness and improve the wettability of the to-be-coated surface where appropriate. The grit blasting machine used initially was a Guyson F1200 using 180-220 μm alumina particles and was replaced after fire damage with a Guyson F1400 with their Honite 13 CSS8 glass bead, also supplied by Guyson (UK) with a nominal size range of 106 – 212 μm, made from a soda-lime glass bead. Where suitable, this improved the consistency from sample to sample

within a batch and the coating thickness over an individual sample. Substrates that were not blasted or polished, which would have reduced the roughness of the aluminium or removed any imperfections, such as small scratches that may have been imparted onto the surface when machined, are referred to as smooth aluminium or as-received aluminium and are tested throughout as a reference value.

Once machined or grit blasted, the substrates were cleaned using acetone and then distilled water to remove any machining grease and residue from the surface. An ultrasonic bath was used to remove dust or debris from the substrates or coatings submerged in distilled water and then dried using compressed air.

The discs used in the ice accretion experiment described in section 4.6.2 measured 190mm in diameter and 8mm thick and were made from aluminium 5083/NS8. The preparation and cleaning of these discs also required cleaning with acetone and distilled water; however, they were not ultrasonically cleaned due to their size.

4.2 Raw materials

Polydimethylsiloxane (PDMS), by the name of Sylgard 184, is a two-part silicone elastomer with room-temperature cure capabilities produced by Dow Corning and purchased from Farnell. Silicon carbide fibres labelled as nanofibers by the seller, Sigma Aldrich, however, are referred to as submicron or microfibres in this research as the diameter is quoted as <2.5 μm with a length to diameter ratio greater than 20 and a 98% trace metal basis. Nano diamond powder with a spherical size ≤100 nm was purchased from Jichang Metal Processing Ltd. (China). Multi-wall carbon nanotubes (MWCNT) purchased from Sigma Aldrich (purity>95%) with the dimensions, outer diameter of 6-9 nm and 5 μm in length, which were produced by chemical vapour deposition. Xylenes (≥98.5%) (mixture of isomers, referred to as xylene in this document) and acetone (≥99.5%) were purchased from Sigma Aldrich. Two grit blasting media were purchased from Guyson (UK), the first was 180-220 μm alumina particles, and the second was a ceramic zirconia-based blast medium with a nominal size range of 250 – 425 μm. A 1.2 mm thick 1050 aluminium sheet was purchased from the faculty stores and machined to specification by the faculty workshop technicians, initially sourced from Smith Metals (UK). Aluminium 5083/NS8 discs were purchased from and machined by Laser Expertise Ltd (UK).

4.3 Preparation of coatings

Polydimethylsiloxane (PDMS) became the focus of research as a matrix material after trials alongside some polyurethane variants that less reliably wetted the substrates when the thickness was reduced. PDMS performed better in this category and has been well-studied in icephobic research [59][72][87][88]. Producing a range of coatings to compare these properties was achieved by adjusting the thickness through the manufacturing process and adding silicon carbide as a filler material to alter the coating's thermal properties. Surface properties such as the surface's topography and water contact angle are strongly linked to icephobic performance. The surface of the as-received aluminium substrates was tested as a reference material.

The PDMS used as a matrix material in all composite coatings comes in two parts and is mixed with a 10:1 of base polymer and curing agent to form the Polydimethylsiloxane elastomer. This ratio can be adjusted to tune the modulus and hardness according to the product information; however, reducing the fraction of the curing agent resulted in a tacky surface, suggesting incomplete curing. Research has shown that when cured at higher temperatures, the modulus of the PDMS was higher for the brand used in this work [89]. Sylgard 184 can be cured at room temperature or 25°C but the lab temperature varied significantly throughout the day and year, so a furnace was used, which could be set to 25°C; however, it could not reliably hold this temperature, especially on hotter days. A curing temperature of 30°C was selected as it was the lowest possible that could be reliably maintained. The curing time for this polymer at room temperature (25°C) is 48 hours and decreases to 10 minutes at 150°C. The samples would be cured for 48 hours at 30°C with a post-cure period of 1 hour at 60°C to complete the curing process.

Different mixing methods were trialled with varying success. From the product information, the base polymer has a viscosity of 5.2 Pa ·s, and the mixed polymer (base and curing agent) has a viscosity of 3.5 Pa ·s. Adding filler material increased the viscosity of the subsequent suspension. The primary filler material used in this research was SiC submicron fibres, which were found to be susceptible to clumping, which poses multiple issues that affect the produced coating if unmitigated and additional issues arise depending on how this was mitigated. If unmitigated, undispersed fillers are in visible clumps, the suspension contains a lower wt% of the filler material than intended. Any agglomerated particles are more likely not to be fully wetted by the matrix material, introducing voids into the coating or impacting the surface roughness of the cured coating as the particle distribution has not been controlled. Multiple options were trialled to mitigate this issue. Three mixing techniques were

explored: magnetic stirring, speed mixer dac 150.1 fvz capable of mixing from 300 – 2500 rpm using polypropylene mixing cups, submerging an ultra-sonic probe, Cole-Parmer model CV33.

The Pot life of Sylgard 184 is listed as 1.4 hours once mixed. For early coating production, this was ample time to ensure effective mixing, particularly for the lower filler fractions used. Adding fillers alongside the curing agent was preferred due to the lower viscosity of the mixture compared to the base polymer. However, the coating process using a spin coater was completed one substrate at a time. Adding the risk that when making larger batches the properties of the mixture and subsequent coating may be impacted. Xylene was utilised as a solvent to adjust the viscosity when mixing fillers into the base polymer before the curing agent was incorporated. This was not necessary when mixing the PDMS components with no filler content.

PDMS with no filler content was mixed using the speed mixer at 1000 rpm for 2 minutes and visually inspected for any separation of liquids as the viscosity of the curing agent was very low; any curing agent not incorporated into the base polymer would have been clearly visible. Air bubbles incorporated into the liquid during mixing were of concern as a source of variance in the properties of the resulting coating. As the polymer is transparent and colourless, the viscosity of the mixed material and the length of time used for curing the risk were determined to be low, so porosity would occur and not be noticed. However, as this method was ineffective when including fillers, magnetic stirring was favoured to remain consistent with the other coatings produced. The lowest speed setting capable of overcoming the viscosity was used to minimise the introduction of air for a period of 10 minutes.

4.3.1 Developed coatings

During the manufacturing process, the proportion of filler used was calculated as a ratio to the base polymer from the two-part elastomer kit to simplify the values when measuring each constituent part to minimise human error. For example, a PDMS coating was mixed with a 10:1 ratio of the base polymer to the curing agent, and a PDMS coating with 5% filler content would be mixed with a ratio 100:10:5 of base polymer to curing agent to filler material, producing a PDMS coating with 4.3 wt% of the filler material. All mixing ratios, respective filler wt% and labels are listed in Table 4.1 and Table 4.2. When referred to, coatings are called by their label such as 5% SiC, which represents 4.3wt% of SiC submicron fibres in a PDMS matrix. A 10% SiC coating had twice as much filler in

the mixing ratio. However, this does not double the wt%, which would be 8.3wt% SiC in PDMS.

Table 4.1 Early coatings produced and tested with the pull test, all coated samples' substrates were grit blasted prior to the application of the coating.

Surface label	Filler content	Mixing ratio*
Smooth Al	-	-
Sandblasted Al	-	-
PDMS-1	0	100 : 10
PDMS 1%-1	0.9wt% SiC	100 : 10 : 1 SiC
PDMS 5%-1	4.3wt% SiC	100 : 10 : 5 SiC
PDMS-2	0	100 : 10
PDMS 1%-2	0.9wt% SiC	100 : 10 : 1 SiC
PDMS 5%-2	4.3wt% SiC	100 : 10 : 5 SiC

** 100 : 10 represents the base polymer : curing agent used for Sylgard 184 PDMS*

Table 4.2 The coatings and surfaces tested using in the CAT and both electro-thermal de-icing tests with grit-blasted substrates

Surface label	Filler content	Mixing ratio*
Smooth Al	-	-
Sandblasted Al	-	-
PDMS	0	100 : 10
1% SiC	0.9wt% SiC	100 : 10 : 1 SiC
5% SiC	4.3wt% SiC	100 : 10 : 5 SiC
7.5% SiC	6.4wt% SiC	100 : 10 : 7.5 SiC
10% SiC	8.3wt% SiC	100 : 10 : 10 SiC
20% SiC	15.4wt% SiC	100 : 10 : 20 SiC
10% SiC, 1% MWCNT	8.3wt% SiC, 0.8wt% MWCNT	100 : 10 :10 SiC : 1 MWCNT
20% SiC, 2% MWCNT	15.2wt% SiC, 1.5wt% MWCNT	100 : 10 : 20 SiC : 2 MWCNT
5% SiC, 2.5% Diamond	4.3wt% SiC, 2.1wt% Diamond	100 : 10 : 5 SiC : 2.5 Diamond
POTS Smooth	-	-
POTS rough	-	-

** 100 : 10 represents the base polymer : curing agent used for Sylgard 184 PDMS*

As research progressed, testing coatings through a range of thicknesses highlighted the influence of the substrate's roughness upon the coating's performance below a certain thickness. Going forward, these samples were made using as-received aluminium as a substrate when coatings were made that

may be influenced by this property. The thickness of each coating tested is mentioned as the data is presented in later chapters.

4.3.2 PDMS nanocomposite coatings

The speed mixer was ineffective at incorporating fillers into the base polymer with the addition of a solvent to reduce the viscosity. An ultrasonic probe was trialled and was successful however SEM images indicated significant fibre damage to visible fibres. The average diameter of visible fibres was much higher than that of the magnetically stirred samples, suggesting that lower diameter fibres may have experienced more damage with this method. Magnetic stirring was the chosen method.

Filler material was portioned using a four-point mass balance, and the boat was washed into the beaker being used to mix the polymer with xylene to ensure transfer of the contents of the weighing boat. The polymer base and any additional xylene was then added to the beaker to begin mixing. After 5 – 10 minutes, the mixture was inspected for visible clumps at the beaker wall that were not incorporated into the liquid. If present, the beaker was tilted or its position above the magnet adjusted to change the relative position of the stir bar in the beaker to impact the agglomerations. If unsuccessful, additional xylene was considered, and then a last resort was the careful use of a stainless steel spatula to reposition the agglomeration. Once incorporated, the mixture was further stirred for 60 minutes at the lowest possible speed setting for the viscosity of the mix. If the mixture passed visual inspection, the curing agent was then added and stirred for 10 minutes.

Later studies using higher filler fractions required an adjustment to this process. The coatings with an additional filler alongside SiC or with a SiC mixing ratio of 10% or higher to the base polymer required the initial mixing to be completed in xylene alone to fully wet and suspend the powder before the addition of the base polymer. If significant difficulty was incurred in dispersing all the agglomerations, a high volume of xylene was sometimes necessary. Possibly influenced by the room temperature and humidity, the main contributing factors were the proportion of fillers used and the size of the batch being produced. As both the size of the stirring bar and its relative size to the width of the beaker used and the depth of liquid varied its effectiveness. This ratio could result in the separation of the liquids after mixing, often presenting after curing when the ratio of solvent to base polymer exceeded 1:1. As reducing the xylene used during the mixing was not possible without incurring significant agglomeration within the mixture, the mixture was heated while being stirred to 50°C promoting evaporation of the

xylene in the fume cupboard. The mixture would slowly become more viscous as the solvent evaporates, leaving the fillers dispersed within the polymer base. If the viscosity rose such that the stir bar was not functioning, small amounts of xylene were added to allow the addition of the curing agent and ensure it was mixed well. The mixture was allowed to cool back to room temperature beforehand to prevent the curing process from beginning too soon. Unfortunately, managing the viscosity was not a reliable process and required adjustment from a set recipe to produce a suspension that was well mixed using less vigorous methods with a viscosity suitable for spin coating.

Spin coating to produce a desired thickness was not possible as the resulting thickness was governed by many factors other than the speeds and times used to coat the substrates. Assuming a sufficient excess of the mixture is applied to the substrate, the thickness was impacted by the wettability of the substrate, and what the mixture contains, which was assumed to affect the surface tension and its viscosity. The spin coating process using a Laurell WS650MZ-23NPP was completed in two stages to distribute the material. The first was 20 seconds at 250 rpm followed by a second stage of 60 seconds with a speed ranging from 250 – 5000 rpm, with most samples made using 500 – 2000 rpm. An example of a variation would be necessary to produce a comparable PDMS coating using no filler or solvent of a thickness of roughly 80μm on sandblasted aluminium the second stage was 650 rpm and 600 rpm on smooth aluminium. Producing a 5% SiC coating from a 3 g (base polymer) batch using 0.5 ml of xylene with a comparable coating thickness required 400 rpm on a rough aluminium substrate. Thick coatings over 400μm thick were not spun at a high speed. The liquid was spooned on until it appeared the surface tension would not allow additional material without spilling, or a single stage of 100 rpm was used to improve the distribution of the liquid.

4.3.3 Coating the discs

Coating the discs described in could not be done by spin coating due to their size. An adjustable Elcometer 4340 automatic film applicator, where a blade with an adjustable height is pushed across the flat bed pictured in Figure 4.1 with an adjustable blade Figure 4.2. Multiple passes to slowly reduce the thickness of the uncured polymer on top of the disc was most effective, rotating the disc between passes. For discs with an uncoated section the polymer was applied after the desired pattern of the uncoated sections was covered using Tamiya 5 mm masking tape for curves, which is a tape made from a soft resin that can be stretched when applied to produce curves without creasing. The discs were

cured in the same manner as other substrates, 48 hours at 30 °C. However, when an uncoated section was needed, the polymer was left to cure for 16 – 24 hours to allow the polymer to set to a fixed geometry but not be completely cured. The tape would then be removed with the PDMS directly on top of it. The tape adhesive did appear to be affected by the uncured polymer and required some cleaning with the use of a nitrile glove to remove some residue before completing the curing period and a post-cure at 60°C for two hours rather than one due to the adhesive interaction. Attention was once again paid to the areas of removed material to clean the area without introducing debris or abrasive damage to the coating or exposed disc.

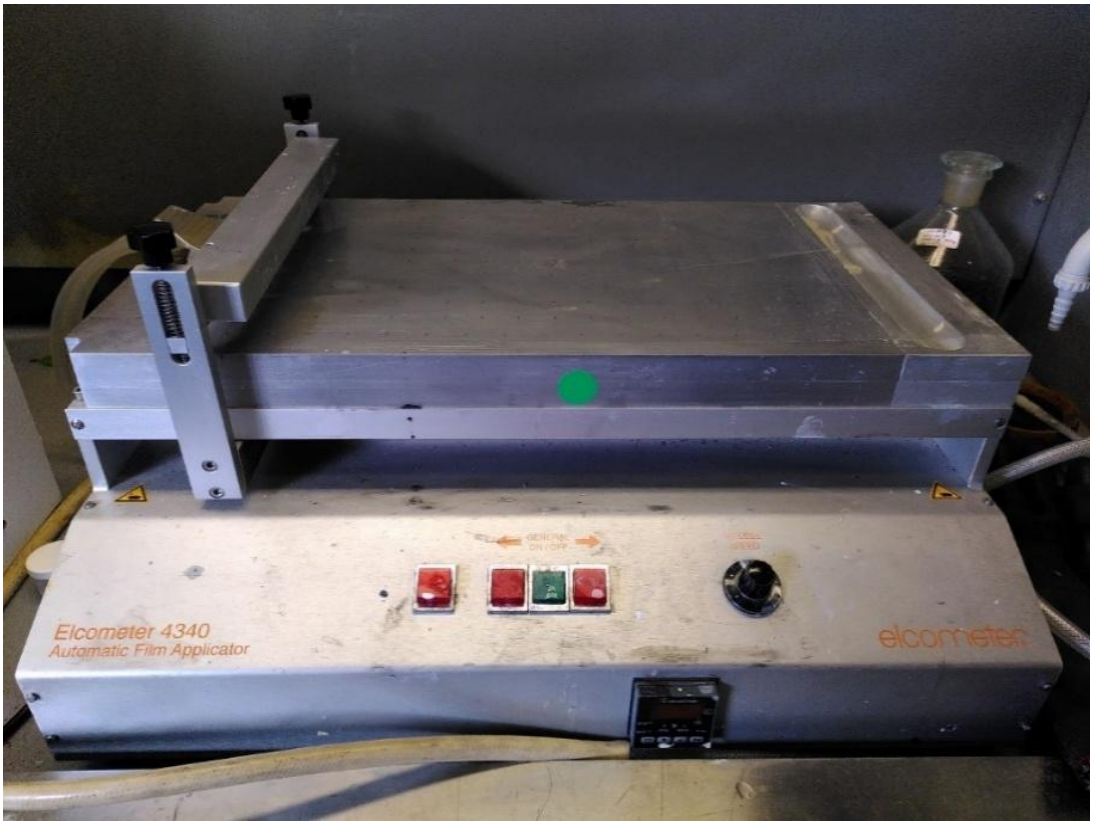

Figure 4.1 Elcometer 4340 Film applicator used to spread the uncured polymer over large substrates, with its table dimensions measuring 600 mm x 305 mm.

Figure 4.2 Blade with an adjustable height that works with the film applicator to spread material by being pushed over the substrates covered in an excess of the uncured polymer. Pictured atop the Film applicator table in Figure 4.1.

4.3.4 Samples for thermal diffusivity analysis

As the coatings profile over the substrates used for testing was influenced by the surface tension of the pre-cured liquid, and slicing an elastomeric material to a required geometry is also challenging, a small 50mm by 50mm open-topped mould with removable walls was purpose-built. The purpose is that the samples used for testing thermal diffusivity must be a 10mm square or disc of a 2 – 2.5mm thickness for testing through the sample's depth and a 25.4mm disc that is 1mm thick to test the in-plane thermal diffusivity. Issues arose when cutting or slicing samples to size as the material undergoes strain as it is cut. Initially, long cylindrical plugs with a 10mm diameter were trialled, but this resulted in high porosity despite attempts to degas the material using a vacuum furnace and difficulties cutting the material to have flat and parallel faces. A perfect solution was not found, but it was reduced significantly. The mould with a flat base was filled to an appropriate depth for the samples required and allowed to cure. A small sheet of the coating material could be peeled from the mould after the walls have been removed. The centre of the sheets was flat, as the distance from the walls was sufficient to remove the influence of surface tension on the geometry. Sharp scissors were found to be the best tool to cut 10mm square samples, and a 25.4mm circular sample was cut using an Ateco stainless steel round cutter.

4.4 Surface topography

Two optical methods were trialled to assess the surface topography of the tested coatings and surfaces. Success was achieved using an Alicona G5 infinite focus with carbon coated samples to overcome the optical transparency of PDMS. The carbon coating was performed using an Edwards 306 evaporation coater. The guideline for using this coater for SEM sample preparation is to apply a 20 nm layer. Using the equipment's estimation for the thickness of applied carbon and limiting this value to roughly 10 nm provided the most utility. Heavier deposition clearly impacted the surface topography Figure 4.3. The sample on the right, with a much heavier coating, is significantly more reflective and appears to have a fractured scaly surface produced as the carbon cooled. Most measurements were taken using a 5x optical zoom over a preferable higher magnification of 20x, which would provide better detail due to the difficulty in obtaining measurements at this zoom. Some surfaces were coated twice with the carbon coater, and applying two thin layers with time to cool between applications reduced the prevalence of cracks and ridges in the applied carbon. When applying two coats, the distance between the samples and the carbon rods was maximised to reduce the rate of deposition per unit area of the coatings. The carbon coater used was an Edwards Coating System E306A using sharpened graphite rods under vacuum.

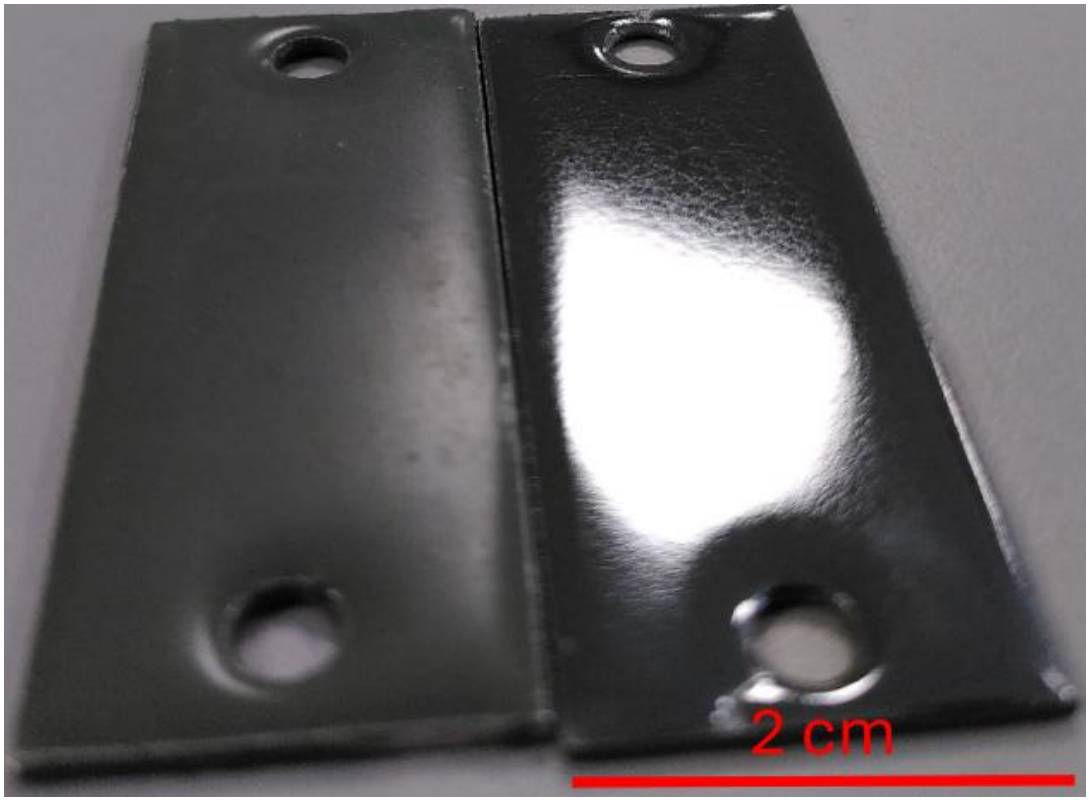

Figure 4.3 Two 10% SiC samples coated via carbon sputtering with the right-hand sample is much more reflective with a scaly appearance from a heavy deposition.

The location of the roughness profile contributes significantly to the obtained result when by observing 1500 profiles, which maximised the scanned area within each image, using a cutoff wavelength of 250μm. The preferred characterisation was the surface texture properties of the entirety of the captured surface, filtering the dataset's waviness with a cutoff wavelength of 563.9μm.

4.5 Material and coating properties

4.5.1 Wettability

The water contact angle (WCA) was tested using an FTÅ 200 with each sample tested with five sessile droplets placed in a line along the centre of the 50 mm length of the substrate with care to test away from the edge where the coating

may be less flat due to the surface tension of the pre-cured polymer affecting the geometry near the edge seen in Figure 4.4 and displayed in Figure 4.5.

Figure 4.4 Colour gradient over the surface of 10% SiC in PDMS where darker regions near the edges are raised due to the surface tension dictating the distribution of the uncured polymer. Substrates are 20 mm x 50 mm.

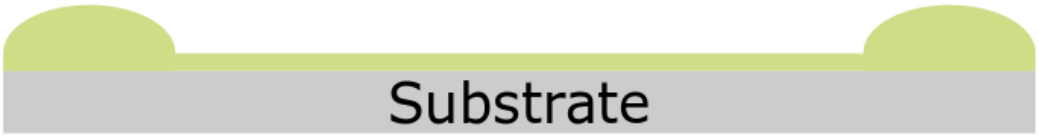

Figure 4.5 Cross-sectional diagram of the coating thickness change from one edge to the other.

4.5.2 Thermal diffusivity

For samples to be tested in the low temperature LFA 467 hyperflash, it is necessary provide a black body surface and this is typically achieved by application of graphite spray. However, some difficulty was encountered in this process as the deposited material tended to crack and peel from the polymer surface as it dried due to its low surface energy and relatively smooth surface.

The thermal diffusivity was tested at 25°C as this was the lowest temperature that could be tested at the time.

4.5.3 Coating thickness

The coating thickness was measured using a QNix 8500 coating thickness gauge, which utilises changes in the magnetic field to determine the distance between

the probe and metallic substrate. Each substrate was measured away from the edges of the substrate in a line down the length of the sample along the centre to maintain within the tested area of each sample. Care was taken to remain away from non-flat regions where the thickness was influenced by the surface tension and edges of the substrate. This can be seen in Figure 4.4, showing five samples of 10% SiC with a visible border of darker material where the coating is thicker.

4.6 Icing facility and methods

A Design Environmental ALPHA 1550-40H was used for the ice formation experiments. A portable freezer box was adapted for the static electro-thermal de-icing test and the pull test to measure ice adhesion strength. The ice adhered to the samples in these tests was completed using a Peltier plate, Para Cooler O supplied by Weinkauf Medizintechnik.

4.6.1 Environmental chamber and equipment design

The environmental chamber, Design Environmental ALPHA 1550-40H, was utilised for both ice growth experiments described in this section. The disc experiment used the same drum and motor for the centrifuge test (CAT), with the motor used to spin aluminium discs upon which cold water was dripped in a freezing environment to study the freezing and structures formed by large droplets impinging the static central axis point of a rotating body.

The second larger construction for the blade icing experiment housed a motor in a closable box with the door-containing face measuring 800mm by 800mm and with a depth of 700mm. A port in the roof was cut to allow piping into the box, and some small vents in the rear wall to allow some airflow to and from the rest of the chamber. The motor rotated 3D-printed turbine blades while a simulated cloud of small droplets, produced by a nebuliser, was pumped through the port in the roof. Aiming to mimic a cloud passing over an operational wind turbine in freezing conditions or, conversely, a helicopter flying through a cloud.

4.6.2 Ice accretion upon a rotating disc

A header tank of water on top of the chamber was held at room temperature and fed through a tube entering the chamber through the door at the seal when shut.

The water tank has a second overflow compartment with a circulating pump to maintain a consistent head by keeping the primary tank full, from which water was drawn with a gravity head of 1395 mm Figure 4.6. The temperature of the chamber was set to -14.5°C as this is within the range that mixed icing could occur [15]. The kinematic viscosity of water at this temperature is 1.211× 10^{-5} m^2/s [90].

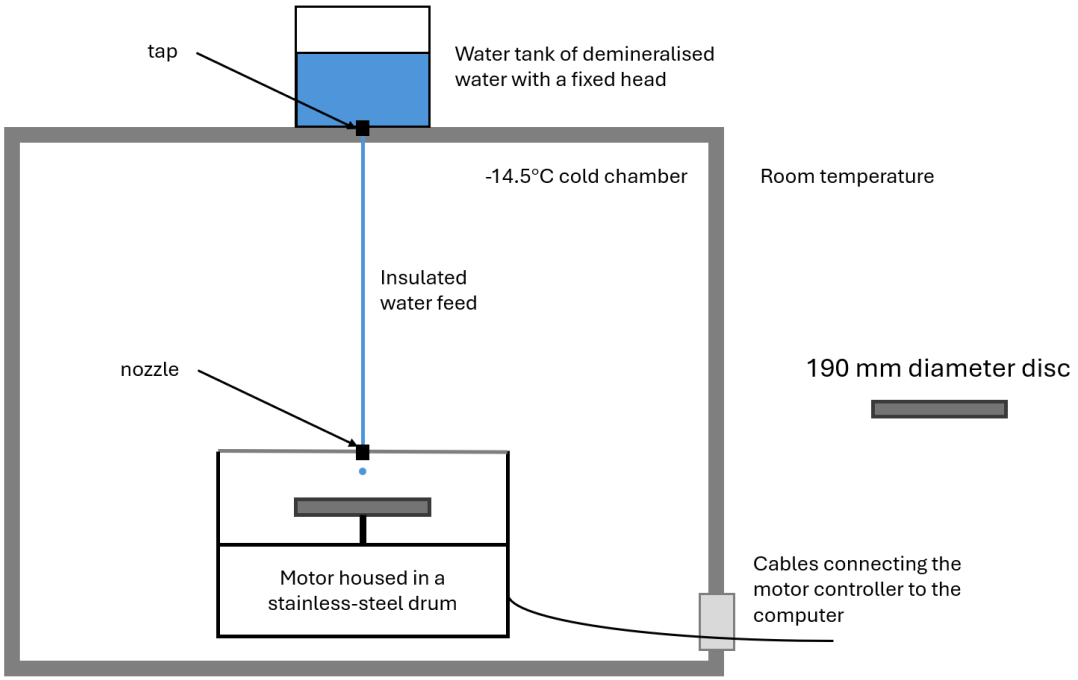

Figure 4.6 Schematic of the disc icing experiment.

Considering the Reynolds number of the disc as if the droplet was perpendicularly striking the leading edge of a win turbine blade, appropriate revolutions per minute could not be tested for the tip. Comparing the blade tip of a Siemens Wind Turbine SWT-2.3-108 [91] an equivalent Reynolds number would require a rotational speed of 3.2× 10^5 rpm for the discs used, which had a diameter of 0.19 m. As this experiment was a preliminary investigation concerning the weight of the disc with the additional mass from the grown ice that may form asymmetrically, a low-speed of 1800 rpm was selected out of caution with the motor limit being 4500 rpm. The Reynolds number at this speed for the disc was calculated to be 1.4× 10^5, while the same order of magnitude of that experienced by the tip of the comparison turbine, in real terms, this flow would have been experienced only 0.30m from the root of the 53m long blade. This means this preliminary test is not directly comparable to a meaningful

section of the blade however a Reynolds number of 10^5 is, for many aerofoils, a transition value from a mixed boundary layer to a fully turbulent boundary layer [92]. This speed could be considered comparable to the turbulent conditions of a wind turbine. However, the data obtained could not form the basis for any strong conclusions when considering this application where the radius of the disc represents the chord length of the selected turbine Figure 4.7.

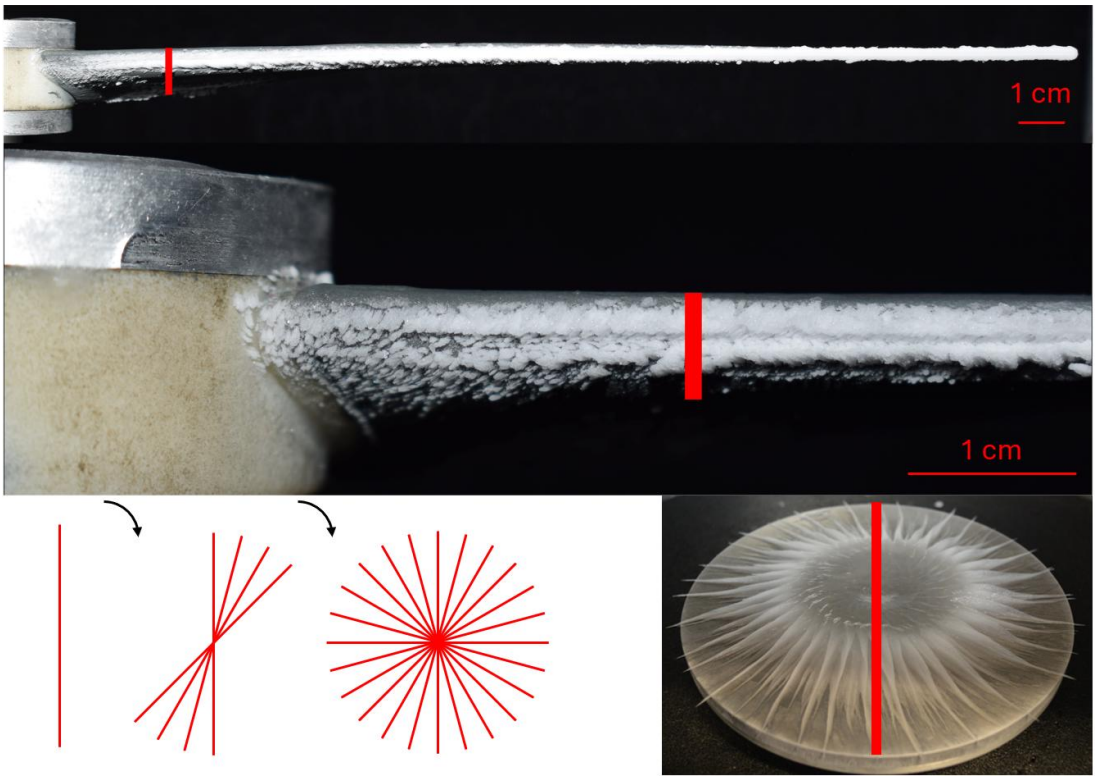

Figure 4.7 Attempted simulation of a section of a blade using a spinning disc.

Controlling for a droplet's size is not a reliably precise measurement however the drip rate could be controlled. The flow rate could not be controlled for a drip rate of one drop per second, measured over a minute before the test was completed. Accounting for any potential flow rate deviations due to droplet size by measuring the mass of the ice formations produced.

The disc was mounted to the motor shaft, and a frame fixed to the drum was aligned the water feed. The chamber was allowed to then reach the testing temperature of -14.5°C before engaging the motor to spin the disc up to speed, which was followed by attaching the nozzle to the brackets above the disc. The timer starts with the start of the flow of water, stopping the accretion after 15 minutes. Using a Nikon D3200 with a shutter speed of 1/40 and ISO of 1600,

photographs of the iced discs were collected from above. A laser scanner, Micro-Epsilon ScanCONTROL 2900-10BL, scanned two 20mm wide strips of ice as the disc was rotated at 1rpm. The scanner took 100 profiles a second for a total of 6000 per strip, the locations of each scanned ring are shown in Figure 4.8. One stip was located at the edge of the disc or the tips of the ice thorns if within the disc, with the other strip centred at the radius where the ice transitions from glaze to mixed and rime ice. An example scan can be found in the Figure 4.9.

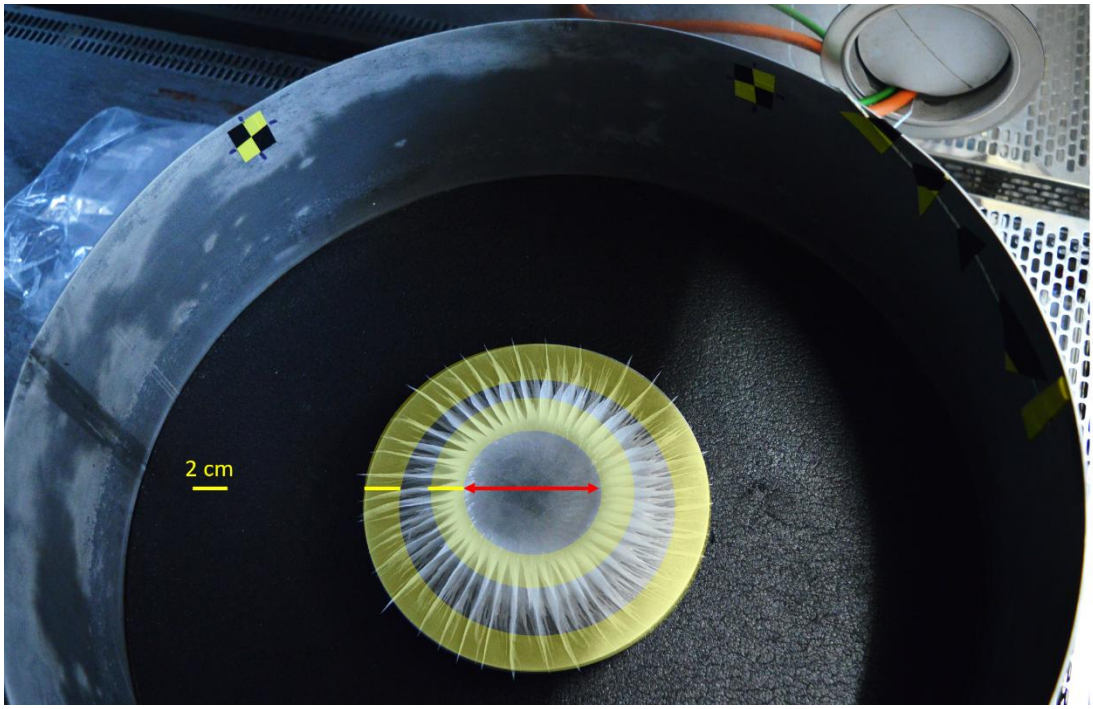

Figure 4.8 Diagrammatic overlay of the two bands scanned of the disc highlighted in yellow. One at the transition from glaze ice near the centre and the other at the edge of the disc. 100 scans were taken per second, and the disc spun at 1 rpm, obtaining a total of 6000 scans. With the area spanned by the arrow made from glaze ice.

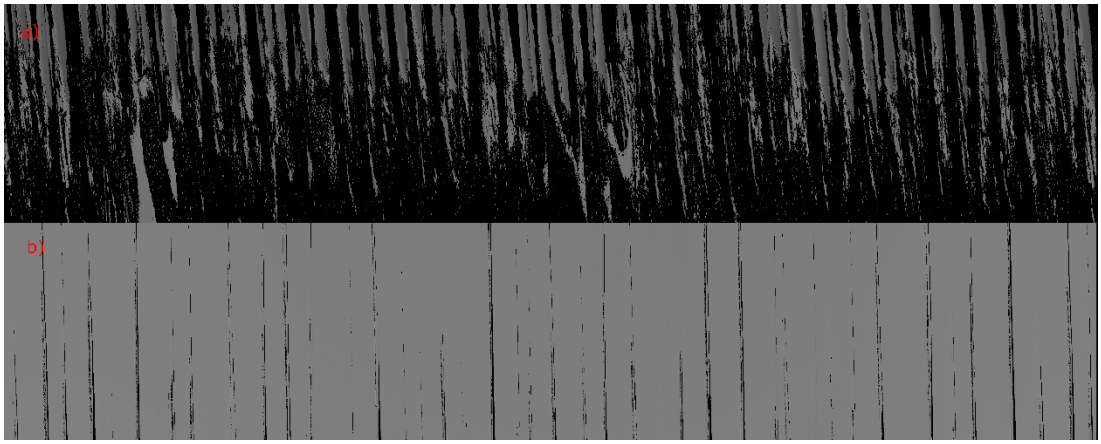

Figure 4.9 a) Scan of the inner and b) outer rings taken of the protrusions at the transition point and edge of the disc respectively, taken of the aluminium disc.

The disc was then removed with the ice still attached, and its mass was recorded to the nearest gram. The mass of the disc was known to allow the mass of the ice accretion to be inferred. Using a metal rule, the diameter of the glaze ice formation was measured at four different locations. To minimise any damage to the applied coatings, where applicable, the ice was left to thaw with the discs then stored in an air-tight bag with silica gel when not in use and kept in the chamber before testing so as to be held at the testing temperature.

Six discs were tested which are described in Table 4.3 and Figure 4.10 where a patterned surface was tested with a mixed surface of a PDMS coating discs with the aluminium beneath exposed in pre-determined positions.

Table 4.3 Surface description of each disc.

Disc name	Coating thickness (μm)	Description
Sandblasted	-	Top surface was sandblasted using 180-220μm alumina particles
Aluminium	-	As received finish
PDMS	258±17	Coated with Sylgard 184
PDMS 5%SiC	206±2	Coated with PDMS containing 4.3 wt% SiC
Cross	119±7	PDMS coating with a 1 cm wide cross of uncoated material
Strip	170±3	PDMS coating the same as the cross except a 2 cm radius is left coated at the centre
Petal	66±3	two arcs of removed material with a 7 cm radius that cross at the centre and edge of the disc , repeated every 120°

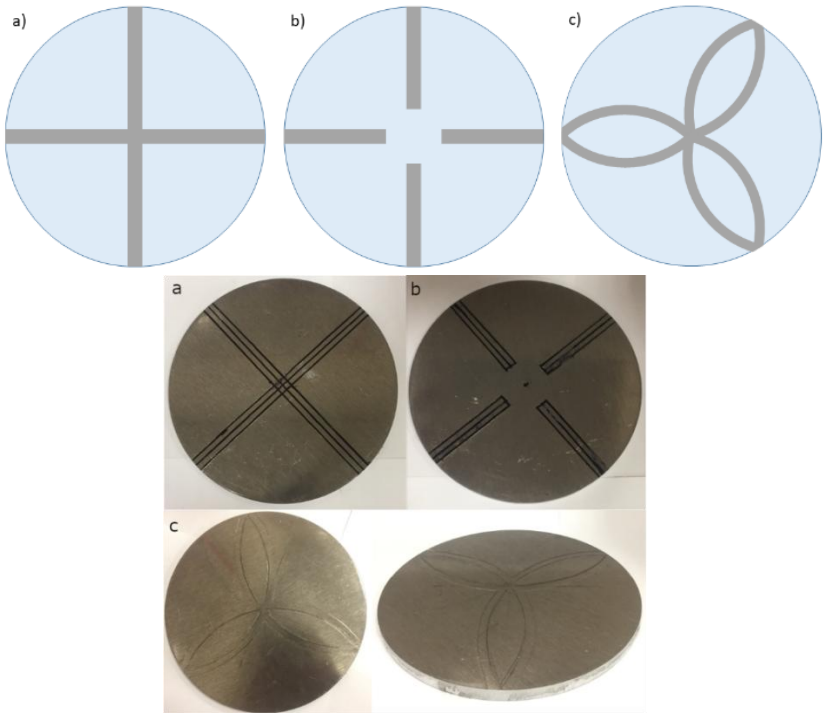

Figure 4.10 Diagram and corresponding photos of the patterned discs a) cross, b) strip and c) petal. All have a 190 mm diameter.

4.6.3 Blade icing

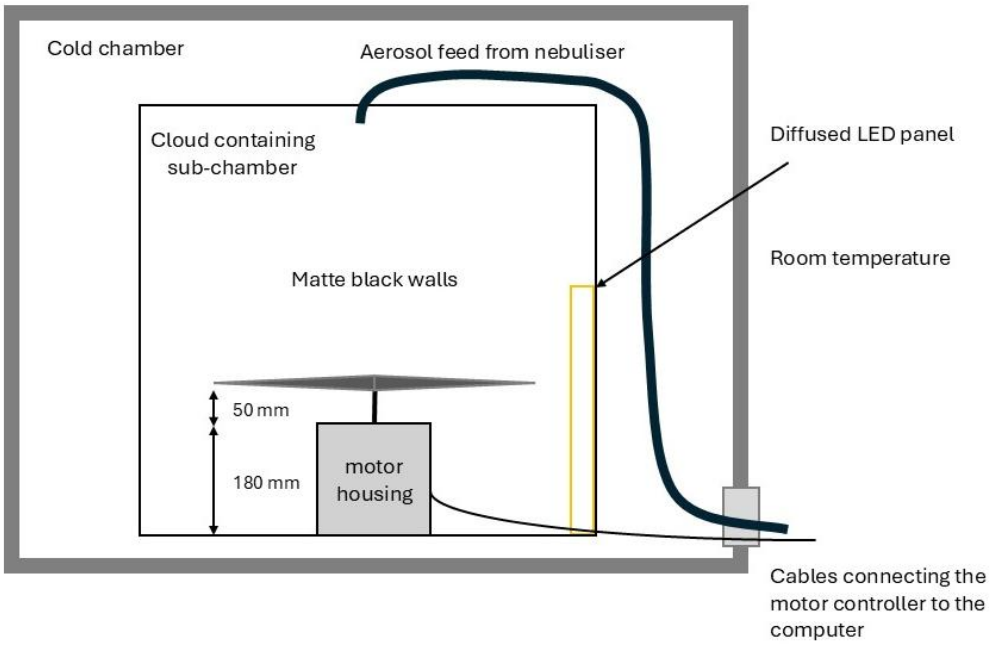

Figure 4.11 Schematic of the cloud chamber.

In the centre of the stainless-steel box created for this experiment, the motor is housed at the centre in a sealed 180mm housing with the shaft pointing upwards to which the 3D printed turbine blades made using RS PRO 3D Printer Filament PLA were mounted Figure 4.11, Figure 4.12.

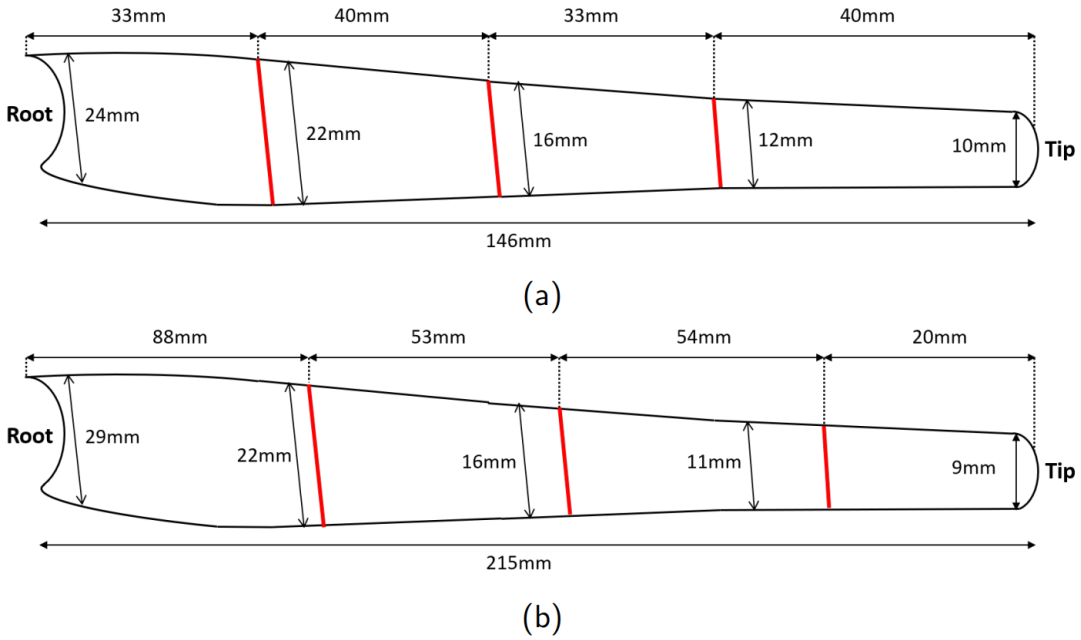

Figure 4.12 Diagram of both blades used with the chord lengths at each drawn line shown here in red and their location along the blades a) small b) large.

A simulated cloud was produced by an Omron NE-U17 Ultrasonic nebuliser, which was upgraded to an Omron NE-U780 Ultra Air Pro Nebuliser after a fault with the equipment. Both were operated at the maximum air volume and nebulisation settings. The first, Ne-U17, produces droplets with a Mass Median Aerodynamic Diameter of 4.4 μm, Independently measured from the manufacturer by SolAero Ltd to BS EN 13544-1:2007+A1:2009. The second, NE-U780, produces 4.6 μm droplets measured by Omron, the manufacturer, Figure 4.13. Both nebulisers have a maximum nebulising rate of 3ml/min when nebulising saline solution at 26°C and a maximum air volume of 17 l/min.

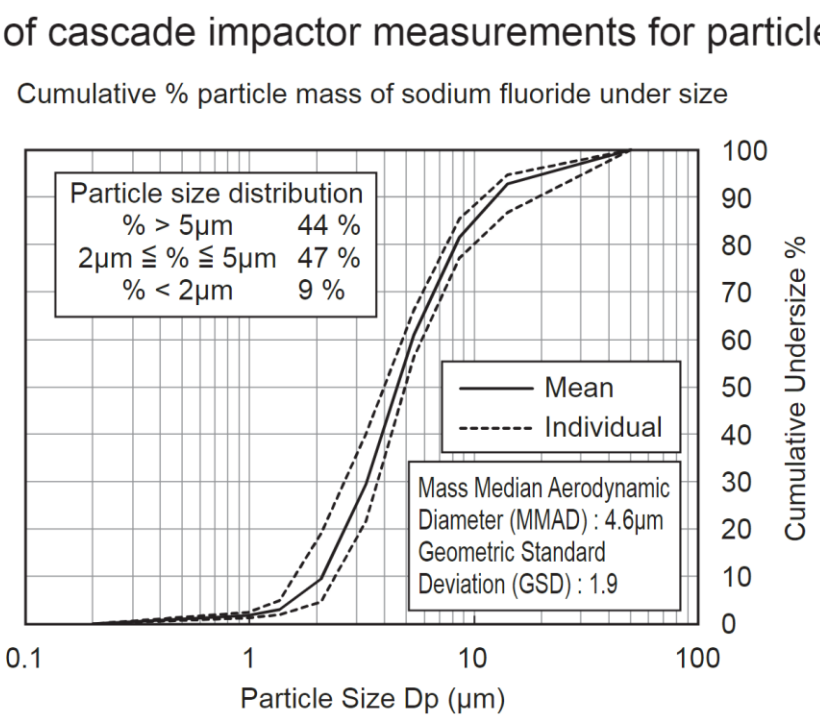

Figure 4.13 Supplied droplet data used for analysis measured for a 2.5% NaF salt solution [93].

The experiment begins with engaging the motor to bring the blades up to the chosen rpm for that test. The nebuliser is switched on and the exposure to the simulated cloud was timed. The nebuliser's output was piped from room temperature into the top of the box through a port cut. Due to this delay and a changing water content within the box as the cloud is piped, a consistent exposure through different time periods of the test's duration cannot be controlled. Moreover, as a range of rotational speeds and environmental temperatures were tested, the proportion of the cloud consisting of solid ice particles and droplets ranging in temperature from recently injected into the chamber to supercooled would require a separate analysis for each speed and environmental temperature tested. With a time progression analysis to provide cloud properties at each window of time due to the cumulative addition of nebulised droplets into the box. To maximise the time available, specific analysis of the simulated cloud was not completed, and the icing window was considered comparable to a cloud passing over a wind turbine with a supercooled surface. With some knowledge of the initial droplet diameter prior to entering the cold environment with the assumption a proportion of droplets freeze homogeneously in the air over time at a rate influenced by the air temperature and airflow induced by the spinning blades. Therefore, the liquid water content

has been assumed to fall within the given ranges in ISO:12494 2017, as shown in Table 1.4 and Table 2.4, with the respective densities for each icing regime.

Table 4.4 Icing regime properties (ISO:12494 2017) [94]

Icing regime	Density (kg/m^3)	LWC (g/m3)	Air speed	Temperature (°C)	Appearance
Glaze	900	> 0.2	High	0 to -5	Transparent
Mixed	600 to 900	< 0.2	Low	<-10	White
Rime	200 to 600	< 0.2	Low	<-5	Opaque

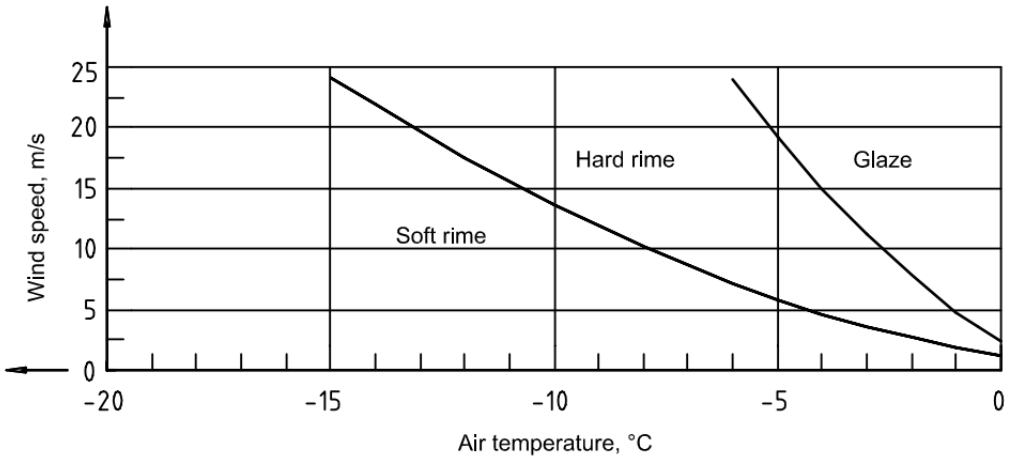

Figure 4.14 Environmental conditions that produce each ice type (ISO:12494:2012), the curves shift to the left with increasing LWC and decreasing object size [14].

Once the time of the test had elapsed the nebuliser was switched off, and the blades decelerated to a stop. Once stationary, the chamber was opened without delay to allow the cloud to vent and prevent further accretion or structural changes. Early testing utilised a fixed position stand to take photographs of the blades to document the accretion from above and the tips of the blades. As many features were not captured this way and the time required to operate the camera stands, issues were encountered due to melting, causing significant discrepancies between photos of different angles of the same blade and from blade to blade. The consistent positioning was sacrificed for user-determined positioning, allowing photos of the leading edge to be taken with colder temperature tests and photos of abnormal structural features or differences between tests, such as tip growth or shedding. A light panel and the use of matte black paint on the internal surfaces of the box were used to improve the detail capture within the photos. Flash was not typically used. On occasion, a flash and

no flash photo was taken to compare details that may have been highlighted or visible in one versus the other.

Between tests, the blades were dried with paper towels as melting was rapid, so removal when solid was not possible. The door to the box and the chamber was then closed to allow the temperature to return to the selected environmental temperature and remove any humidity for 15 – 20 minutes as significant air exchange between the room and chamber occurred during data collection.

The images, taken with a Nikon D5300, were analysed considering the Stefan number, Reynolds number and Stokes number and their influence on how the structures were formed. Estimating the mass of ice accreted, the cross-sectional geometry of the ice growth at the tip, which formed a rhombus. The angle of the rime growth from the leading edge at the blade's root and, in some cases, rime growth ripples were noticed forming along the leading edge. The wavelength was investigated with relevance to the position along the length of the blade. The transition point where within a single accretion between glaze and rime ice growth was dictated by the experimental conditions, particularly temperature. As in lower temperature tests, glaze ice did not form, and there is no transition point, so the temperature gradient was nondimensionalised using the Stefan number as thermodynamics dictate the process, specifically the temperature at the boundary. Where a transition point exists a shard of growth would also extend past the tip of the blade. Suggesting glaze ice formation that is delayed results in the travel of the droplet along the length of the blade before solidification. The length of the shard produced, and the blade length were then nondimensionalised to consider how the delay in freezing shifts the distribution of accreted ice away from the root and its influence on the transition point.

4.7 Thermal de-icing

This section describes the unloaded thermal de-icing experiment using a coldbox custom-made by Trent Thermal (UK) from an electric cool box made by Dometic (UK), where the addition of an icephobic coating to an aluminium surface requiring electro-thermal de-icing was tested to assess the coating's impact.

4.7.1 Adhering ice

As ice adhesion is typically strongest with glaze ice [14] due to its high density and low porosity, controlling for glaze ice at the interface with the substrate was deemed a high priority for controlling reliability by testing the worst ice capable of forming at the chosen testing temperature of -10°C, which is commonly selected within the field. A significant benefit is that if the interface is glaze ice it is transparent, and so any defects such as bubbles or cracks are clearly visible, which would require the sample to be discarded. A bubble or crack reduces the contact area of the ice with the surface being tested, changing the stress when a given force is applied and causing stress concentrations. In thermal de-icing, this is not the primary concern with cracks and bubbles as the forces present are not the primary cause of adhesion failure. The formation of a melt layer for the weight to become sufficient to remove the ice is. A bubble or crack in the ice at the interface could reduce the melting required before adhesion failure, assuming the melt layer's critical depth is constant. Amorphous mixed ice would also produce a consistent interface however any significant defects like a trapped bubble would not be clearly visible and may go undetected when quality assurance of each prepared testing sample is completed. Another source of error would be spilt ice, where the substrate's surface was wet elsewhere prior to freezing or water was squeezed out of the mould as it froze and expanded. This can present in a thin film between the mould and substrate or a more obvious bead of ice away from the cube that has formed outside the mould completely. If removed, any spilt ice would represent a loss of mass that could impact the measurement and removing the ice would require additional handling that would introduce heat into the substrate or mechanical loading that could stress the interface and impact the result.

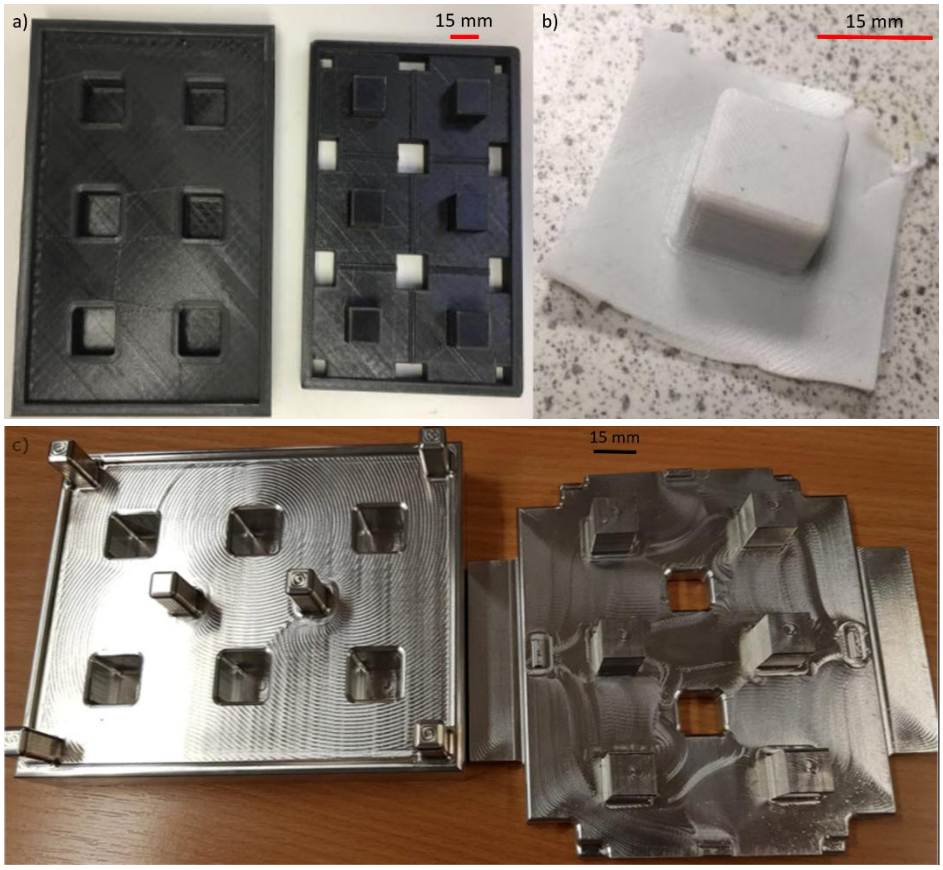

Figure 4.15 a) 3D printed prototype for a mould to make 15 mm ice cube moulds that formed 15 mm ice cubes. b) a mould produced by the prototype with large wings around the cube itself to facilitate its delicate removal. c) the final mould machined from an aluminium block.

Shop-bought ice moulds minimise the margin between each cube, as any wasted space is inconvenient for the user. As removing the moulds is necessary for this test, having very little additional material that can be gripped and levered to remove the mould is extremely difficult. This requires more handling and a higher risk of damaging the ice-surface interface through applied moments, which will vary significantly between each sample as it is extremely difficult to control. Figure 4.15 shows the moulds made to produce the 15 mm ice cube moulds. The samples were frozen overnight upon a Para Cooler O Figure 4.16, Cold Plate produced by Weinkauf Medizintechnik. Initially, the plate had an acrylic box fitted over the top of the cold plate as it was open to the air. This was replaced by a transparent acrylic lid, which was a flat sheet. This allowed better access for fine adjustments and reduced the trapped air volume.

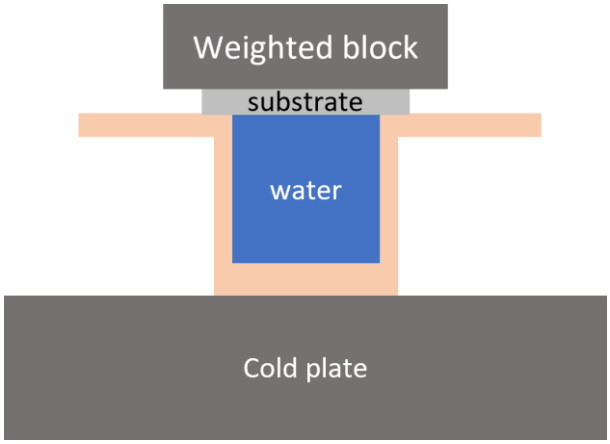

Figure 4.16 cross-section view of a mould during the freezing process using the Para Cooler O cold plate to adhere ice to the substrates for thermal de-icing testing. An aluminium strip maintains a seal between the mould and substrate while impacting the freezing fronts so that the interface at the surface of the substrate is glaze ice with any imperfections away from the testing surface.

As the water had two freezing fronts originating from the weighted block or the cold plate, the use of rubber for insulation between the mould and the cold plate was utilised to ensure the fronts met away from the ice-surface interface and that the freezing progressed slowly enough for that region to reliably be defect-free glaze ice. The last mould iteration using the aluminium mould shown in Figure 4.15 to make the ice cube moulds have a thicker layer for the face parallel and opposite to the substrate. This made this face stiffer and less capable of being deformed when the ice expands, reduces the heat transfer to the ice when the moulds are removed and the need for a layer or neoprene underneath it, which was previously required for other moulds, to slow the freezing process.

4.7.2 Static electro-thermal de-icing

The purpose of this test is to isolate and analyse the energy cost associated with thermally de-icing a surface or coating. Using a cold environment to hold a sample while a heater was supplied with a known current and voltage until adhered ice falls from the surface. Recording the time taken to de-ice allows the heater's energy consumption can be inferred to isolate and consider the impact of a selection of coating material and surface properties on a coating's proficiency in a thermal de-icing scenario.

The coldbox in which the testing occurs was custom-built with a structural frame affixed to the lid that suspends the sample seating block and heater in the cold

box when closed. For all testing the temperature was set to -20°C and an operational testing temperature of -10°C. It was left for two hours to cool all the contents before testing. The environmental temperature of -20°C was chosen as it was close to the limitations of the equipment, which has a minimum temperature of -22°C and provides adequate cooling between and during each test. The active cooling remained on throughout the test to better simulate an engineering application by mitigating some of the heat lost to the surrounding structures and air rather than transferred through the substrate to the ice.

The coldbox suffers from having a large lid, so when a sample is placed in or removed from the box, significant air displacement occurs. To account for this, each testing day, or after a break longer than one complete testing run, a dry run was completed. where the test is run without a sample with an opening of the lid to place and remove a ghost sample and heat the seating block to 5°C. The purpose of this is to minimise any systematic error that could be caused for the first sample, where the suspended supporting structures and air are colder than they would be for sequential tests where the temperature of the seating block is the primary variable of concern.

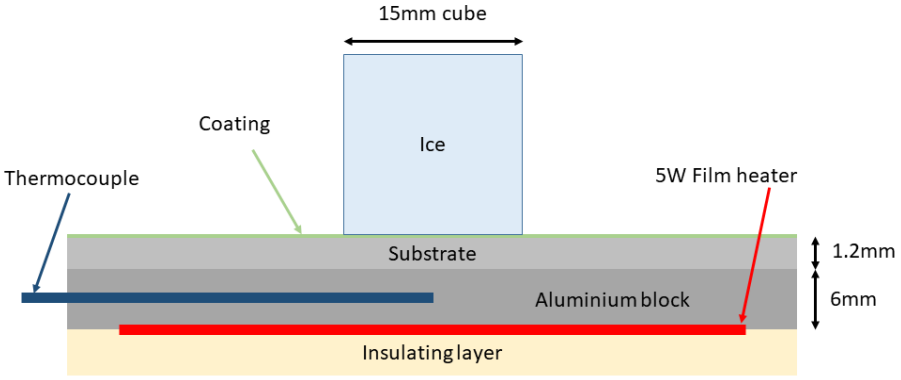

Figure 4.17 Cross section of the original aluminium seating block illustrating the relative position of the thermocouple and heater to the surface to be de-iced.

The aim of the test is to measure the energy required to de-ice the tested surface from a starting point of -10°C. This is the temperature that the samples are held on the cold plate. However, the thermocouple in the seating block can only provide an approximation of the temperature at the surface due to its location. As polymer coatings are being tested, it can not be assumed that the temperature change of each surface at any given measured temperature will be consistent. A reasonable assumption would be that the temperature change of a smooth and

sandblasted aluminium surface would have a strong correlation with the temperature of the seating block, but there would possibly be a discrepancy in the melting and shedding due to the different surfaces. So, if no ice was adhered to either aluminium surface, the temperature change of the surface through a heating cycle would be comparable. This is mentioned as ideally knowing the temperature of the surface at the point the ice detaches and at what time it reached 0°C would be insightful when drawing conclusions about a surface's performance and clarity for reproducing this experiment with different equipment. More meaningful comparisons could then be made between experiments. As seen in Figure 4.17, the thermocouple does not read the temperature at the surface, but of the seating block, imaged in Figure 4.18.

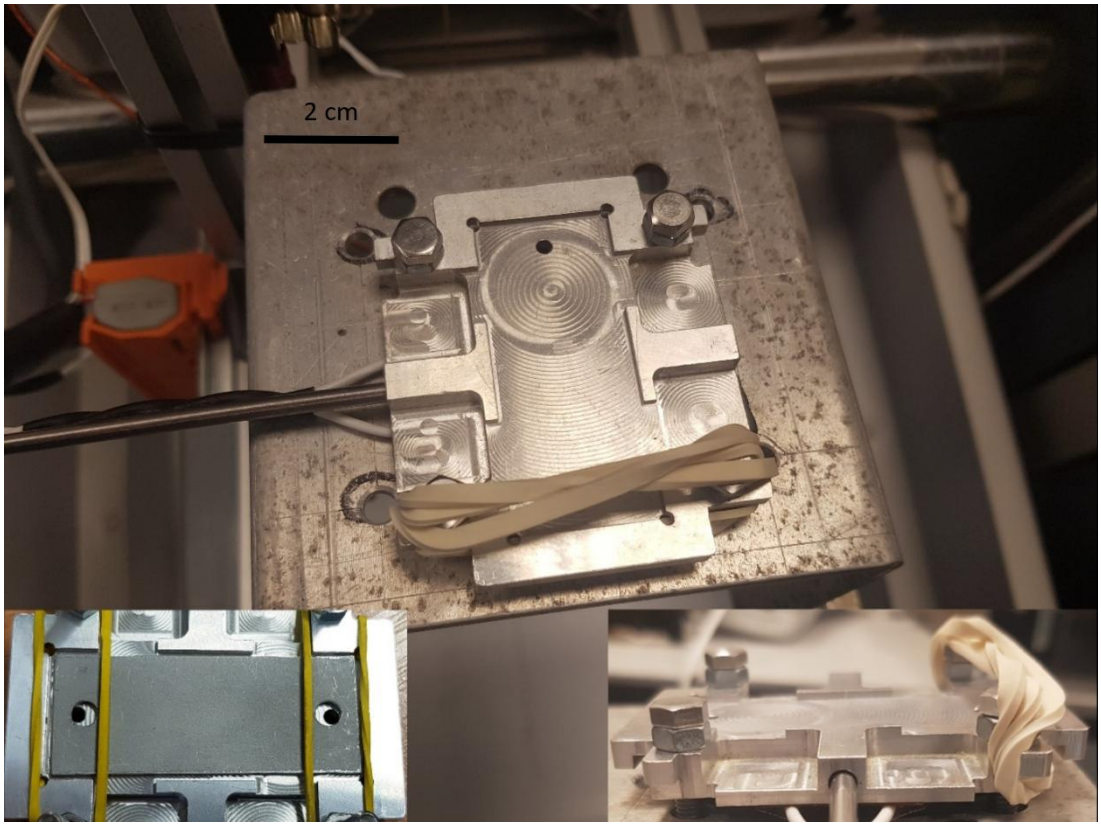

Figure 4.18 Photos of block with a recessed area of depth equal to the thickness of the substrates so the surface sits flush with the block if there is no coating applied. The clamping mechanism has been replaced with elastic bands to provide consistent thermal contact between the substrate and seating block that conforms to the thickness of any coating applied. In practice, only one elastic band was used above the ice cube so as to not impede its fall.

The design of the seating block aimed to minimise its mass. The footprint of which was reduced to the size of the film heater and allowed it to be bolted to the frame on which the holes for the old fixings can be seen. The orientation was changed so the overhanging hook that holds the elastic band was not impeded by the thermocouple. Only one elastic band was used as it was sufficient to clamp the sample at the top. The second elastic band significantly delayed the loading and removal of samples while affecting the results in some cases where the ice slides and momentarily comes to rest on the elastic band across the surface below it. It would have been positioned where the black bar labelled bolt in Figure 4.19 symmetrically to the other. The seating block was recessed to reduce the material between the heater and the substrate, and edges were provided to locate the substrate in place. Two holes can be seen in the recess that align with holes in each substrate, Figure 4.18. These were designed to allow bolts to protrude from the recess and provide another locating feature. This was deemed unnecessary as loading samples with them was more complex and, therefore, slower and more variable, with no significant benefit over the rubber band alone. When a tested sample is removed, the band must be placed atop the bolt head as seen in Figure 4.18, so a sample can be quickly loaded with one hand with the other holding the coldbox lid to then use the free hand to nudge the band off the bolt heads and onto the sample, holding it flush with the block.

Sample transfer into the coldbox from the cold plate was carried out with nitrile gloves to mitigate heat transfer and any dirt or grease to the sample. Loading the sample took roughly five seconds from lifting the lid over the cold plate and shutting the lid of the coldbox, during which the sample was exposed to room temperature air. The loading of the sample is made when the thermocouple reads -10.5°C. Once loaded, the temperature of the block will rise to roughly -9.5°C before beginning to cool again. Once the temperature reads -10°C, the power supply to the heater is switched on, and a stopwatch was started. A USB camera in the lid and led light could be used to monitor the sample. It became practice to not use the camera to anticipate the shedding of the ice as depending on the surface the ice may begin to move or twist for several seconds before being shed. The time was recorded when the ice struck the bottom of the cold box, a short fall from the substrate. As if the ice shifted from melting but did not detach and the heater is switched off, the sample may refreeze, which is the equivalent of forming runback ice on a heated aerofoil. This method reduced human error when compared to measuring the time at first motion. As this initial motion could be very slight and considering several tests would be completed across a four-to-six-hour period on most working days of the week, occasional misjudgment was inevitable and so was avoided. Once the result was recorded, the sample was removed from the seating block, and the rubber band was reset and left to cool back to the operating temperature.

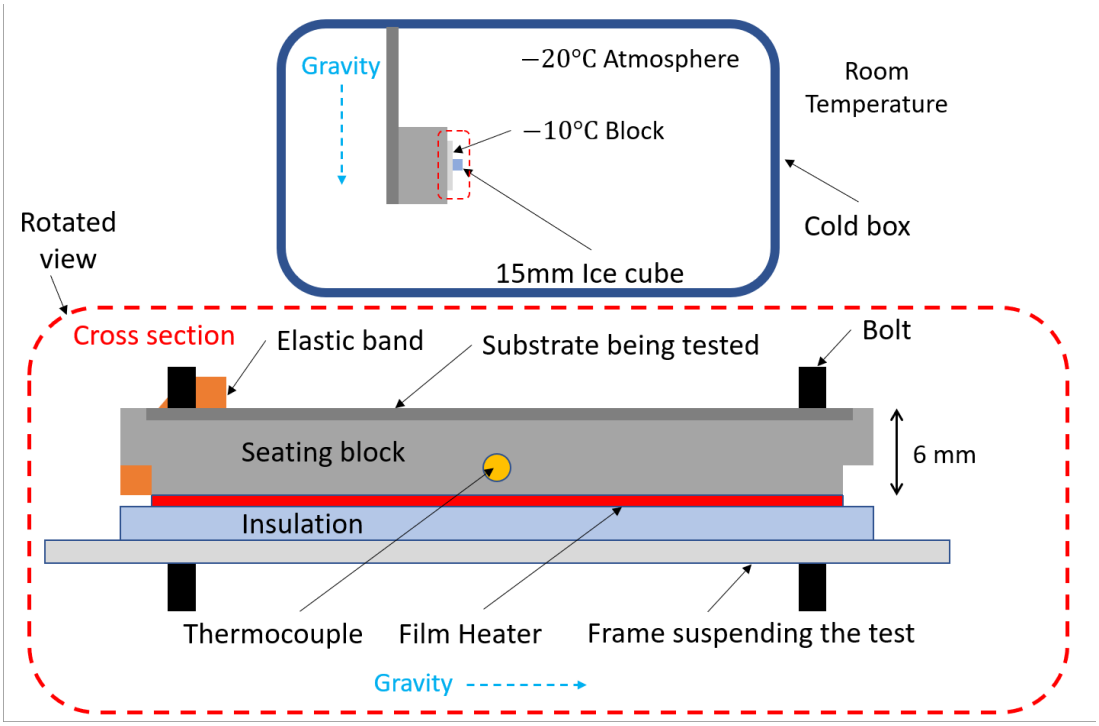

Figure 4.19 Cross sectional diagram of the second iteration seating block and clamping mechanism.

With a 10 W powers supply the film heater had a power density supplied of 2.8 kW/m^2. This was increased from 5 W initially used to mitigate any potential variation caused by the impact of the cooling system. As the coldbox has an active cooling system with an unknown programme, it is unknown whether the refrigeration system would vary during the experiment. It was assumed that as the temperature of the seating block remained consistently above the target temperature of the coldbox of -20°C it would be consistently trying to cool the contents. This would leave the heat flux lost to the air and surrounding structures to be a function of the time and temperature difference. As the film heater's effectiveness is limited by heat losses and the cooling system, which was assumed to be fixed, the longer the experiment, the greater the proportion of the energy consumption measured was spent fighting the cooling system. If a coating is particularly insulative, the rate of temperature change may slow to significantly affect the result as a greater proportion of time is spent with a high ΔT between the walls of the cold box, air within the box, and the seating block. If this occurs, a linear trend may deviate if it becomes significant. Increasing the power supply reduces this opportunity; however, it could limit measurable differences between two similar surfaces if systematic errors are of a consistent magnitude for what is now a shorter test.

4.8 Mechanical de-icing

Two mechanical de-icing methods were used to measure the ice adhesion strength of the surfaces. The shear stress at adhesion failure was inferred from the peak force applied to a known iced area during mechanical de-icing. The two methods consist of a pull test with a load cell used to measure the peak force during the test and the centrifuge adhesion test (CAT) where a known mass of ice is spun until the centripetal acceleration required to keep the ice adhered surpasses the ice adhesion strength of the surface.

4.8.1 Mechanical pull test

The pull test aimed to provide an accessible method of testing ice adhesion strength in the same environmental conditions with as similar preparation as possible as the static electro-thermal de-icing experiment.

In practice, the force is not applied in the same plane as the surface. For example, the centrifuge method applies shear stress at the surface stress by increasing the centripetal acceleration until adhesion failure and so the force that the ice-surface interface must apply to the ice. The geometry of the ice determines the area of attachment and the position of its centre of mass around which the centripetal acceleration acts. For a cube such as those produced for this experement, the centre of mass is proportionally further from the surface relative to the area of attachment than if the ice was half the height. A more accurate measurement would be obtained if the ice adhered to the surface covered a larger surface area and is not thick, so the centre of mass is closer to the surface. For the centrifuge method, this poses a problem as reducing the depth of the ice adhered reduces the maximum centripetal acceleration that can be tested, and all else is equal, as the mass has been decreased or the adhered area has been increased. Limiting the maximum adhesion strength that the equipment could measure.

As ice adhesion strength testing lacks standardisation of the type of shape and its specific geometry, relative results to a reference such as aluminium are commonplace, as well as the calculated stress required for adhesion failure. Certain testing parameters may favour different mechanisms being explored. If the centre of mass is proportionally higher for one centrifuge experiment when compared to another, or the force applied in a push or pull test produces different moments between other testing methods. Elastomeric coatings utilising interfacial cavitation to reduce a surface's ice adhesion strength could have their

results influenced disproportionately if this parameter is changed when compared to a coating or surface utilising a different mechanism. In light of this, the initial harness used was flat-walled, applying pressure across an entire face of the ice Figure 4.20.

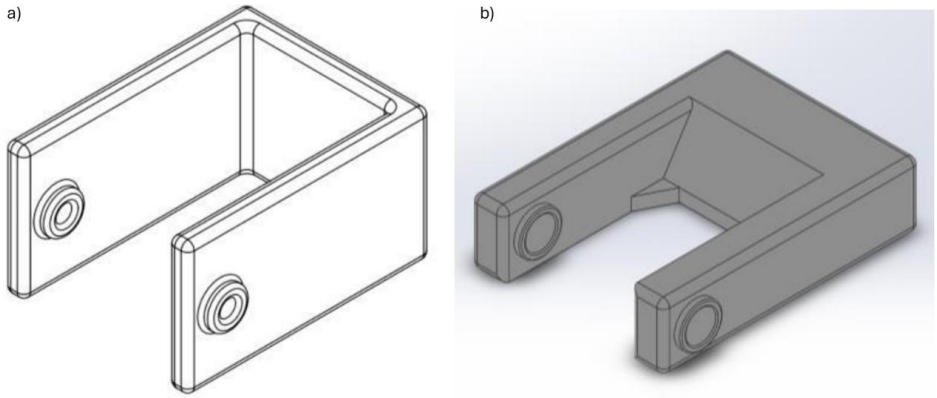

Figure 4.20 a) initial harness b) second harness designed to apply the pressure close to the surface with a 15 mm internal width to match the ice.

The centrifuge method is regarded as being highly reliable and more consistently repeatable between laboratories. This pull test was designed with the idea that the results obtained may provide a more accurate value of ice adhesion strength from a mechanics perspective and, if reliable, allow additional context to ice adhesion values measured using a centrifuge method by altering the height above the surface that the force is applied. A comparison of results obtained with the force applied as shown in Figure 4.21, a flat harness and the harness in Figure 4.21 flipped so the force is applied away from the surface to apply a larger moment. If viable and a meaningful difference could be measured, insight into the mechanisms at play and their relative impact may provide granularity to a surface's performance qualities. The second harness applies the force at a height of 1 mm above the surface rather than 7.5 mm, as with the flat-faced harness, which would be in line with its centre of mass as it is a cube.

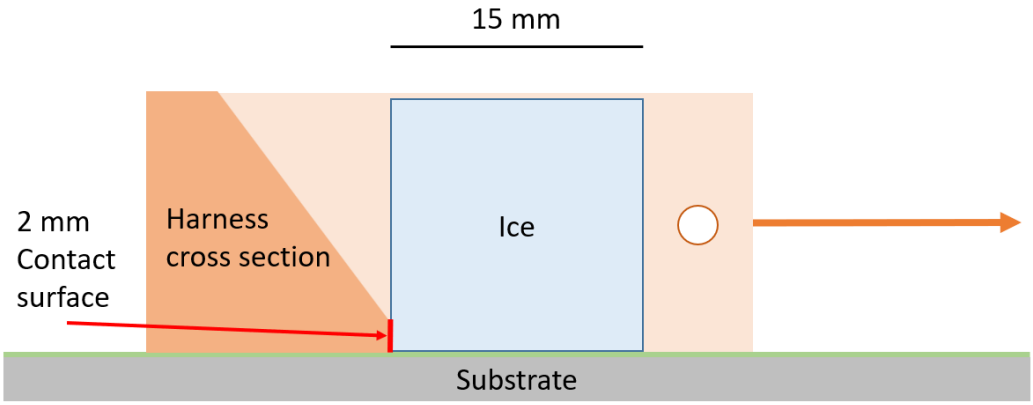

Figure 4.21 Harness that was designed to apply the force as close to the surface as possible, which suffered from an applied moment.

The harness is pulled via an aramid fibre string, chosen due to its stiffness to minimise any strain during testing. The string is fed through a port in the lid ,over a nylon pulley and to a load cell at the same height Figure 4.22.

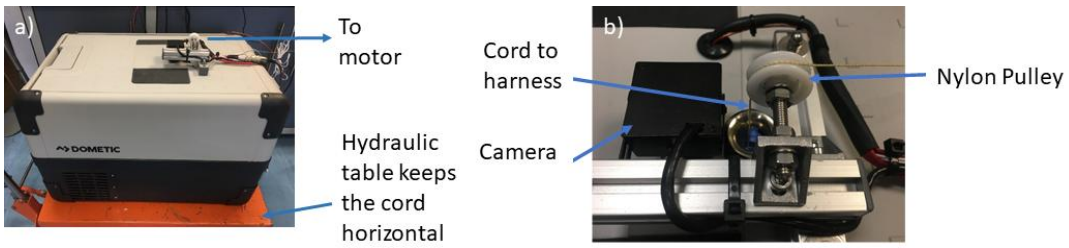

Figure 4.22 a) view of the coldbox and b) pulley system attached to the lid.

The other side of the load cell is tied to an axel on a stepper motor that winds in the cord until the ice detaches. The cord can be wound due to a spring in series with the load cell and cord attached to the harness. A peak force is recorded from which the ice adhesion strength was inferred, assuming pure shear stress at failure and no moment about the plane of the surface.

4.8.2 Centrifuge de-icing

A Design Environmental ALPHA 1550-40H was used to produce a cold environment within which testing could take place. With testing completed at a temperature of -10°C and samples frozen within the same chamber at that

temperature overnight. The centrifuge equipment itself consists of a stainless-steel drum with a 500 mm diameter and 300 mm depth Figure 4.23. A MOOG G403-2053A servo motor is fixed within the drum and used to rotate a carbon fibre arm measuring 3 mm by 20 mm by 385 mm, providing a clearance of 57.5 mm from the internal wall of the drum. The area of adhered ice was 1.38 cm^2 with a total mass including the mould of 2 g and the centre of mass roughly 3 mm above the adherend Figure 4.24.

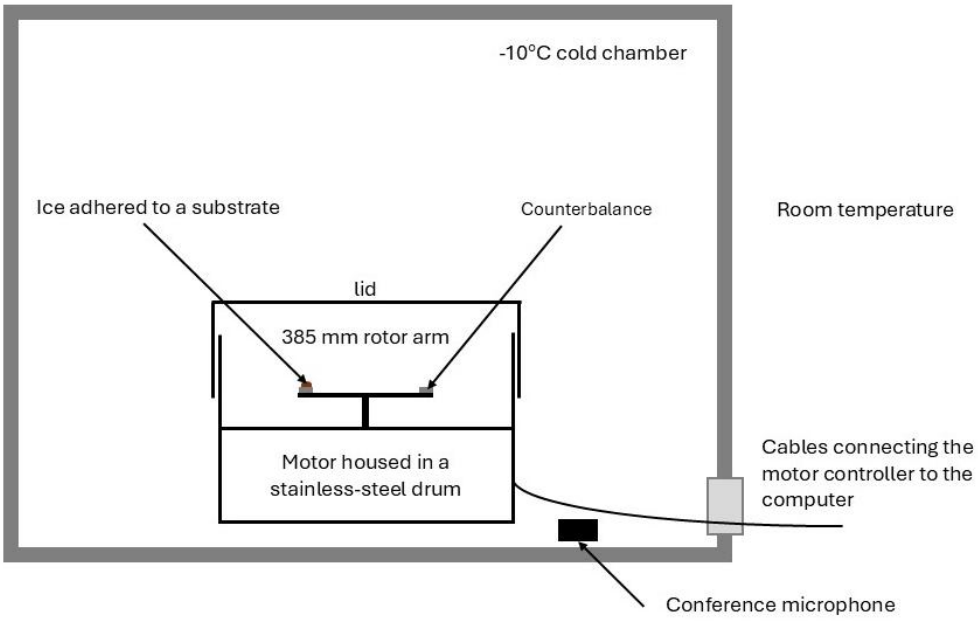

Figure 4.23 Schematic of the CAT.

Figure 4.24 Image of the steel drum and rotating arm used in the CAT.

The substrates tested are identical to those tested in the other experiments described in both electro-thermal de-icing tests and the pull test; however, different ice moulds were used in the experiments using the coldbox. Experiments in the larger chamber used elliptical hemisphere silicon moulds were purchased and individually cut from the sheet with no flange remaining around the cavity as the moulds were left in place during the test. Each mould is filled with 1.3 ml of distilled water using an adjustable pipette before the substrate is placed on top of the mould with the surface to be tested face down. The substrate and mould were carefully inverted and placed upon a strip of plywood, which is used as a sample tray to provide a stable method of moving all substrates at once without direct handling. Additional benefits include ensuring that the surface substrates are placed upon are dry and at room temperature. Mitigating any risk of not incidentally adhering ice to the underside of the substrate between it and the metal internal walls of the environmental chamber and slowing the freezing by insulating the substrate from direct contact with the metal floor of the chamber promoting glaze ice formation at the ice-surface interface.

The motor has a maximum speed of 4500 rpm, an acceleration of 30 rpm/s equivalent to π rad/s, and a deceleration of 200 rpm/s was used. The initial

methodology used one arm with each sample unscrewed and replaced between tests. To reduce direct handling of the substrates each sample was bolted to its own carbon fibre arm before adhering the ice. A counterweight was bolted at the opposing end to reduce induced structural vibration. A secondary benefit was that this required one bolt to be removed and replaced at the axis of rotation in the centre of the arm rather than the two bolts affixing the sample to the arm. The legacy protocol within the laboratory was to allow a minimum of five minutes after replacing the sample being tested and leaving the chamber to allow the environment to return to the testing temperature with any equipment that was handled. The time waited before beginning the test was extended to 10 to 15 minutes, depending on the room temperature on the test day. The decision behind these two changes was influenced by the experience provided by the electro-thermal de-icing research and how sensitive the testing procedure may be. The detachment of the ice was recorded when the ice struck the drum wall using a microphone placed within the chamber. From this, the shear stress was inferred and the ice adhesion strength of the surface can be determined.

4.9 Electro-thermal de-icing with a dynamically applied shear load

This experiment attempts to produce a more service-like operational environment of an icephobic coating that could be retroactively applied to an engineering structure with a legacy thermal de-icing system in place. Either the surface's intended purpose is to enhance this system or a passive surface is being trialled, and knowing its impact upon a thermal de-icing system's performance is required as a safety precaution. Providing insight into the performance of the surface in a mixed loading condition where a shear stress is applied to the ice-surface interface during a thermal de-icing cycle.

A mixed loading experiment was performed in the Design Environmental ALPHA 1550-40H chamber, where a rotating arm is spun at a fixed speed, thereby applying a fixed centrifugal shear stress at the ice-surface interface while electro-thermal de-icing occurs. Each substrate was bolted to a seating block before ice was adhered. The block was bolted to the rotating arm to sit on top of a 25 W film heater and thermocouple that were adhered to the arm. Changing the sample being tested required swapping the seating block bolted to the arm. Unlike the electro-thermal de-icing test a variable power supply was implemented, and the temperature of the film heater was fixed. As the arm spins faster, more heat is lost to the cold environment. A 5 W supply was incapable of

raising the temperature to 0°C at low speeds from the -10°C testing temperature due to the airflow-induced heat loss.

The chamber was set to a temperature of -10°C for freezing the samples overnight to maintain a consistent freezing process as with the centrifuge. In the following morning, the environmental chamber would then be set to the chosen temperature for that day's testing 60 – 90 minutes before it began. The testing temperature was always -10°C for every environmental temperature tested. As the film heater could be programmed with a feedback loop using the PT100 thermocouple on its surface, the target temperature was set to -10°C between tests. This feature provides the most reliable starting temperature of the samples as the coldbox experiments as with the that electro-thermal de-icing test, the start must be timed to begin when the temperature read -10°C, rather than being held at that temperature. The centrifuge experiment used the same environmental temperature as the testing temperature, as no heating was involved. However, no in situ thermocouple was in place, and the only temperature reading available was that of the chamber's air temperature. So, any discrepancy in the handling of samples when loading them would impact the substrate temperature as the door is closed. As such, the delay necessary before an accurate test can be performed could vary from sample to sample or day to day. The feedback temperature control in this experiment provides an additional mitigation while reducing the potential for human error when timing the beginning of the test to coincide with the temperature of the seating block reaching -10°C.

The speed was limited in this experiment by the necessary addition of a Mercotac model 430 mercury slip ring, capable of operating down to -30°C at a maximum operating speed of 1200 rpm. The rotor arm was larger than that used in the centrifuge Figure 4.25. Also cut from 3 mm carbon fibre sheet and measured 60 mm by 600 mm. With the radius of rotation experienced by the ice of 0.275 m in the dynamic test and 0.1675 m in the centrifuge test.

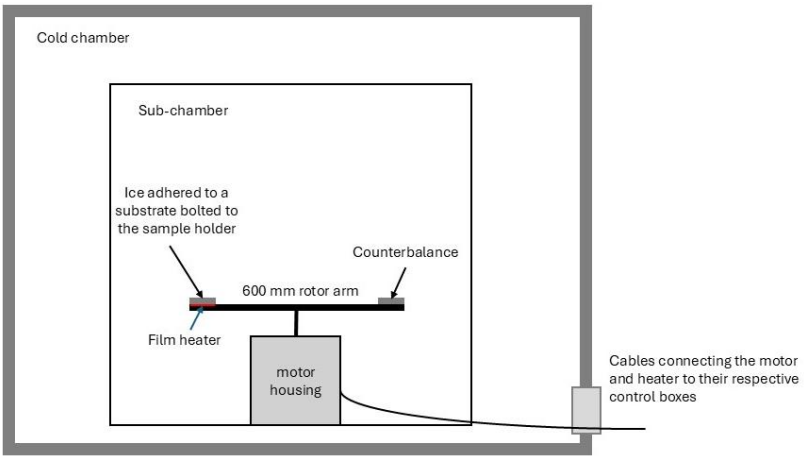

Figure 4.25 Schematic of the dynamically loaded thermal de-icing test.

As this experiment required four bolts to be replaced between tests, wing nuts were implemented despite their less aerodynamic profile due to their size, which mitigated the increase in handling time required to swap samples between test runs. Once exiting the chamber, a mental note of the ' 'chamber's temperature would be taken and subsequently monitored to assess its progression to the target temperature to make a judgement on the time waited until the next test would commence. The time waited until the test was a minimum of 15 minutes, taking additional care if swapping the sample took especially long, the chamber's temperature response and return to the target was slow, or a high room temperature and humidity on the testing day was a concern.

The chosen speed of the test is inputted using the encoding software with an acceleration and deceleration of 200 rpm/s. Two controller boxes were used, one for the motor and one for the film heater and thermocouple Figure 4.26. The latter was used to set a target temperature, and the power supply to the heater was automatically adjusted based on the measured temperature, the rate of temperature change, and the target temperature. Before the test began, the target temperature was set to -10°C and the arm was stationary. The first step was engaging the motor and waiting until the target speed was reached. Then, the target temperature was changed to 60°C from which the time to detachment was measured. This temperature was sufficient for thermal de-icing for the majority of testing parameters used and maintained with reasonable stability throughout all test speeds. The time to detachment is measured audible from a conference microphone in the chamber and headphones listening to them in real-time. The motor was then switched off, causing it to decelerate at the selected rate of 200 rpm/s and the target temperature of the film heater was reduced to -10°C.

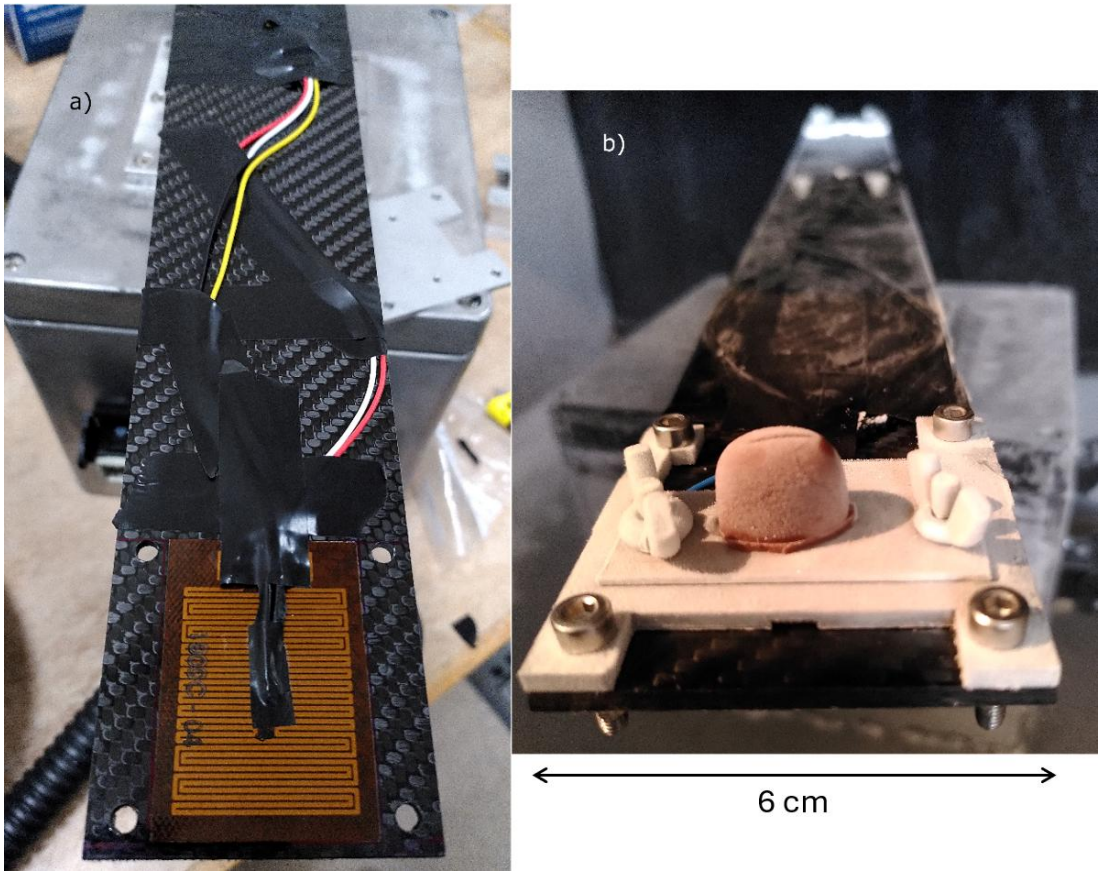

Figure 4.26 Dynamic thermal de-icing a) rotating arm with the film heater and thermocouple taped to the top surface and b) a sample holder with sample bolted to the arm with ice adhered to the to-be-tested surface. For scale, the arm is 60 mm wide and 600 mm long.

Once the temperature fell below -5°C, the chamber was opened, and the sample was changed. The seating block was changed with each substrate already attached, all of which were stored in the environment chamber. The measured temperature of the heater after replacing the sample was always -10°C, suggesting the colder temperature of the seating block was sufficient to cool the heater to or below -10°C. In some initial tests where the environmental temperature of the chamber was set to -10°C, then the temperature of the heater was allowed to fall to -10°C, rather than below -5°C, before replacing the sample. Due to the size of the stainless steel box encaging the motor and arm, entering the chamber to change the sample was not viable as with the CAT. When changing the sample the door to the chamber was opened as little as possible while the researcher leaned in, to reduce airflow in and out. This additional window for air exchange between the chamber and the room is the primary reason for extending the waiting time to 15 – 20 minutes from the 10 – 15 minutes

for the CAT. This is important because the air temperature is more relevant for the thermal de-icing and the low airflow between the enclosed box with vent holes and the rest of the chamber.

Chapter 5: Environmental factors dictating the ice accretion process on rotating bodies

Two surfaces in an identical engineering application may influence the ice structure formed upon it, and so testing the de-icing capabilities with one ice structure at a given temperature may not provide the most accurate method of predicted performance. This aspect has been explored in current research, analysing the freezing of individual droplets, assessing the time delay before freezing occurs [29][39], ice accretion within wind tunnels [13][82][95], numerical studies [96][97][98][99] and the Adverse Environment Rotor Test Stand (AERTS) which is a large-scale rotational icing study [81][100]. This work considers the approach that the surface influences both fluid mechanics and thermodynamics in a freezing scenario. Isolating sections of an aerofoil simulated with the spinning disc experiment. While the scale is much smaller than used in the AERTS facility, it was hoped this methodology would prove more accessible for reproduction while providing valuable insight into the formation of ice accretions rotating engineering structures such as a wind turbine or rotorcraft blade. A significant boundary for this type of testing to become widespread is the scale of equipment needed.

5.1 Blade icing

When adjusting the chord length at the tip to account for the ice accretion at the end of the highest Reynolds number was 9.48 $\times 10^4$, with the critical value typically quoted as 10^5 and small turbines operating below 5×10^5 [101][102]It was assumed that the Reynolds number did not achieve values comparable to those of turbine blades [92]. This comparison was made by using a simplified assumption for this experiment by calculating the Reynolds number as if modelling a flat plate. The Stokes number for three different droplet diameters was calculated to assess whether the aerosol being used was heavily influenced by the airflow. The three values chosen for consideration were 2 μm, 4.6 μm and 10 μm. Taken from the manufacturer's analysis 9% of droplets produced from a 2.5% NaF solution were under 2 μm. The mass median aerodynamic diameter was found to be 4.6 μm and reading from the nebuliser's documentation Figure 4.13, roughly 15% of particles were 10 μm or larger. The more commonly used variable is the mean volume diameter (MVD) of the droplets, it is assumed that these values are not too dissimilar [103].

The Reynolds number did not reach a critical value of 10^5 often quoted for wind turbines for the large blades tested. However, this value was calculated under a simplified assumption of a flat, smooth plate and is likely an underestimate for the tested conditions.

5.1.1 Rime ice formation

A dry growth regime produces rime ice, which is more porous and, therefore, has a lower density than glaze ice. As droplets freeze upon impact rather than impact a liquid layer in the process of freezing, the time scale allows the liquid to be mobilised before freezing completely. Resulting in a denser ice formation in different geometric structures. The density is heavily influenced by the liquid water content (LWC) of the air and the median volumetric droplet diameter (MVD). A low MVD and low LWC will result in a soft rime formation that is less dense and has a lower cohesion strength than hard rime, which occurs with a higher MVD and LWC.

5.1.1.1 Tip structure

Rime ice formed on the rotating blades in the coldest temperatures tested, specifically -6°C, -8°C and -10°C. At the lowest speed tested of 500 rpm in a -10°C

environment, the Reynolds number at the tip, with a chord length of 9 mm, is 8.65×10^3. It can be seen in Figure 5.1 that the ice formation suggests that laminar flow is present as the leading edge of the accretion is flat and perpendicular to the flow, and the direction of growth is parallel to the airflow.

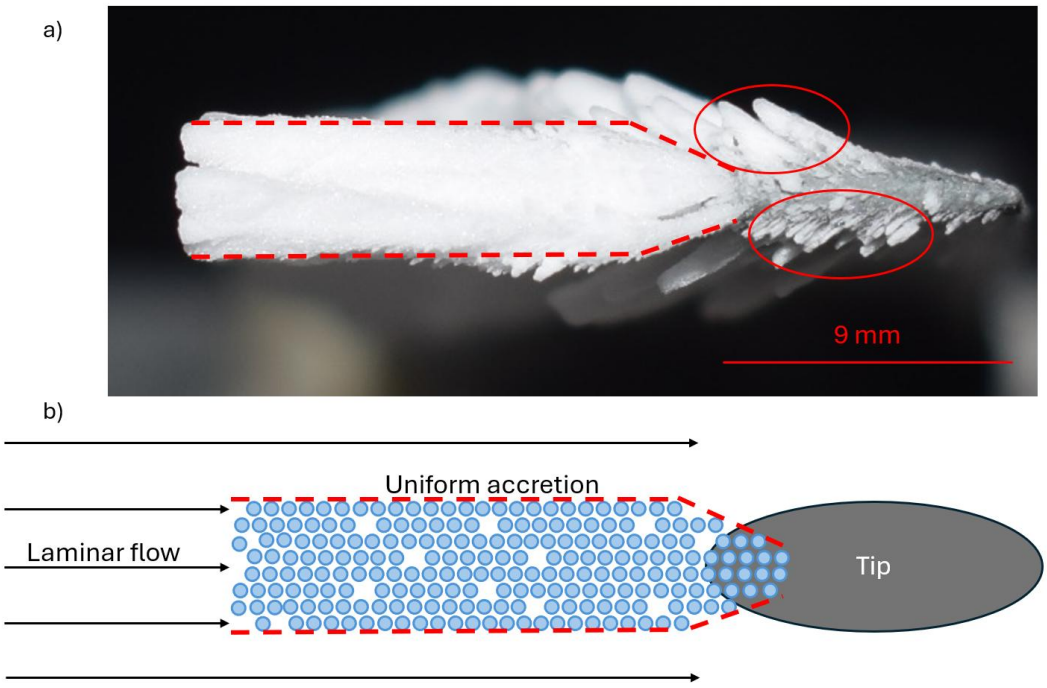

Figure 5.1 a) tip photo of a 500 rpm, -10°C accretion after 10 minutes and a corresponding schematic b) describing the airflow characteristics that explain the structure of the accretion. Parallel horns circled in a) show a close proximity between one another, having nearly grown to form a unified structure.

This structure did not persist with higher motor speeds and warmer temperatures, and the accretion transitioned to a rhombus-like profile where the ice grew into a tip on the leading edge of the accretion Figure 5.2. To investigate the change in this formation, the droplet behaviour and the flow properties were linked to the ratio of the area of the shard portion to the total area of the accretion at the tip. The area of which was calculated using pixel coordinates in Matlab.

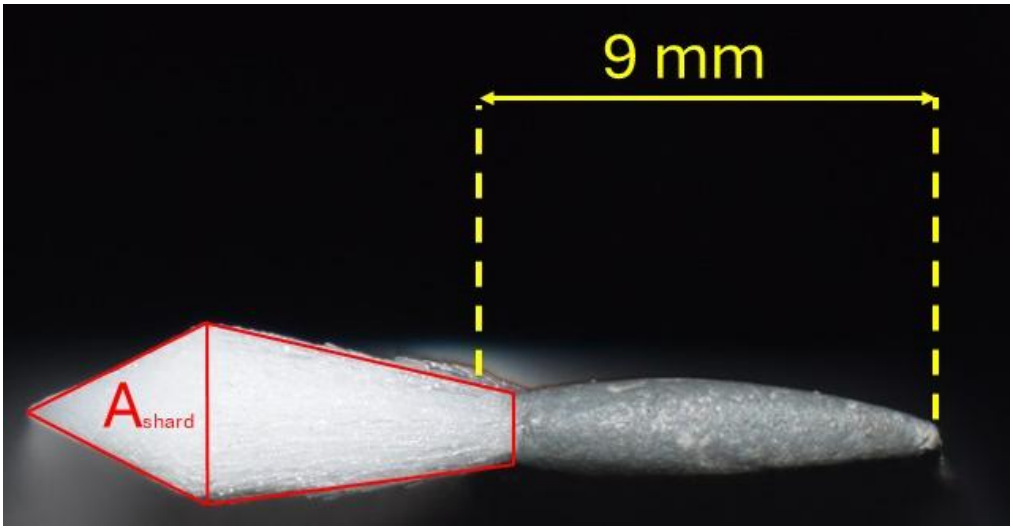

Figure 5.2 Tip formation in a -10°C environment at 3000 rpm with the area split into to segments, the shard and the remaining area described as the trapezoid.

Characterisation of the simulated cloud environment was not completed, and parameter assumptions were extrapolated from the manufacturer's data with a MMAD of 4.6 μm. Data was also compared for a 2 μm and 10 μm droplet to more accurately capture the range of St that was present during testing. The distribution these values were taken from is shown in Figure 4.13, where the fluid medium tested was a 2.5% NaF solution in water. The purpose of the nebuliser is to allow for the inhalation of medicine values for water alone, which are not available in the literature, only for solutions. These additional values were used in the calculations to better represent the range of droplet sizes present and, therefore, provide a more comprehensive analysis of the behaviour of the vapour.

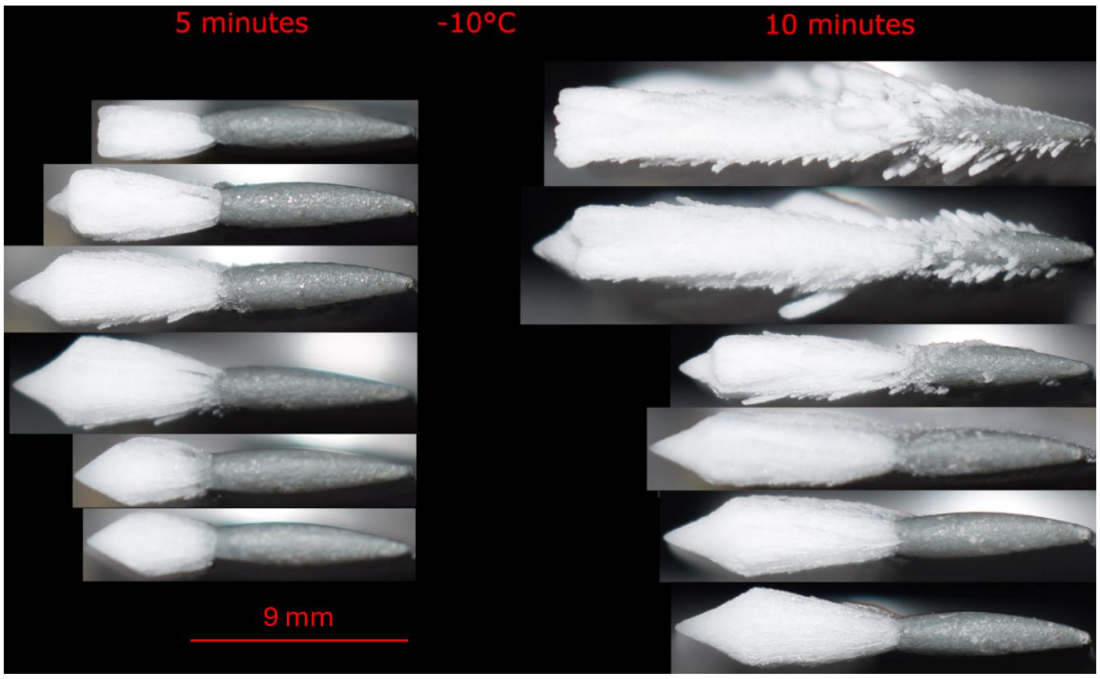

Figure 5.3 Tip growth at -10°C with images taken after 5 and 10 minutes of accretion. Each elapsed time was tested at 500 rpm through 3000 rpm at 500 rpm intervals. Displayed from 500 rpm at the top of each respective stack and increasing the speed to 3000 rpm as the bottom the bottom image.

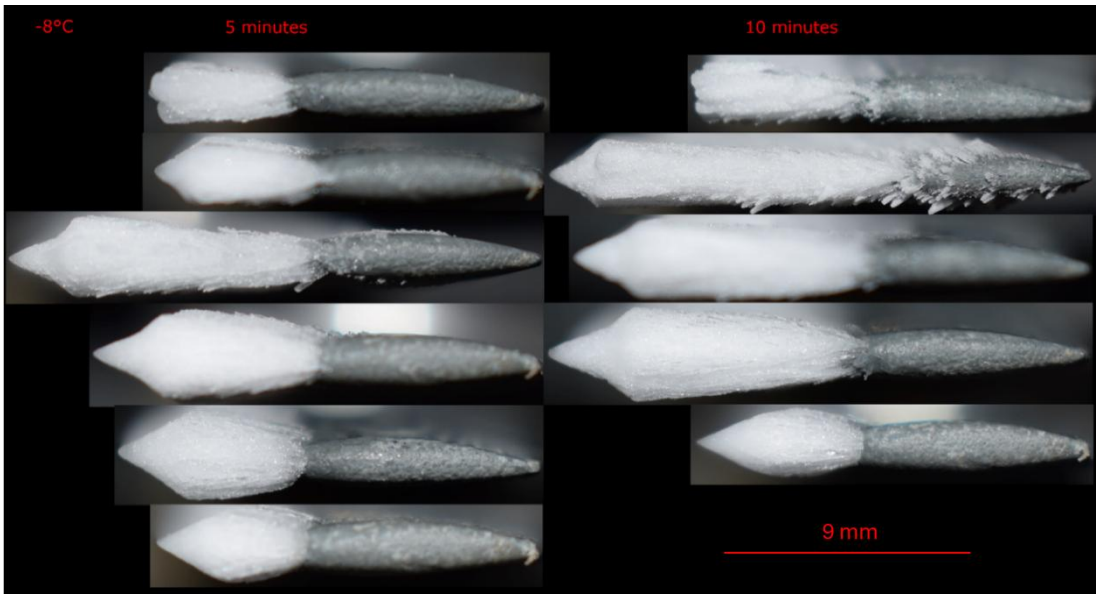

Figure 5.4 Tip growth at -8°C with images taken after 5 and 10 minutes of accretion. Each elapsed time was tested at 500 rpm through 3000 rpm at 500 rpm intervals. Displayed from 500 rpm at the top of each respective stack, increasing the speed to 3000 rpm as the bottom image. (no data for 3000 rpm 10 minutes at $-8°C$)

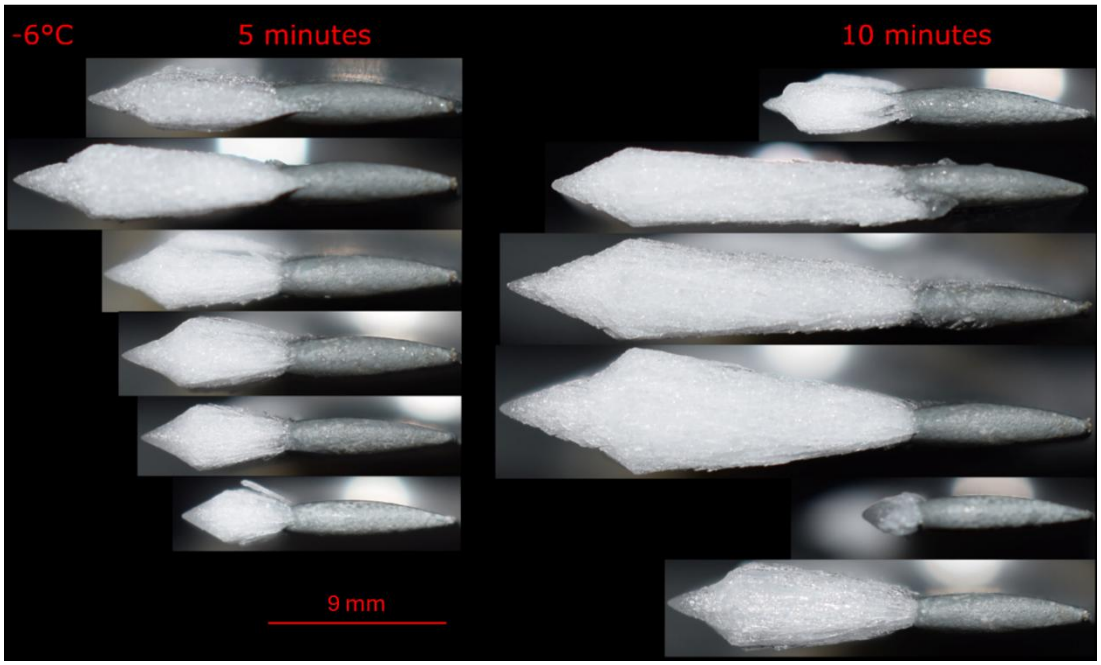

Figure 5.5 Tip growth at -6°C with images taken after 5 and 10 minutes of accretion. Each elapsed time was tested at 500 rpm through 3000 rpm at 500 rpm intervals. Displayed from 500 rpm at the top of each respective stack and increasing the speed to 3000 rpm as

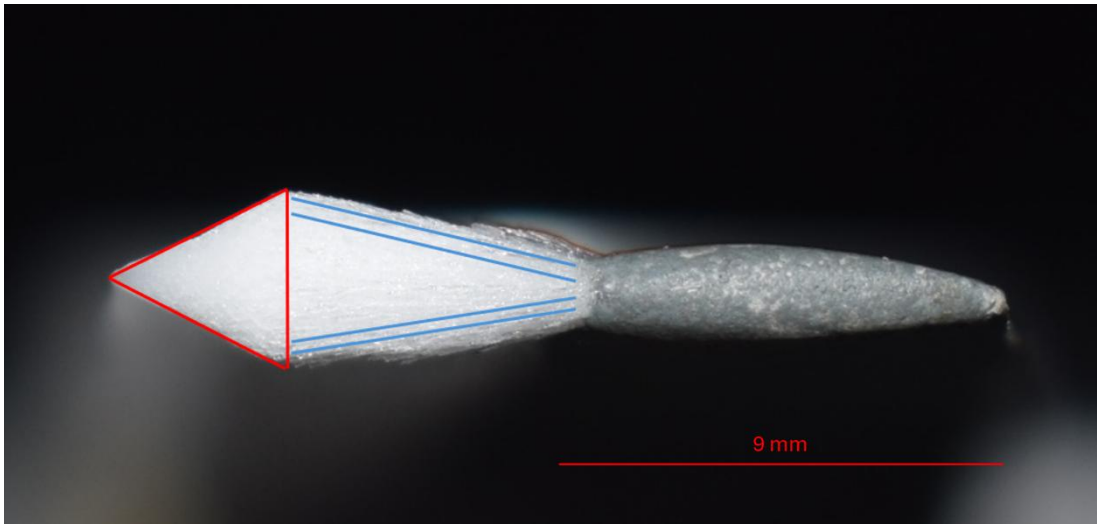

Figure 5.6 In the -10°C testing, the structure at the tip was seen to lack a visible internal structure at this scale in the shard highlighted in the red triangle and the rest of the formation formed in a layered structure parallel to the lines in blue.

The accretion, when split into two portions, appeared to have different structures within each region. The shard appeared much more unstructured to the eye, and

the portion behind it was very structured, with parallel layers forming above and below the initial accretion. Tests at -5°C did not show this structure, displaying less opacity and no longer white in colour, meaning that a dry growth regime was no longer taking place Figure 5.7. Dot-to-dot lines have been used in some figures. They are undesirable but improved the legibility by making each dataset easier to follow.

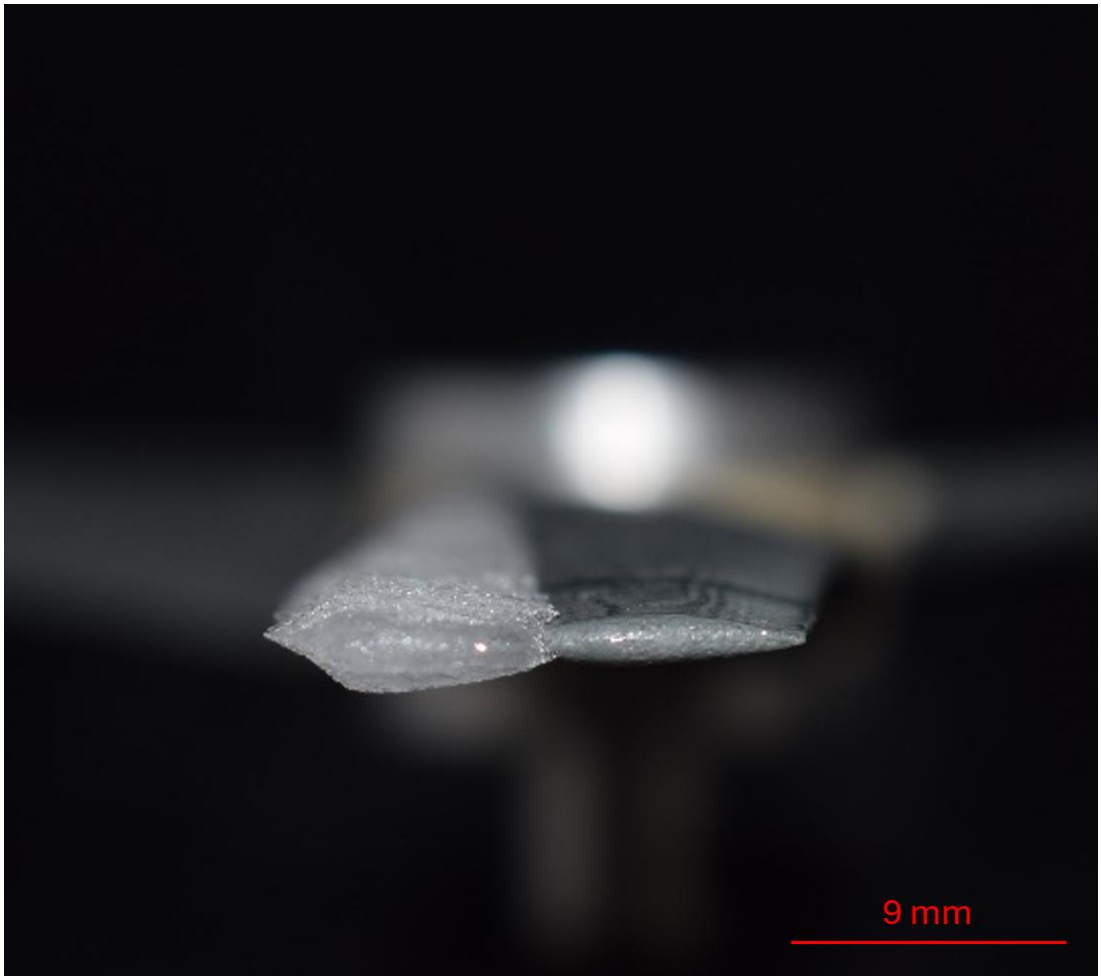

Figure 5.7 An example image taken from a 1500 rpm 5-minute accretion in a -5°C environment displaying less opacity and no longer white, suggesting it is no longer a rime ice structure as less porosity is present.

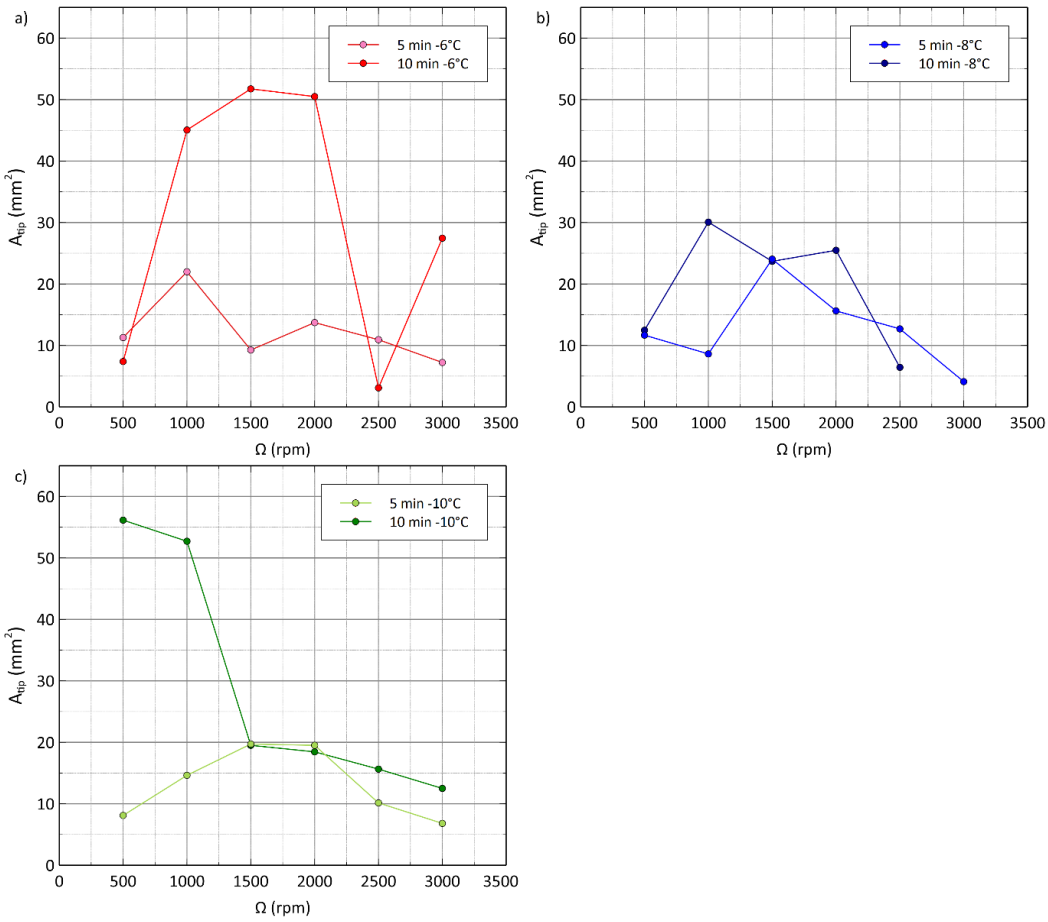

Figure 5.8 The area of the tip accretion, Figure 5.6, viewed down the leading edge, with results shown in Figure 5.3, Figure 5.4 and Figure 5.5. Plotted against the motor speed of each test. (no data for 3000 rpm 10 minutes at $-8°C$)

The total accretion was seen to generally be higher for longer test times, the 2500 rpm, 10-minute result was impacted by significant shedding during the test. To link the properties mentioned the area of the shard was related to the area of the full accretion as fraction to form a non-dimensional parameter. This was then compared to the Reynolds and Stokes number to test whether a relationship was present.

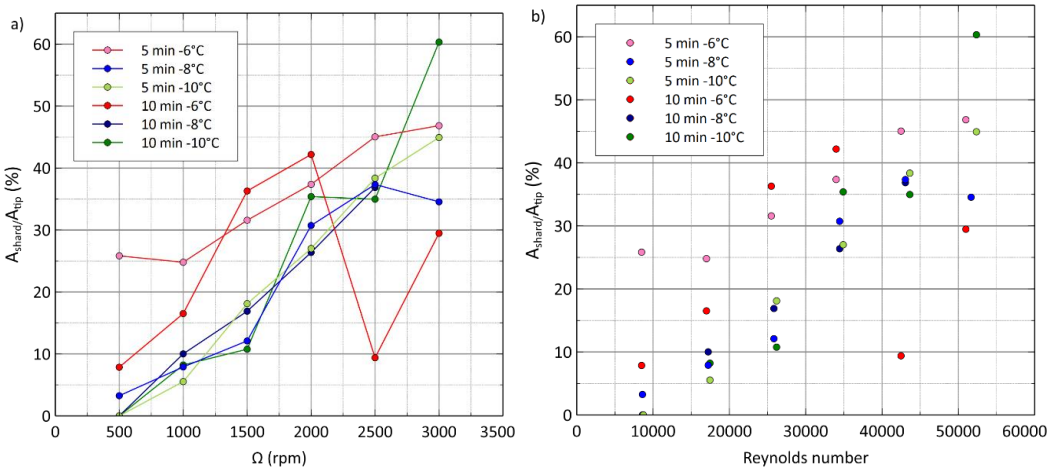

Figure 5.9 a) the proportion of the accretion that is the compared to the motor speed and b) the Reynolds number.

Looking at Figure 5.9, a linear relationship between the motor speed and the accretion can be seen. The proportion of the accretion that is the shard, as seen in Figure 5.9, provides insight into the proportions of each growth mechanism present, with the shard indicative of wetter growth at the stagnation point. With the shard indicative of wetter growth at the stagnation point. The 10-minute, 2500 rpm result for -6°C is low due to shedding occurring mid run which may also be relevant to the 3000 rpm results. The Reynolds number changes with the environmental temperature as it affects the dynamic viscosity and density of air, better relating the results from test to test by contextualising both the environmental conditions and volume of air swept during the test which is proportional to the motor speed.

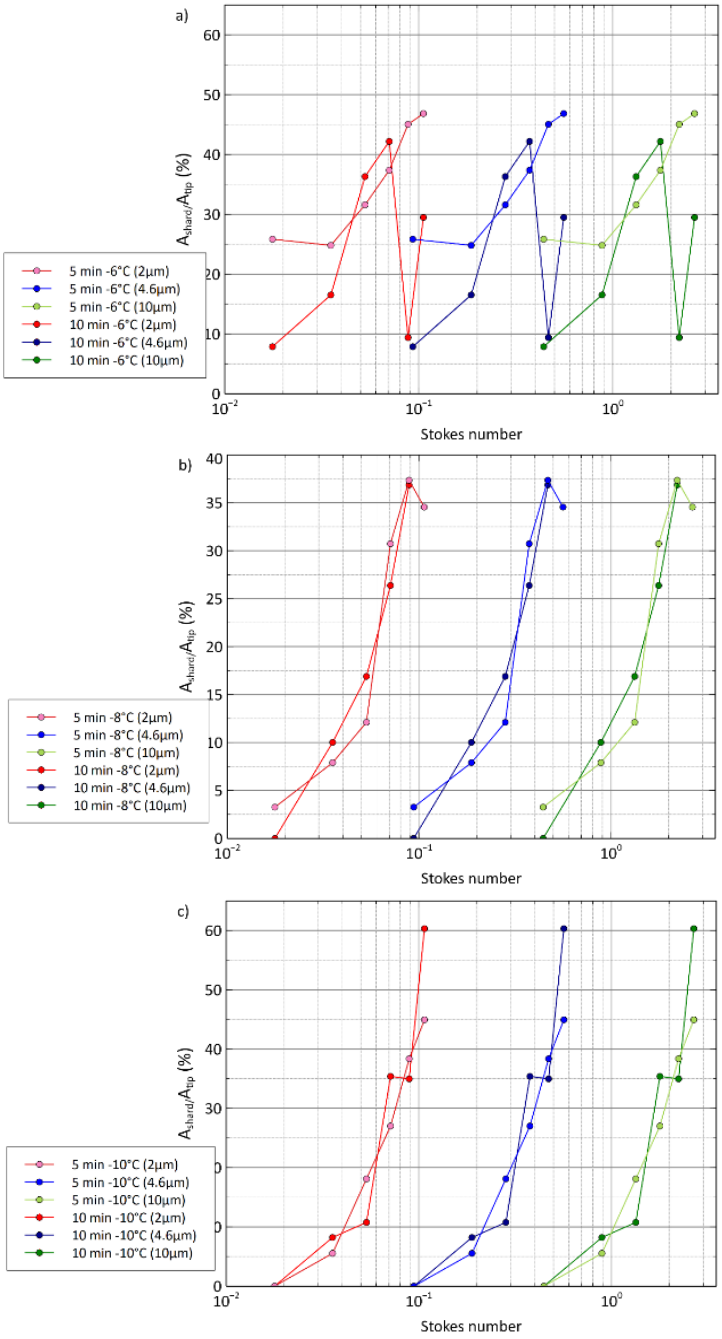

Figure 5.10 Comparisons of the shard proportion to the stokes number for three droplet diameters at a) -6°C, b) -8°C and c) -10°C.

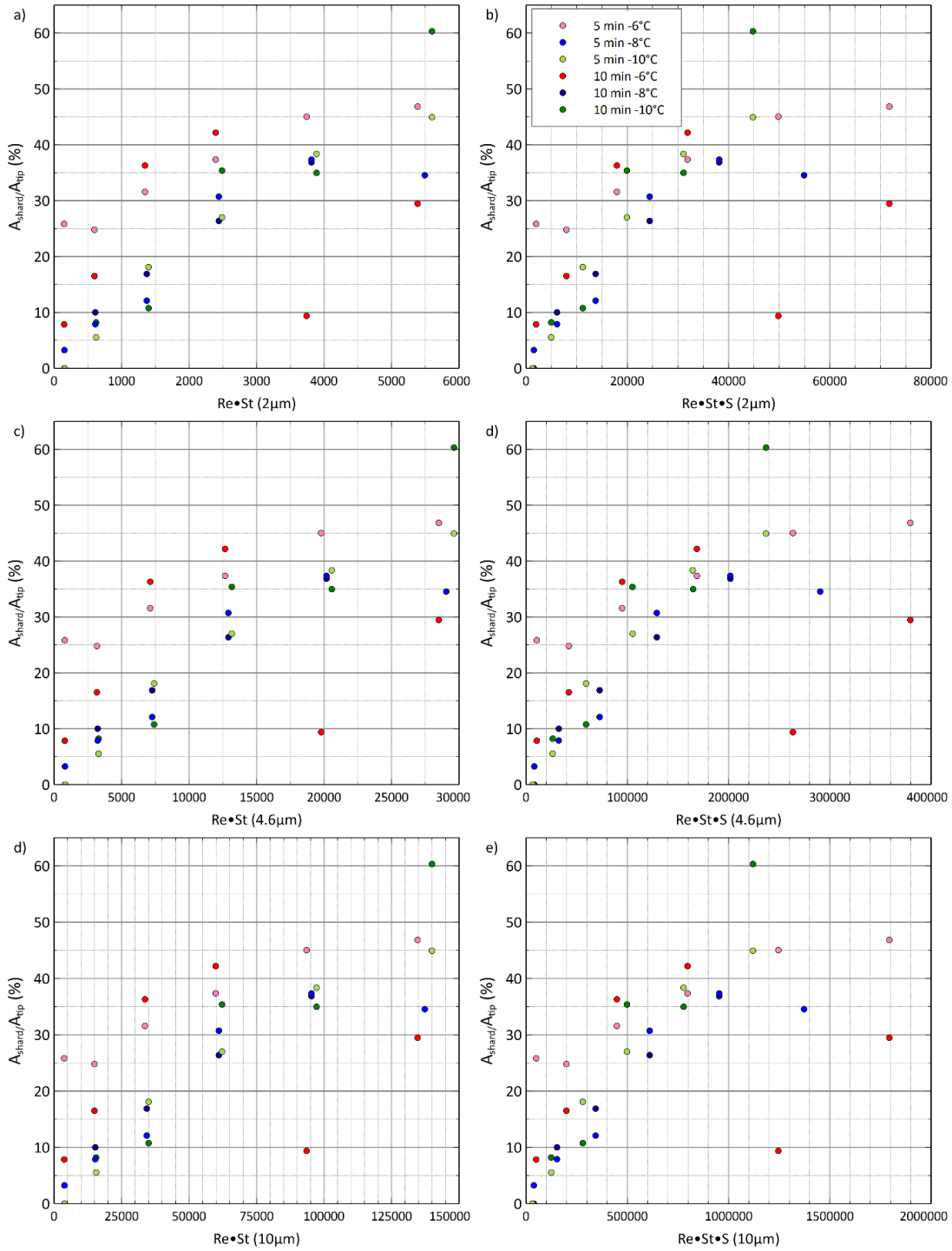

Figure 5.11 Relating the shard proportion to both the Reynolds number and Stokes number for three droplet diameters a) 2 µm, c) 4.6 µm and e) 10 µm. Then accounting for the growth rate by including the Stefan number for each temperature b) 2 µm, d) 4.6 µm and f) 10 µm. The key is relevant for all graphs.

For both -8°C and -10°C lower values of $Re \cdot St$ show strong correlation for the first five of their respective datapoints and the diverge significantly Figure 5.10, Figure 5.11. The results for -6°C do not follow the same relationship and is initially

much more sensitive to the rotational speed, and so increase in the Re·St, for the 10-minute tests while much less sensitive for the 5-minute tests and a much higher proportion at lower speeds in the shorter test. As shedding was clear for the 2500 rpm 10-minute test at this temperature the prevalence and impact was unknown on the observed data and trends for speeds above 2000 rpm for all temperatures but most notably -6°C. After accounting for the growth rate by including the Stefan number the data shows a stronger correlation than accounting for only the flow parameters.

5.1.1.2 Rime ripples

An additional feature present in the rime accretions was a change in geometry along the leading edge, with portions near the root showing clear uniform ridges which become more chaotic as the radius increases. The ripple's wavelength and amplitude were analysed for each portion of the blade to assess the observed changes with the factors influencing the flow properties and droplet behaviour Figure 5.12.

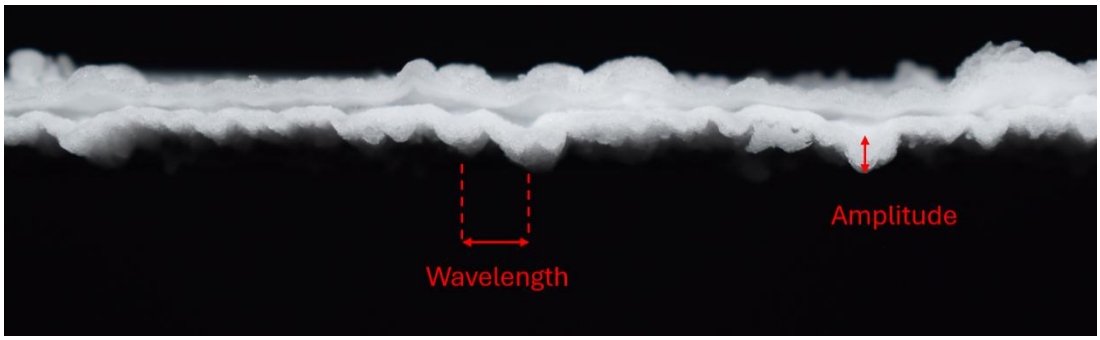

Figure 5.12 The wavelengths and amplitude were identified for each portion of the blade using pixel coordinates and related to the length of the blade. This image shows the wavelengths and amplitude referred to in this section.

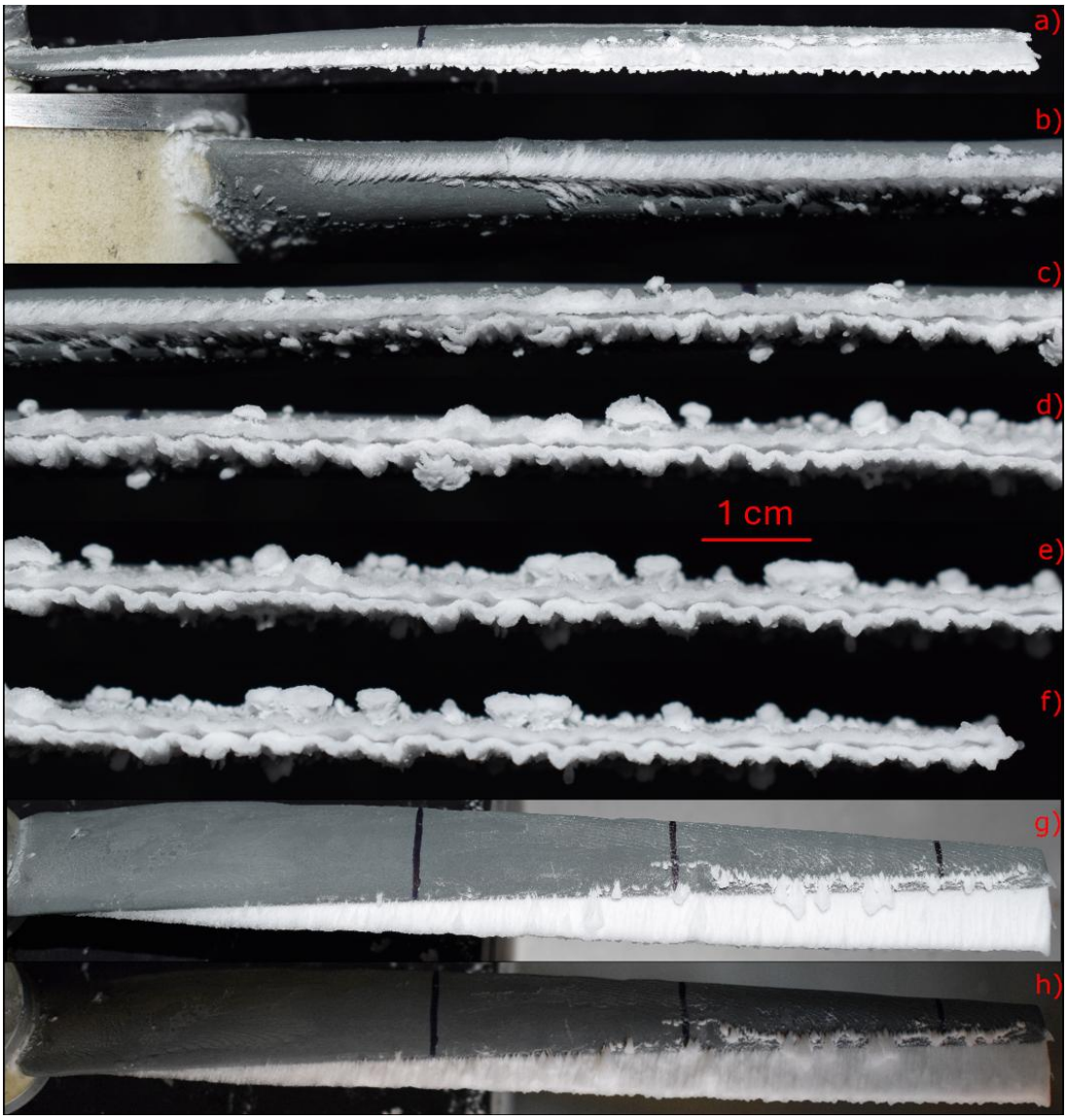

Figure 5.13 Photographs of a blade after 10 minutes in icing conditions at -10°C and a rotational speed of 500 rpm. The overall view a) of the blade and zoomed-in images along the leading edge listed downwards from root to tip, b) through f) for which the scale bar is relevant. Clear structural changes are present along the leading edge of the blade. g) and h) show a plan view of another blade from the same test with and without flash, respectively, with a blade length of 215 mm.

The analysis was simplified to consider the most significant ripples present. It is possible that multiple frequencies are superimposed upon each other, so identifying a basic relationship was the aim. All analysis considers only results obtained at -10°C, Figure 5.13.

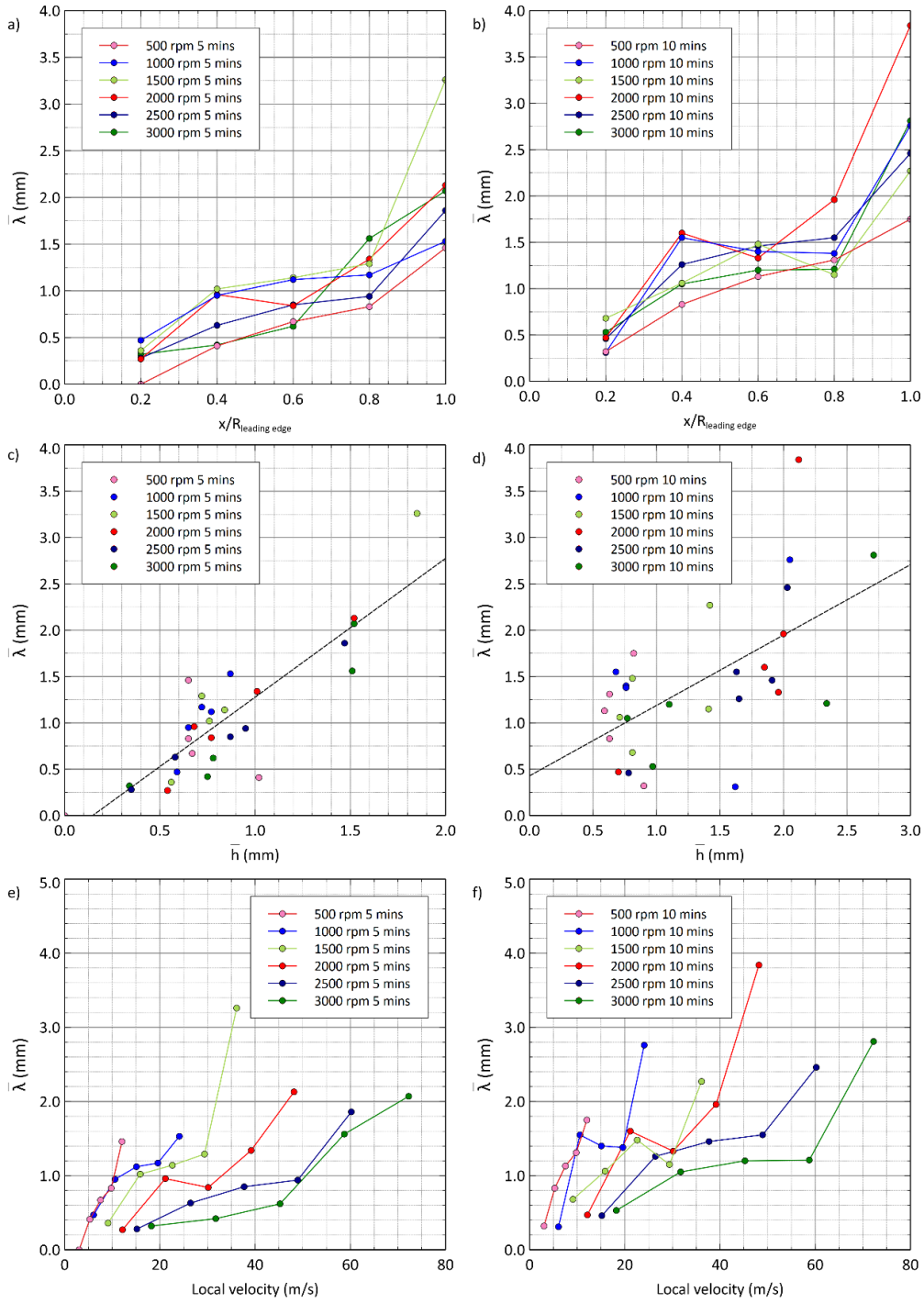

Figure 5.14 a) and b) show the relation between the wavelengths at each section of the blade for 5- and 10-minute tests respectively. c) and d) relate the amplitude of the ripples along the blade for 5- and 10-minute tests respectively. d) and e) relate the average wavelengths of the ripples to their respective local velocities. With $x/R_{leading\ edge}$ representing the relative position the measurements were taken along the leading edge at 20 percentile intervals. All data collected at -10°C. In graphs c) and d) a linear relationship was observed

and plotted with a dashed black line with gradients of 1.5. 0.76 and a y-intercept of -0.2 and 0.4 respectively.

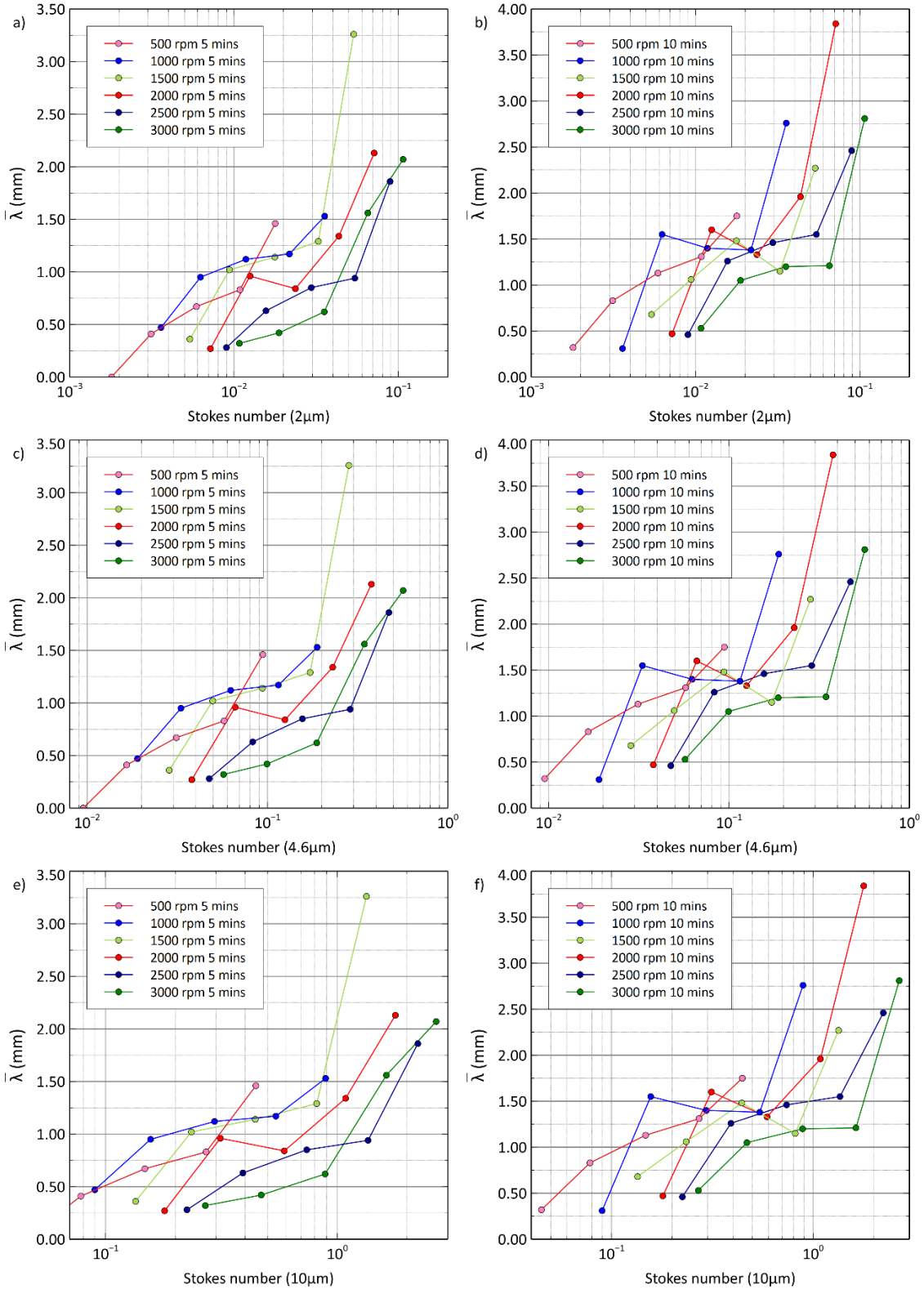

Figure 5.15 The wavelength of the ripples plotted against the local Stokes number for each droplet diameter and the time elapsed. a) 5 minutes, 2 μm, b) 10 minutes, 2 μm, c) 5 minutes 4.6 μm, d) 10 minutes, 4.6 μm, e) 5 minutes, 10 μm and f) 10 minutes, 10 μm.

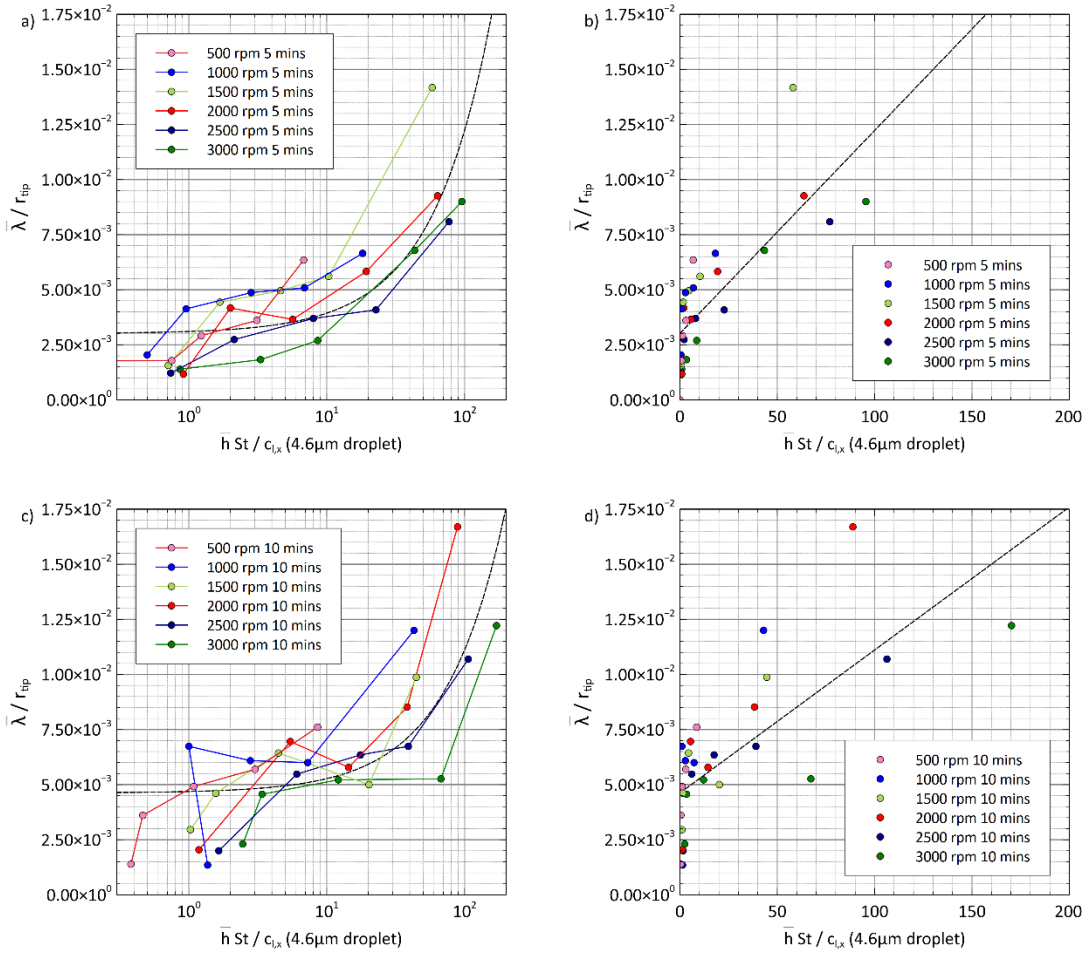

Figure 5.16 The wavelength non-dimensionalised with the radius of the tip plotted against a non-dimensional function containing the amplitude, Stokes number and local chord length for three droplet diameters a) 5 minutes, 4.6 µm with a log x-axis, b) 5 minutes, 4.6 µm with a linear x-axis c) 10 minutes 4.6 µm with a log x-axis, d) 10 minutes, 4.6 µm with a linear x-axis.

The wavelength for 500 rpm and 5 minutes at the 20th percentile was recorded as zero, and the graphs in Figure 5.15 and Figure 5.16.

The relationship observed has been defined as (14).

$$\frac{\bar{\lambda}}{r_{tip}} = fn\left(\frac{\bar{h}\,St}{c_{l,x}}\right) \qquad (14)$$

Where $\bar{\lambda}$ is the average wavelength of the section, r_{tip} is the radius of the swept area, $\bar{h}$ is the average amplitude of the waves of the section, St is the Stokes number of the droplet and $c_{l,x}$ is the chord length at the percentile of the leading edge being measured at position x. This relationship could inform better icing

mitigation strategies by providing understanding or predictive capabilities for the shape of the accretions, which would then impact the aerodynamics and dynamic loading of the aerofoil. Some accretion structures may add risk or reduce the tolerance of the maximum size of the accretion before significant failures occur. Similarly, understanding and predicting the structure of the accretion could be utilised to study the shedding and partial shedding behaviour of the ice upon a blade and how an icephobic surface alters it. If irregularities are caused by any wavelengths present form stress concentrations, this could alter the prevalence or position of cohesive failure. For readability, the data was presented in Figure 5.16 with linear-log plots as they cluster at near-zero values in a) and c), with linear plots of each in b) and d), respectively. Knowing the wavelength and amplitude of ripples forming within ice accretions can be utilised through CFD to understand their negative impact more precisely and better understand the safe limits of operation.

Considering the influence of the Stokes number across the range of present droplet diameters would only be important when comparing simulated clouds with a different distribution present. Alongside any compounding length scale differences, the Stokes number non-dimensionalises. A greater or smaller range of St would impact the rate and distribution of impinging droplets across the leading edge and, therefore, the structure of the ice accretion. As only one simulated cloud type was tested, and therefore the distribution of Stokes numbers, this additional parameter cannot be considered to complete the function above (14). Values of the Stokes number in this test at the tip shown in Table 5.1, and all values in the appendix.

Table 5.1 Range of Stokes numbers present at the tip at -10°C.

RPM	Tip speed (m/s)	St at tip for each droplet diameter			Stokes number present at tip		distribution factor
		2 µm	4.6 µm	10 µm	St_{range}	St_{MMAD}/St_{range}	
500	12.04	0.018	0.094	0.446	0.428	0.2204	0.094
1000	24.09	0.036	0.189	0.891	0.855	0.2204	0.189
1500	36.13	0.053	0.283	1.337	1.283	0.2204	0.283
2000	48.17	0.071	0.377	1.782	1.711	0.2204	0.377
2500	60.21	0.089	0.471	2.228	2.138	0.2204	0.471
3000	72.26	0.107	0.566	2.673	2.566	0.2204	0.566

5.1.2 Glaze and mixed icing

Glaze ice forms with a wet growth regime dictated by a low solidification rate relative to the environmental conditions. The Stefan number describes the rate of freezing in environmental conditions. If a supercooled droplet impacts the surface, a phase of rapid freezing occurs until the remaining liquid reaches the boundary temperature, which is the freezing temperature of water in this Stefan problem. The second freezing phase is an adiabatic process where the rate at which the latent heat of fusion is released dictates the growth rate [60]. Where the droplet is not supercooled and impacts a sub-zero surface without a significant difference between it and the solidification temperature, the rapid initial phase does not occur, the droplet temperature falls to the freezing point, and the adiabatic phase occurs. This process can be defined with a one-dimensional Stefan condition, with the left phrase describing the rate of latent heat released per unit area and the right-hand phrase the heat flux.

The slower freezing process that occurs during the formation of glaze or mixed icing increases the time that the water exists as a liquid. During this time, the liquid is subject to airflow and centripetal acceleration, which influence its position relative to the blade. These forces depend on the blade's characteristics and the rotational speed. In non-freezing conditions, impinging droplets on the leading edge will travel along the chord length before shedding from the aerofoil or travel down the leading edge and be shed from the tip. In glaze icing conditions, the motion of the droplets before completely freezing will influence the distribution of the ice accretion along the blade. Studying the mass distribution of glaze ice accretions and then compared with that of rime ice was identified as a possible route for analysing the formation process. Where deposition of water vapour is the primary accretion process forming in a dry growth regime, the ice geometry produced will be significantly influenced by the airflow properties. That is the dominating factor dictating the position of small droplets with a Stokes number significantly below 1. Alternatively, the rate of impingement is low enough to limit wet growth. The locomotion of the water over the solid surface will have a greater degree of influence than the airflow initially carrying the droplet.

Analysing rime growth within this experiment showed that the extension of the growth perpendicular to the leading edge was proportional to the position down the blade length, where x is the radius of the point minus the radius of the hub, and R is the length of the total length of the leading edge and r_{tip} is R plus the radius of the hub, the size of the accretion was proportional to x/R. Producing an accretion with a consistent angle deviation from the leading edge. Under the assumption that this is caused by deposition being the primary freezing

mechanism, the experimental factors impacting this growth are a function of the time duration, LWC, Reynolds number, density of the ice and motor speed.

As the environmental conditions shift from promoting dry growth to a wet growth regime, the density of the ice increases, and it becomes less porous. In a laminar dry growth environment, it was observed that the angle of the rime accretion was consistent relative to the leading edge. Until the growth area becomes comparable to the area of the blade and the angle deviates from the angle at the root Figure 5.17. Under the assumption that this represented a linear growth proportional to the droplets that impinged the surface, it was considered how this angle would vary for glaze or mixed icing scenarios. As within wet growth, the liquid can move relative to the blade before solidification. This could manifest as a reduction of the icing angle as the mass distribution is skewed to the tip of the blade. The rime angle at the blade root is there for the function of the swept area over the test, the Reynolds number and the average density of the ice. These properties encapsulate the rate of impinging water volume and the freezing mechanism present. Image analysis was completed using pixel coordinates in Matlab, comparing these factors for mixed and glaze ice accretions to infer what relationships are present.

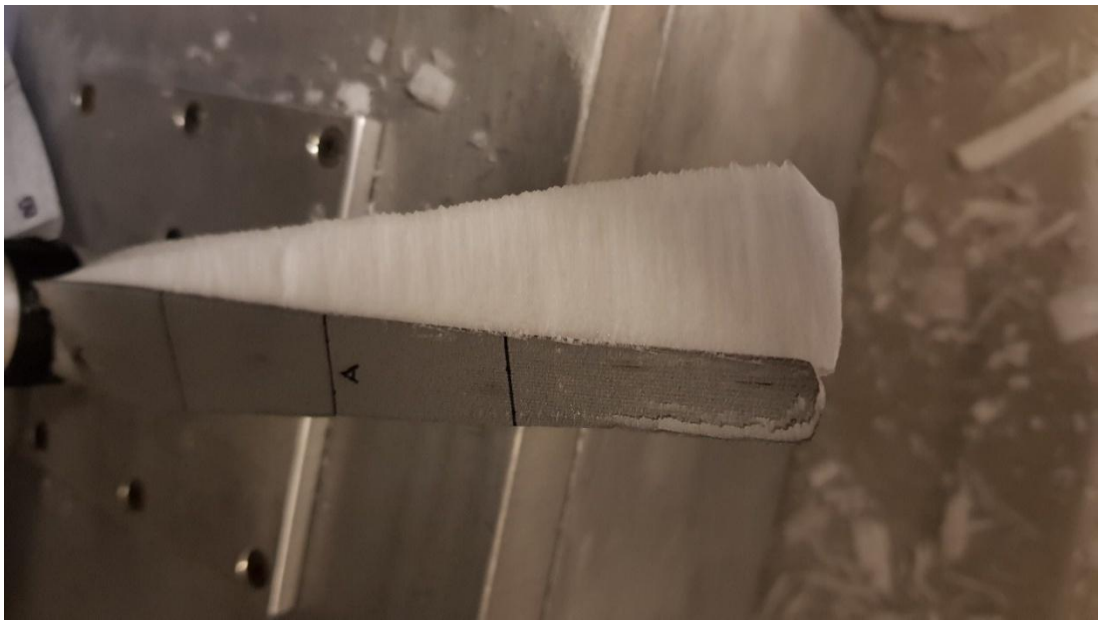

Figure 5.17 View from above of a rime accretion proportional to its position along the leading edge. With accretions this large, the angle of the rime begins to deviate from the linear progression of the angle at the root on the 145 mm long blade.

5.1.2.1 Rime angle

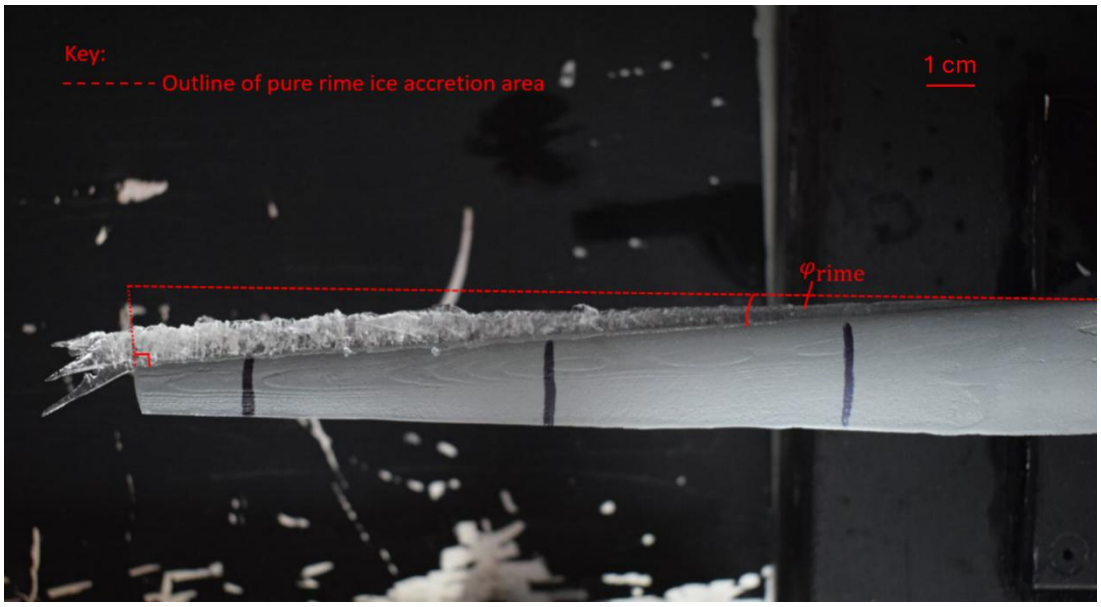

Figure 5.18 Comparing the rime angle of an accretion to the glaze ice adhered towards the tip of the blade.

The data in this section was collected using the smaller 146 mm blades with the rime angle, φ_{rime}, was measured from the accretion at the blade's root, where no wet growth occurred. A linear relationship was quickly observed between this angle and the length of time of the test, and for rime, only accretions would extend to the rest of the blade and no significant growth features outside the radius of the tip, as seen in Figure 5.17. It is applied to wetter accretions, as shown in Figure 5.18, to compare the relative mass distribution between that seen and a theoretical rime accretion.

The rime angle represents the expected maximum ice accretion for the tested parameters if an entirely dry-growth regime was present. The ice's volume is a function of the rate of impinging droplets along the leading edge, which is primarily governed by the volume of swept air and the radius from the axis of rotation at any given point. This provides a theoretical maximum accretion that wetter growth can be compared to as the rime growth increases linearly along the leading edge which is proportional to the position along the leading edge, which does not occur when wetter growth is present. The rime angle was confirmed to be proportional with the time elapsed for all temperatures Figure 5.19 a), and the speed was less strongly tied to the rime angle for -2°C and -4°C where Ωt shows no strong correlation. However, -6°C had a stronger linear correlation with Ωt than with t alone Figure 5.19 b). This could be indicative of the rate of solidification being slow enough to mitigate a higher frequency of impinging droplets due to a higher Ω as this factor also increases the droplets'

speed relative to the surface, reducing the opportunity window, increasing the likelihood of each droplet shedding before freezing The rime angle was then compared to the Reynolds number at the tip c) and the average density of the accretion d). Correlations of the Reynolds number were only identified for the rime accretions observed at -6°C.

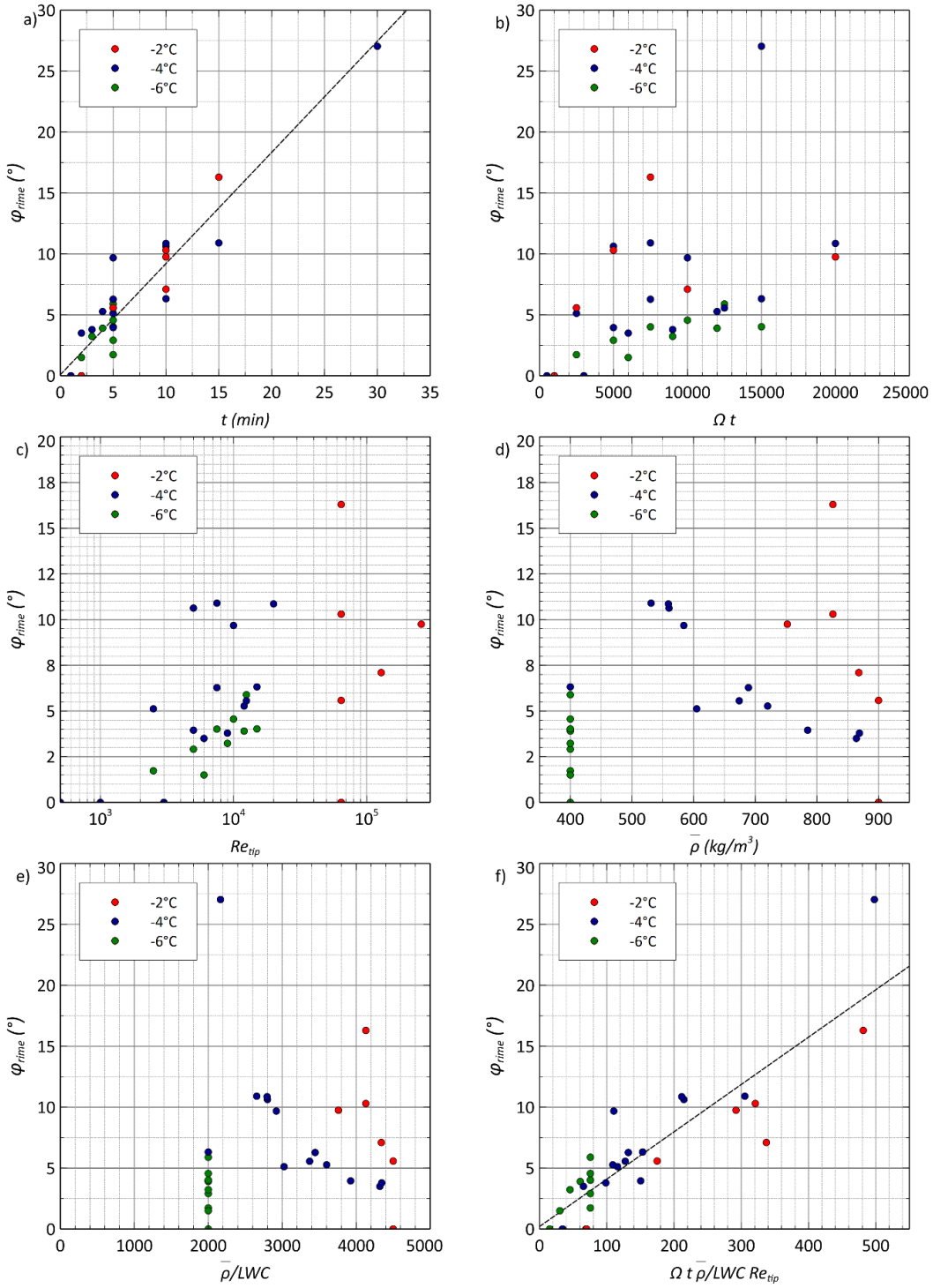

Figure 5.19 The rime angle plotted against a) time elapsed, b) total revolutions of the blades during the test, c) Reynolds number at the tip, d) average density of the accretion, e) The average density divided by the LWC, which was assumed to be constant at 0.2 g/m^3 as it was not tested for and f) a function of the revolutions completed and density related to the LWC and Reynolds number at the tip.

Relating all the identified parameters that may influence the rime angle were combined into a non-dimensional function shown in Figure 5.19 with a gradient of 3.9×10^{-2} and a y-intercept of 0.2. The Individual factor with the strongest correlation is with the accretion time shown in Figure 5.19 a). It is noteworthy that the higher density of the ice had a strong negative correlation with the rime angle at -4°C and for -2°C to a lesser extent. This factor has had an impact by reducing the stacking of the data in f), which is apparent in a).

5.1.2.2 Glaze angle and mass distribution

The observations of the rime angle also led to analysis of the point of transition from rime at the root to glaze ice along the leading edge, visible in Figure 5.20.

Figure 5.20 An example of the ice transitioning from rime to glaze down the blade. 500 rpm, -2°C, 15 minutes.

Where this occurs will be a function of the Stefan number, S, and the distribution of mass along the blade. The mass distribution will depend on how far water can travel before ultimately solidifying. The Reynolds number was used to quantify this factor. As the tip growth signifies both a shift in mass and the potential for water to be shed from the tip before freezing, its length was identified as a factor in relation to the length of the blade. Figure 5.21 highlights the significance this factor can pose and highlights that simplifying the analysis to its length does not wholly account for the shift in mass as they did sometimes form with significant three-dimensional structures.

Figure 5.21 a) A plan view and b) tip growth viewed from the leading edge formed after 15 minutes at 500 rpm in a -4°C environment.

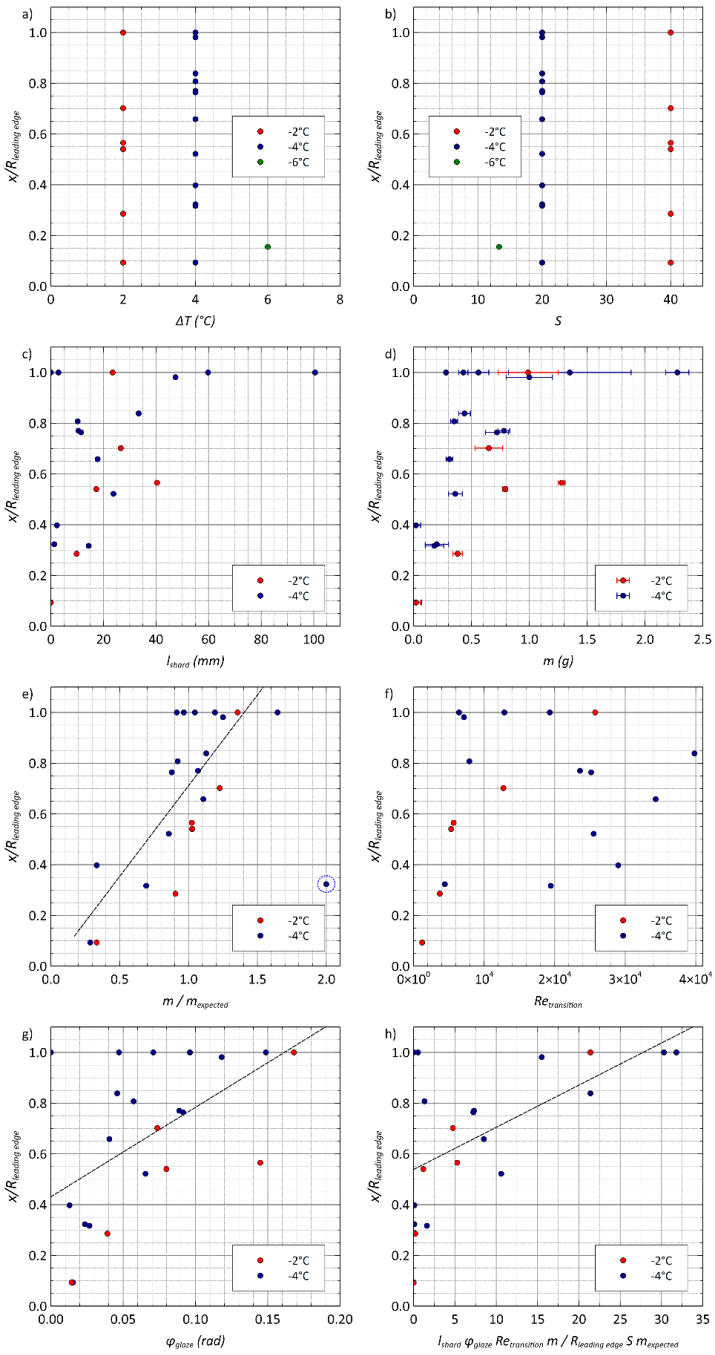

Figure 5.22 The point of transition was measured from the root and related to the length of the blade and then plotted against identified environmental conditions and other dimensions of the accretion: a) the temperature difference between the liquid and solid boundary at the point of freezing, b) the Stefan number, c) the length of the shard as a fraction of the leading edge, d) the measured mass with error bars indicating the difference to the expected value if it were a rime accretion, e) the measured mass compared to the expected mass with an anomaly circled and excluded from the line of fit, f) the Reynolds number calculated at position x, g) the angle of the glaze ice compared to the leading edge, h) a dimensionless function combining all the identified variables.

There was a loose correlation between the length of the ice shard extending from the tip and the transition point occurring closer to the tip Figure 5.22 c). The ratio of mass measured compared to the expected mass if the accretion formed in a linear structure of rime ice shows a linear correlation to the transition point. A notable outlier circled in blue was not included in the linear fit. At -2°C, there was a strong correlation between the Reynolds number, f), at the point of the transition and the position of the transition. There was no correlation at -4°C. However, it must be noted that this was skewed by the transition not occurring or past the tip, with accretions producing a shard that favoured longer accretion times, as seen in d). The angle of the glaze ice showed a weak correlation with the position of the transition, with the warmer temperature tested at -2°C, resulting in a shallower accretion angle.

Relating all identified factors into the function plotted in h) to form (15).

$$\frac{x}{R_{leading\ edge}} = fn\left(\frac{l_{shard}\varphi_{glaze}Re_{transition}m}{RSm_{expected}}\right) \quad (15)$$

This shows some correlation; however, the measured mass used an estimation of the ice density and compared it to the expected mass if a pure rime accretion occurred, which showed the strongest correlation. This equation lacks complete consideration for factors that could not be accurately measured, such as liquid shedding, ice density and variations in the 3D geometry of the accretion. Using what meaningful measurements were available for these factors has shown they impact the transition point from the data obtained. From this, icephobic coatings' impact on ice accretion structures can be analysed to understand the fluid mechanics present during the accretion. Analysing this alongside accretions in the disc experiment could form a basis for modelling accretion structures.

5.1.2.3 Nucleation points

Nucleation is a key point of interest in icephobic research, as delaying it reduces the risk of ice accretion within a given time window and the rate of the initial accretion. Horns, seen in Figure 5.1, grow close together in parallel so that the continual growth of each horn would amalgamate. Figure 5.2 highlights that the trapezoid area between the shard and the tip had a layered structure. Some images captured at warmer temperatures, Figure 5.23, show clear points where an initial nucleation site is visible from which further growth occurs. At warmer temperatures with an entire wet growth regime, the nucleation sites are not visible, and in very dry growth regimes, they are sufficiently small that image capture of the white ice was inadequate to quantify the frequency of the nucleations confidently.

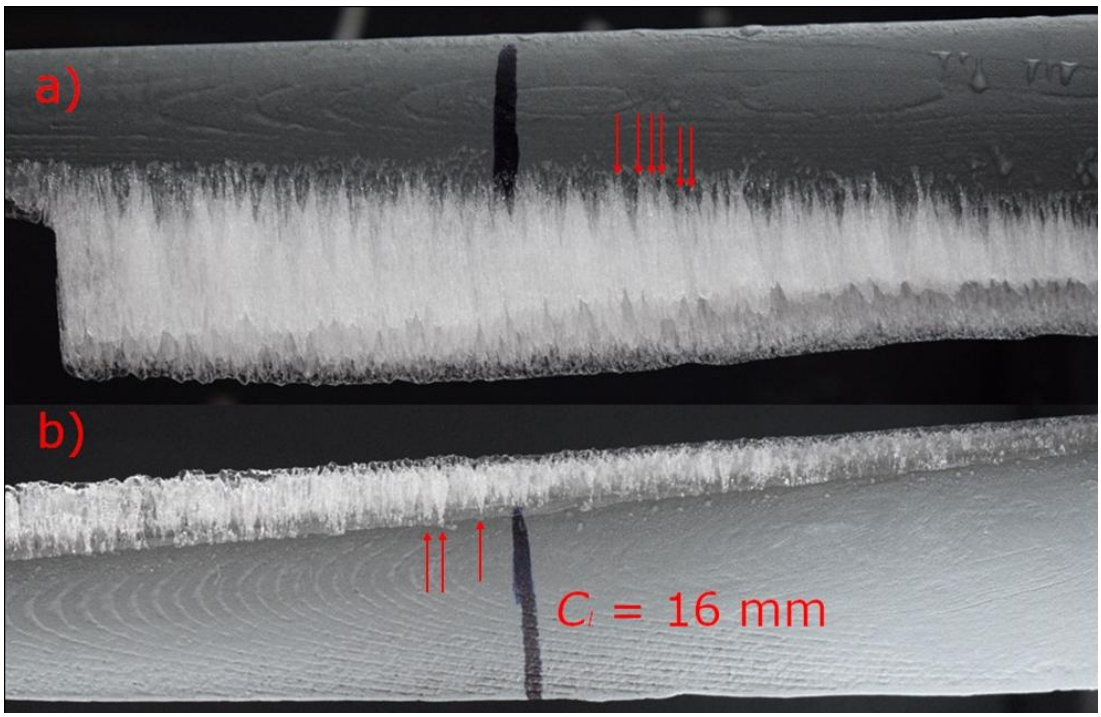

Figure 5.23 Images of the large blade taken when optimising lighting for data collection a) run for 10 minutes at 1500 rpm at -4°C and b) 4 minutes at 1500 rpm at -3°C showing visible nucleation points at each arrow. With the black lines along the chord, each 16 mm long.

Figure 5.24 shows the accretion after 5 minutes, with each image taken from a different run. Short-duration exposure produced a thin glaze accretion, highlighting that the initial cloud conditions may not be sufficiently supercooled. Following this, after three minutes, mixed ice is visible.

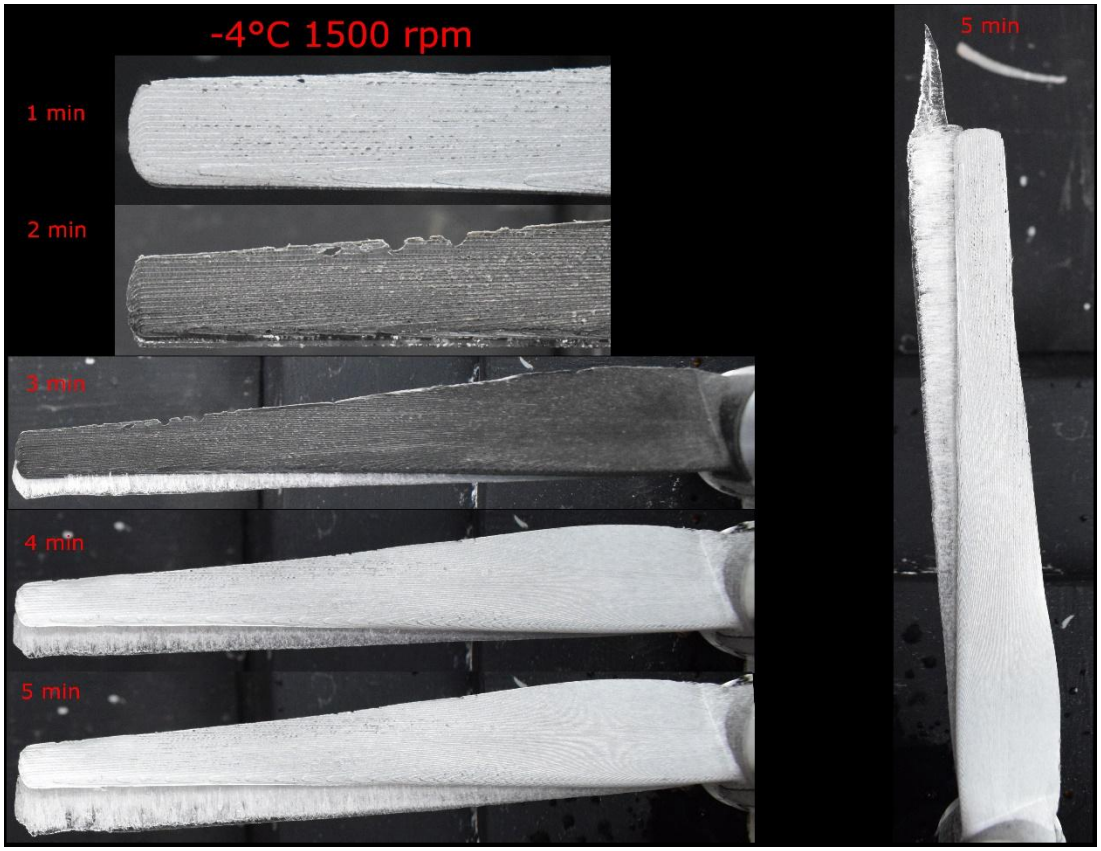

Figure 5.24 Growth progression on the smaller blades with plan photos taken showing growth progression from 1 minute to 5 minutes. For scale, the chord length at the tip in each image is 1 cm.

Reducing the temperature produced more opaque ice, as expected, while increasing the ribs' frequency perpendicular to the leading edge. Obtaining clear images of these more minor features was not possible, and quantifying them is made more challenging as they stack on top of one another, so knowing the position across the thickness of the blade may be pertinent when analysing the frequency of nucleation sites.

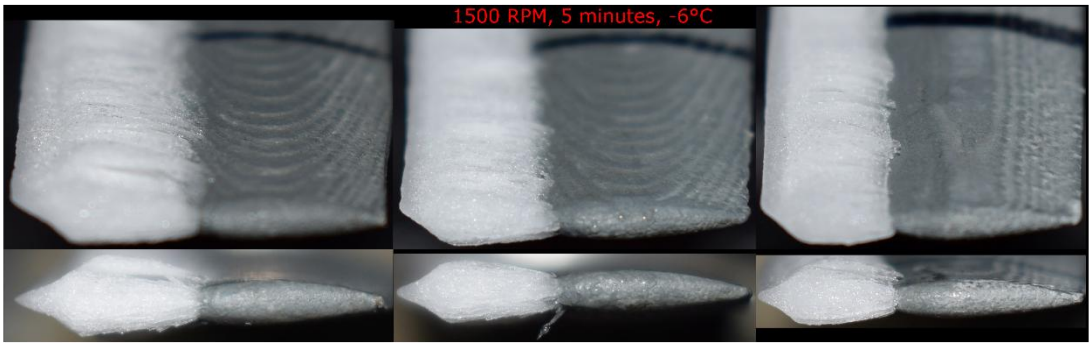

Figure 5.25 Tip shots taken at -6°C after 5 minutes or accretion at 1500 rpm. For scale, the chord length at the tip is 9 mm.

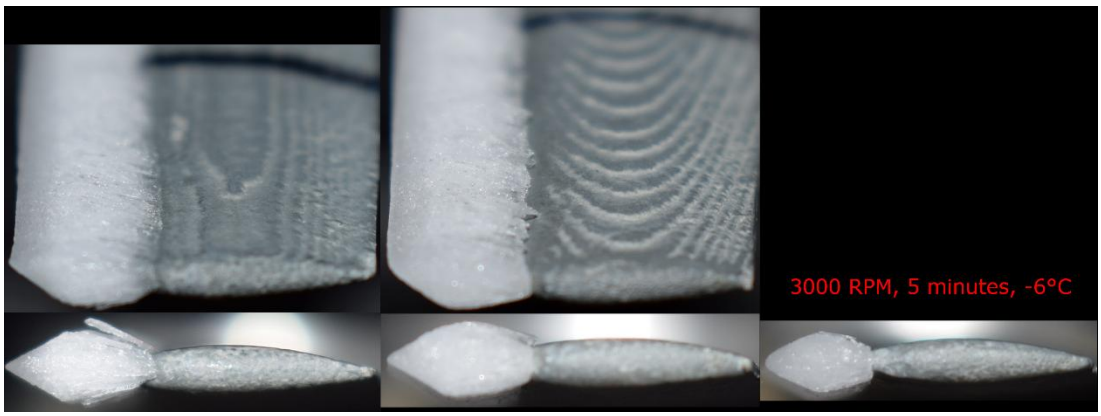

Figure 5.26 Tips after 5 minutes in -6°C at 3000 rpm. For scale, the chord length at the tip is 9 mm.

Increasing the speed improves the homogeneity of the ice, making identifying separate ribs more difficult, as shown in Figure 5.26 and Figure 5.27. With the speed reducing the height, each rib protrudes from the growth.

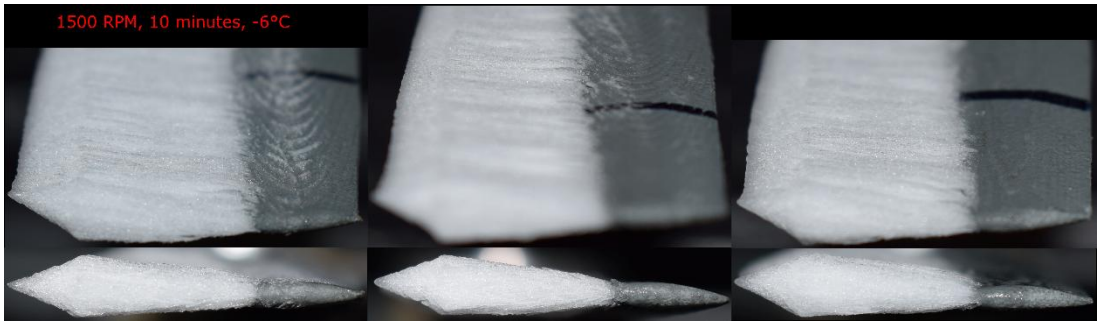

Figure 5.27 Tips after 10 minutes in -6°C at 1500 rpm. For scale, the chord length at the tip is 9 mm.

Comparing Figure 5.25 and Figure 5.27, the growth after 10 minutes is whiter and opaque, whereas the ice in Figure 5.26 is slightly translucent, but the ribs are slightly more defined. Figure 5.28 at -8°C, the ribs protruded further from the growth, giving the top surface a rougher appearance than that visible in Figure 5.27.

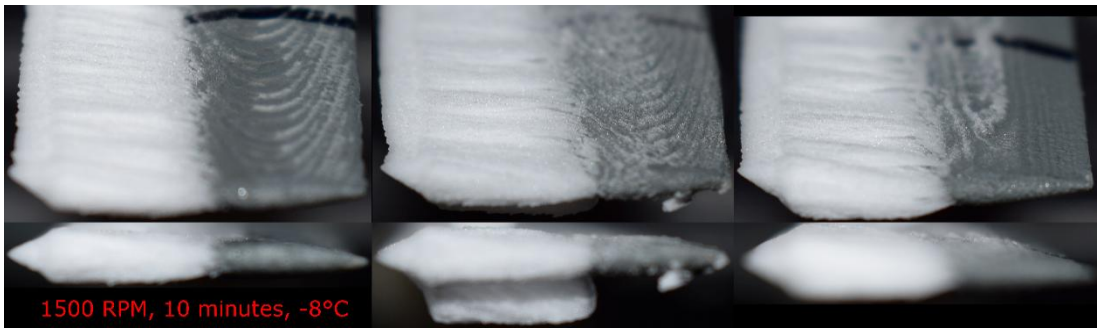

Figure 5.28 Tips after 10 minutes in -8°C at 1500 rpm. For scale, the chord length at the tip is 9 mm.

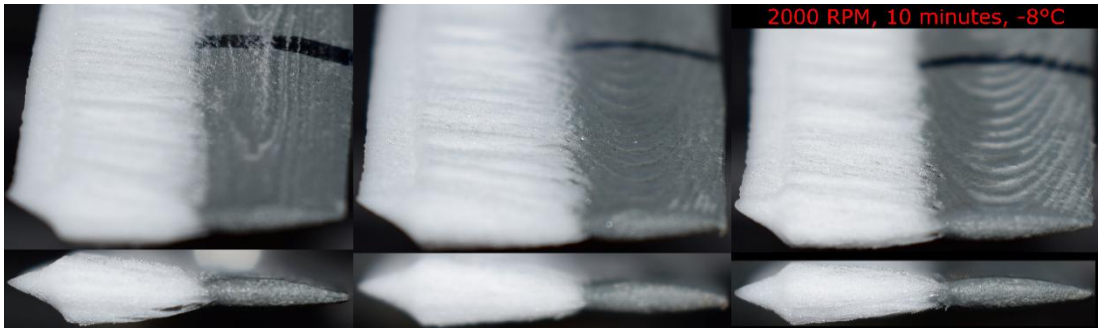

Figure 5.29 Tips after 10 minutes in -8°C at 2000 rpm. For scale, the chord length at the tip is 9 mm.

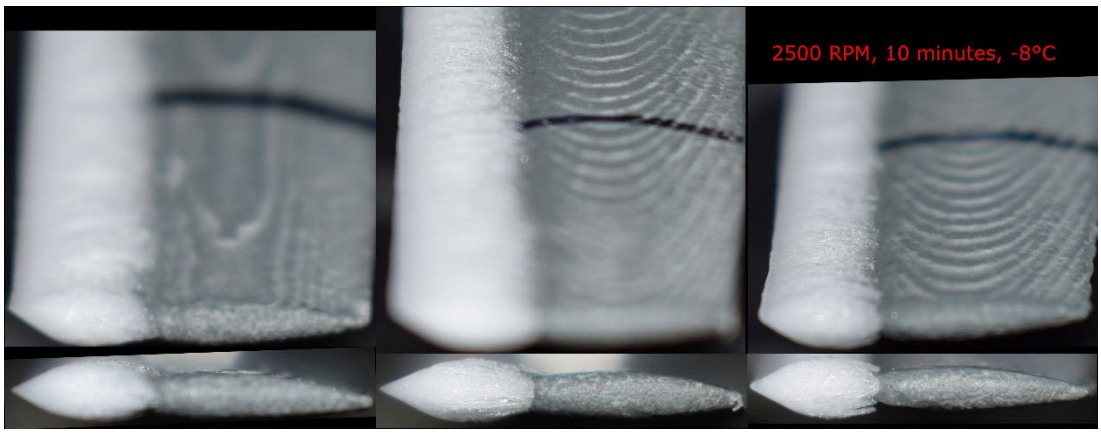

Figure 5.30 Tips after 10 minutes in -8°C at 2500 rpm. For scale, the chord length at the tip is 9 mm.

Comparing the accretions shown in Figure 5.28, Figure 5.29, and Figure 5.30, the roughness of the top surface again appears to be reduced at higher speeds. Considering the horn growth at low speeds and low temperatures, the more prominent visible points of nucleation at warmer temperatures in mixed ice and the visible structure of the tip growth, it appears that there is a link between this structure and the substructures formed after nucleation.

The frequency of nucleation will be proportional to the probability that any droplet will solidify depending on the Stefan number, and the rate of impinging droplets will be dependent on the LWC, as well as both the Reynolds and Stokes numbers. The lamella structure of the trapezoid forms as horns grow from nucleation sites until they amalgamate into a singular structure. A higher frequency of nucleation increases the competition for space and reduces each horn's size. Higher speeds produced smoother accretions, suggesting drag limits the growth of specific horn geometries, further increasing the competition for space. Due to the inability to accurately quantify this parameter, specific analysis

was not completed. However, the ice structure at the tip with a lamella structure in the trapezoid portion likely has layer thicknesses dictated by the frequency of nucleation sites and airspeed. Colder accretions at higher speeds produce denser geometric features of the structure. At colder temperatures than tested here and at higher speeds, this observation may result in an entirely uniform-looking structure aligning with soft rime conditions [14]. Entirely wet growth occurs when the nucleation site frequency trends to zero and there is no unique competition between individual growth features.

5.2 Ice accretion on a rotating disc

Rotating discs were explored as a means of simulating a simplified accretion process on an aerofoil, with the radius of the disc representing the chord length of an aerofoil and the central axis or rotation behaving as the stagnation point where the motion of a large droplet is simulated striking the leading edge and then travels along the chord. This was considered potentially beneficial as an accessible method of simulating a particular point along the leading edge of a turbine or helicopter blade. At a comparable length scale of a full-size aerofoil, huge equipment would be required to perform such a test. Moreover, if an icephobic coating was employed, how would damage to the coating, resulting in areas of exposed aluminium, affect the accretion process? Studying the accretion process in this experiment was to investigate how the surface impacted the growing regime. The first parameter that was investigated was the radius of the glaze ice forming in the centre of the disc. As the centre is where the velocity is the lowest, the dwell time of the droplet is proportionally the most significant, increasing the window of opportunity for a wet grow regime. When the droplet travels along the disc's radius, the boundary layer's depth decreases as the free stream velocity increases. With the impinging water being in the form of discreet droplets every second, the dwell time would be reduced sufficiently, producing an intermittent presence of a wet phase. Where the water can stagnate, at the centre of the disc or leading edge of an aerofoil, a wet phase may always be present, allowing the accretion of glaze ice.

This radius of glaze ice formed at the disc's centre was of interest as glaze ice has the strongest adhesion when compared to lower-density accretions that form mixed and rime ice [14]. A method of manipulating the growth regime to reduce the area of glaze ice formed would be of interest for de-icing applications by reducing the present ice adhesion strength in a particular icing scenario by producing more favourable ice formations with lower adhesion strength than glaze ice. Low ice adhesion surfaces could be further improved by utilising an additional mechanism, if present, to reduce the ice adhesion strength by impacting the growth regime to provide a compounding benefit.

The transition point from glaze to mixed ice represents where a more discreet freezing process occurs as the surface tension destabilises the geometry of the liquid boundary of the pool undergoing wet growth as the velocity increases, producing discreet droplets as the liquid and ice expand over the disc forming ice protrusions Figure 5.31.

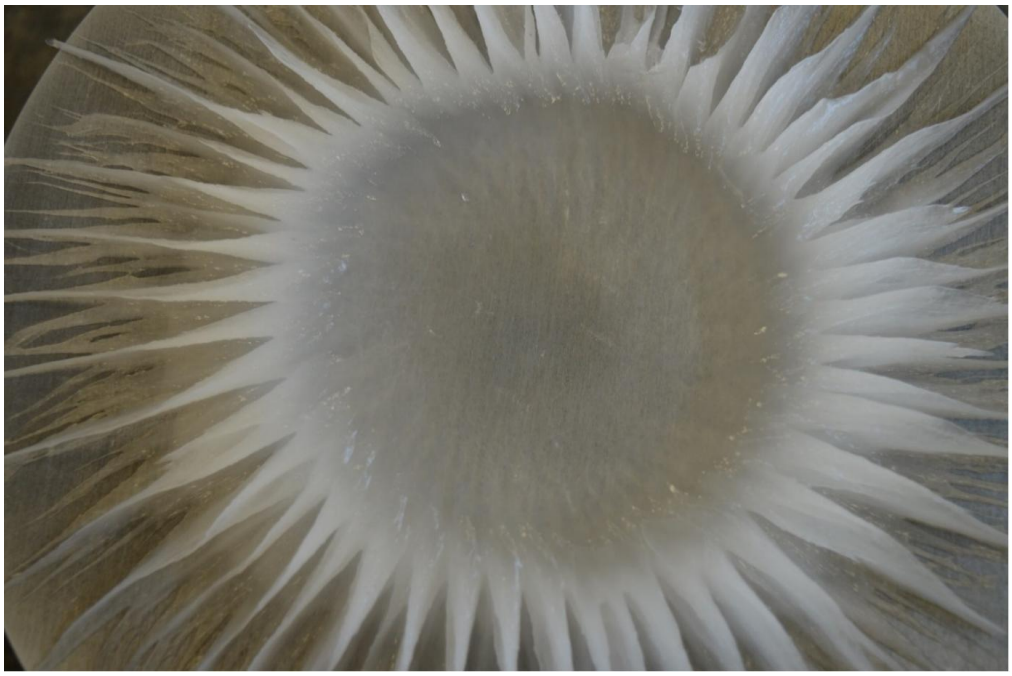

Figure 5.31 Aluminium disc after 15 minutes of accretion at 1800 rpm, -14.5°C.

How the wavenumber and curvature of the protrusions formed changes relative to the radius of the glaze ice radius and the mass of the adhered ice was investigated to analyse the growth mechanisms present and whether it could be utilised for predicting ice formations and guiding icephobic coating design.

Six surfaces were investigated at a temperature of -14.5°C in 15-minute tests at 1800 rpm with the patterned coatings exposing the substrate. At this motor speed, with a radius of 0.095 m and using the kinematic velocity of air at -14.5°C to be 1.211×10^{-5} the Reynolds number is 1.40×10^{5}. This means the Reynolds number is approaching the transition value for aerofoils to reach a mixed boundary layer. Compared to a Siemens Wind Turbine SWT-2.3-108 with a blade length of 53 m, root chord of 3.4m and a speed range of 6 to 16 rpm, this experiment is equivalent to 0.3 m from the blade's root.

The droplets were sufficiently large such that wet growth occurred in the centre of the discs where glaze ice formed. The radius of the glaze ice for each surface is listed in Table 5.2.

Table 5.2 Radius of glaze ice and total mass of accretion.

Disc	Glaze ice radius (mm)		Mass of ice	
	Image analysis	manual	measured (g)	mass:radius
Sandblasted	43±2	40±3	78±10	1.8
Aluminium	39±1	36±2	63±7	1.6
PDMS	39±1	37±4	76±13	1.9
PDMS 5%SiC	39±8	39±16	63±24	1.6
Cross	36±2	33±4	83±3	2.3
Strip	37±3	34±3	68±6	1.8
Petal	33±2	32±2	78±13	2.4

The radius of the glaze ice was largest on the sandblasted surface, with the PDMS and PDMS 5% Sic coatings achieving the same radius as the as-received aluminium. The patterned coatings produced a significantly smaller radius with a 15% reduction when comparing the petal disc to the aluminium.

Table 5.3 Protrusion angles that were measured at the point of transition and at the edge of the disc were then related to the radius of the glaze ice.

Disc	Protrusion angle (°)				Protrusion angle:radius		
	inner	outer	change	o:i	inner	outer	change
Sandblasted	8.5	2.0	6.5±1.5	24%	0.20	0.05	0.15
Aluminium	5.3	1.0	4.3±1.8	19%	0.14	0.03	0.11
PDMS	5.5	1.6	3.9±0.5	29%	0.14	0.04	0.10
PDMS 5%SiC	5.5	2.2	3.3±0.3	40%	0.14	0.06	0.08
Cross	5.5	1.8	3.7±1.5	33%	0.15	0.01	0.09
Strip	5.5	2.1	3.4±1.1	38%	0.15	0.06	0.09
Petal	4.3	0.9	3.4±1.6	21%	0.13	0.03	0.09

The ratio between the initial protrusion angle and the radius of the glaze ice was consistent for all discs except the sandblasted aluminium. The angle of the protrusions at the edge of the disc as a percentage of the initial angle, o:i in Table 5.3, did not share the same correlation. Looking at Table 5.4, the Reynolds number at the transition point from glaze ice shares a weak correlation with the change in angle, $\Delta\phi$, when normalised to the radius of the glaze ice. A larger glaze radius reduces the distance a droplet travels from the transition point to the edge of the disc. Despite this reduced distance, the protrusions experience a larger angle change. A large glaze radius increased both the initial protrusion angle at the transition point and the angle change rate.

Comparing the radius differences between aluminium and the sandblasted surface, a 4 mm increase in the glaze radius for the sandblasted surface

decreases the perpendicular length. Each protrusion must span from 56 mm to 52 mm, while changing its angle by 4.3° and 6.5°, respectively. So, the droplet changes its freezing path per centimetre of travel perpendicular to the edge of the disc by 0.77 $°\mathrm{cm}^{-1}$ for aluminium and 1.25 $°\mathrm{cm}^{-1}$ sandblasted aluminium, respectively.

Table 5.4 The Reynolds number at the radius of the glaze ice and the change in protrusion angle to its perpendicular length

Disc	Glaze radius (mm) Image analysis	Reynolds at transition point	ΔΦ (°)	Perpendicular distance (mm)	curvature ($°\mathrm{cm}^{-1}$)
Sandblasted	43±2	6.36E+04	6.5	52	1.25
Aluminium	39±1	5.77E+04	4.3	56	0.77
PDMS	39±1	5.77E+04	3.9	56	0.70
PDMS 5%SiC	39±8	5.77E+04	3.3	56	0.59
Cross	36±2	5.32E+04	3.7	59	0.63
Strip	37±3	5.47E+04	3.4	58	0.59
Petal	33±2	4.88E+04	3.4	62	0.55

Analysis of the wavenumber of the protrusions, Table 5.5 shows no correlation between the measured parameters or Reynolds number; an example of the scans taken per run can be seen in the methodology.

Table 5.5 shows the wavenumber of the protrusions from the glaze ice.

Disc	wavenumber (mm^{-1})
Sandblasted	1.4±0.8
Aluminium	2.3±0.4
PDMS	0.4±0.1
PDMS 5%SiC	1.3±0.9
Cross	0.4±0.1
Strip	1.2±0.8
Petal	1.2±0.8

5.3 Discussion

5.3.1 Ice accretion on the leading edge of a blade

The hypothesis is that a detailed understanding of ice growth mechanisms dependent on the environmental conditions present could provide predictions of the ice structures that form, which, in turn, may be more effectively mitigated by specific icephobic or hydrophobic mechanisms that could influence the growth mechanisms that were initially present. This may result in unexpected differences between the measured and predicted performance of the implemented coating. Understanding the influence of the coating on the ice accretion's structure would reduce the need for iterative design of the coating.

5.3.1.1 Simulated cloud conditions

Controlling the cloud conditions across all experiments was impossible as the properties changed with the chosen method using a nebuliser to produce vapour. The simulated cloud production method used was consistent throughout the test. The experiment begins at 0% humidity, meaning there is a delay until the LWC reaches saturation or the rate of change becomes small. So, the growth rate will depend on the time period within the experiment duration, for example, the second minute or the fifth minute in Figure 5.24. The temperature primarily dictated the density and structure of the accretion as it is a Stefan-type problem with the droplet diameters in the cloud unchanged from test to test. The icing regime was primarily controlled by the growth rate, described by the Stefan number and the rate of droplets impacting the surface. It was assumed that before cloud saturation occurred, the average temperature of the cloud was warmer than that at the point of saturation, favouring a wet ice growth regime for the initial accretion, visible in Figure 5.24. Unless the environmental temperature, with some influence of the air speed present, was sufficiently cold to reduce the droplet's temperature below the threshold where rime accretion could occur for the MVD produced by the nebuliser.

5.3.1.2 Stream conditions and rime ripple wavelengths

Two blade sizes were available for testing, with longer blades producing a more desirable range of Stokes numbers where a mixed behaviour of inertia or flow vector dominant droplets existed within the test. The smaller blades lacked rigidity and as much surface area to study but did experience a higher Reynolds number at the tip due to a larger chord length. Calculating an accurate or

representative Reynolds number was not explored due to the complexity of the experiment's initial conditions and its dynamic changes through the duration by virtue of the ice accretion being studied. Critical Reynolds numbers for wind turbines are often quoted as being in the region of $2 - 5 \times 10^5$ [101][102] which was not achieved based on a smooth flat plate calculation. In section 5.1.1.2 no direct link between the Reynolds number alone and the wavelength of the rime ripples was identified so the flow conditions may have been comparable for each speed tested. However, the local velocity did show some correlation and is represented in the Stokes number. The chord length was used to non-dimensionalise the amplitude of the ripples as this was the characteristic length of the blade used in both the Stokes and Reynolds number calculations and the size of the ripples will be linked to the volume of impinging droplets, which will increase with x/R. As the local velocity is a term in the stokes number does not require an additional term. the amplitude accounts for the increased surface area of larger ripples ability to grow faster which may result in the envelopment of neighbouring ripples, increasing the wavelength Figure 5.16.

The clustering of amplitudes between 0.5 and 1 mm represented 67% and 58% of the data for the 5- and 10-minute tests, respectively. This could indicate that the accretion rate earlier in the process was more consistent from test to test. However, it is much more likely due to difficulty in isolating and measuring the ripples. Due to their small size, increasing measurement difficulty and, therefore, the relative size of discrete errors stemming from precision. Discerning features from one another was more straightforward for the larger accretions in the 10-minute tests combined with the reduced clustering, which suggests better precision may mitigate this. This data suggests that the critical Reynolds number was not met. It could be the case that a more in-depth analysis would find otherwise, as this analysis used the average wavelength and amplitude, which become more irregular from the root to the tip. This change in regularity could be a symptom of laminar flow becoming turbulent and causing multiple wavelengths to be superimposed upon one another. If the flow is below the critical point, then the inconsistent distribution of the simulated cloud in the early stages of the test, prior to its saturation, may be the cause. Where irregularities in the ripples influence future deposition, such as an erroneously prominent feature relative to the time of accretion, it continued to grow faster due to a larger surface area than neighbouring ripples.

5.3.1.3 Geometry of rime accretions at the tip of a spinning blade

The tip growth analysis in section 5.1.1.1 was hampered the most by image focus for this experiment due to the small size of the tip. Attempts to standardize the

photography of blades were unsuccessful due to the number of photos required and the limited time window to do so because of melting. The accretions were much smaller than those in the rotating disc experiment and at warmer temperatures. Ideally, fixed positions would have been used, and the images could have been improved with orthorectification. It may be necessary to photograph one feature type per accretion to permit this improvement in the quality of the data collected. This significantly limits the breadth of data collection, making capturing unusual or irregular features less likely. As this experiment has novel aspects, identifying which features could be analysed was necessary, and unexpected features could highlight shortcomings in the methodology or equipment design that may need to be accounted for.

The geometry of the tip growth was very reliable when the conditions for a dry growth regime were present. Due to the means used to instigate each test, the first nucleation was likely mixed or glaze ice, which can be seen in some photos in section 5.1.1.1, where the ice in contact with the blade does not appear as opaque or white as the rest of the accretion, this observation is more prevalent at warmer temperatures such as Figure 5.4 and Figure 5.5. Additionally, the tips of the shard in Figure 5.5 of the tips of the shards formed at $-6°C$ appear to be much wetter growth. This clearly indicates that this formation is dominated by the Stokes number, where larger droplets are prone to impinging on the leading edge near the stagnation point. As they experience a much longer relaxation time, they do not deviate as readily as smaller droplets with the streamlines around the blade. As they have a larger volume, they can produce a wetter growth regime for specific Stefan numbers than smaller droplets, as the solidification rate is not sufficiently quick to completely freeze the droplet upon impact or before more droplets impinge the surface. This feature becomes less visible at colder temperatures, with the only apparent presence at $-10°C$ above 2000 rpm, Figure 5.3. This can be explained by the rate of droplet impact increasing with velocity and the solidification rate remaining consistent between tests at the same temperature. The trapezoid structure between the shard and the blade appears more ordered than the shard, with lamella-like structures of rime ice growing perpendicularly to the blade's surface. It was assumed that the core of the accretion, in line with the stagnation point, was the densest in any cross-section taken in plane with the chord length of the blade. If the conditions permit the growth of mixed ice due to the mechanism that forms the shard described above, as the accretion continues to grow, the shard's tip extends in a comparable, but not identical, manner. The trapezoid then elongates in this layered structure. Droplets with an extremely low Stokes number will impinge much less frequently than larger droplets, with smaller droplets more capable of deviating from their initial path with the airflow around the ice. The probability of where they impact will be a function of their initial trajectory and their ability to

deviate with the streamlines. This means that the top and bottom face of the accretion will be formed from a higher fraction of smaller droplets than in the same plane as the tip of the shard and stagnation point. As smaller droplets are more prone to a dry growth regime, the lamella structure is likely caused by the deposition of droplets with a low Stokes number combined with any large droplets that impact there or closer to the central plane if the growth rate is sufficiently slow to allow some water to flow over the surface due to drag. The Stefan and Stokes number governs the diameter of droplet this applies to.

At 500 rpm, the tip velocity is sufficiently slow such that the Stefan number is large enough for a dry growth regime for all droplet sizes in the cloud below -8°C, where a discrete freezing process occurs, with each droplet solidifying before another strikes the surface [15]. The lack of a shard formation, the top and bottom surfaces of the tip growth remain parallel with the direction of flow, and the fact that its leading edge is perpendicular to the flow indicates this (Figure 1.1). It is unknown how impactful the laminar flow present is on the formation of this geometry. Another test would be required with a much higher Reynolds number and with either much smaller droplets or a proportional increase in the characteristic length with the free stream velocity such that the Stokes number remains comparable. As the droplets used here are quite small, increasing the chord length with the speed would be more achievable, only requiring wider blades, as increasing the chord length both increases the Reynolds number and reduces the Stokes number.

Looking at the 10-minute tests in Figure 5.3 for $-10°C$, the runs at 1500 rpm at 1000 rpm in the 10-minute tests at $-8°C$ in Figure 5.4, further accretion occurs behind the leading edge in the form of rime horns. This feature can be considered to both form and remain due to the lower speeds and is only present in colder temperatures. As at lower air speeds, the stokes number is lower, and the vector changes of streamlines will be much slower, presenting a more significant opportunity for deposition to occur, or a long enough dwell time, on these accretion horns that may nucleate from a larger impinging droplet. As the airspeed is also low, the fragile structure is less prone to being dislodged by drag forces. As they grow, they protrude above and below the tip growth and are more exposed to the airflow, accelerating their growth by striking more droplets. The tip image used for the 10-minute, 500 rpm analysis for $-10°C$, shown in Figure 5.1, is in the appendix alongside a different angle where these horns are more visible.

As the speed increases, the tip growth shape becomes more aerodynamic, with a smoother transition from the shard to the rest of the tip growth. The horn growth witnessed at low speeds is likely the mechanism that produces the lamella structure in the trapezoid area of the tip growth at higher velocities. Here, the

horn grows above and below the primary accretion at the leading edge, but its geometry is limited by the airflow so that extreme-looking horns visible in Figure 5.1 are stripped from the surface, and the accretion evolves to produce a wedge shape as the horns hug the existing accretion or are destroyed by drag. Repetition of this process would produce layers of the horns atop one another and appear in the lamella structure observed. If this is the case, one could expect that the speed of the adjacent airflow would limit the thickness of each lamella as more prominent horns will be more susceptible to drag forces and stripped from the surface entirely or trimmed until the resulting geometry is sufficiently aerodynamic for the present environment not to be shed entirely.

It follows that as the velocity increases, the Stokes number also increases as the chord length of the blade and relaxation time of each droplet remain constant from test to test at a given temperature. This increase describes a more significant proportion of droplets striking the stagnation point, explaining the linear relationship between A_{shard}/A_{tip} and the motor speed. As the results are much more correlated between the -8°C and -10°C tests the freezing mechanism is more comparable Figure 5.9. After accounting for this by including the Stefan number for each temperature, the ratio is much more predictable. The 5-minute, -6°C result with the lowest $Re \cdot St \cdot S$ value produced at 500 rpm lie significantly above the trend suggesting a disproportionally high level of wet growth Figure 5.11. This is likely caused by the warmer temperatures and lower airspeed conditions in this test, which are more sensitive to the initial conditions of the simulated cloud before it reached saturation and an equilibrium temperature. A warmer cloud would promote more glaze ice accretion due to a slower solidification rate, and the Stefan number used here would be too low for the true conditions for this specific result. This data shows that the tip shape can be reliably predicted for known flow, temperature and cloud conditions.

5.3.1.4 Shedding

The trend begins to flatten off past the initial linear trend, which is likely an indication of how shedding impacts growth with the images taken for the 2500 rpm. Shedding was apparent on all blades, suggesting the limitations of the accretion were consistent across the blades. It is unknown whether the point of shedding would remain the same if the test were run for longer, as the initial icing conditions forming the adhesive layer for the first accretion may have been notably warmer, producing denser ice than the second accretion after the shedding. However, if the shedding resulted in cohesive failure of dry growth ice from the wetter growth attached to the blade, which remained adhered, then the accretion limit would likely be unchanged as the structures would be consistent.

Notably, the shedding was not across the leading edge, where one blade might shed roughly a third of the ice and another half. The cause of this is likely irregular features producing stress concentrations within the accretion. The fracture would be caused by the closest stress concentration to the tip that first meets the threshold of failure, as the centripetal acceleration is highest at the tip, where weaker points in the accretion may exist closer to the root, but the stress does not exceed the point for cohesive or adhesive failure before a less severe structural weakness further down the leading edge triggers failure as it experiences higher forces.

After the breakdown in trend, the remaining results split. Unfortunately, the data for 10 minutes at 3000 rpm in $-8°C$ was not collected so strong conclusions cannot be drawn. However, from the data available, it can be seen that the $-10°C$ trend did not break down and the warmer the temperature, the greater the deflection from the initial relationship identified. This is most likely caused by the link between ice adhesion strength to a surface and the temperature, where colder temperatures are typically more strongly adhered [46][55]. If the initial accretion across all tests were a comparable wet growth regime producing high-density glaze ice on which the further accretion grew, then this would explain the variation in this observed breakdown. If the ice structure at the interface was comparable but the temperatures after this accretion reached equilibrium at different temperatures, then the apparent ice adhesion strength would vary with temperature, thus changing the maximum size of accretion that could grow before shedding.

Assuming the growth regime and accretion rate are consistent through any given test such that the density of the ice is constant throughout would directly equate the area of the tip growth to the mass of adhered ice. For a surface with a known ice adhesion strength, the point of shedding could be predicted for the ice type present.

The motor speed and the ice adhesion strength of the surface limit the maximum mass of adhered ice, comparing the tip area of the ice accretion to the total number of revolutions seen in Figure 5.8 generally increasing the time of each accretion window increased the total area at the tip for a given speed. Most follow the trend of increasing area with speed and decreasing after 1500 or 2000 rpm, where the total revolutions no longer correlate with the total ice accretion.

5.3.1.5 Predictability of the tip accretion

As lower speeds reduce the volume of the simulated cloud swept by the blade, the opportunity for droplets to impinge the surface is reduced, reducing the

growth rate. The accreted ice experiences a lower angular acceleration, allowing it to increase its mass further before it sheds. A higher velocity would also cause the Stokes number to be more impactful, leading to a more significant proportion of the accretion forming the shard. Assuming that the shard portion would trend to 100% of the accretion for very high-velocity applications is reasonable. With the velocity limiting the potential growth, the accretion cannot grow the trapezoid section before shedding occurs as it becomes increasingly unstable. If the ice adhesion strength of the surface was altered to be higher or lower by the environmental temperature change or the surface properties, the critical mass to shed will change and the time to shed with it for a given growth regime of the ice. How this interplays with the flow properties of impinging droplets and the prevalence of cohesive failure could be predicted with further experimentation and modelling.

Considering how the tip accretion grows, the size of the shard does not change as much as the ice between it and the leading edge for low speeds, while for high speeds, its portion of the tip growth has a linear correlation. This is likely dictated by drag forces requiring any growth to be more aerodynamic at higher speeds. This relationship was seen in the data shown in Figure 5.9 and visualised in Figure 5.32.

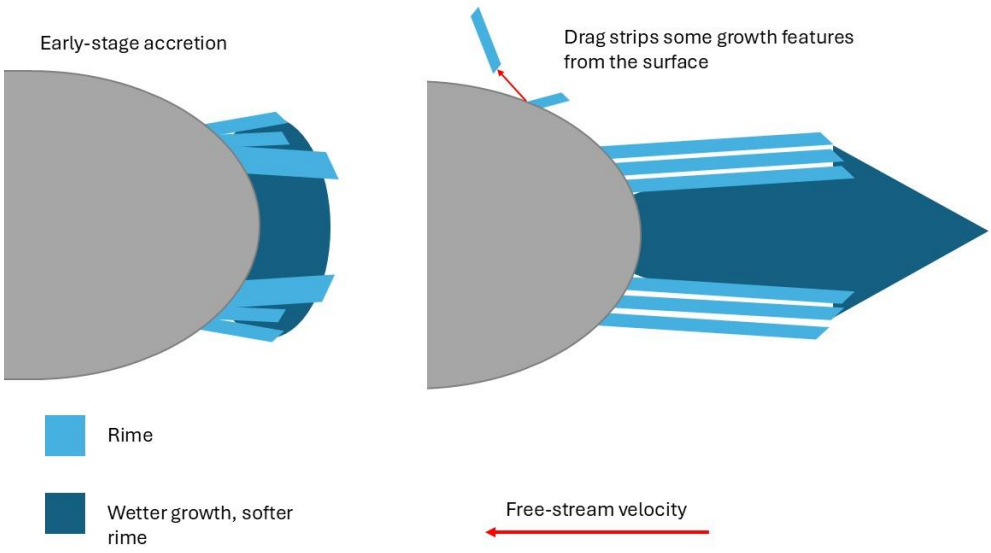

Figure 5.32 Drag forces limiting growth geometries.

As the motor speed increases, the area of the tip grows at a faster rate than the trapezoid. It grows until it peaks at around 2000 rpm, then the shard and total tip

areas decrease. However, the decrease in area measured for the shard occurred at a lower rate than the entire accretion. Ignoring the impact of shedding, this can be considered due to the Stokes number rising with the local velocity, increasing the average diameter of droplets forming the accretion as more droplets cross the threshold of becoming inertia dominant and the time window for complete solidification to occur before the next droplet strikes is reduced. Reducing the proportion of accretion formed by the deposition of small droplets. Extending this idea to a much higher local velocity, increasing both the Reynolds and the Stokes number, the proportion would be expected to reach 100%. As drag forces become more significant, they may act as an iterative sculpting process by trimming non-aerodynamic horns as they form.

Comparing the trend for -6°C to colder temperatures is not ideal as the initial cloud conditions appear to be impactful upon the trend, but the lower gradient and higher y-intercept of the 5-minute tests in Figure 5.11 d) may be indicative of what wetter growth regime caused by a delayed freezing regime relative to the conditions would look like. In this case, due to the delay in the produced cloud reaching its equilibrium temperature and saturation rather than a lower heat flux associated with the surface. This would also support the concept that ice accretions following the initial growth are then dependent on the surface properties of the ice and not the underlying surface of which the impact fades with the growth Figure 5.33. If the maximum ratio of A_{shard}: A_{tip} is limited by the temperatures influence on adhesion strength, then altering the adhesion strength of the surface combined with a variation of the thermal conductivity may mean the maximum mass is reached through a range of these areas depending on where on the growth profile the ice adhesion limitation falls. If the impact of the thermal conductivity on the initial accretion has not been normalised to the general trend of ice growing upon ice, the structure at the point of shedding would be different Figure 5.33 b).

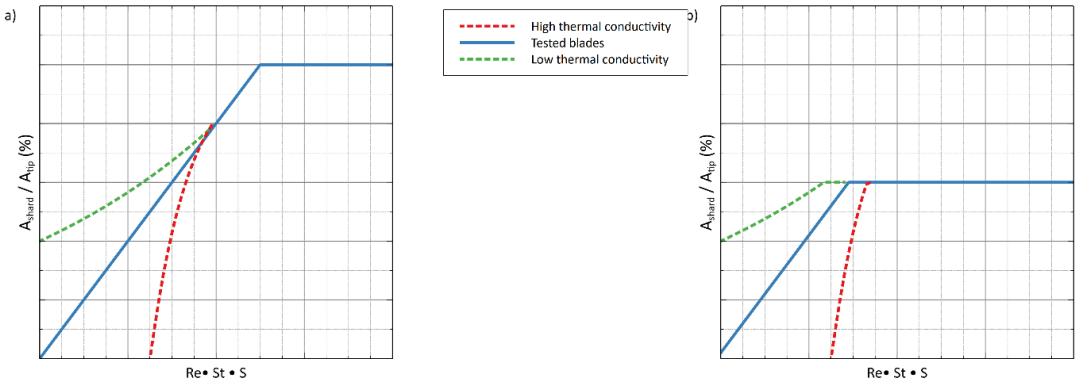

Figure 5.33 Potential trend variations due to the surface's thermal conductivity with a) normalising the ice growth before reaching the critical mass to shed and b) shedding occurring before the surface's impact on growth has been removed.

However, the trend in Figure 5.33 b) may not result in a linear cutoff as shown because the initial accretion's growth regime would be different, changing the density of the ice and, therefore, the adhesion strength with each surface and heat transfer to the initial accretion which its porosity would impact for the same conditions [14]. Much longer tests where multiple shedding occurs would be necessary to understand how the growth structure is limited.

Another consideration is that the radius of the leading edge is likely a significant contributing factor to the trapezoid growth, where a larger radius often is seen producing more horns that grow with a steeper angle compared to the flow which is perpendicular to the leading edge, at AERTS for example [81]. These horns have been shown to grow with a wetter regime on a larger scale leading edge, suggesting that the thickness of the trapezoid seen here is limited significantly by this length scale and a leading edge with a larger radius may reduce the angle change seen here between the shard and trapezoid sections of the tip accretion to produce an accretion that's geometry appears not to be so easily split into two sections, caused in this work by the two accretion processes of horns growing and forming a lamella structure behind the shard produced by droplets impinging the leading edge and the subsequent accretion, with the relative rate between both formation processes controlled by the Stokes and Stefan numbers present. The resulting accretions on larger radii conform more to the original geometry of the aerofoil or are seen in glaze icing conditions where horns do not produce a lamella structure, and a jagged cross-section can be seen and a concave leading edge to the ice [7][80][81]. This is possibly evidence of the sculpting capability of the drag forces becoming ineffective for this geometry of aerofoil and density of accretion, which has a stronger cohesive and adhesive strength than rime, which was the growth regime horns formed in this work. Additionally, the low radius may

impact the drag coefficient significantly compared to large-scale testing, which is altered more by the horns formed in this work due to their relative size.

An important characteristic that was not considered was the Weber number (16) [104][105][106], which represents the relationship between the drag forces present and the surface tension of the droplet, as this could help describe the smoothening of the change from shard to tip as speed increases, most notably in the 2500 and 3000 rpm 5-minute tests at $-10°\mathrm{C}$ Figure 5.3, and the 2500 rpm 10-minute tests for $-8°\mathrm{C}$ Figure 5.4. It is a crucial parameter when scaling glaze ice accretion as it describes the effect of drag on the wet film present in a wet growth regime.

$$We = \frac{\rho v^2 l}{\sigma} \tag{16}$$

Where ρ is the density of the fluid, v the particle's velocity, l is the characteristic length, which is the diameter of the droplet in this case but can be replaced with the thickness of a water film on the surface, and σ is the surface tension at the water-air boundary. As the velocity increases, the droplet is more readily deformed by drag forces, which would lead to larger impinging droplets experiencing a wet growth regime to be stretched in the direction of the flow. In the plan view, analysing the tip would likely result in the rounding off of the shard-trapezoid boundary seen in this research Figure 5.2. For much higher velocities, it is reasonable to assume that the linear relationship shown in Figure 5.11 would continue for the A_{shard}/A_{tip} increasing, as the maximum size of the trapezoid area diminishes. The Stokes number scales with the velocity, and the Weber number uses the velocity as a second-order term as speed increases. At warmer temperatures, where the Stefan number plays an increasing role and the density of the ice increases, horn structures are more prevalent. In other studies, the Weber number for the film thickness plays a more significant role than that parameter for the droplet as the growth rate falls [107]. As the tip formation seen here is analysing a predominantly dry growth regime, known as the ice is white and opaque [14], the Weber number for the film thickness is not relevant.

Considering the surface's hydrophobicity, as this is utilised as a method of delaying freezing by reducing the solid-liquid contact, it can be expected that the resulting accretion of a static droplet would occur in a wetter growth regime, assuming a static droplet, and be more sensitive to the Weber number of the film thickness Figure 5.34. The film thickness would likely be increased with an increasing WCA as the film would be more sensitive to the surface tension for a film of a given volume. This dimensionless parameter only considers the surface

tension between the water and the air. A hydrophilic surface would readily wet and produce a large but very thin film. So, the ice accretion process forming the shard would be favoured as a wetter growth regime is induced. However, the position of the water is more sensitive to the airflow as the Weber number for the film is larger, reducing the dwell time and increasing the thickness of the shard relative to the aerofoil. If the delay in freezing is substantial enough, a shard may not form, and horns on either side of the leading edge would be expected until the scale of each horn forms a well in which very slow wet growth can occur as runback of the droplet is limited. This can be seen in Figure 1 of the glaze and mixed ice tests in [81] in the AERTS facility.

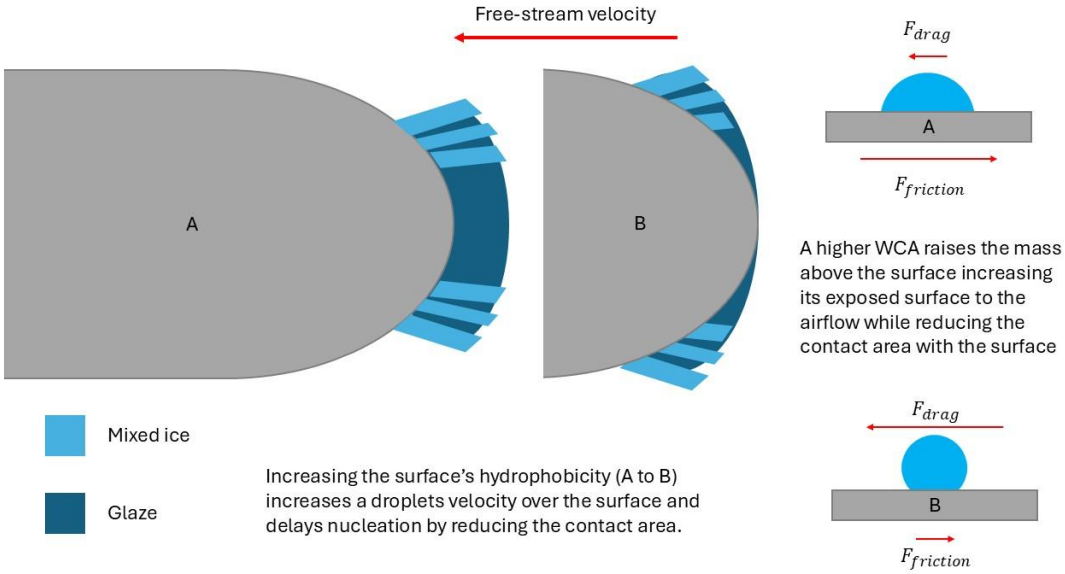

Figure 5.34 Potential implications of increasing the hydrophobicity of surface A to that of B.

The leading-edge portion between horns is much more transparent and homogeneous. Linking this concept back to this study, hydrophobicity may be impacting the freezing process in a comparable manner to the Stefan number, where a higher WCA, mainly if the surface utilises trapped air between asperities, slows the initial growth rate by reducing the contact area and dwell time. Looking at Figure 5.11 a) where the growth formation is compared to the Reynolds and Stokes number, but not the Stefan number, the $-6°C$ data sits above that of the $-8°C$ and $-10°C$. It may be pertinent to predict ice formations to consider that the surface's hydrophobicity and thermal conductivity manipulate the impact on the Stefan number. As once accounted for along with the initial cloud conditions

in this test, the Stefan number increases the correlation noticeably. The initial cloud conditions may change the Stefan problem significantly where a droplet at the phase change temperature (0°C) strikes a supercooled surface rather than a supercooled droplet striking a surface that is the phase change temperature. In the first instance, the latent heat is transferred to the supercooled surface and in the second instance, the latent heat warms the supercooled liquid when transferred into sensible heat. When the simulated cloud has not yet been supercooled at the start of the test, the Stefan problem changes throughout with the changing boundary conditions. Once the ice has formed further into the test, the boundary temperature is 0°C, and the droplet temperature is assumed to be the air temperature.

In a scenario with a supercooled droplet and boundary temperature that is supercooled or warmed by the latent heat of solidification to the phase change temperature, the Stefan number is inversely proportional to the temperature difference between the ice boundary and the environment. As it relates to latent heat and sensible heat, altering the surface to manipulate the heat flux will impact the Stefan number's reliability to account for the growth rate in this observed relationship, as the boundary conditions could change more readily. As hydrophobicity impacts both the heat transfer and Weber number, a single-order coefficient to account for its impact on the Stefan number's reliability in the prediction may not be sufficient.

As increasing the dwell time for a droplet on any surface increases the opportunity for locomotion, a higher dwell time on a hydrophobic surface would result in larger potential travel distances within that time. This means that accounting for the decrease in growth rate that may be present for a droplet on a more hydrophobic surface would also require a second coefficient to account for the additional change in position as the droplet travels faster over the surface—spreading the accretion wider above and below the leading edge. A hydrophilic surface would produce a thinner film that is less impacted by the drag forces as the Webber number of the film is now smaller. As the film is flatter, the surface area and potential heat transfer are higher. Resulting in faster freezing and slower locomotion over the surface. Potentially presenting itself as preferentially freezing at the stagnation point with a thinner accretion thickness where a hydrophilic surface could produce a proportionally higher A_{shard} and a hydrophobic producing a proportionally smaller A_{shard} by distributing the ice further over the surface, forming horns. Between which eventually fill and flatten, the process returns to the measured trend as ice accretion occurs on ice, not the surface. A simplification of this relationship is illustrated in Figure 5.35, assuming a consistent growth rate and identical topographies.

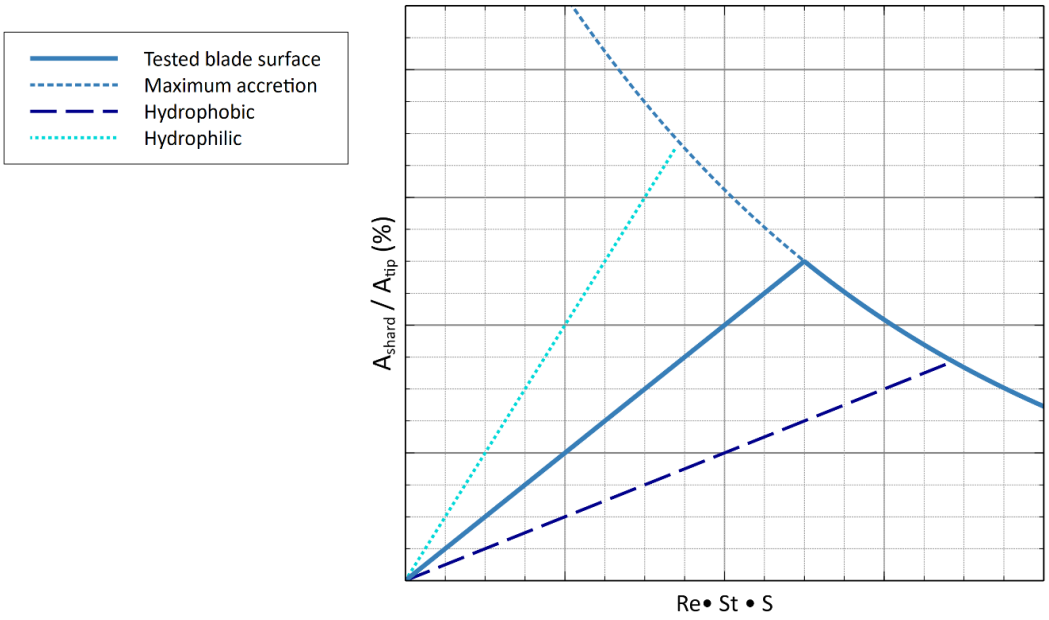

Figure 5.35 Potential influence of hydrophobicity on the structures formed assuming a consistent growth rate assuming identical roughness based on observations from the disc icing experiment.

A significant flaw in this prediction is the impact of ice adhesion strength influencing the growth processes as drag acts as a filtering process where the ice adhesion strength is balanced with a horn's aerodynamic profile and whether the drag force upon it exceeds the adhesion strength. A governing factor on a surface's ice adhesion strength is its surface energy, which is often determined or assessed by proxy through WCA and CAH testing. For identical surface topographies and thermal and mechanical properties, a lower surface energy would impact the friction between a sliding droplet and the surface. Changing the position where it freezes due to the surface's hydrophobicity. The proceeding accretion will also be more susceptible to drag forces as the ice adhesion strength is lower due to reduced electrostatic forces [41][46].

So, low surface energy delays the growth rate, reduces the window of opportunity for nucleation as a function of contact time and surface area, and promotes shedding. Using this to critique the relationship in Figure 5.35, lower surface energy may promote wetter thorn growth away from the leading edge. However, it goes some way to mitigate denser ice accretions with a higher ice adhesion strength by lowering the surface's inherent ice adhesion strength so it is less severely impactful. It would then follow that a lower surface energy surface would promote a more aerodynamic ice accretion. While the formation of glaze

thorns may occur at a higher frequency, they would be more readily removed by the airflow prior to compiling into a lamella structure, as seen in the rime growth in this work. The lamella's thickness is a function of the Stefan number, Stokes number and hydrophobicity, with a more hydrophobic surface slowing the growth rate for a given S and St spreading the nucleation sites wider apart across the leading edge and promoting wetter growth, forming more strongly adhered horns, less frequently.

5.3.1.6 Transition point along the leading edge

In mixed icing conditions present at $-2°C$ and $-4°C$ on the small blade, the growth regime changed from mixed ice to glaze ice at some point along the leading edge. One result for $-6°C$ was measurable and included in the first two graphs, a) and b), in Figure 1.22, comparing the position along the leading edge where the transition occurred and the temperature and corresponding Stefan number, respectively. For clarity, it was not included in later graphs. The transition point represents a threshold change in freezing conditions and density, compared to the mass distribution along the blade and the expected mass if it were a pure rime accretion. This is of interest as altering the surface would be pertinent to this position and the mass distribution, which would be an important factor when deciding threshold limits of what level of accretion is acceptable for safe coating operation to combat. If the coating changes the mass distribution, an iterative design process may be required to adjust the coating to meet the initial parameters used to define success.

A feature commonly present in this temperature range was a shard extending past the tip's radius. This is caused by the film or droplets travelling to the tip along the leading edge and freezing before shedding. In the same manner, an icicle is formed. The size of the shard was measured, and although it often formed with a three-dimensional geometry, the simplest method to quantify it was used to reduce error, which was its length. This shard extending from the tip is probably the most dangerous form of accretion in terms of potential damage to the turbine and the vicinity of its shedding. Its position relative to the blade gives it the momentum and moment arm about the hub, causing asymmetrical loading after it sheds from one blade and not the others. The projectile could also cause significant damage. As this feature also drags the centre of mass towards the tip, its size was identified as a factor that could influence where the transition point occurred.

With the distribution in Figure 5.22 c) and d) sharing a substantial similarity, it suggests that the size of the shard and overall mass are likely linked and compared to the transition point in each figure, respectively. The ratio of

measured mass to that expected for a rime accretion showed a strong correlation. Suggesting that the rime angle can be used as a predictor to determine the amount of water shed from the surface prior to freezing when compared to the transition point, e). There was a strong correlation between the $-2°C$ data and the Reynolds number at the transition point, suggesting that the speed at which the droplet travels down the leading edge after impinging is the dominant factor for warmer temperatures. However, four of the tests were at 500 rpm with different durations, and as it is the Re at the transition point it will scale with the position at any given angular velocity.

The angle of the glaze ice compared to the transition displays a difference between the two temperatures, with accretions more likely to transition closer to the tip for a given size of accretion, here measured by the angle of the glaze ice compared to the leading edge, at the colder temperature of $-4°C$. Combining all the identified factors only produced a weak correlation, h). The most helpful finding in this analysis was the insight that the rime angle of the accretion provides in wetter growth mechanisms to the mass of the overall accretion when comparing it to the transition point. The correlation was stronger than that of the transition point compared to the angle of the glaze ice accretion, which depends on the mass being distributed away from the root.

5.3.1.7 Potential future analysis to quantify ice nucleation and the structure of the resulting accretion

A test not possible with the images taken in this work would be to determine the thickness of the lamella and the density or frequency of nucleation points to correlate them with the factors mentioned in section 5.3.1.5. How this may present itself is shown in Figure 5.36. Figure 1.23 shows two images taken at warmer temperatures when testing for the most optimal lighting for data collection, where each point of growth can be seen amongst the mixed ice and some resemblance of layering seen in the tip growth analysis for rime ice. Figure 5.37 shows a different angle of a tip shot used in this study where the structure described can be seen but not from above, allowing this further analysis. Ideally, the frequency of nucleation points and the thickness of lamella would be analysed to test for a correlation with Re, S and St which could be seen by eye but not adequately captured in images. Describing this formation process would allow the analysis of the tip growth to be extended along the leading edge as the stages through the growth process identified would have been substantiated with evidence or discarded. However, they could not be quantified in this study. The impact of the surface properties could then be tested and compared with the measured changes in this study on the tip formation that occurs through a range

of temperatures and speeds for one surface. To see if the relationships identified are maintained, shifted, requiring additional coefficients, or are no longer applicable.

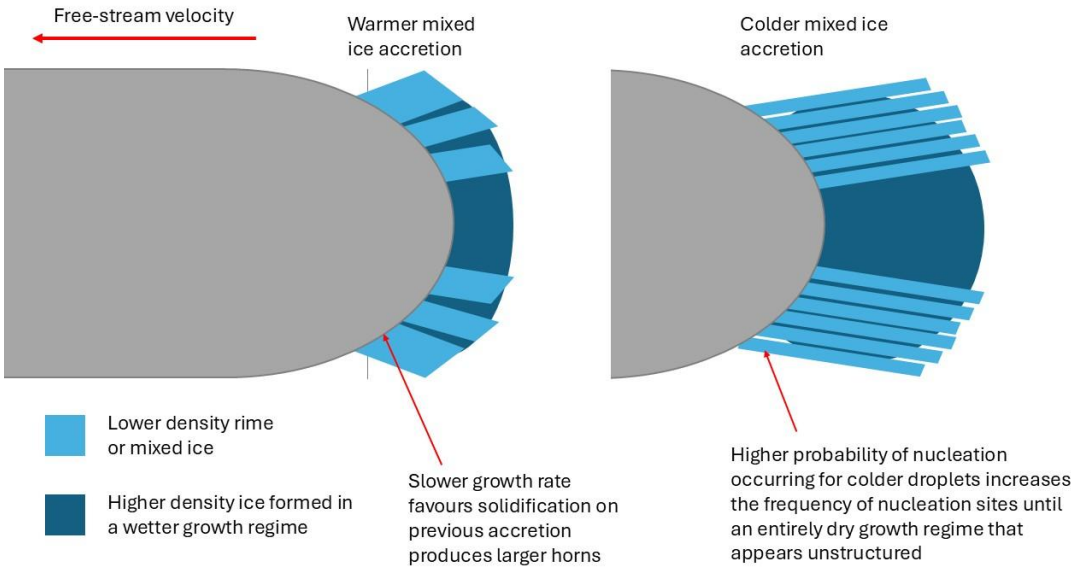

Figure 5.36 Visualisation of nucleation rate impacting the structure.

Figure 5.37 A different angle of the tip in Figure 5.4 formed at -8°C after 5 minutes at 2000 rpm where the horns compiled into lamella are visible but not easily quantifiable as from above appear unstructured with little contrast to the camera.

The benefits of hydrophobicity and low thermal conductivity for an icephobic coating will be the most significant in a wet growth environment as any slowing of the accretion will not pose the risk of shifting a dryer growth regime into forming glaze ice, which as a denser form would more strongly adhere to the surface. As any increase in delaying nucleation will depend on a reference material's baseline time, any proportional decrease in heat transfer will be more significant in these environmental conditions, providing a more significant opportunity for the droplet to shed from the surface. The disc experiment could be a simple way to analyse this mechanism and its importance. A higher surface velocity may mitigate the reduced heat transfer rate, which would cause denser ice accretion. A higher droplet velocity across the surface may also mix more air into the accretion, nullifying this potential negative.

5.3.2 Ice accretions on spinning discs

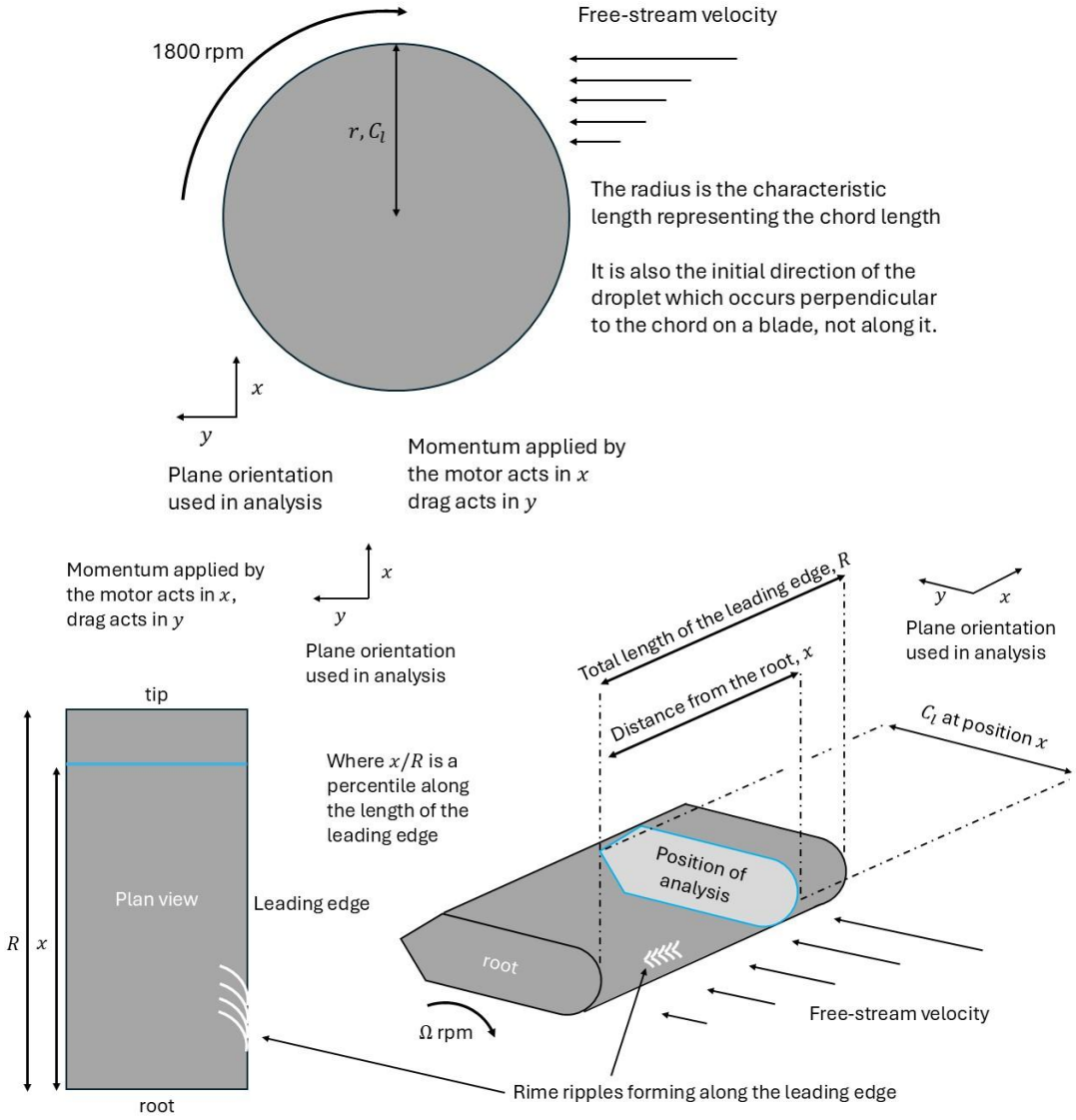

Figure 5.38 shows the disc and blade schematics that illustrate the analysis used.

As the velocity that is applied to the surface is in a different plane than in a wind tunnel or blade icing experiment, the analysis of droplet and film behaviour was altered to reflect this. The Reynolds number of the droplet's initial conditions is very low to mimic the initial conditions of impacting the stagnation point on the leading edge, and the Reynolds number of the test uses the edge of the disc to represent the free-flow speed. Considering the Weber number, the drag forces are always perpendicular to the centripetal acceleration. On a spinning blade, the vectors are swapped, and drag drives the droplet down the chord length

(represented by the radius of the disc in the Reynolds calculation). The centripetal forces are perpendicular to the chord along the leading edge. So, any influence of the Weber number of the film when considering the accretion geometry must be scaled such that angle deviations perpendicular to the chord are more sensitive to the Weber number for a spinning disc and the distance along the chord where the ice accretes is sensitive to the angular velocity. In the blade icing experiment, the angle of deviation from the chord depends on the angular velocity, and the drag depends on the position along the chord. As the disc attempts to analyse a specific point along the leading edge and the accretion formation at this position, this factor must be the basis of any analysis. With friction countering the inertia and drag, the influence on the observed result will depend on the relative scaling between the two in each test. As each direction is flipped, so is the curvature of the protrusions. With the disc formations beginning parallel to the radius and curving away, the accretion on the blade's initial vector is not parallel to the chord length but curves towards it. As the Reynolds number of the disc is low, a comparison of the accretion to that of near the root of a commercial wind turbine was used. Comparing the accretion to that achieved in the blade-icing experiment at the root may be most applicable as this formation is simple in structure, and the Reynolds number was calculated using a simplified assumption of a flat plate, which likely results in an underestimation for the blade.

The image shown in Figure 5.13 b) shows this expected protrusion pattern with the ripples curving into the direction of the chord, the curvature of which would be represented by the protrusions on the discs curving away from the radial chord, which represents the chord length of the blade.

On the blade, the ripple angle relative to the chord could be simplified to a ratio of inertia to drag, where a high-drag environment would cause the ice accretion to follow the chord length, and a low-drag environment would cause it to follow the leading edge. On the spinning disc, the curvature of the protrusions with respect to the radius could be simplified to a ratio of drag to inertia, where a high inertia causes the protrusion to not deviate from the radial chord, and a high-drag environment causes it to deflect more. So, a high-drag scenario produces less curvature on a blade and more curvature on the disc. This concept is backed by the measured curvature on the four un-patterned discs, Table 5.4. As the speed is constant between all tests on the discs, the applied inertia and relative air velocity can be considered consistent with the position along the radius. This leaves the friction of the surface impeding the droplet the only remaining factors on its position at solidification and the surface area of the droplet relative to its volume, which is dominated by the WCA of the surface and the resulting change in the drag coefficient of the droplet. The friction will also be related to the

hydrophobicity of the surface. Sandblasted aluminium produced a lower WCA than aluminium, although the discs themselves or the same alloy used were not tested. This would explain the difference observed in the protrusions.

The curvature on the sandblasted aluminium was 1.25 $°/\mathrm{cm}$ and 0.77 $°/\mathrm{cm}$ for the aluminium. Suggesting that the drag forces were more dominant for the sandblasted aluminium, which would align with the expected influence of the surface's hydrophobicity on the droplet's path. Unfortunately, this is not conclusive due to the high errors present for the aluminium disc, totalling 43% of the curvature value. The second difference between the two surfaces is the glaze ice. Considering the coated discs with PDMS and PDMS 5% SiC, the error measured in the difference in angles was much smaller. However, the radius of the glaze ice was very variable for PDMS 5% SiC. The error of measurements of the PDMS disc were sufficiently small such that the total error in the curvature was only 13% and 23% for the sandblasted aluminium. A measurable difference was present between these surfaces that can be explained by the difference in hydrophobicity with the WCA of a different aluminium alloy sandblasted by the same media of 87°, described in section 5.1.1, and the WCA for PDMS ranging from 100° to 115° depending on the age of the sample, section 5.2.1. These discs were tested when the coating was young, so the WCA at the time of testing was likely at the high end of this range.

The presence of glaze ice indicates a longer dwell time for the slower wet growth regime to be present. This can also be approximated with the fiction the droplet experiences. A lower WCA promotes slower growth and a larger glaze ice radius at the centre, as any increase in inertia is inhibited by greater friction. Comparing the sandblasted disc and the PDMS disc, shown in the appendix, the protrusions on the PDMS disc remain as mixed ice past the transition point, while on the sandblasted aluminium, they return to glaze ice after the transition. This suggests that the breakdown of the pooling in the centre due to an instability of the surface tension releases some energy, and the droplet's initial acceleration was high until the friction on the sandblasted surface dominates and a wet growth regime returns.

Relating to Figure 5.35 and conceptualising how WCA may impact the ice formation on the blade. This observation is very promising for icephobic coatings as the reduced contact area with the surface is associated with a higher WCA, which is also a less thermally conductive material and does not promote a wetter growth regime. Even in this low-velocity environment, the benefits of a higher WCA in reducing friction across the surface outweigh any reduction of the apparent growth rate. A more hydrophobic, lower thermal conductivity surface did not induce denser ice growth as some accretions formed with no ice at the centre; a delay in accretion was also observed. A higher WCA would likely

increase the instability of a liquid film where droplets separate from any larger body of water more readily with a smaller maximum diameter of this pool as the surface tension at the liquid-air boundary becomes more dominant than the solid-liquid boundary. The diameter of the droplet separating from the film would also be influenced by the velocity of applying shear within the liquid, so it may scale with the radius of the disc.

The overall accretion mass was not substantially different between discs, Table 5.2. This supports the concept that the surface or coating only has a significant bearing on the initial accretion process upon it, and accretion on the following ice is unrelated to it, but rather the properties of that ice. The delay supports the conceptual relationships in Figure 5.35, where a higher WCA reduces the friction between the droplet and the surface and delays freezing, such that the mass is distributed over a wider proportion of the chord by delaying accretion. Producing a broader base for further accretion to grow, forming a lower A_{shard}/A_{tip} structure.

Furthermore, the glaze ice that forms at the disc's centre could be compared to the positions of the horns that form on a blade. Again, the inverse presence of inertia and drag could be used to interpret these two formations. The glaze radius on the disc comprises an exposed surface or thin accretion at the centre, which grows thicker along the radius until the transition point where the protrusions form. It may be possible to relate the applied inertia along the radius of the disc to the drag in a wind tunnel or blade icing experiment and the position at which glaze ice horns form to inform modelling techniques better. The drag on the droplet at the stagnation point on the leading edge and the centre of the disc is assumed to be zero. The relationship between the glaze thickness at each point along the radius represents the probability that a glaze horn would form along a chord length on a blade.

A more comprehensive 3D scan of the ice formations on the discs would provide an accurate height at the transition point and its radius, along with the thickness of the ice within the glaze accretion at the centre, presenting the potential to model where horns may form on an aerofoil. If a higher rpm were used in the disc experiment, it would be reasonable to assume the glaze radius would increase, assuming the time for a droplet to freeze is consistent. It would then follow that the peak thickness at the transition point would be smaller, and the relationship between glaze thickness and its radial coordinate would be scaled with the angular velocity. Unless, of course, the higher velocity induces any liquid film to destabilise at a smaller radius.

As with the Weber number, it relates the drag force and the cohesion force of a droplet or film, and it could be used to relate the inertia to the cohesion forces.

The radius of the glaze ice at the centre is related to the film thickness. A higher WCA causes a droplet's experienced relative acceleration to the disc surface to increase at a rate that outpaces the increase in the height of its centre of mass above the surface. The change in area is a second-order term, and the film thickness in the Weber number is a single-order term. Considering a droplet on a surface with a WCA of 90° and 180°. The distance between the centre of mass and the surface is its radius, r, for a WCA of 180°, and the contact area is zero. The radius of the droplet with a WCA of 90° is equal to its height, its centre of mass equal to $3r/8$ and its contact area πr^2. When considering the Weber number, the reduction of contact area will scale much faster than the increase in droplet diameter or film thickness. A further visualisation of this is shown in Figure 5.39.

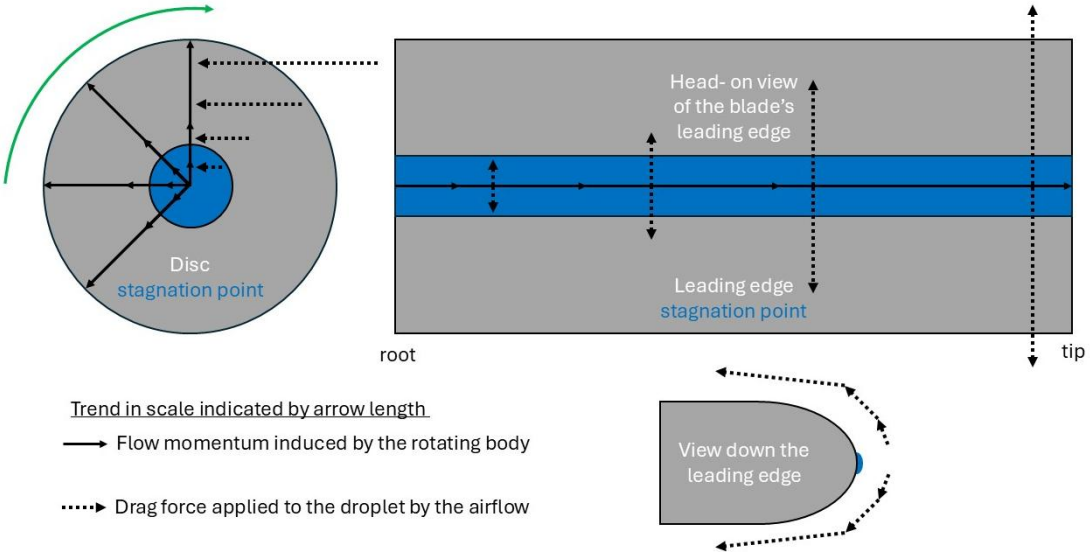

Figure 5.39 How drag affects droplets differently between the two experiments by removing one dimension plane of the blade to simplify analysis by studying a disc in its place.

5.4 Summary of ice accretion experimentation

The ice accretions formed with the rotating disc and blade icing experiment have great potential for predicting small-scale accretion features at a chosen point along the leading edge of a blade using a larger-scale accretion within a smaller piece of equipment. The data could be used alongside modelling to inform icephobic coating design and testing.

Difficulty adequately capturing small features was encountered in the blade icing experiment. Using the disc could help mitigate the shortcomings of reducing the scale of an entire turbine to a diameter of 0.46 m. Unfortunately, no meaningful conclusion could be drawn from analysing the wavenumber formed on the discs shown in Table 5.5. As the Reynolds number tested was low and relevant only to the root of a blade, the consistent structure present in the blade icing experiment near the root, as shown in Figure 5.13 b), may be why. The errors in this value were colossal and had no apparent relationship. The potential factor impacting the wave number would be the hydrophobicity, which could increase the droplets' velocity and cause the surface tension of the water to dominate more readily, producing instability at a smaller glaze radius while causing any droplets to shed from the film to be a smaller diameter. This reduction in diameter might lead to a larger wavenumber at first consideration, as more frequent shearing of droplets from the stagnant pool would lead to more protrusions. It may also not deviate significantly as the change in instability would be primarily observed in the glaze ice radius, where the critical velocity where droplets shear from the film is related to the surface tension at each boundary. This could present itself as the change in the total number of waves is balanced by reducing the glaze radius, producing broadly consistent wave numbers. The error in the data obtained was too significant for this analysis.

This more frequent shearing from the film on hydrophobic surfaces might be valid for the initial accretions but may flip as more ice grows. As the difference in surface energy of the ice compared to the hydrophobic surface would be more significant than that for sandblasted aluminium, a bias may occur where the hydrophobic surfaces are effective at reducing dwell time and contact area, and the further accretions preferentially occur on ice. Where this difference is small, the probability of growth occurring on the substrate or ice is more comparable, resulting in a larger wave number. It would follow then that the sandblasted aluminium would have the highest wavenumber for the least hydrophobic surface, but this was not the case. A possible cause would be that it is both a function of thermal conductivity and WCA, and the more hydrophilic surface of the sandblasted disc compared to the aluminium reduced the droplet velocity sufficiently compared to the time to solidify that the bias of further accretions occurring on top of the ice was not present. This result highlights an opportunity for further learning into the progression of dynamic ice accretion on different surfaces and using the information gathered to better interpret more complex scenarios such as the blade icing experiment.

The blade icing experiment showed much more potential for understanding the ice accretion process with the operational and environmental properties tied to several visible features in the resulting accretion where the shape and structure

of both hard and soft rime accretions have been shown to be predictable. Linked to the flow and cloud properties at the tip Figure 5.11 and along the leading edge Figure 5.16. The distribution of ice across the blade in glaze and mixed ice accretions has been associated with the locomotion of droplets across the surface before solidification Figure 5.19. If the ice transitions from glaze to mixed ice along the leading edge, what influences where this occurs Figure 5.22. Experimentation of this kind, married with modelling, could be a great asset in predicting ice accretions and testing surfaces to mitigate them while analysing how those changes to the surface change the resulting accretion. The disc icing experiment allowed for assessing the impact of the surface properties in a dynamic accretion scenario, simulating equipment much larger than itself. The blade icing experiment was much more fruitful and provided greater depth of insight than the disc experiment; however, it is limited by its scale, which could be mitigated when testing is paired with the disc experiment to inform modelling methods. The disc provides greater detail into the fluid mechanics before solidification that could be utilised when comparing icephobic coatings. Similar coatings may not produce significantly different results in the blade icing experiment, but slight variations may be more apparent on the disc or a full-size application.

Chapter 6: Electro-thermal de-icing energy consumption and its dependence on a coating's properties

Icephobic research broadly aims to find zero-energy, passive solutions to engineering problems caused by icing, with a significant focus on aerofoils on fixed-wing aircraft, rotorcraft, and wind turbines. Coatings designed to enhance current thermal de-icing systems could provide a stepping stone towards this goal if they can be shown to be effective and cost-efficient. Before a zero-energy solution can be used to replace thermal de-icing systems, robust safety testing is paramount, as failure of an icephobic coating to perform when it is the only de-icing safety feature could cause catastrophic failure and pose a significant risk to life.

As a coating may be designed with a low thermal conductivity in mind to minimise latent heat transfer[84][108], thereby delaying ice formation, its impedance to a thermal system could be severe. If an icephobic coating relies on delaying heat transfer as part of its performance to reduce icing incidents, and then the mechanism for detachment fails or underperforms, requiring the heating system to be used, the coating may significantly increase the time and energy cost to remove the ice. As the coating insulates the surface from the supercooled water and the heater from the ice, a factor as simple as coating thickness could significantly affect the safe operation of an electro-thermal de-icing system Figure 6.1.

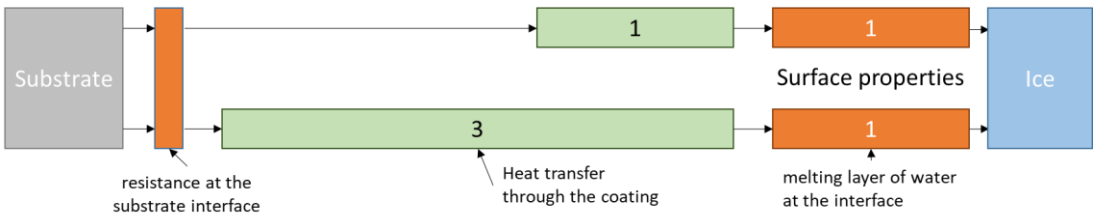

Figure 6.1 Static de-icing energy cost breakdown associated with the coating comparing a coating's performance breakdown with identical surface and material properties but of a different thickness.

6.1 Grit-blasted aluminium

Aluminium is a commonly used material in aerospace applications [12] and is commonly used as a reference material when testing a material or coating for icephobic performance. Having aluminium as a reference material is vital as results can vary significantly depending on the type of test, equipment, and methodology used. Performance must, therefore, be in the form of a measured value relative to aluminium to provide greater clarity to widely tested properties such as ice adhesion strength. Grit blasting was employed to alter the thermal de-icing performance of aluminium by increasing its surface roughness.

6.1.1 Water contact angle

As-received aluminium has a WCA of 98.1±2.4° (n=6), which was reduced to 86.6±1.8° (n=3) by increasing the surface roughness via grit-blasting. Increasing the surface area of the aluminium increased the hydrophilicity. After two years, the grit blaster and blasting media were replaced, and the WCA was retested for rough aluminium, as received aluminium and aluminium were roughened with the new grit blaster. There is no known change in the aluminium sheet supply used throughout the experimentation. However, the as-received, or smooth, aluminium's WCA remained reasonably consistent at 101.2±1.1° (n=40) from 98.1±2.4° (n=6), the samples were not the same substrates, but from the same supplier; the original samples grit-blasted aluminium, which were used in several de-icing experiments over this period, WCA rose to 107.3±1.2° (n=8) from 86.6±1.8° (n=3) and aluminium roughened with the second grit blaster achieved a WCA of 96.1±1.9° (n=28).

6.1.2 Roughness

The grit-blasted aluminium shows an increased roughness with r_a and r_q Increasing from 1.00 to 1.41 μm and 1.29 to 1.76 μm respectively. Aged rough Aluminium showed a decrease in surface roughness to fall below aluminium's with an r_a of 0.77 μm and an r_q of 1.03 μm. Both Aluminium and rough aluminium with a carbon coating have a comparable roughness to one another with a r_a of 1.21 and 1.26 μm respectively, and a r_q of 1.55 and 1.59 μm. Grit blasting the aluminium increased the average distance between the asperities, as shown by the rise in the measured r_{sm} by 25% with a r_c of 5.25 μm for the grit-blasted aluminium. Indicating that these asperities are on average the largest of the

aluminium surfaces. Based on these factors, the differences in WCA can be explained with the increased roughness of the grit-blasted aluminium making the surface more hydrophilic due to the increased surface area and aluminium not being a hydrophobic material. The older rough aluminium that experienced wear so that the peaks of asperities were flattened reduced the roughness while having the most negative skew, r_{sk} of -0.31, and the highest kurtosis, r_{ku} of 4.77, suggesting that the valleys of the profile changed less over time and may function to trap air in the surface, increasing the WCA. This is also indicated by the older grit-blasted aluminium presenting an r_z lower than the as-received aluminium, which is lower than the new grit-blasted aluminium.

Comparing these samples indicates a more pronounced difference between each surface type than any change incurred due to the carbon coating. The aged rough aluminium has an S_q 53% of the unaged rough aluminium. The aged rough aluminium also has the most negative skew measured in this subgroup, -0.64. Some surfaces were carbon coated as a means to verify the validity of results for transparent coatings that were difficult to characterise. The coating thickness applied ranged from 10-20 nanometres according to the equipment used. This was not verified directly by any characterisation methods, only its impact on the surface roughness measurements. All values are tabulated in the appendix.

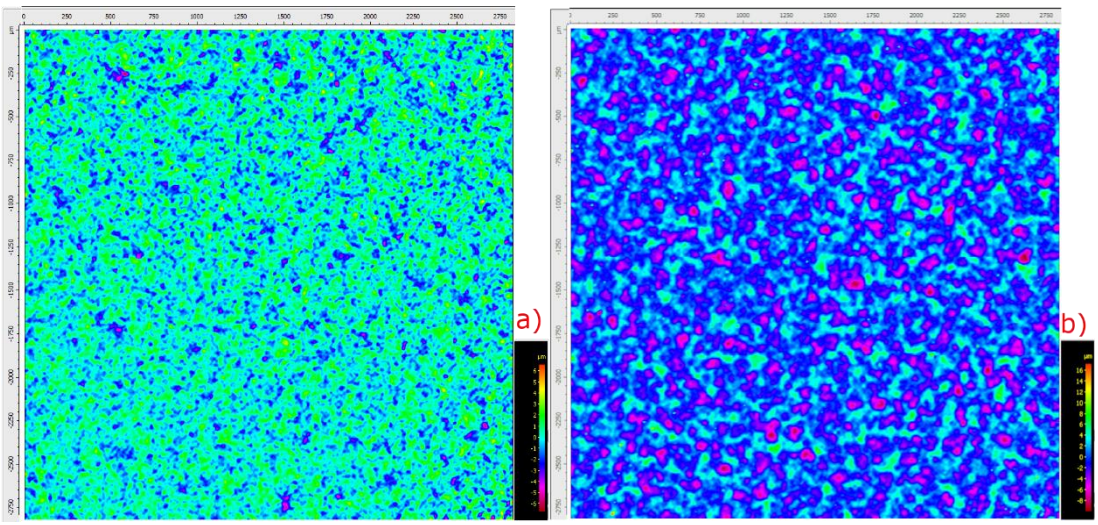

Figure 6.2 Filtered overlay of a) aged rough aluminium and b) rough aluminium recently grit blasted with the Honite media.

Aged rough aluminium shows much smaller deviations in surface height, with valleys being more prominent than peaks Figure 6.2. Rough aluminium shows a greater range of asperity heights with higher, more regular peaks. This visual

comparison shows the main differences between the two, with the older grit-blasted surface being less rough and having lower asperity peaks.

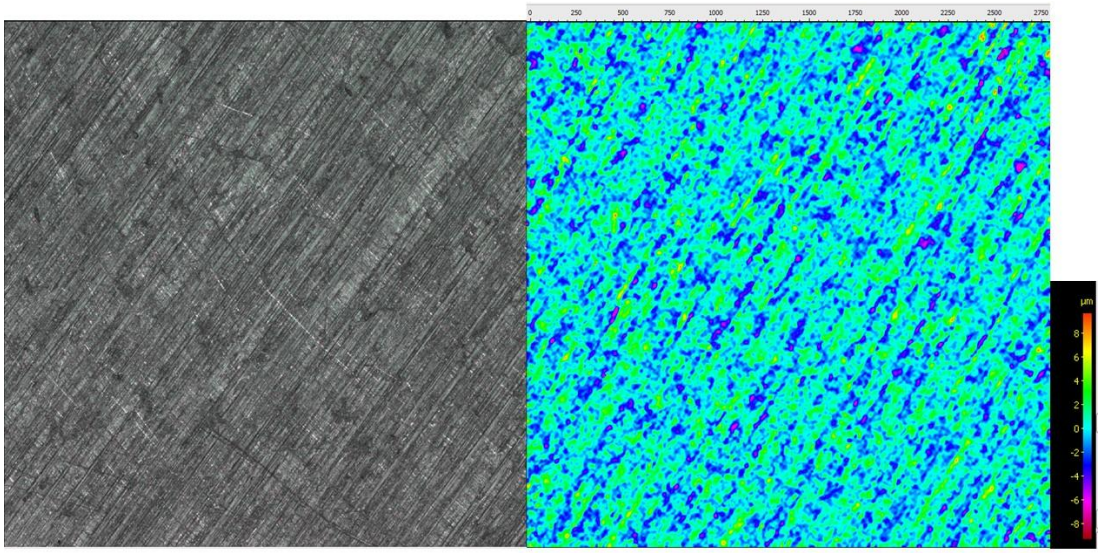

Figure 6.3 Image of aluminium and its filtered overlay.

Aluminium displays a clear textural direction in Figure 6.3. The grit-blasted surface shown in Figure 6.2 does not display the same uniformity in its topography. Indicating that grit-blasting the surface has meaningfully altered the topography and increased the surface roughness.

6.1.3 Thermal de-icing

The grit-blasted surfaces have a higher energy cost than the as-received aluminium. Increasing the roughness by grit-blasting increases the energy cost of de-icing from 1.03±0.07 kJ to 1.07±0.10 kJ. This aligns with ice adhesion strength research showing an increase with surface roughness due to mechanical interlocking of the ice and asperities and increased surface area of the interface.

6.2 Associated energy cost of electro-thermal de-icing PDMS

PDMS is a common choice for icephobic coating research as it is a hydrophobic elastomer. A low Youngs modulus icephobic coating can induce cracking at the interface when any adhered ice is placed under mechanical shear loading. PDMS is a silicon elastomer with a low surface energy, is well studied, and has a wide range of uses. It was chosen as a candidate material aiming to improve the aluminium surface for static thermal de-icing, specifically Sylgard 184. Not only do silicone polymers have a low Youngs modulus [59], but they also have a high Poisson's ratio [64], which can be beneficial in crack formation as when the coating is deformed in the direction of the shear loading, it also has significant deformation on the surface in the plane perpendicular to the shear load. A higher dichotomy of strain at the interface with the ice prompts stress concentrations to form, which causes a crack to form [53]. A high Poisson's ratio compounds with a low Youngs modulus, emphasising this mechanism to reduce its ice adhesion strength. The Young's modulus of ice varies significantly with its density and can reach 9 GPa.

A straightforward method of improving icephobicity is to reduce the material's surface energy. The most efficient method for thermal de-icing would be to coat the surface with a self-assembling monolayer such as POTS, which is a highly fluorinated compound. This has been utilised to increase a surface's hydrophobicity, and by virtue of being a SAM, it would add a negligible thickness and mass to the surface. This, in theory, would improve the thermal de-icing performance significantly on paper but would not be viable due to durability concerns.

6.2.1 Water contact angle

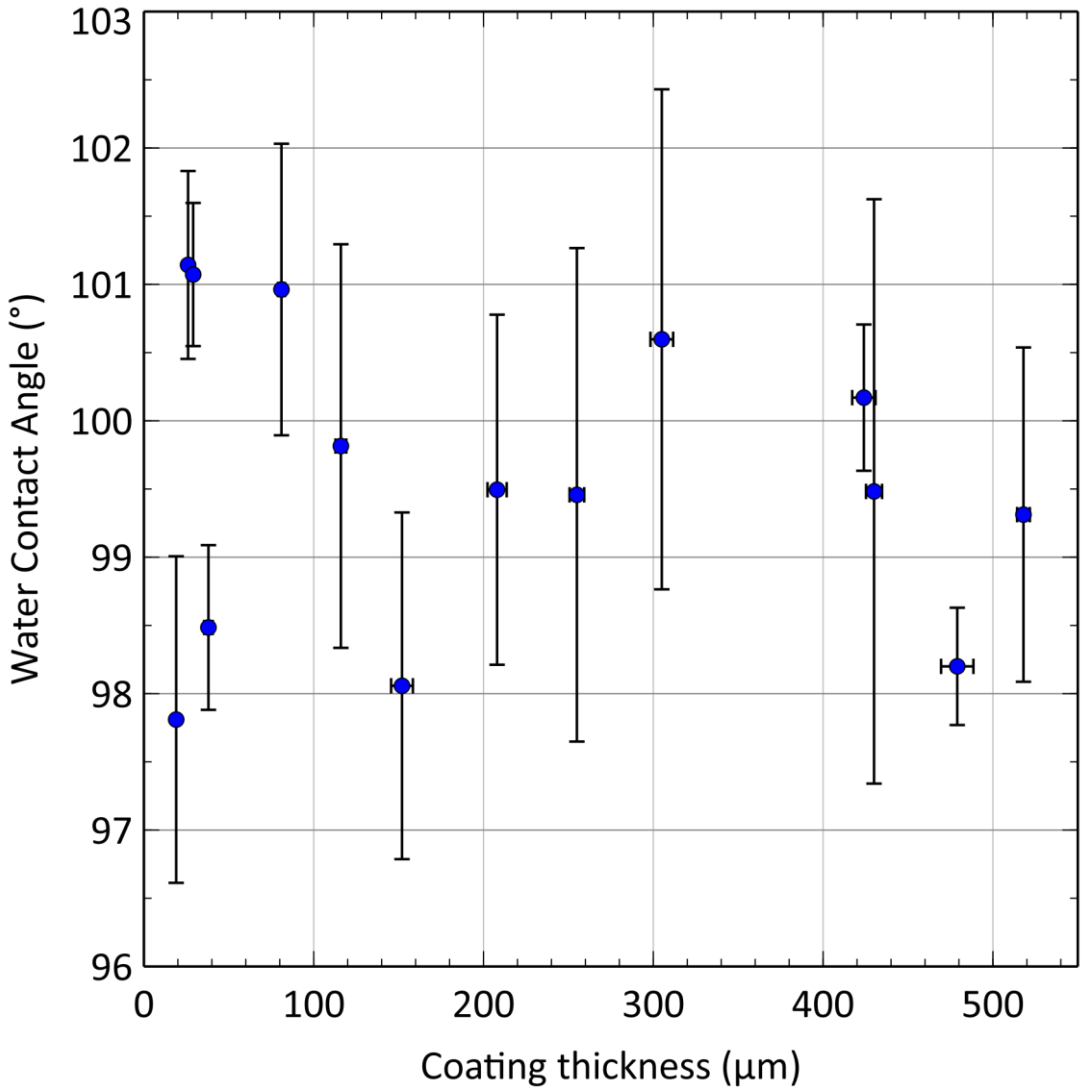

Figure 6.4 WCA of PDMS coatings over a range of thicknesses.

The water contact angle for PDMS was measured to compare with the previously tested aluminium surfaces along with the surface roughness to compare and contrast the different surface properties and their relative impact on thermal de-icing when adding a coating of significant mass onto the substrate Figure 6.4. The WCA was confirmed to be independent of coating thickness, averaging $99.6 \pm 0.4°$, indicating the production method did not impact the surface roughness across the range tested. The testing of these samples occurred several months after they were produced. Fresh samples coated on both as-received and grit-blasted aluminium substrates achieved $114.6 \pm 0.4°$ with an average thickness of $38 \pm 11 \mu m$. Thicker coatings of the same age, ranging from 200 to 400 μm, achieved $108.2 \pm 0.7°$.

6.2.2 Roughness

The surface roughness of PDMS was measured with and without carbon coating to verify whether it significantly impacts the readings and confirm whether accurate comparisons can be made. Thin PDMS coatings could not be accurately measured with the substrate interfering with the data. In turn, it is important to know the roughness parameters of the surface, how they may change with the coating thickness, and their impact on the de-icing performance of the coating.

The high kurtosis of the 115 μm thick coating illustrates the impact of the carbon ridges on the results due to the cracks forming sharp peaks, coupled with a much more negative skew, suggesting the ridges significantly affect the average height of the profile. This sample also has a considerable standard deviation for the Rsm of 119%, as seen in the tabulated results in the appendix. The values of the carbon-coated sample that is 13.8 μm thick of these parameters are comparable to the very thick coating (430 μm) that did not require carbon coating to counter the optical transparency of PDMS, suggesting this result can be considered for discussion. From this, it was determined that thin carbon coating could be utilised, and when combined with the WCA not having a significant variance over the thicknesses tested, the assumption could be made that the surface roughness was reasonably consistent for PDMS.

6.2.3 Thermal diffusivity

The thermal diffusivity of all PDMS-based coatings was measured by laser flash, in-plane and through-plane. Two different geometries and production methods were used to test the through-depth thermal diffusivity and one for the in-plane measurements, see section 4.5.2.

The thermal diffusivity of PDMS was found to be $0.111 \pm 0.001\ mm s^{-1}$ with a standard deviation of 4% when tested through the depth of the cut sample material. In-plane tests showed a thermal diffusivity of $0.287 \pm 0.070\ mm s^{-1}$ with a standard deviation of 42% with some data at $0.147\ mm s^{-1}$ and the other results were much higher at $0.357\ mm s^{-1}$. The disparity between the in-plane and through-depth values is not understood and may be influenced by the polymers' structure or inadequate samples produced with imperfect geometry.

6.2.4 Thermal de-icing of PDMS coatings

The time to de-ice was measured by placing a substrate, with a glaze ice block adhered to the surface, into an actively cooled coldbox and held in place in a frame containing a film heater and thermocouple. The heater was supplied with 10W of power, and the time for the ice to detach is measured. This test was performed to assess the impact of surface properties and thickness of the coating material on the energy cost associated with thermal de-icing a surface Figure 6.5.

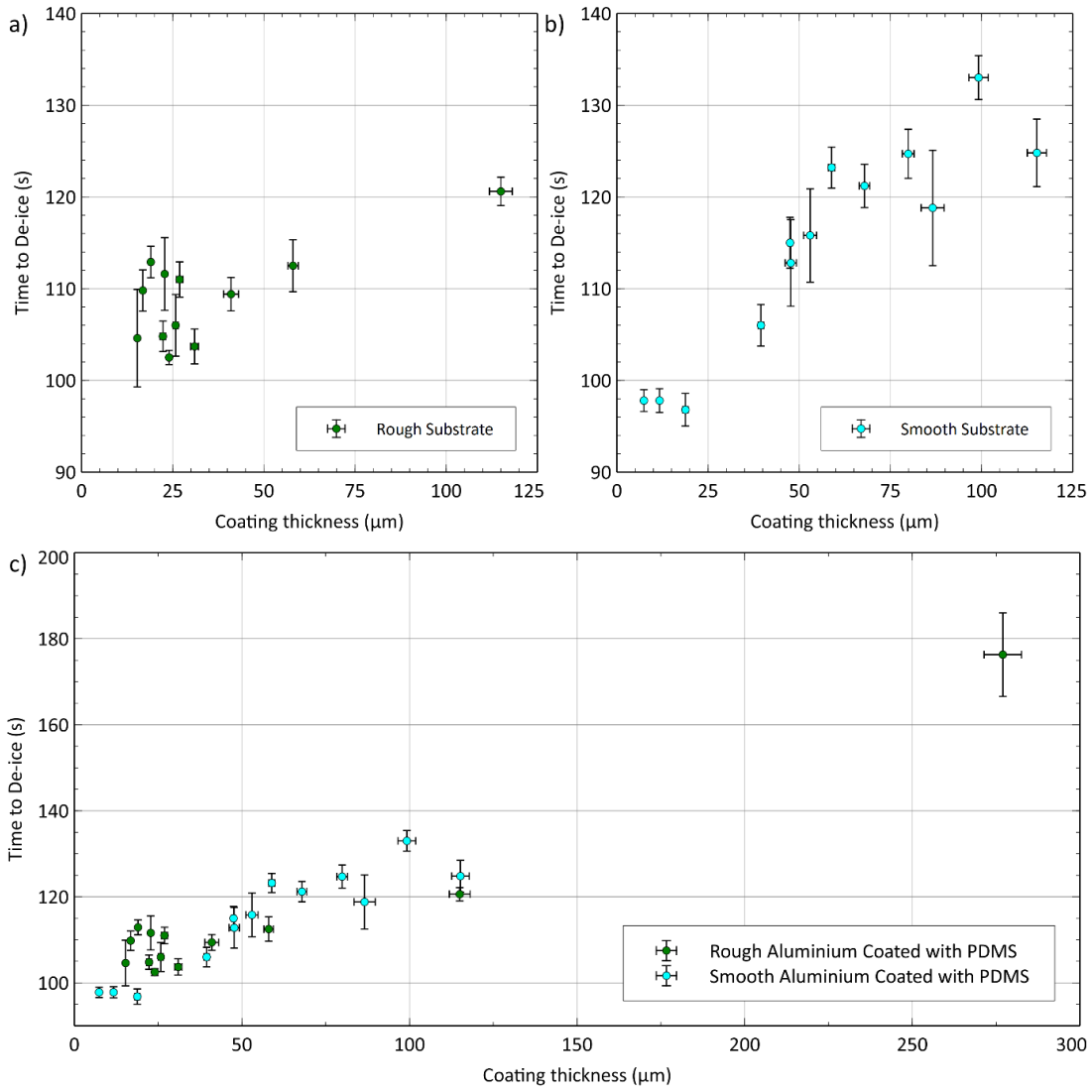

Figure 6.5 de-icing energy cost of PDMS coated onto a) rough aluminium with samples that have a coating thickness below 125 μm b) smooth aluminium c) Both datasets in their entirety.

In theory, the time to de-ice should rise linearly with thickness as it is limited to well under 1mm. The rate of cooling should not change significantly, and all other variables are controlled, including the surface properties. Testing samples coated upon substrates with different topographies was done to consider at what thickness ranges the substrate may impact surface quality and reliability for the methods used. This limited the conclusions that could be drawn from further testing using this methodology. Coating grit blasted substrates appeared to produce a more uniform coating upon visual inspection due to improved wetting of the uncured polymer on the rougher surface. However, the predictability of the coating thickness was limited at higher speeds of the spin coating process, leading to the clumped samples from roughly 15 to 30 µm Figure 6.5 a). Lower-thickness coatings were possible on the as-received aluminium surface Figure 6.5 b).

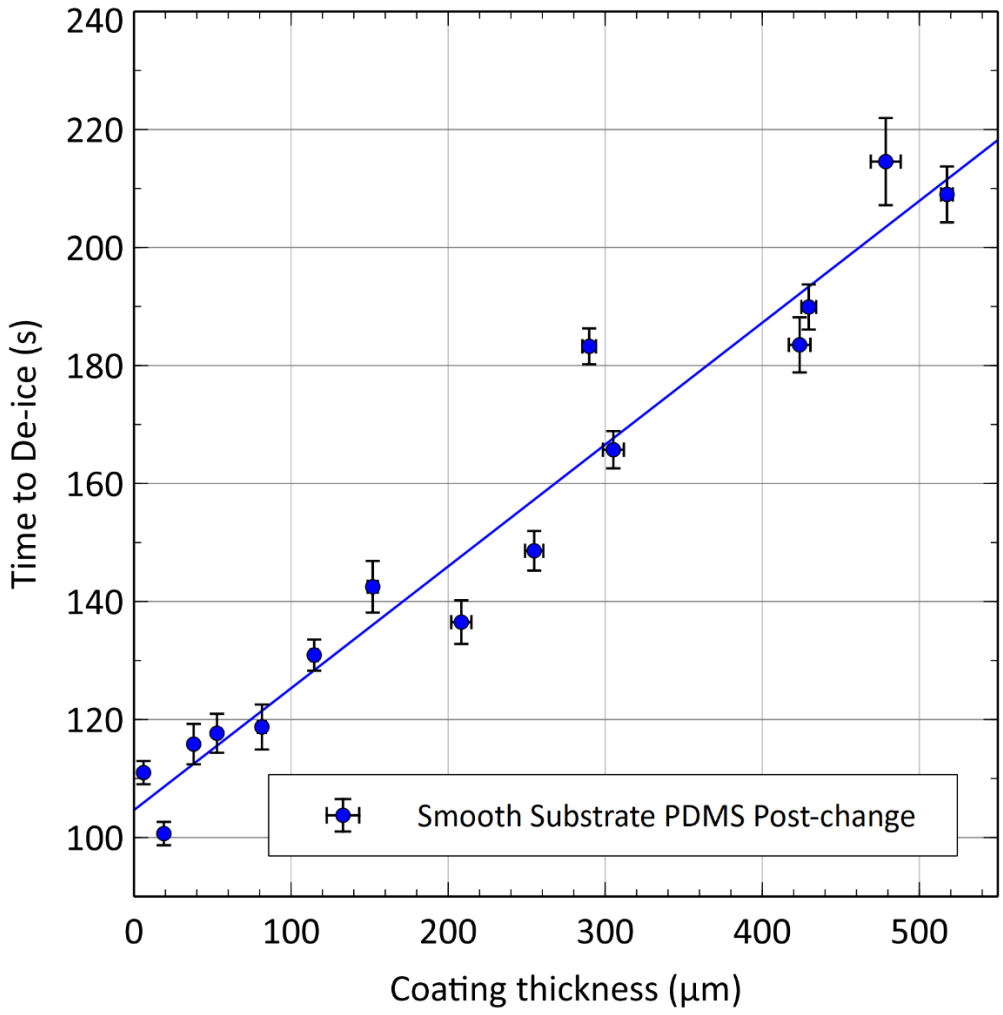

Figure 6.6 Thermal de-icing of PDMS coated upon smooth aluminium over a range of thicknesses exceeding 500 μm, samples produced and tested post lab fire.

As smooth aluminium did not exhibit the higher unreliability of the relationship between coating thickness and time to de-ice at lower thicknesses, further testing of PDMS without any filler material was completed using substrates that were not grit-blasted Figure 6.6.

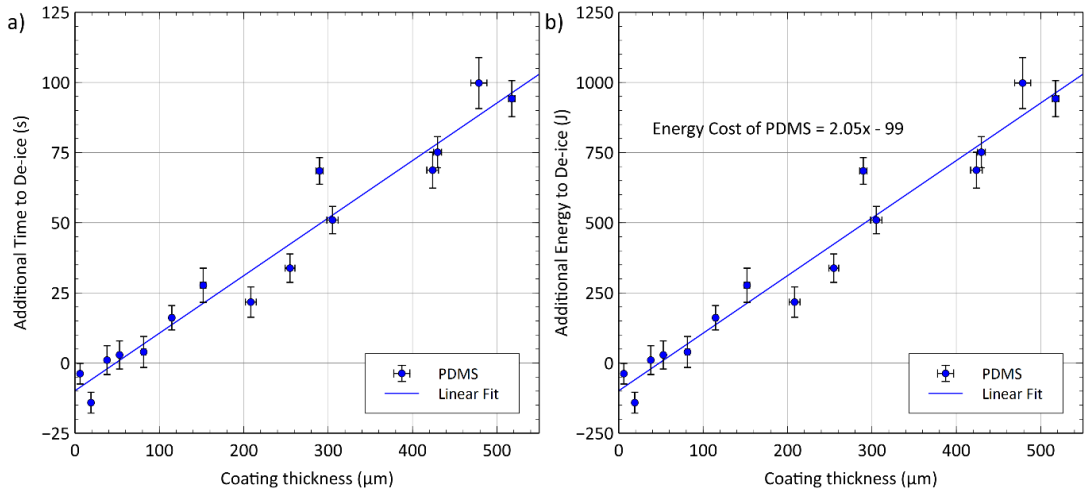

Figure 6.7 a) The time to de-ice PDMS across a range of thicknesses after removing the time to de-ice aluminium to provide a time value associated with the coating. b) the same data in a) converted to energy cost using the known power consumption of the heater.

Taking the raw time values displayed in Figure 6.6 and taking the result for smooth aluminium from it, the time difference between the coated and uncoated surface can be displayed to assess the relative benefit or cost in terms of time to de-ice Figure 6.7 a), the error for the additional time to de-ice is the summation of the error for the aluminium result ($\pm$1.3 s, n=29) added to the error of each respective data point in Figure 6.6. As the power supply to the heater was fixed to 10W, this additional time to de-ice can be converted to an energy saving or cost, as shown in Figure 6.7 b). From the linear regression, two properties can be inferred: the gradient indicates the additional energy cost for every micron increase in coating thickness. For PDMS, this is 2.05 J/µm; the y-intercept indicates the relative energy cost or saving associated with the coating surface properties when compared to aluminium if the coating had no thickness. For PDMS, this indicates an energy saving of 99 J. If a coating was required to improve other hydrophobic or icephobic properties of a surface but not increase the thermal de-icing energy, this can be inferred from the x-intercept, which is roughly 50 µm for PDMS. If the surface quality is poorer, the y-incept would be positive. For example, rough aluminium requires an additional 34 J.

Increasing the thickness of the PDMS resulted in a linear increase in the energy consumption of the heater required for de-icing, as expected. For context, the film heater is placed on the back of a 6mm thick aluminium plate with a 1.2mm deep recess to flush the substrate surface with the holding plate. The focus of the plate design was to minimise its size and, therefore, contribution to the energy cost for de-icing to occur, by minimising the mass between the heater and the ice. A 500 μm thick coating represents an 8% increase in the distance from the heater to the solid-ice interface, in the case of PDMS, doubling the de-icing time and energy cost. As the film heater was powered with a 10W supply a 100 s time to de-ice is equivalent to a 1 kJ energy cost to de-ice.

It is imperative that this contextual information is presented when studying this performance metric. As mentioned in the selection for PDMS a SAM such as POTS (1H,1H,2H,2H-perfluorooctyltriethoxysilane) would improve the thermal de-icing performance of the substrate with a negligible addition of mass. Preliminary data for this was collected and is presented in the appendix. A key concept when considering the performance of a coating in testing of this kind is displayed in Figure 6.1, where the impact of both surface properties and the bulk material must be considered for the chosen application. This is why the thermal diffusivity is presented above in section 6.4.3. These two properties of the coating may dominate the electro-thermal de-icing performance of thicker coatings, which could be unfairly compared to surface modifications without this context.

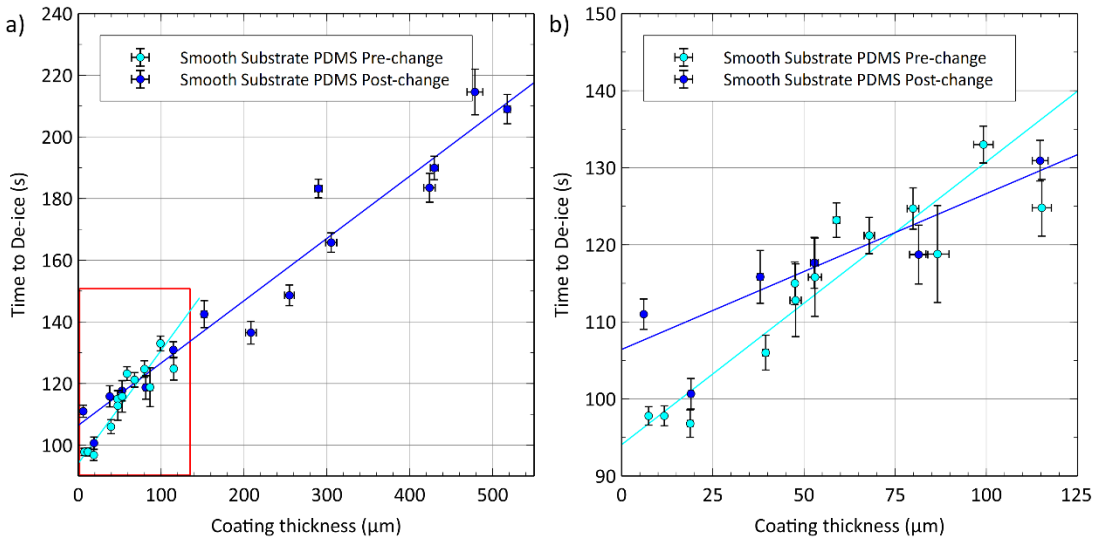

Figure 6.8 a) Comparing the time to de-ice PDMS before and after an uncontrollable environmental change occurred, using smooth substrates b) selection of the data highlighted by the red box in a)

Figure 6.8 shows the result of PDMS samples made and tested before and after some uncontrollable environmental changes. The result from aluminium before was 102.5±1.8 s (n=29). This rose significantly to 114.8±1.7 s (n=46). The value afterwards also benefited from air conditioning stabilising the room temperature, which improved the reliability of the data, roughly having the standard deviation. The new value with no air conditioning during summer was 127.2±2.0 s (n=106), during which some days the room temperature exceeded 28°C. The days with the higher temperatures generally had a much larger range of results. The results before the changes to the environmental conditions in Figure 6.8 were obtained in colder months of the year with no air conditioning present but central heating maintained a consistent room temperature from day to day.

As the discrepancy is assumed to be due to potential changes to the de-icing equipment that could not be quantified, the respective aluminium reference value was used from the same period in which any testing was performed.

Assuming the surface properties are consistent across all coating thicknesses, the associated energy cost with the surface properties will be fixed as the surface temperature and the thickness the melt layer must reach for de-icing will be consistent. Below 48 μm the coating could provide an energy saving as seen from the gradient in Figure 6.8 b), after which the coating increases the cost for thermal de-icing. This is particularly noticeable for the data before the environmental change occurred, which reached 2.5 $J/\mu m$ when the coating thickness reached 50 μm. Above 100 μm the surface properties have a diminishing proportional impact on static thermal de-icing performance. With the thermal properties of the bulk material becoming a majority factor, the normalised energy cost rises above 1 $J/\mu m$ and the rate of change tapers with any further change. Past this point, increasing thickness clearly had a diminishing effect on the per-thickness energy cost of each sample. Dividing the energy cost by the sample's respective energy cost by its thickness can be used to highlight the sensitivity of any small thickness change on the apparent bulk material's properties.

Normalising any individual sample's energy cost for its thickness cannot be extrapolated to predict the energy cost at a different thickness. Looking to Figure 6.7 b), appreciation for the fixed difference between two surfaces associated with the y-intercept and the linear increase in energy expenditure with coating thickness is the necessary context for comparing different coatings and similar experiments. If this data was limited to 50-100 μm, the apparent normalised energy cost could be read as below 1 $J/\mu m$, which would appear to be a much more successful coating. Understanding this simplifies coating design criteria to the surface properties and thermal diffusivity when no significant shear load is present.

6.3 PDMS containing thermally conductive filler material

As the coating may impede the active de-icing system's performance, increasing the PDMS coating's thermal diffusivity could produce a viable coating. The effect size of this solution would be much smaller than that of a successful passive solution; however, it may be beneficial as an intermediary improvement. If a filler in the PDMS can also improve its durability, it may prove cost-effective.

Silicon carbide was selected as the primary filler material having a thermal diffusivity comparable to many metals with a higher Youngs modulus, which could combat abrasive wear. Widely available in various powder sizes, it is commonly used as an abrasive material for its strength and hardness. It is also available as submicron fibres with an aspect ratio greater than 20.

6.3.1 Roughness

The roughness of each composite was measured to see the impact of the fibre-fraction on the surface and how both impact the thermal de-icing performance.

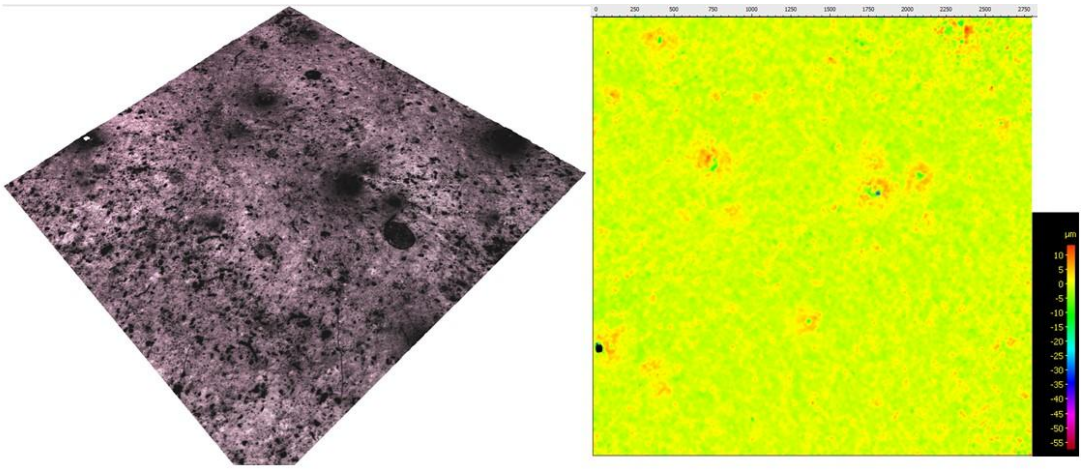

Figure 6.9 Carbon coated 5% SiC coating that is 40μm thick with no visible cracks from the carbon but significant areas of debris on the surface.

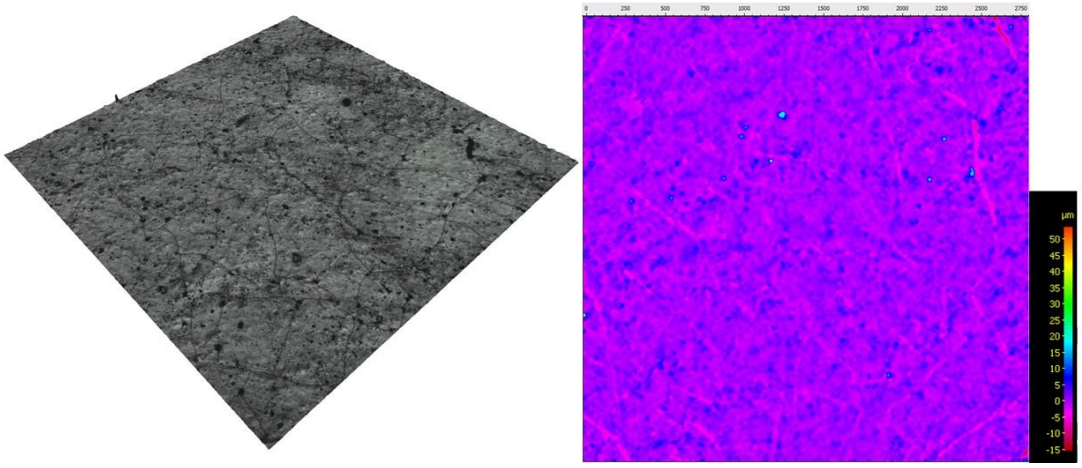

Figure 6.10 Carbon coated 5% SiC coating that is 174μm thick showing some cracking of the carbon and spots of debris highlighted as cyan in the filtered overlay. Coated with carbon in two stages, each application of a minimal amount of carbon was used to minimise cracking.

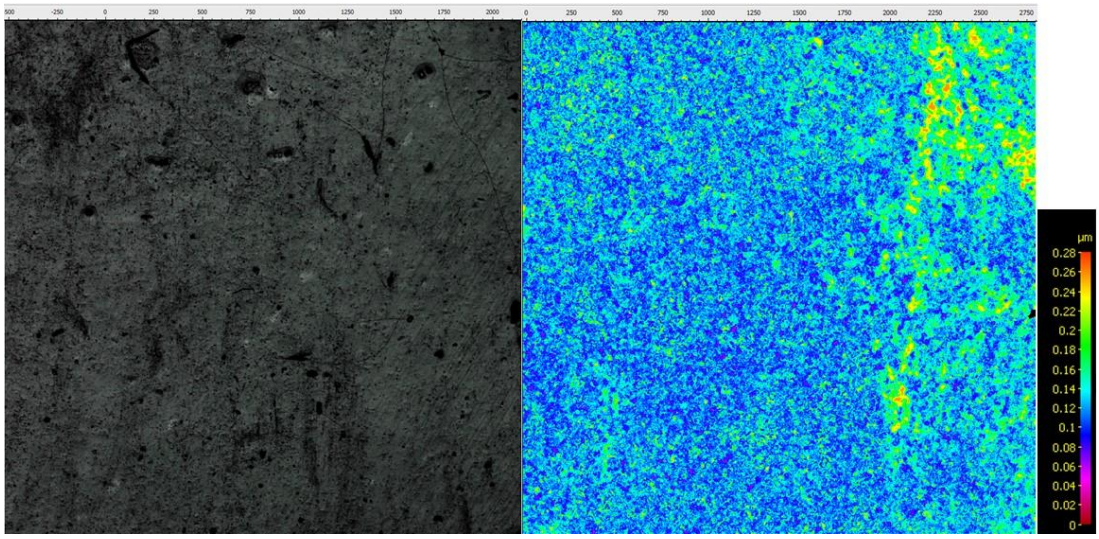

Figure 6.11 Carbon coated 5% 325μm thick PDMS coating top-down view and filtered overlay of surface roughness.

All coatings that were carbon coated have a kurtosis above three, suggesting sharp features that ridges formed by the carbon will contribute to and, therefore, reduce the reliability of the data. This could be due to the topography of the surface as the only visible ridges in the imaging are on the 174 µm thick sample Figure 6.10, with the thinnest sample being several years old embedded debris visible in Figure 6.9.

The S_q of the thickest sample of 5% is comparable to that of the thickest PDMS sample. And a comparable kurtosis suggests this result is viable for discussion.

While the kurtosis of the thinner samples is significantly larger, this may not be caused only by the carbon coating or observed surface debris. The roughness and surface properties of these coatings are tabulated in the appendix.

6.3.2 Water contact angle

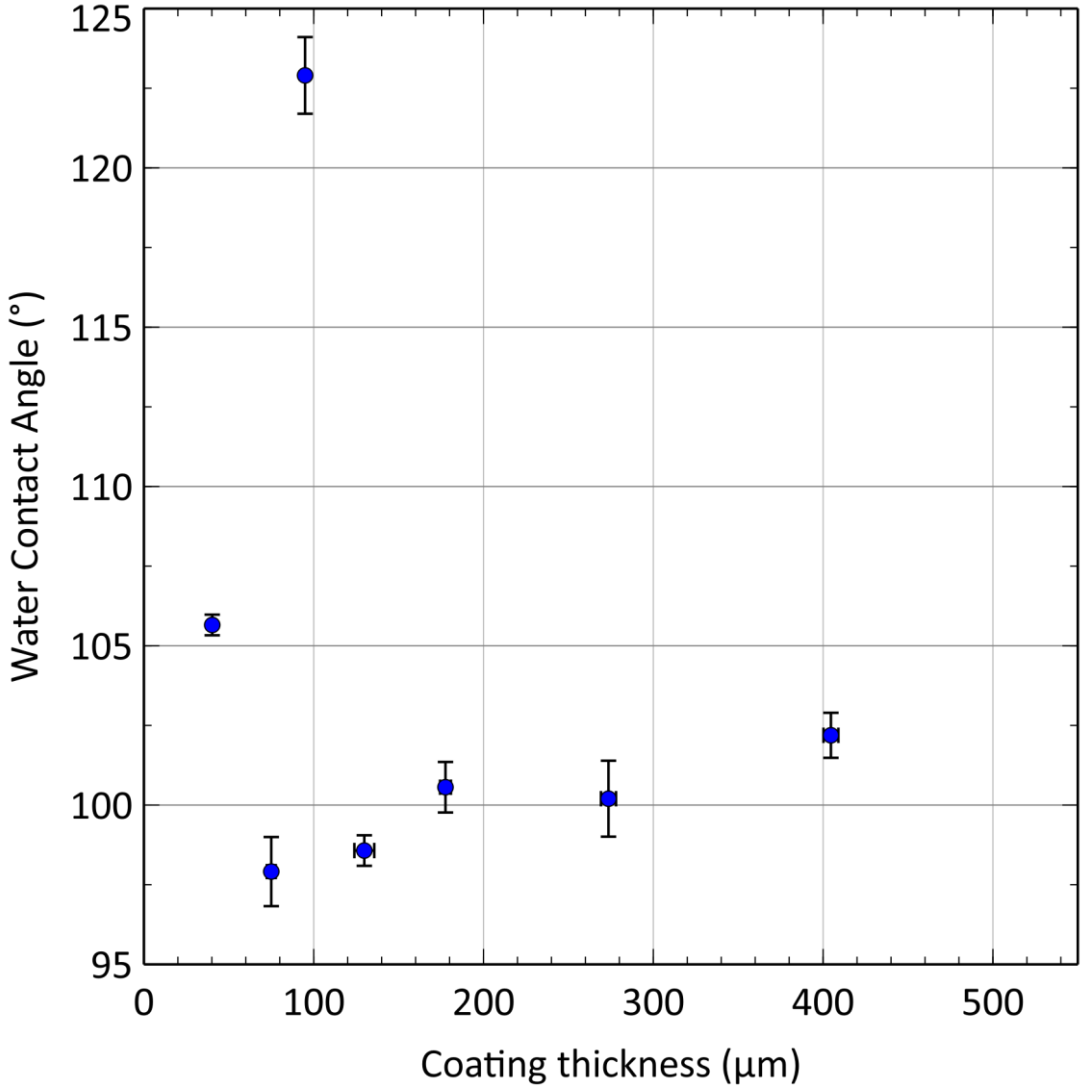

Figure 6.12 WCA of 5% SiC coatings.

Testing of samples several months old indicated no significant change in WCA with thickness, with the average being 100.1±0.4°. Fresh samples of 5% SiC PDMS coatings had a WCA of 105.7±0.3° at 40.2±0.8 μm and 122.9±1.2° at 94.9±0.5 μm, Figure 6.12.

6.3.3 Thermal diffusivity

The through-depth thermal diffusivity using 2.5mm thick samples was measured at $0.194 \pm 0.002\ \mathrm{mm}^2/\mathrm{s}$ with an in-plane thermal diffusivity of $0.441 \pm 0.021\ \mathrm{mm}^2/\mathrm{s}$. It was expected that some difference may be present here if any isotropic alignment was present. As the matrix polymer alone showed a difference between these two values, no meaningful conclusions can be drawn. If the value could be tuned to favour one plane over another, modelling could be utilised to design scenarios where surfaces are partially or entirely iced. Additionally, if the ice-facing portion of the coating had a much lower in-plane diffusivity but higher through-depth thermal diffusivity, this would impact the solidification of individual droplets and the efficiency of the electro-thermal de-icing system for a given filler content. Primarily, this measurement is important for predicting any difference in performance from the base polymer or other composites. The through-depth thermal diffusivity of the 5% SiC coating is 75% higher than that of PDMS, and the in-plane value is 54% higher than the PDMS alone.

6.3.4 Thermal de-icing

Testing the thermal de-icing of the PDMS composites to provide insight into the potential benefit of thermally conductive filler materials, *Figure 6.13* and Figure 6.14.

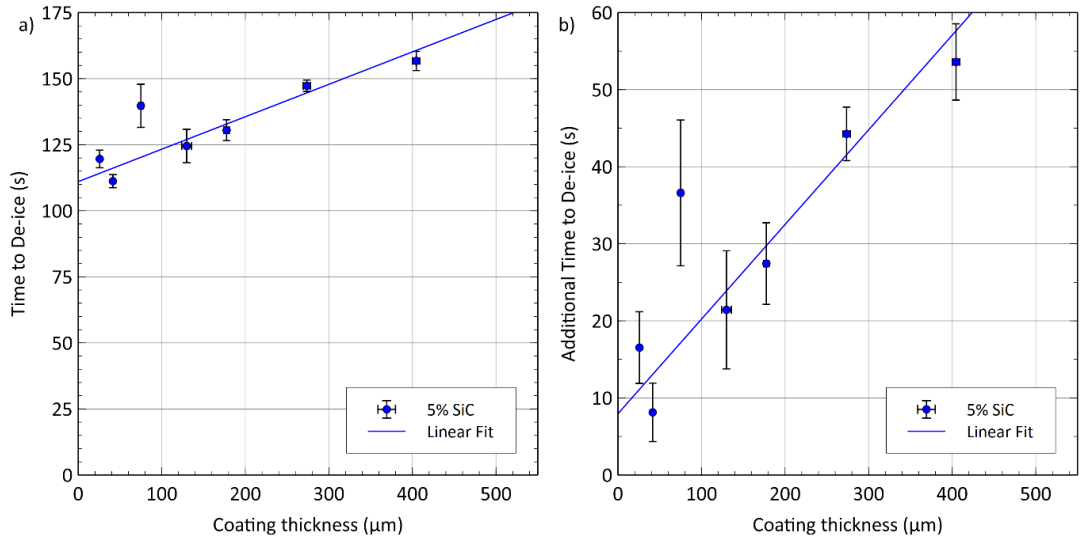

Figure 6.13 Static thermal de-icing of 5% SiC coatings a) time to de-ice b) adjusted time to de-ice.

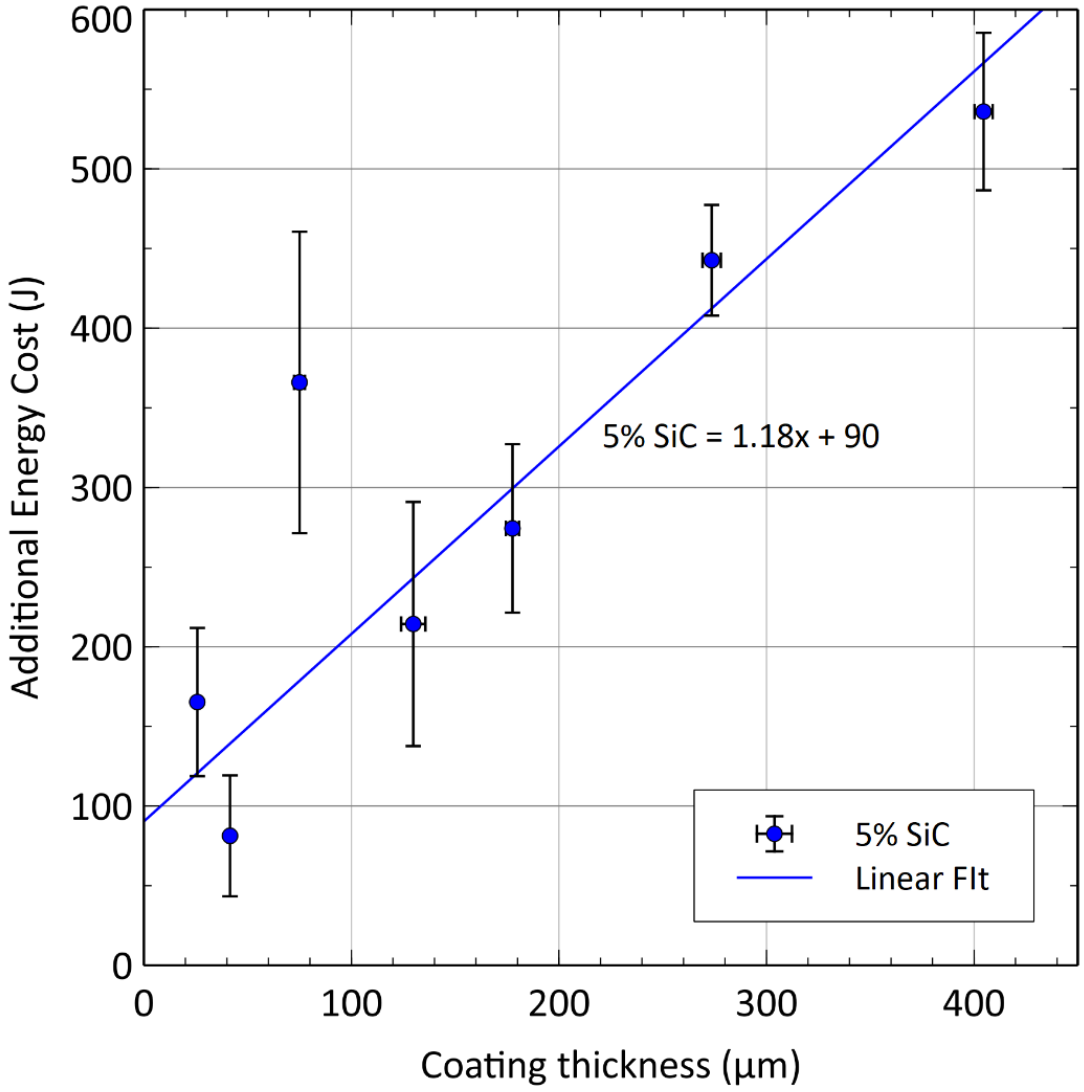

Figure 6.14 Energy cost to thermally de-ice a surface if coated with 5% SiC in PDMS

After adjusting the result to remove the de-icing cost of aluminium, the y-intercept is 90 J, indicating a large negative impact of the coating's surface properties compared to the increase for grit blasted aluminium, which was 34 J.

6.4 Diversifying filler content

As SiC fibres successfully increased the thermal diffusivity and reduced the per-thickness energy cost of de-icing of the PDMS a range of fibre inclusions was studied. Some coatings were also combined with carbon nanomaterials to consider whether the effect of the fibres could be augmented.

6.4.1 Roughness

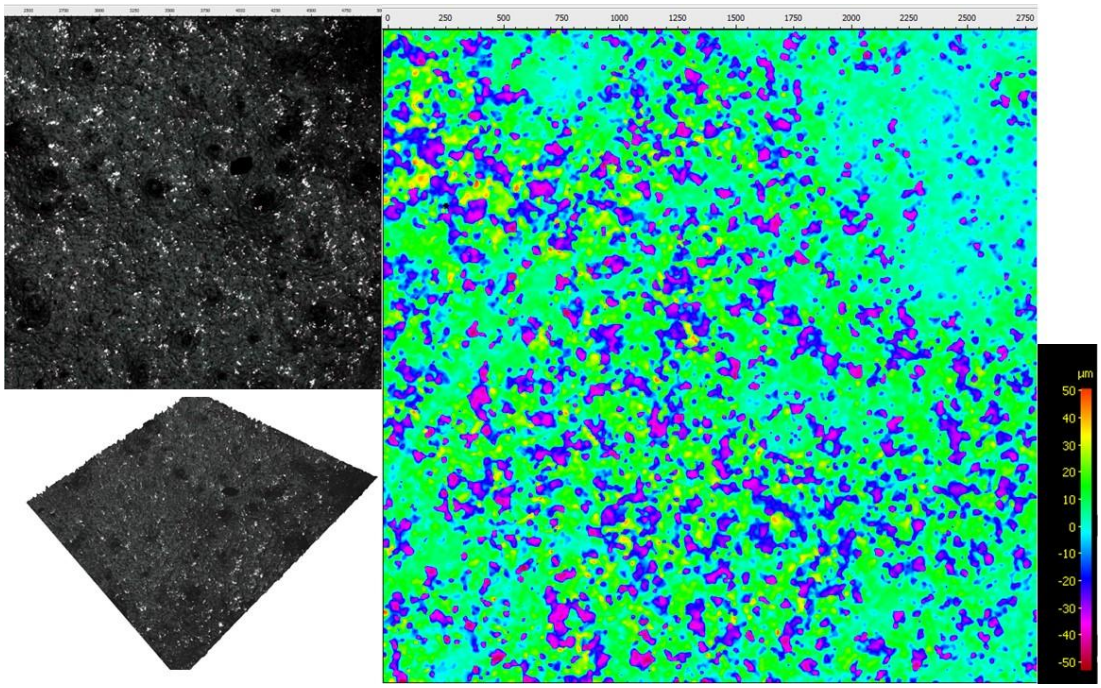

Figure 6.15 56 μm thick 10% SiC coating with areas where the substrate is visible.

The visible substrate in Figure 6.15 indicated that carbon coating was necessary for reliable measurements. The substrate appears as bright patches in the black-and-white image and pink in the filtered heat map. Carbon coating was also necessary for thin PDMS coatings due to its transparency in separating the surface from the substrate. Higher filler fractions did not remedy this issue, as seen in Figure 6.15.

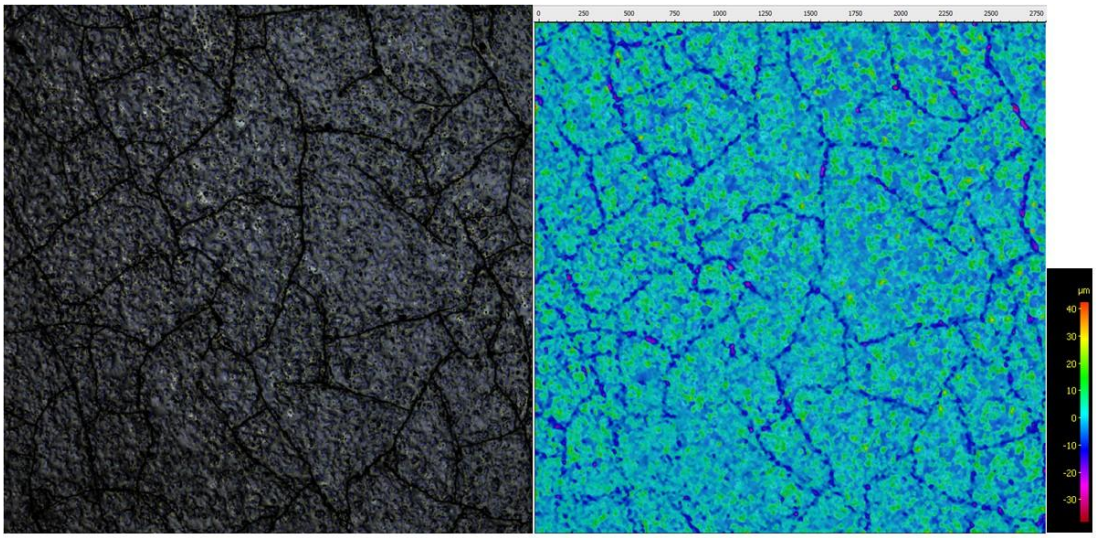

Figure 6.16 215 μm thick 10% coating with significant cracking of the carbon coating.

In Figure 6.16 there is visible cracking. However, unlike on PDMS, the ridges appeared to be lower than the surrounding material. It was observed that the higher the SiC content of the PDMS, the more susceptible to cracking of the applied carbon coating. The presence of this cracking, as in Figure 6.16 or visible substrate, such as in Figure 6.15, was used to remove the results from these samples from analysis.

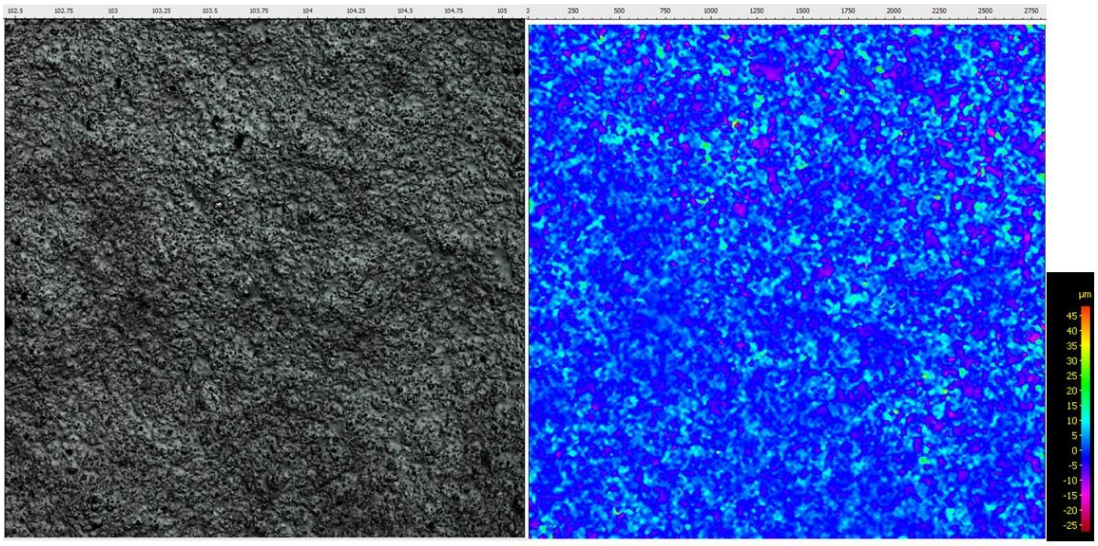

Figure 6.17 60 μm thick 10% surface with one thin layers of carbon coating.

Thin coatings of carbon were found to be less prone to cracking, however, in this example, Figure 6.17, a large range of heights was found, which may indicate some regions affected by transparency.

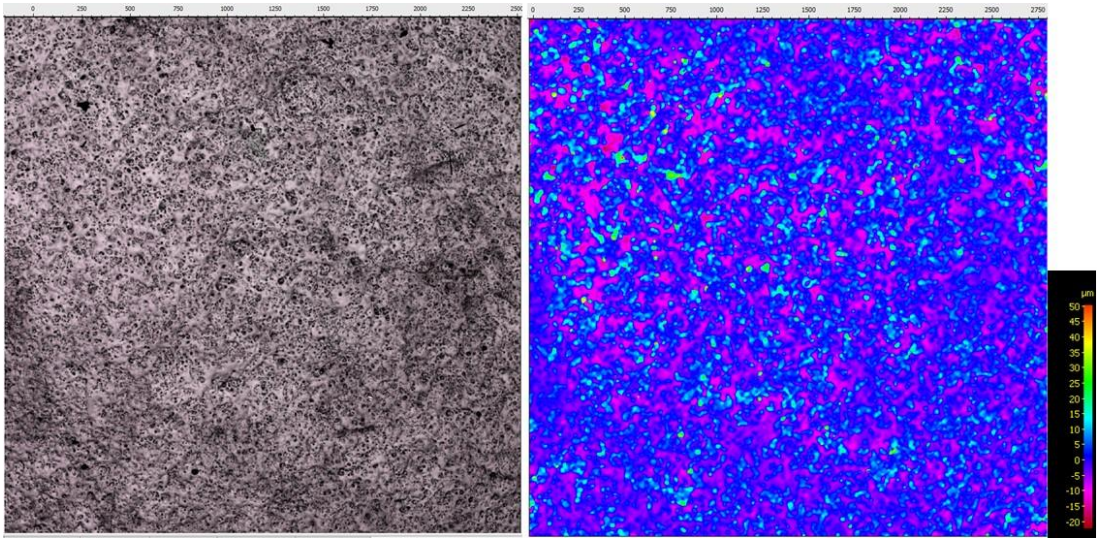

Figure 6.18 126 thick 10% surface with two thin layers of carbon coating.

Two light coats of carbon were applied to the sample in Figure 6.18, which showed no visible cracking but maintained the large range of heights observed in Figure 6.17.

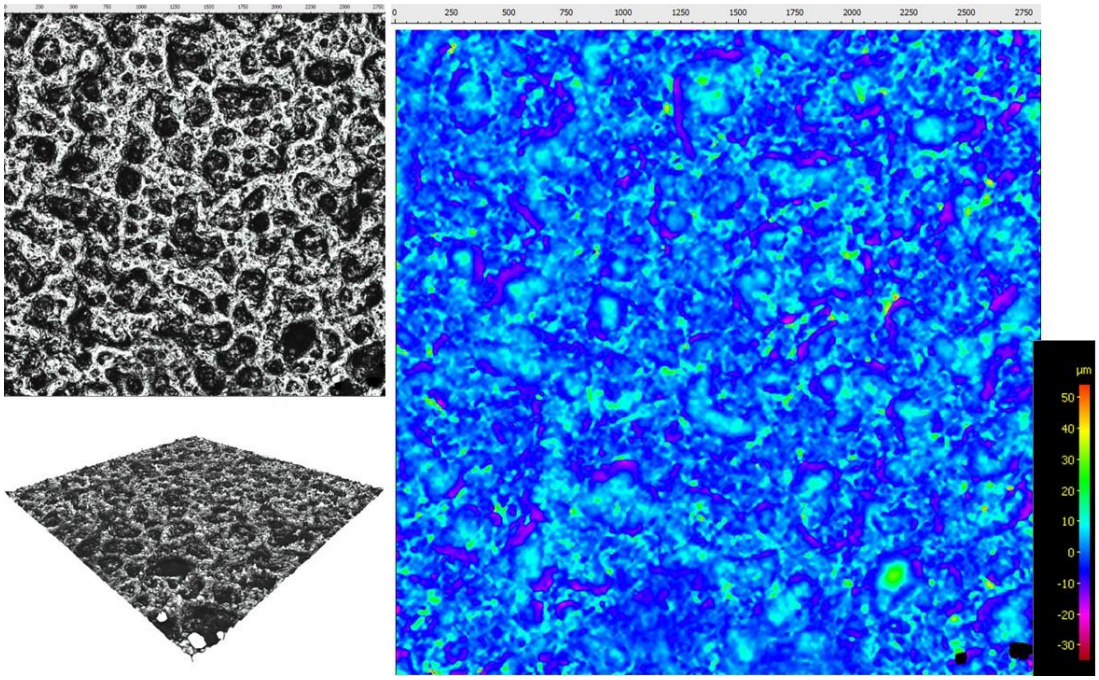

Figure 6.19 60 μm thick 20% coating with gaps in the data with a thin carbon coating and no visible cracks.

Coatings containing 20% proved very difficult to quantify due to apparent high porosity, with every capture containing some gaps, including when highly influenced by cracking of applied carbon.

All coatings measured have a higher kurtosis; however, due to a consistently higher roughness for all coatings compared to PDMS, this may mean that data obtained from captures with no visible cracking may be representative of the surface and suitable for analysis. With 10% SiC with a coating thickness of 126 µm having a r_a of 3.38$\pm$0.44 µm, and a 60 µm thick sample less rough with a r_a of 2.58$\pm$0.47 µm. This was unexpected as the thickness reduces it approaches the length scale of the filler, which could then impact the surface topography to a greater degree. A 60 µm 20% SiC coating was measured to have an r_a of 3.15$\pm$0.38 µm. This sample, shown in Figure 6.19, shows gaps in the data so it cannot be considered. However, it does pose a concern about the veracity of the data collected, as to both the naked eye and comparing the images in both Figure 6.17 and Figure 6.18, the 20% SiC sample was expected to be much rougher. This could be an artefact of inadequate characterisation of porosity at the surface of this sample.

6.4.2 Water contact angle

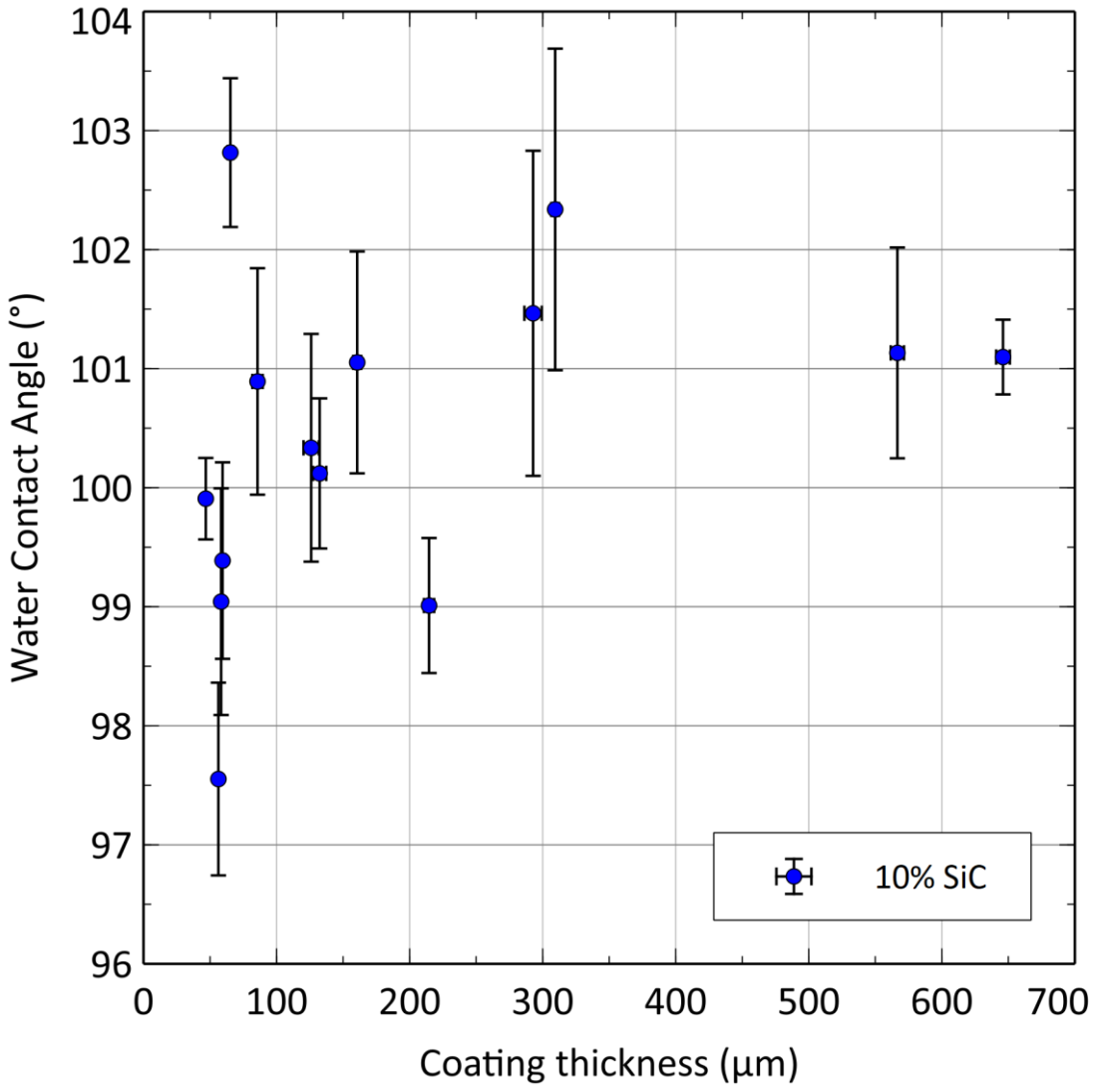

Figure 6.20 WCA 10% SiC in PDMS.

PDMS coatings with a higher fraction of SiC fibres showed no significant change in WCA with coating thickness however, the range decreased inversely with coating thickness, suggesting the surface finish becomes more consistent as thickness increases. The average WCA for 10% SiC in PDMS was 100.4±0.8°. The age of the samples at the time of testing was comparable to the range of thicknesses of 5% SiC in PDMS shown in Figure 6.12, which had a result of 100.1±0.4° showing no difference in hydrophobicity between the two fibre fractions or PDMS without any fibres, 99.6±0.4°.

1% SiC PDMS coatings made with a thickness of 48±0.5 µm and 343±9.9 µm achieved 107.6±0.6° and 130.3±1.1° respectively. The highest value measured for the thicker coating was 135.5°. The thicker of the two coatings were tested

when freshly made, while the thinner samples were several months old after several thermal de-icing tests. 5% SiC PDMS coatings of similar age and thickness to the 5% SiC PDMS coatings had a WCA of 105.7±0.3° at 40.2±0.8 μm and 122.9±1.2° at 94.9±0.5 μm.

6.4.3 Thermal diffusivity

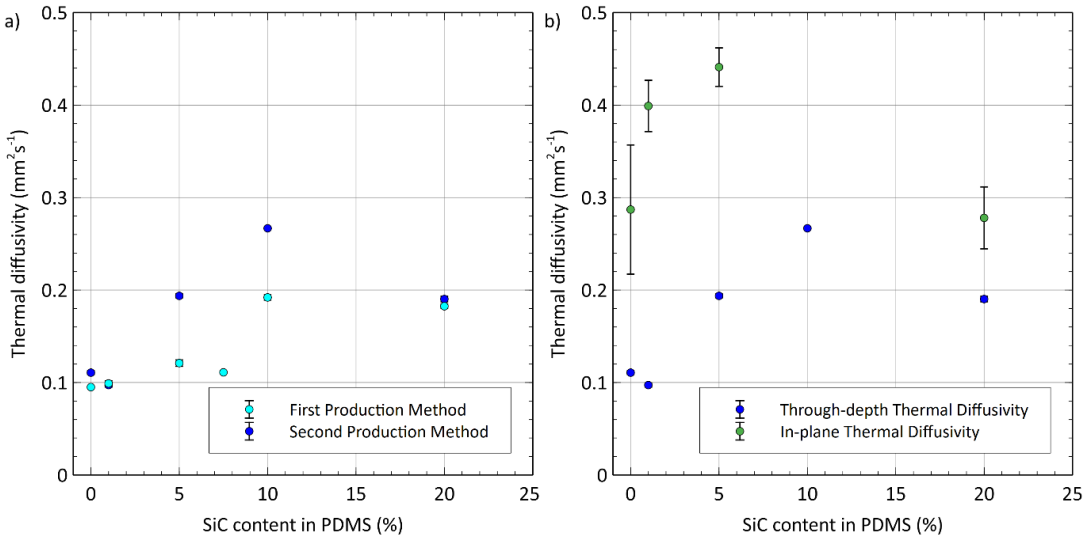

Figure 6.21 a) thermal diffusivity of SiC PDMS composite b) the anisotropic thermal diffusivity of SiC PDMS composites. The content is not wt%.

Increasing the fibre content led to an increase in thermal diffusivity up to 10% (8.3 wt% SiC), 20% showed a decrease towards the PDMS result. Usable in-plane values for PDMS and 10% PDMS could not be obtained to assess anisotropic thermal diffusivity. The most significant ratio between the thermal diffusivity between the planes tested was achieved by the 1% SiC in PDMS material. The highest in-plane value obtained was the 5% SiC in PDMS. There is a linear increase in the through-depth value of thermal diffusivity when increasing the fibre content up to 10% for this material geometry and manufacturing methods.

6.4.4 Electro-thermal de-icing

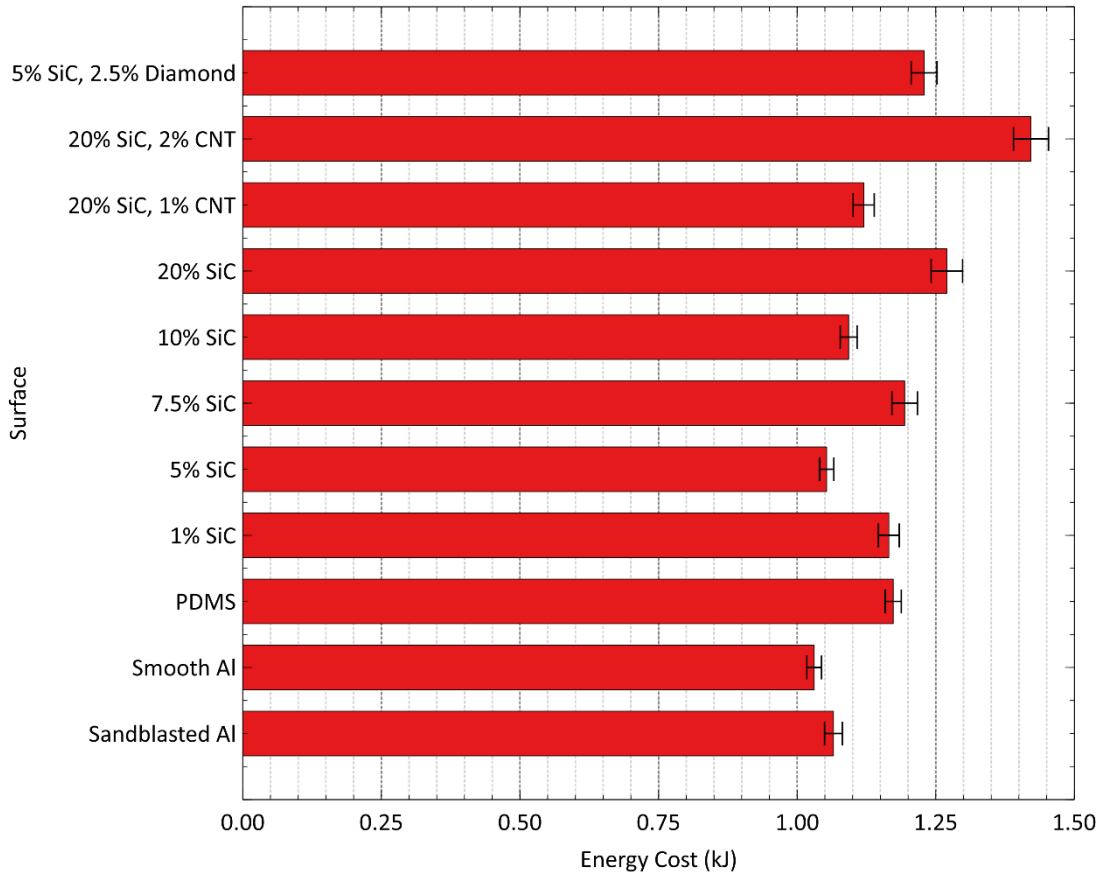

Figure 6.22 PDMS containing thermally conductive fillers and their respective thermal de-icing performance.

Combining carbon nanomaterials did not cause a noticeable reduction in energy cost, with some combinations showing a significant increase, which were not explored further in Figure 6.22. Further experiments after improving the manufacturing process produced a more reliable surface for higher fibre content material, 10% SiC in PDMS. The surface produced was visibly smoother and had a more consistent appearance that was more comparable to lower fibre content coatings. A range of thicknesses tested for static thermal de-icing indicated a less reliable trend between energy cost and coating thickness.

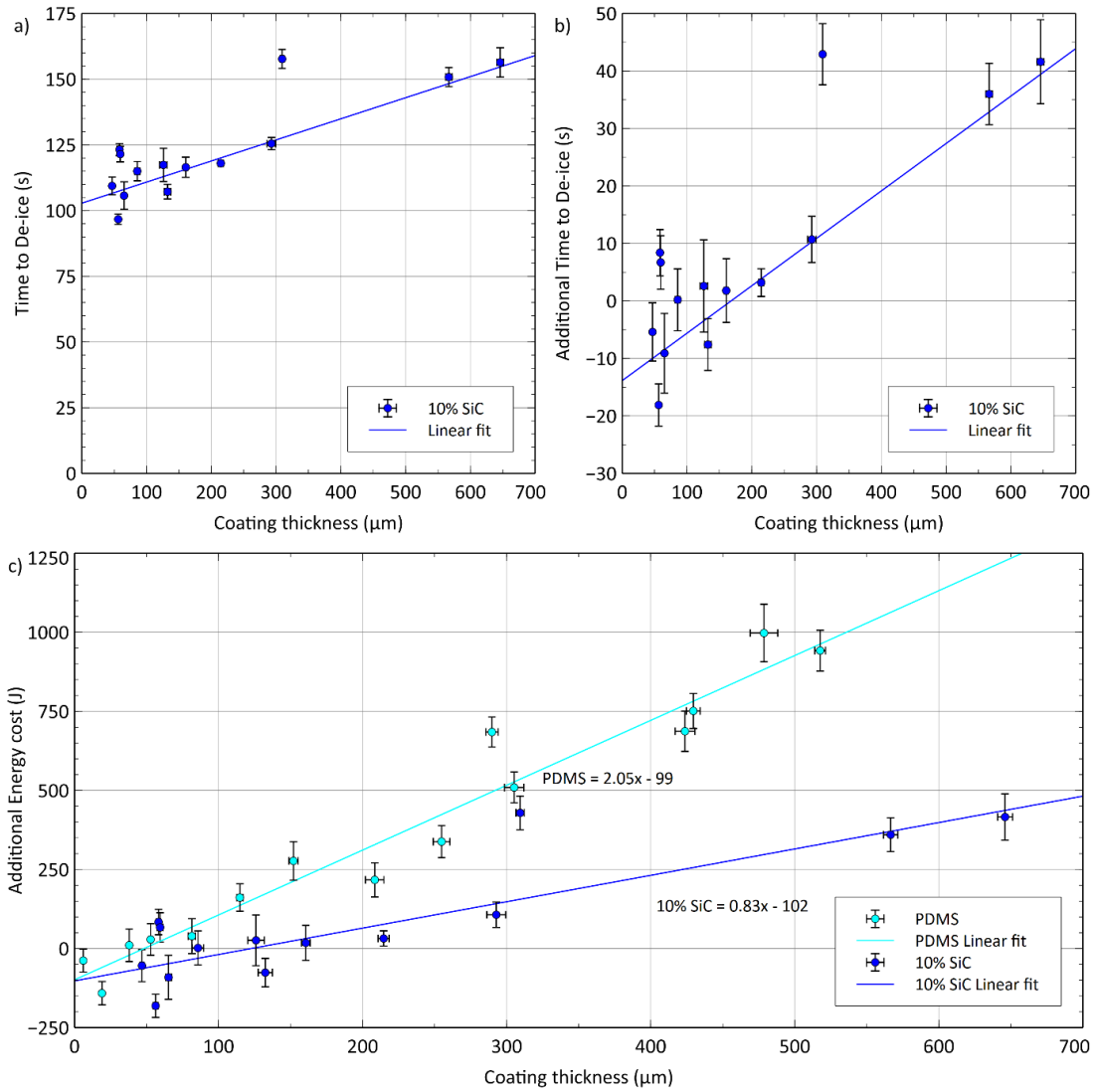

Figure 6.23 a) 10% SiC time to de-ice b) adjusted time to represent only the coating c) Comparing the adjusted result of 10% SiC in PDMS to PDMS.

Further studies indicated significant potential for energy saving with SiC inclusions reducing the increase of energy cost with coating thickness Figure 6.23 with the per-thickness cost of PDMS being 247% that of 10% SiC with a comparable y-intercept of -102 J Figure 6.23. Comparing the 10% SiC coatings performance shows a near-zero cost at a much higher thickness than PDMS without any fillers, using the gradient in Figure 6.23, up to 122 µm compared to 48 µm for PDMS. With the two samples between 200 and 300 µm thick having a normalised cost of less than 0.51 J/µm at the highest error bar. One sample with a thickness of 309 µm has a much higher cost at 1.39 ± 0.18 J/µm with the two thickest samples having a cost of 0.63 ± 0.10 and 0.64 ± 0.12 J/µm respectively.

6.5 Impact of the environmental temperature on the energy saving threshold

An important consideration when testing the thermal de-icing performance is the experiment's efficacy of utilising the power supplied to the heater to melt the ice. Much of the heat from the film heater will heat the surrounding structures holding the sample, which will be cooled in the cold environment maintained by active refrigeration to a chosen temperature. The difference in temperature between the surrounding air and the sample and the structures holding it will impact the rate of wasted heat loss and, by extension, the efficiency of that instance of de-icing. Increasing the environmental temperature from -20°C to -15°C reduced the time to de-ice aluminium from 114.8 s to 102.5±1.8 s (n=39), translating to a 123 J reduction in energy cost. Utilising a different grit-blaster, rough aluminium was de-iced in 100±2.3 s (n=23), remaining aged rough aluminium made using the previous grit-blaster de-iced in 90±0.9 s (n=27). Adjusted results in this section rely on the aluminium result as a reference of 102.5s.

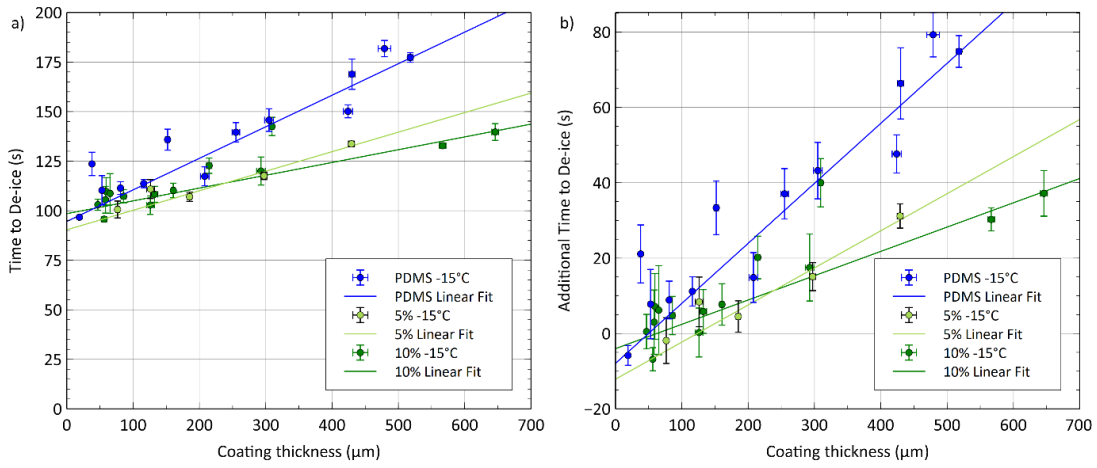

Figure 6.24 Static thermal de-icing in a -15C environment: a) the raw time result for PDMS, PDMS containing 5% SiC submicron fibres and PDMS containing 10% SiC submicron fibres; b) The de-icing results adjusted for the aluminium result.

Testing a PDMS coating with a varied thickness and SiC submicron fibre inclusions indicated that increasing the SiC fibre fraction reduced the additional energy cost incurred by increasing the thickness of the material as indicated by the 10% SiC material has the lowest gradient in Figure 6.24 a).

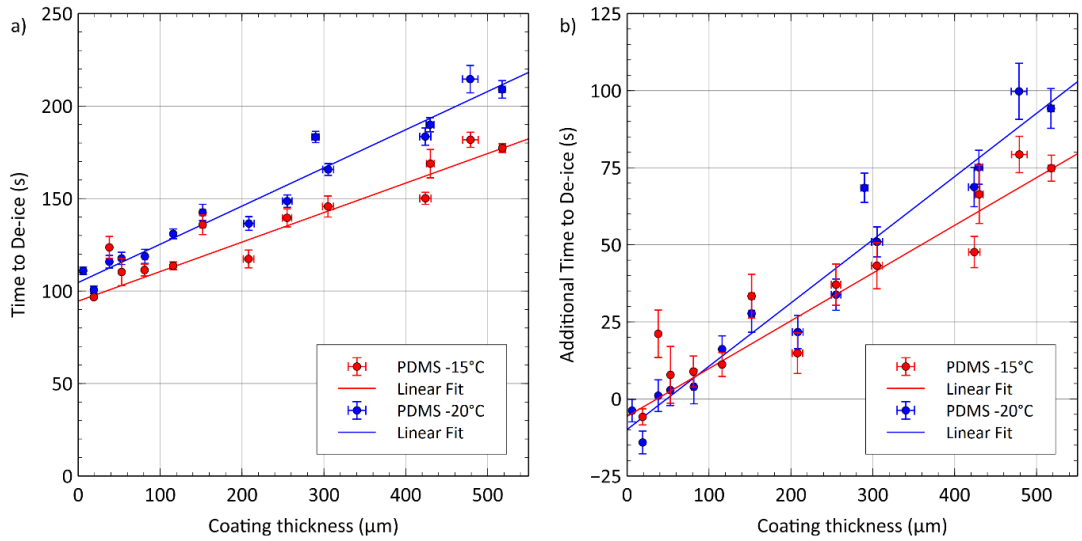

Figure 6.25 The impact of the de-icing energy cost of PDMS when changing the environmental temperature, a) time to de-ice, b) time to de-ice adjusted for their respective aluminium result.

The relative y-intercept of PDMS' line of best fit with an environmental temperature of -15°C, after adjusting for their respective aluminium result, is -5.6s compared to -9.9s for -20°C. with a gradient for -20°C of 0.20 $s/\mu m$ and 0.15 $s/\mu m$ for -15°C, which converts to 2 $J/\mu m$ and 15 $J/\mu m$ respectively, Figure 6.25.

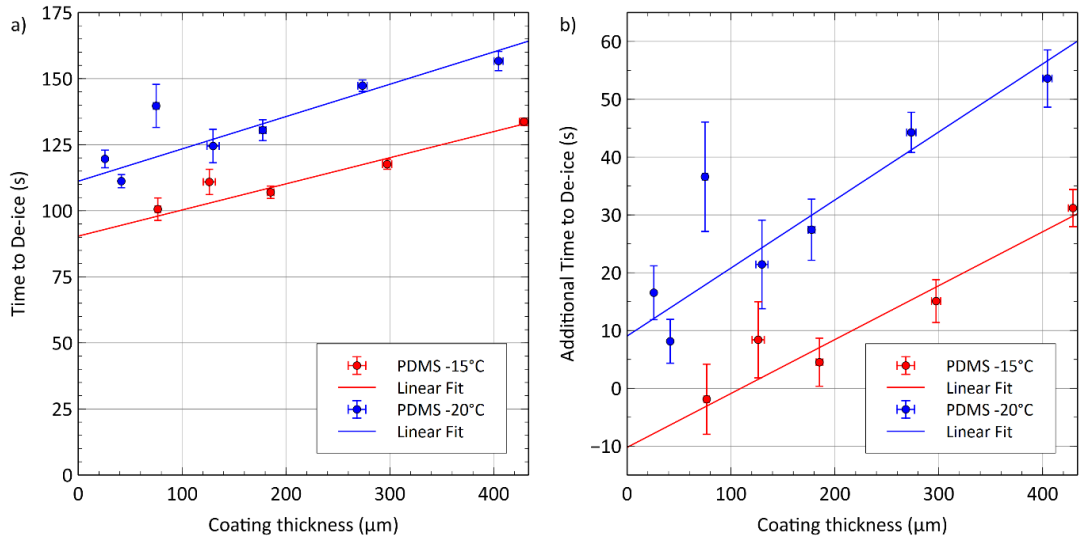

Figure 6.26 The impact of the de-icing energy cost of PDMS with 5% SiC when changing the environmental temperature, a) time to de-ice, b) time to de-ice adjusted for their respective aluminium result.

The y-intercept differs significantly when testing 5% SiC in PDMS, with the y-intercept changing from +9s to -10s when the environmental temperature is increased from -20°C to -15°C. As with PDMS, the warmer environmental temperature results have a lower gradient of 0.09s/μm compared to 0.12s/μm for -20°C, Figure 6.26.

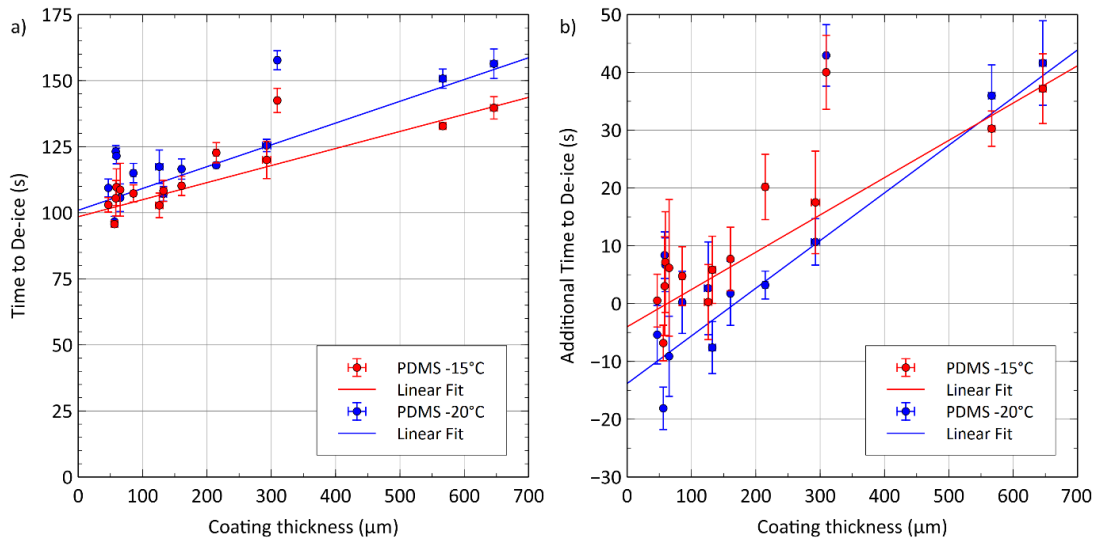

Figure 6.27 The impact of the de-icing energy cost of PDMS with 10% SiC when changing the environmental temperature, a) time to de-ice, b) time to de-ice adjusted for their respective aluminium result.

10% SiC achieved the lowest gradients of 0.06 s/μm and 0.08 s/μm for -15°C and -20°C respectively, Figure 6.27. However, unlike PDMS and 5% SiC in PDMS, the y-intercept is significantly lower in colder environments, with -10s compared to -3s. Comparing the performance of PDMS at both temperatures showed that reducing the environmental temperature from -15°C to -20°C increased the per thickness energy cost of the coating by an average of 31% for the respective average of all samples over 400 μm from 1.39 J/μm to 1.82 J/μm.

6.6 Discussion

6.6.1 The influence of surface properties on thermal de-icing energy costs

The area iced in unloaded thermal de-icing is $2.25 \times 10^{-4}\mathrm{m}^2$. Assuming the latent heat of melting is $336\ \mathrm{kJ/kg}$ and the specific heat of ice as $2.108\ \mathrm{kJ/kgK}$, the glaze ice used has a density of $900\ \mathrm{kgm}^{-3}$, and water $1000\ \mathrm{kgm}^{-3}$, if a $100\ \mu\mathrm{m}$ melt layer on a flat surface must form for the ice to detach at the environmental temperature is $-10°\mathrm{C}$, Figure 6.28, then the minimum energy consumption can be calculated using the following equations (17)(18), where V_{ice} is the volume of ice, $A_{interface}$ the area of the ice-surface interface, L_{ml} the depth of the melt layer, ρ the density of each respective phase, E the energy cost, $L_{melting}$ the latent heat of melting, ΔT the temperature difference between the melting point and the starting temperature and C_p the specific heat capacity of glaze ice.

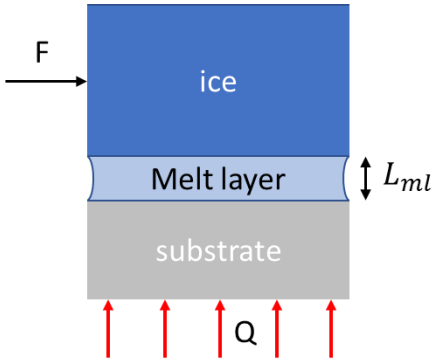

Figure 6.28 The simplest thermal de-icing scenario with the force, F, representing drag or the weight of the ice and Q the heat flux supplied by the heater.

$$V_{ice} = A_{interface} \times L_{ml} \times \frac{\rho_{water}}{\rho_{ice}} \tag{17}$$

$$E = V_{ice} \times \rho_{ice}(L_{melting} + \Delta T \times C_p) \tag{18}$$

Then, the energy cost of forming a $100\ \mu\mathrm{m}$ melt layer is $0.008\ \mathrm{kJ}$ for this de-icing experiment. A Boeing 787 has a total wing area of $377\ \mathrm{m}^2$Only the leading edge requires thermal de-icing systems that consume 45 to 75 kW to raise the surface temperature to the range of 7.2°C to 21.1 °C. If roughly 5% of the wing area is

considered the leading edge at 20 m^2Then, the energy required to form the melt layer alone amounts to 700 kJ, or 16 seconds of operation of the thermal de-icing systems. At 45 kW for every 100 $\mu\mathrm{m}$ increase in the depth of the melt layer, it does not account for environmental cooling during this time. Optimising the surface of the leading edge to minimise the depth of the melt layer is a potential method to reduce the lifetime energy consumption of thermal de-icing systems while potentially reducing the instances of icing, producing further energy savings. Reducing the time to de-ice and the frequency of icing instances also improves flight safety. This chapter considers the relative impact of the surface properties that impact the depth of this melt layer and the coating's thickness and material properties, highlighting how full consideration of both must be explicitly applied to the design application.

Surface roughness is often referred to as only the r_a which is quite uninformative about the surface. Figure 6.29 highlights an example seen where the aged rough aluminium had through wear a flattening of the peaks leaving mostly troughs seen in Figure 6.2 and the result of thermal de-icing with an -15°C environment was 10 seconds faster, 90$\pm$0.9 s, than the newer sandblasted aluminium made with a different blast media, described in section 4.1, which de-iced in a comparable time to the as-received aluminium 100$\pm$2.3 s and 102.5$\pm$1.8 s respectively. It is worth noting that the depth of the melt layer is a proxy for its volume, which could be considered in two parts of the layer, which are clear of asperities and between asperities.

For this reason, measuring the surface roughness using bearing parameters may the best option for future thermal de-icing research as r_a or S_a alone is clearly inadequate. Looking at the rough aluminium surface. It has an S_a twice that of the aged, sandblasted surface and 50% more than the as-received aluminium. All values are tabulated in the appendix. Yet the new sandblasted surface performed very similarly to the smooth aluminium which has an S_a of roughly 25% higher than the old, sandblasted surface. With the S_a of aluminium, sandblasted aluminium and old sandblasted aluminium being 1.25, 1.99 and 0.96 $\mu\mathrm{m}$, respectively. The r_a values for these surfaces were found to be 1.00, 1.41 and 0.77 $\mu\mathrm{m}$ respectively. The ratios of the values are not quite the same with the S_a proportionally larger than the r_a when comparing the increase from aluminium to sandblasted aluminium. Factors that will impact the friction and adhesion of adhered ice with the interface melting will include the skew of the profile, as with the old, sandblasted surface having a heavy negative skew, confirming that its roughness was valley dominant.

The r_{sm} describes the distance between asperities which was higher for both the sandblasted aluminium's but with a higher error on the old, sandblasted surface than the other two surfaces. More regular features are likely to increase the

measured roughness, however, the severity or size of the asperities may have a disproportionate impact that the r_a or S_a does not account for. The kurtosis sheds some light here as the recently sandblasted surface has a r_{ku} of 2.92 $\pm$ 0.45 µm, under 3, implying the roughness features are not tail-heavy in the distribution while the aluminium and aged sandblasted aluminium had a r_{ku} of 3.70 $\pm$ 0.87 and 4.77 $\pm$ 2.43 µm respectively. Showing that the valleys that were common shown by the skew were relatively very deep as the distribution of the height at each measured point was much more tail-heavy for the aged, sandblasted surface. Similarly, the S_q, or r_q, describing the root mean square of the profile is provides more utility for mathematical modelling or lubricant and film thickness predictions than the r_a Which only provides a general idea of the roughness and not the topography.

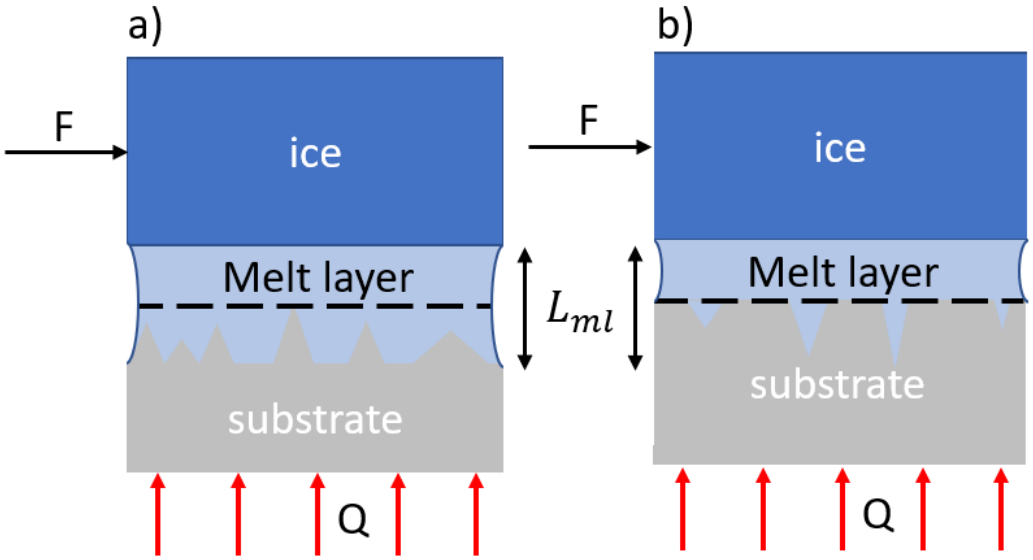

Figure 6.29 Surface roughness increases the surface area for Van der Waals with a) showing a positive skew and b) a negative skew.

If the melt layer being produced has yet to clear all asperities, some shaped features may be more prone to limiting adhesion failure than others, as a much thicker melt layer is required to clear or initiate cracks more readily, Figure 6.30.

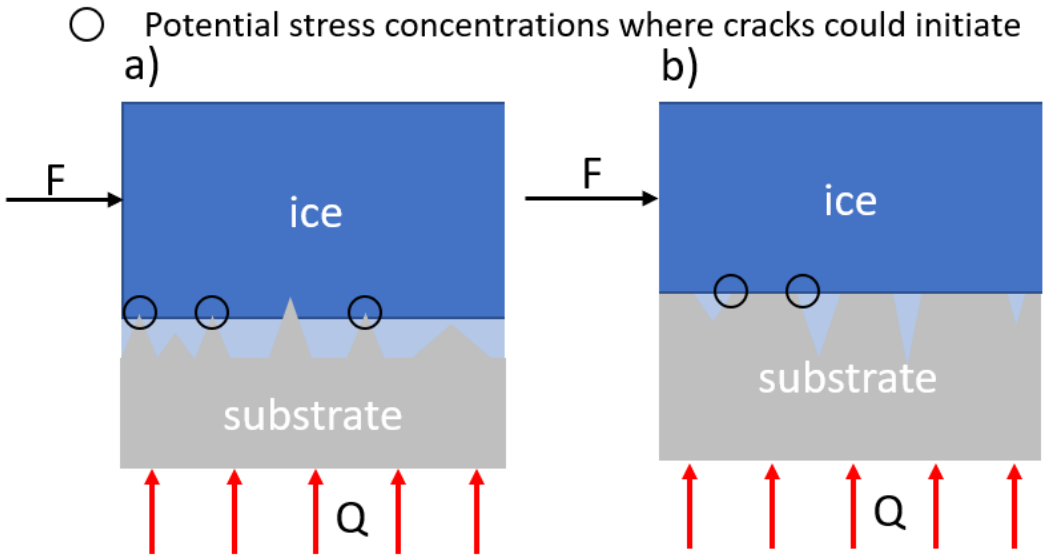

Figure 6.30 The shape of the roughness may determine how thick the melt layer must form above the average surface height or the highest asperities, this figure shows a) positive skew and b) negative skew and potential areas for crack initiation.

The S_{dq}, the root mean square of the gradient, could provide value by selecting for a surface with smoother asperities to minimise the mechanical interlocking of ice. Potentially, the most valuable 2D parameter is the S_{dr}, describing the percentage increase of the surface area from the projected, flat area being measured to the surface. An increase in this area provides an increase in Van der Waals forces between both water and ice with the surface. For thermal de-icing, it would present itself as a thicker melt layer to overcome the surface tension of the water in the film, where a more hydrophobic, lower surface energy, surface with a lower S_{dr} would shed more readily.

A hydrophilic surface will retain more of the melt layer than a hydrophobic surface. If any residual water is left behind, a lower surface energy material will exhibit greater hydrophobic properties, reducing the dwell time of the water. As it is more likely to be shed from the surface, reducing the window of opportunity and, therefore, the probability for it to refreeze. For a Young's model of wetting, the footprint of the droplet reduces the area available for heat transfer for the latent heat of freezing once the thermal de-icing system is switched off and the surface cools. Reducing the potential maximum heat flux and increasing the time of freezing. If the water angle is high, causing the water to bead up into droplets, the water now has a higher exposed surface area that could aid in the shedding of the water via airflow when compared to a flatter film. If the water remains on

the surface as a flatter film, the possibility of supercooled water striking the remaining melt water and nucleating is higher.

Ideally, if the initial interface contains no air, the melt layer would move through a transitional state of wetting to a Cassie-Baxter state as the ice slides along the surface if it is rough rather than remaining in a Wenzel state. If a change in wetting state occurs for a sufficiently hydrophobic surface, it will promote faster post-melt shedding. If the wetting state transitions in this way, any water formed will be shed more easily as less water will be left behind as the relative hydrophilicity of the ice compared to the surface will be higher. Any remaining residue in a wetting state with minimal solid-liquid contact will have a greater propensity to be stripped from the surface by the airflow. Furthermore, the further the ice and melt travels on the surface before shedding, the larger the area that runback ice can form and the potential distance of this ice from the heating element. It is, therefore, important to reduce the volume of melt produced as the liquid will have a greater propensity than ice to run over the camber of the aerofoil rather than detach in the flow.

If the ice initially formed from water in a transitional or Cassie-Baxter state, there is a mixed interface between the ice and the substrate due to air pockets. In a Cassie-Baxter state, the area of ice in solid-solid contact will be less than that in a Young's model. Reducing the volume of ice that must be melted for it or be shed. Reducing the time and energy required to operate the de-icing system, along with the volume of meltwater produced which, reduces the risk of runback ice due to less capillary pressure overall and a lower risk of residue left behind at the melting site or deposited if the ice travels along the surface before shedding. A clear drawback would be the poor thermal conduction of air, which limits the heat flux, which would be most notable for high aspect ratio asperities.

6.6.2 Unloaded thermal de-icing of PDMS and PDMS composite coatings

Testing a range of thicknesses allowed the assessment of the bulk materials' properties on the resulting performance, and comparisons to the aluminium provided a relative improvement or cost associated with the surface properties by interpolating the y-intercept at zero thickness. This method can be used using different equipment to assess relative performance where the gradient represents a per-thickness energy cost of the material in that environment and the surface compared to aluminium. For replication, another researcher could use PDMS and aluminium to reference this or any other work by accounting for

equipment and procedural differences affecting the proportional change between materials. Adding a second material, such as polyurethane coatings or thicker aluminium, would allow for the relative scaling of results between laboratories. As some coatings may be made in such a way that thermal diffusivity measurements are challenging to obtain this testing can be done more thoroughly and compared to database values. Using a second environmental temperature, as in section 6.5, can also improve comparisons between laboratories, as the changes in results can be used to infer the relative environmental heat loss of the heater in each piece of equipment. PDMS, 5% SiC and 10% SiC coatings were all 25% cheaper to de-ice at -15°C than 20°C. As coatings became thinner, with or without filler content, the data became noisier, showing the lack of reliability for this material and the coating methods used for thicknesses below 50 – 100 μm depending on the material, with no filler content coatings less sensitive.

A higher thermal diffusivity reduced the gradient, which represents a lower per-thickness energy cost of the coating material as the temperature of the coating changes more rapidly. This is imperative over thermal conductivity alone as a slow temperature response will be linked to a higher volumetric heat capacity with the optimum value as close to zero as possible. So that the proportion of energy supplied by the heater that is used to raise the temperature of the coating is minimised and, as much as possible, it raises the temperature of the interface with the ice. This improves the heater's response time and cost in conjunction with a coating. Of course, this must be considered alongside the context that it will increase the likelihood of nucleation and the accretion's initial rate of growth.

This property would be important when designing a coating for an application as geometric constraints and performance requirements will be present. Testing a 100μm coating and comparing its improved performance to a thicker coating is a trivial achievement unless producing a thinner coating was desired and previously unobtainable while maintaining its properties.

Figure 6.23 highlights the importance of these considerations. The performance of each material being better or worse was primarily a gamble between the quality of the coating and surface of each material and whether the increased thermal diffusivity of the 10% SiC coatings was sufficient to overcome the variable performance of each sample below 100 μm. The y-intercept suggests the surface properties of the PDSM were superior, which was expected as any filler has the potential to increase the surface roughness or be exposed, changing the surface energy for the worse. For applications with a higher thickness requirement or tolerance, 10% SiC was 60% cheaper than PDMS, while a thinner coating will always perform better, all else equal, this may be desirable where the coating production method is more reliable at higher thicknesses or the

durability allows less frequent maintenance and reapplication. If the coating could be made into a tape capable of being applied to a helicopter's erosion shield, a thinner coating would allow for a doubling of layers applied to suit the blades' needs but would likely increase thermal resistance vs one thicker coating. If the material is relatively fragile, any tearing or fraying of the edge of the tape would limit its effectiveness or may make the application more laborious, as ineffective application would increase risk.

If a coating is designed to work in a passive and active manner, this chapter highlights the importance of balancing these factors where appropriate.

Minimising any thermal resistance at the substrate-coating interface can largely be controlled by altering manufacturing procedures. To consider interstitial media between the coating and substrate, such as gaseous pockets, dust, grease, or if the substrate may form a less conductive coating by oxidation, ensure that the coating is strongly adhered to the substrate. It would then follow that the coating-ice interface should minimise voids, trapped gas or dust so as not to bottleneck the potential heat flux from the coating.

Minimising the heat energy required to raise the temperature of the coating can be done by reducing the thickness of the coating, thereby the volume of material to raise the temperature. If the required dimensions of the coating are fixed, two material properties can be considered. The specific heat and the density of the coating material. If the specific heat and density of one icephobic material is lower than another with a comparable thermal conductivity, it will be more efficient at thermal de-icing. As the rate of heat transfer is similar but the energy needed to raise the temperature of the coating is less, as its volumetric heat capacity is less, it will begin melting any adhered ice sooner as the temperature of the coating rises faster. Selecting suitable materials based on thermal properties of a high thermal conductivity and a low volumetric heat capacity would be selecting materials with a high thermal diffusivity.

6.6.3 Surface roughness of composite coatings

The carbon coating provides an approximation of the roughness values when done with care, using multiple coats each with a low deposition. Minimising the risk of uneven distribution and features, thought to be produced as the sample's surface cools and the carbon layer contracted slower than the underlying polymer, which produced ridges in the carbon. The 5% coatings were found to have a roughness comparable to that of aluminium and PDMS. The higher fibre fraction coatings were significantly rougher with the S_a values at least double that

of the aforementioned surfaces and a consistently positive skew. This could be from the fibres present near the surface, with heavier carbon coatings having a much higher S_{dr}, reaching 72% in one case. This factor was not significantly different between the 5%, PDMS and aluminium surfaces with and without CC. The S_{dg} are comparable suggesting the features are not more jagged or abrupt in geometry. As the water contact angle was reasonably consistent across the range of thickness tested it is reasonable to assume that the surface properties were too.

6.7 Summary

Testing icephobic coatings for their electro-thermal de-icing capability will be imperative for some applications and likely common practice for early adopters to ensure that safe operation is maintained. Using PDMS as an example of icephobic material, the electro-thermal de-icing energy cost has been segmented into two portions. The impact of the surface properties is that they determine the point of adhesion failure. The cost of sufficiently raising the temperature of the bulk material of the coating. The former can be analysed with a comparable approach to passive icephobic solutions, considering surface energy and topography and their respective impacts on hydrophobicity and icephobicity. The latter is dependent on the material's thermal diffusivity. Great care must be taken when designing a coating that must function passively and alongside an electro-thermal de-icing system, as improving the performance in one area could drastically impact the performance in the other. For example, limiting latent heat transfer of freezing through the coating will delay nucleation and reduce the rate of accretion growth. It will also limit the efficacy of the electro-thermal de-icing system, possibly prohibitively so.

The properties identified have been described to allow the use of different equipment for qualitative comparison of different coatings if enough contextual information is present to calibrate relative trends, measure meaningful differences, and diagnose the specific area of improvement, where the energy saved due to the surface properties, additional energy cost per unit thickness, and change in energy cost concerning the environmental temperature allows a holistic view of performance.

PDMS in section 6.2.4, Figure 6.7, showed that with a low-thickness icephobic coating, the energy required to de-ice the substrate was reduced compared to that of aluminium. Increasing the thickness of the coatings produced a linear increase in the energy required to de-ice the surface, as expected. Adding silicon carbide as a filler material at 8.3 wt% reduced the per-thickness energy cost of

the PDMS by 59%, Figure 6.23, with a comparable y-intercept suggesting comparable surface properties, Figure 6.7 b).

Chapter 7: Ice adhesion strength and dynamic electro-thermal de-icing with an applied load

The static electro-thermal de-icing covered in the previous chapter does not account for passive de-icing performance through ice adhesion testing or electro-thermal surface de-icing while shear stress is applied to the surface-ice interface. Additionally, cooling from the airflow that would be present in a dynamic application limits the electro-thermal de-icing system's capability, and the icephobic coating's efficacy is affected by the added load and environmental cooling.

7.1 Ice adhesion testing

Due to a significant gap in experimental research into testing electro-thermal de-icing with a mechanical load present. Small-scale de-icing of an order of magnitude of a few cm^2, the largest tested here being 2.25 cm^2, became the primary focus of the work presented here to limit the complexity and cost of the testing with no influence of interfacial toughness affecting the results. The intention is to extrapolate from ice adhesion testing of icephobic surfaces, a primary focus in the field [12][62], to a new iteration of de-icing experiments. The aim is to study more complex, more applicable operational requirements with the consideration of engineering structures in a de-icing scenario. Replication and improvements upon this type of testing would then provide important information before applying what is learnt to larger-scale experiments of this kind. As such, interfacial toughness was not measured for any tested surface, and all de-icing was completed at a scale where ice adhesion strength is the most relevant property for mechanical de-icing.

7.1.1 Pull test

The surfaces investigated were as detailed in section Developed coatings4.3.1, Table 4.1. Specifically, they were uncoated aluminium substrates as received, and with a sandblasted surface, PDMS containing no filler and PDMS containing SiC fibres denoted 1% and 5%. Each coating was tested at two different thicknesses, which are detailed within Figure 7.1.

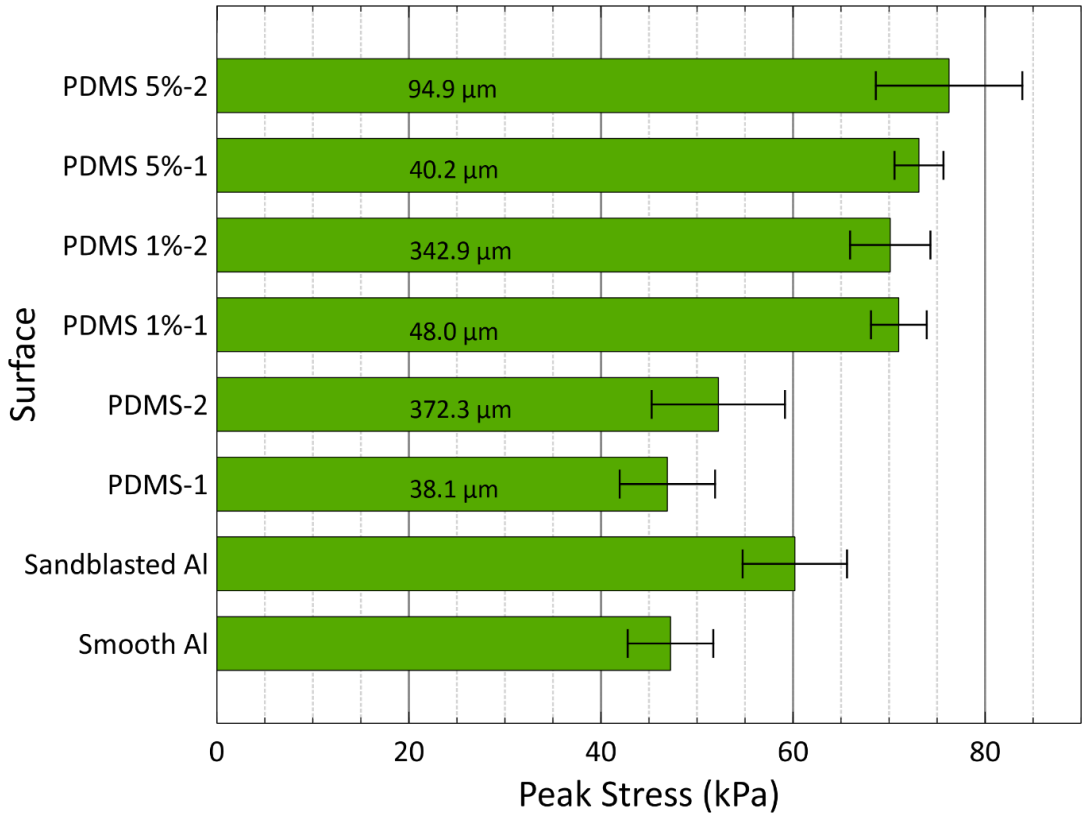

Figure 7.1 Pull test using a stepper motor and harness using the cold box for the thermal de-icing test, converting the peak force measured directly to the stress at the interface at adhesion failure. Coatings denoted with 1 are thinner than the coating of the same material denoted with 2. Each coating's thickness is labelled on the respective bar.

The pull test indicated that the sandblasted aluminium has a noticeably higher ice adhesion strength than the smooth aluminium, which is in line with current literature [49], suggesting a higher surface roughness is indicative of an increased ice adhesion strength due to mechanical interlocking of the surface and ice. PDMS and PDMS containing SiC submicron fibre were also tested at different thicknesses, each of which was respectively different. PDMS containing no filler performed comparably to aluminium, with the thicker PDMS-2 coating showing no significant difference between smooth and sandblasted aluminium. All SiC-containing PDMS performed significantly worse than aluminium, with no discernable difference between the filler fraction and coating thickness.

7.1.2 Centrifuge adhesion test (CAT)

The ice adhesion strength of the surface at -10°C was tested by calculating the inertia of adhered ice from the velocity at the point of adhesion failure. From this, the stress at the interface can be inferred. The procedure details can be found in the methodology section 4.8.2. The coated samples tested are listed in Table 4.2, with the respective thickness for each coating. These samples are not the same samples as those tested in the pull test and are named differently despite their similarity. Uncoated aluminium surfaces were also tested. Smooth aluminium produced a result, as displayed in Figure 7.2, with the coated samples results, while no result could be obtained for sandblasted aluminium. As every sample failed cohesively, the adhesion strength could not be obtained. The iced area was 1.38 cm^2 with the centre of mass of the ice alone 2.6 mm above the surface and the mass the sum of the ice and mould, the true centre of mass was assumed to be at most 0.5 mm higher than this value with the mould thickness roughly 1 mm and mass of the mould 0.7 g to the ice's 1.3 g. This is a worst-case estimation and certainly an overestimation for the geometry used of an elliptical hemisphere with a contact area of radii 5.5 mm and 8.5 mm and a height of 7.1 mm calculated using the known volume of 1.3 ml. With this shape skewing mass towards the surface and the mould marginally thicker at the base, the height of the centre of mass for this experiment and the dynamic thermal de-icing test in section 7.2 is assumed to be around 3 mm.

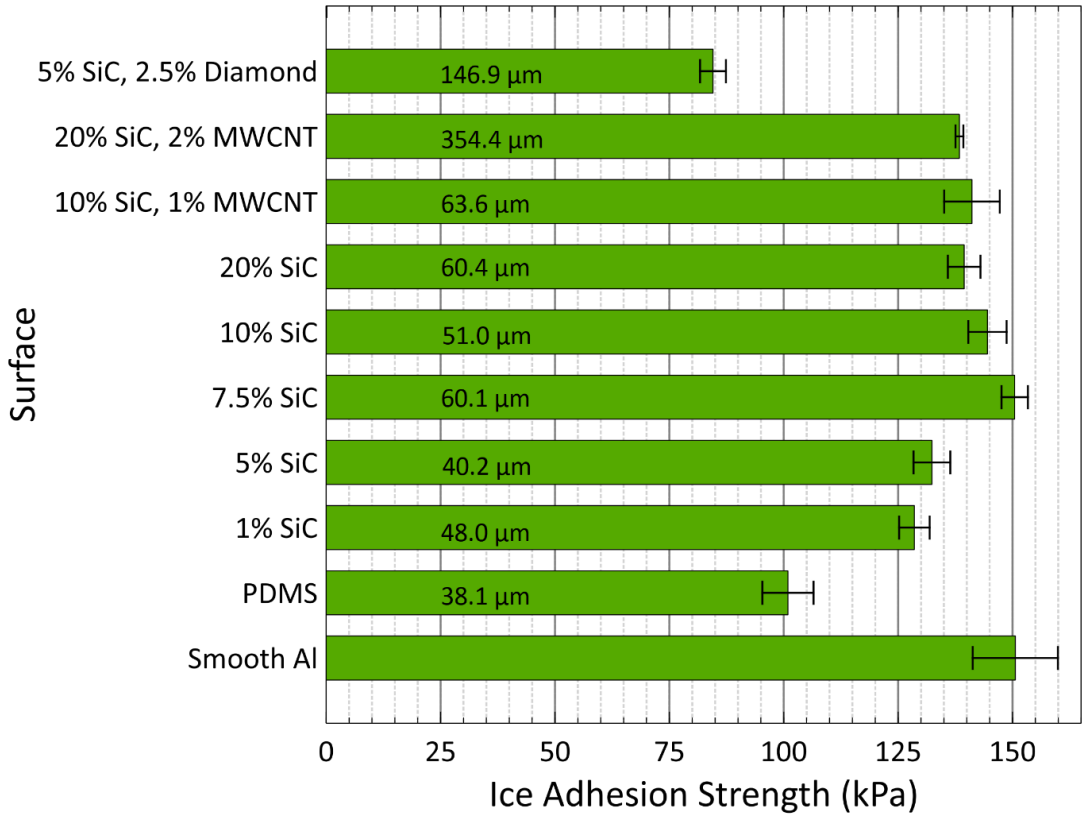

Figure 7.2 Ice adhesion strength measured using the centrifuge method to test unaltered aluminium, PDMS, PDMS containing a range of SiC fibre content, PDMS containing SiC fibres and multi-walled carbon nanotubes, PDMS containing SiC fibres and diamond powder.

Unlike the pull test, a value for the ice adhesion strength for sandblasted aluminium could not be obtained using the centrifuge method as every sandblasted aluminium sample failed cohesively, suggesting the ice adhesion strength of this surface was reliably higher than the cohesive strength of the ice, n=11.

The centrifuge results show a clear difference in the ice adhesion strength between PDMS and aluminium, with the addition of SiC fibres raising the ice adhesion strength of the PDMS. Coatings containing SiC fibres and multi-walled carbon nanotubes showed no significant difference compared to the coatings with the same SiC fibre fraction and no carbon nanotubes. Adding diamond powder to the 5% SiC coating improved the ice adhesion strength significantly, with the 5% SiC coating performing much worse than PDMS and the 5% SiC coating with diamond performing better than PDMS with no filler content. The reliability of this experiment is much improved upon from the pull test, with an average standard deviation of 8% and a standard error of the mean of 3%.

The ice adhesion strength obtained from the centrifuge method, displayed in Figure 7.2, if applied to a 6.4 m helicopter blade and a nominal tip speed of 213 m/s, based upon a Lynx XZ170 helicopter [109]. The predicted critical thickness at adhesion failure is shown in Figure 7.3.

Figure 7.3 a) presents two aluminium results for ice adhesion strength measured via the centrifuge method. Aluminium 1 is data collected in the same period as the rest of the data, and Aluminium 2 at a much later date. Aluminium 2 was not included in Figure 7.2 to improve the readability of the figure and to compare only the data collected together.

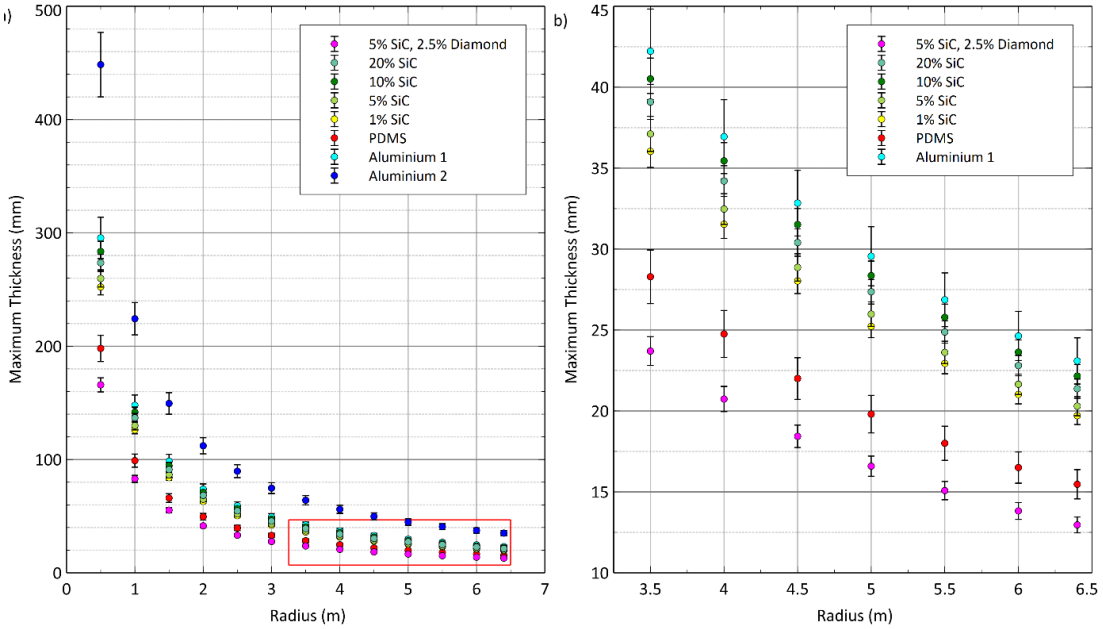

Figure 7.3 a) All centrifuge tested surfaces extrapolated performance if applied along a 6.4 m rotating arm with a tip speed of 213 m/s, b) data in a highlighted with a red box in a) not including the retested value for aluminium, Aluminium 2.

Figure 7.3 highlights the potential for specificity in coating design with this example of a rotary application. Diminishing returns occur as the operational environment changes from the root to the blade's tip, where far higher centripetal acceleration is present. The PDMS-only surface achieved an adhesion strength of 101±6 kPa with a loose definition of icephobic surface's requiring a value below 100 kPa, which can be referred to as high within more recent [51]. PDMS enhanced with SiC and diamond was the only tested surface achieving this threshold with an ice adhesion strength of 85±3 kPa. Other PDMS coatings containing SiC performed worse than PDMS with an adhesion strength in the range 129 – 150 kPa and were closer to aluminium in terms of ice adhesion

strength, measured as 151±9 kPa (Aluminium 1) than that of PDMS, with the higher SiC loadings (coatings having a SiC content > 5%) performing worse.

7.2 Dynamically loaded electro-thermal de-icing

Applying the stress at the interface via a loaded harness increased the complexity of the testing procedure from that of thermal de-icing, increasing both the difficulty and number of operations required compared to the unloaded thermal de-icing. These issues make the CAT a preferred method and form the basis for a thermal de-icing experiment where a shear load is present at the ice-surface interface, applied by a rotational arm. A key benefit of analysis in this manner is the ability to tune the heat flux and speed of the motor to adjust the shear load applied, while a higher applied load increases the relative airflow, increasing the rate of environmental cooling and potential structural vibration.

The samples are comparably loaded into the equipment for the centrifuge ice adhesion testing. However, the equipment is contained in a square box rather than a cylindrical one, which requires less clearance from the walls and may induce a more consistent airflow. The arms in both experiments are made from carbon fibre to mitigate the impact of strain on the results, where deformation of the rotating arm would result in a wider radius at which the sample is spun and affect the inertia of the ice. The arms for the dynamic thermal de-icing are longer and wider, with a larger mass at each end during the experiment. Coupled with any airflow patterns produced in the box rather than the cylinder used in the ice adhesion testing, it would likely cause structural vibration and air resistance to significantly impact the variance of results through a range of speeds. Compared to the static electro-thermal de-icing experiment, the sample loading is less concerning as it requires less direct handling, and all samples always remain in the same cold environment. Both experiments have active cooling systems in place; however, they are much more substantial in the dynamic thermal de-icing equipment by virtue of the size of the equipment and higher airflow. During static electro-thermal de-icing, the impact of the cooling is much more consistent as the main factor is the temperature difference between the environment and the sample. This does vary through the test, and some samples take longer to de-ice, which means the rest of the equipment and substrate will reach higher temperatures before shedding occurs. As the temperature difference rises between the sample and the environment, the heat flux from the substrate to the air will increase. With dynamic thermal de-icing, this same issue is present and can be mitigated by not requiring an environmental temperature much colder than the testing temperature due to the equipment's size. The main issue is the

cooling associated with the airflow, as it will change with the test's rotational speed and the airflow type.

7.2.1 Surface roughness

In this section, the most basic tests were conducted to assess the experiment's functional capability of the experiment and how the additional complexities discussed above impact the results, what possible trends could be present, and whether they are meaningful. Two simple tests were completed with smooth and sandblasted aluminium: changing the environmental temperature for a given velocity, see section 7.2.1.1; changing the velocity for a given environmental temperature, see section 7.2.1.2. The first would be to clarify the relative magnitude of the impact of environmental cooling and surface differences in aluminium. The second changes the applied shear stress, air cooling, which should increase with speed but is subject to the type of airflow at each respective speed and structural vibration.

7.2.1.1 Environmental Temperature and Time to De-ice

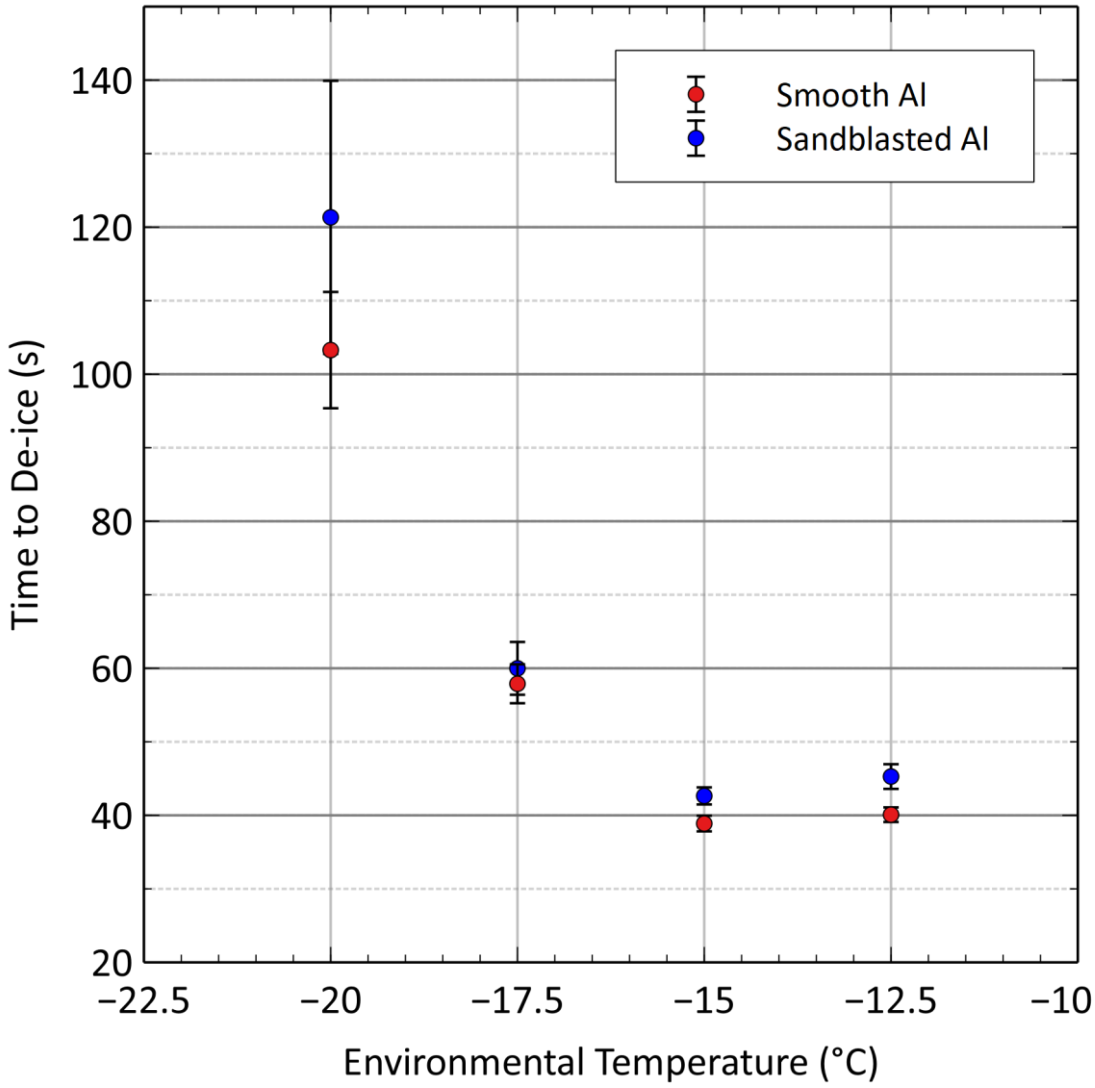

Figure 7.4 Measuring the impact of the environmental temperature when de-icing a -10°C surface with a shear stress of 3.6 kPa applied with 285 RPM.

Electro-thermal de-icing was timed with a 3.6 kPa stress applied and an operating/starting temperature of -10°C with both aluminium surfaces and a range of environmental temperatures is shown in Figure 7.4. These tests were conducted to assess the impact of airflow cooling on the time to de-ice. An environmental temperature of -15°C was selected, as the results were comparable to -12.5°C, but allowed a faster turnaround between tests where the equipment must be cooled down. The heater maintains the temperature of the tested side of the arm to -10°C for a consistent starting point. Each test indicates that smoother aluminium is a more efficient surface, with some tests suggesting no significant difference with overlapping error bars, which are widest at colder temperatures.

7.2.1.2 Increasing the Applied Stress

At 57 rpm, the centripetal acceleration on the adhered ice is 9.8 $\mathrm{m/s^2}$, with a multiple increase in RPM increasing the applied stress by the square of that multiple. For example, 114 rpm would have four times the acceleration. The maximum RPM the slip ring can operate prevented testing closer to the ice adhesion strength of aluminium. Figure 7.5 shows the range of speeds that could be tested and the calculated equivalent applied stress at the ice-surface interface with each point at a multiple of 57 RPM.

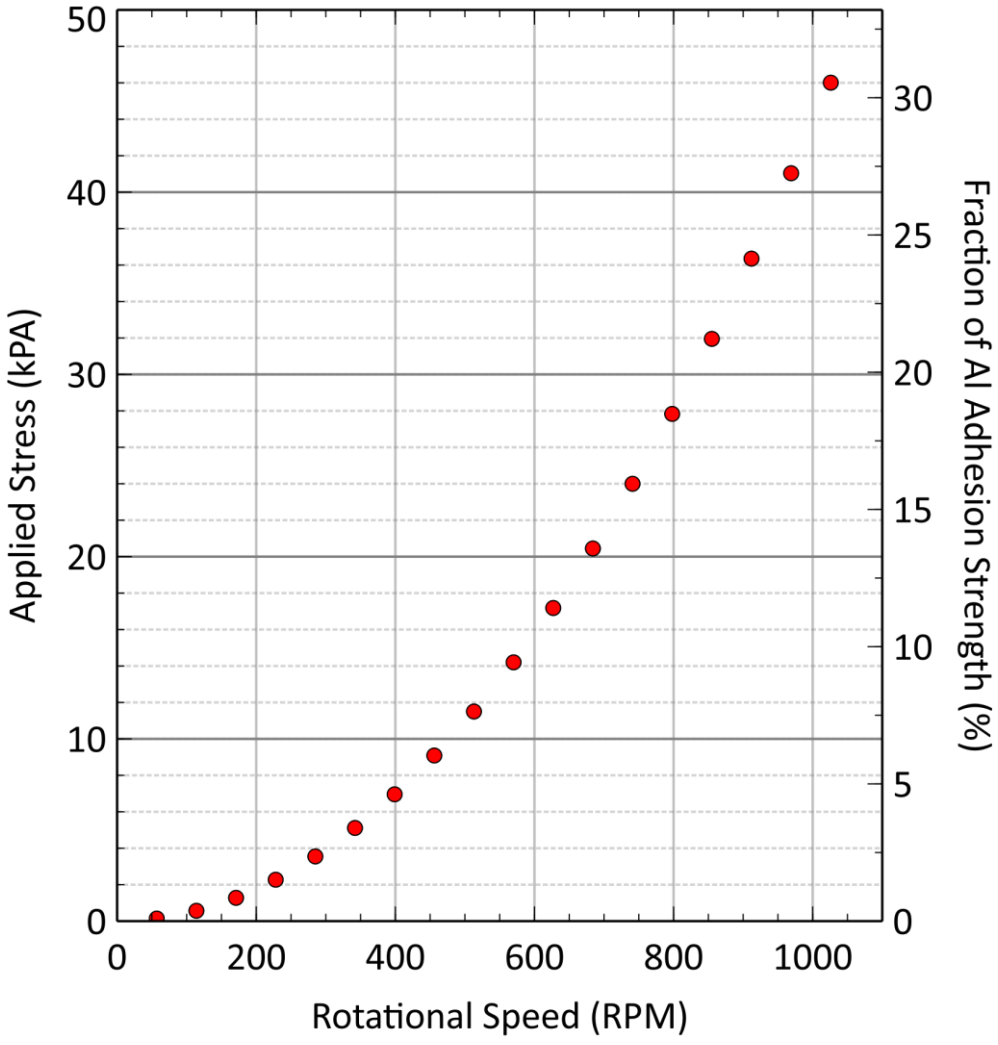

Figure 7.5 The range of RPM that could be tested and the stress applied to the ice-surface interface by the rotational acceleration. The applied stress as a percentage of aluminium's ice adhesion strength initial value is shown on a secondary axis. The value used was measured by the centrifuge method and denoted by Smooth Aluminium, as shown in Figure 3, with a value of 151 kPa.

The hypothesis this experiment is testing is that as the applied load increases, the energy cost to de-ice the surface thermally would decrease, all else equal, as the ice adhesion strength of a surface typically falls as the temperature rises [46]. A larger applied load would likely require a thinner melt layer before detachment if the ice adhesion strength does not fall below the applied stress before melting, as the capillary pressure is more readily exceeded.

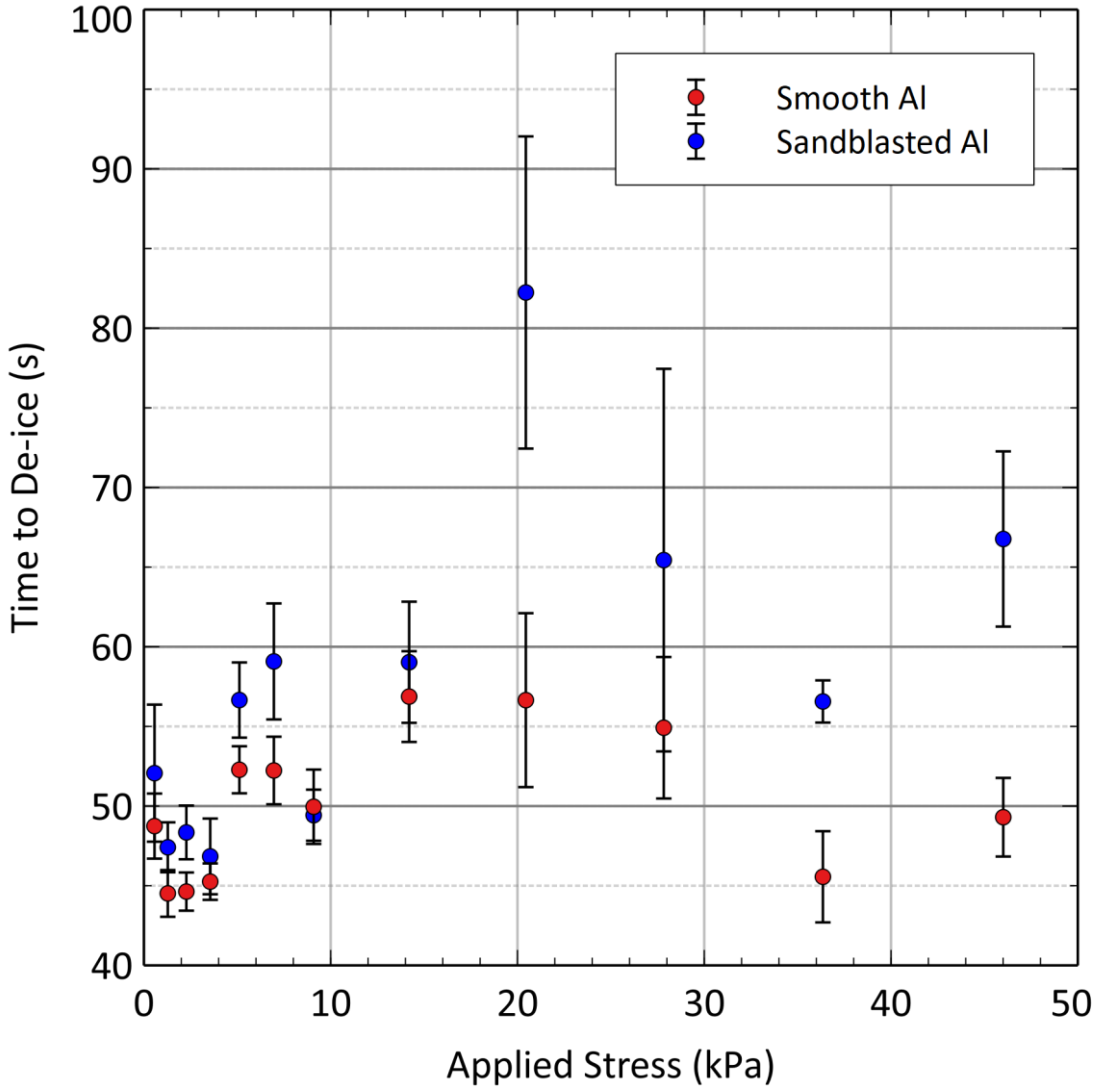

Figure 7.6 Time to thermally de-ice smooth and sandblasted aluminium across a range of applied shear stresses via centripetal acceleration.

Increasing the applied stress under identical heating and environmental temperatures, Figure 7.6, did not produce a clear trend with the time to de-ice. The dynamic thermal de-icing of sandblasted aluminium took longer than smooth aluminium across the range of applied stresses. Indicating the

importance of the surface properties to varying degrees across the testes stress range. An accelerometer was not used, so how each rotational velocity tested impacted the vibration present in the arm is unknown. Whether the airflow changed consistently with the rotational velocity of the arm or the length of time the test required to shed the ice is also unknown.

7.2.2 PDMS

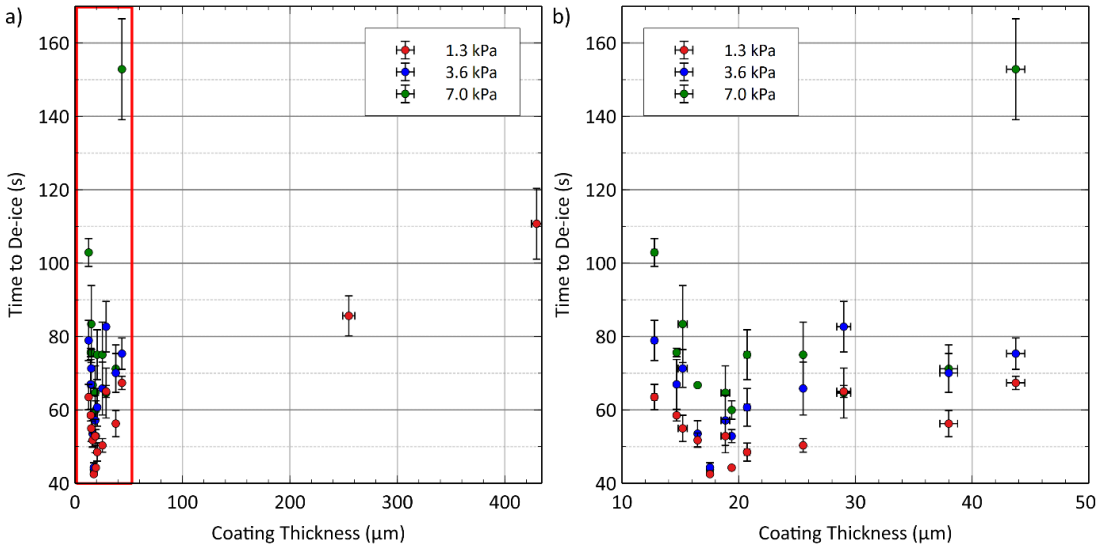

Figure 7.7 Dynamic thermal de-icing a) PDMS with a range of thicknesses testing at three different speeds corresponding to three different interfacial stresses, b) displaying the area highlighted in a) with a red box covering a reduced section of the data.

Selecting a range of appropriate applied stresses to test required consideration of the proportion of the adhesion failure for the material is high, cooling and vibration will play an increased role in the result. Furthermore, as coated substrates, having more material between the heater and the ice would require a longer time for the heating to affect the ice-surface interface. As the rotational speed increases and the coating thickness increases, an equilibrium will be reached where the thermal conductivity of the coating matches and then is exceeded by the cooling rate by the passing air, and the ice is never shed as a steady state is reached. This occurred with the two thickest samples at 3.6 kPa and 7.0 kPa, so the result could not be recorded, Figure 7.7.

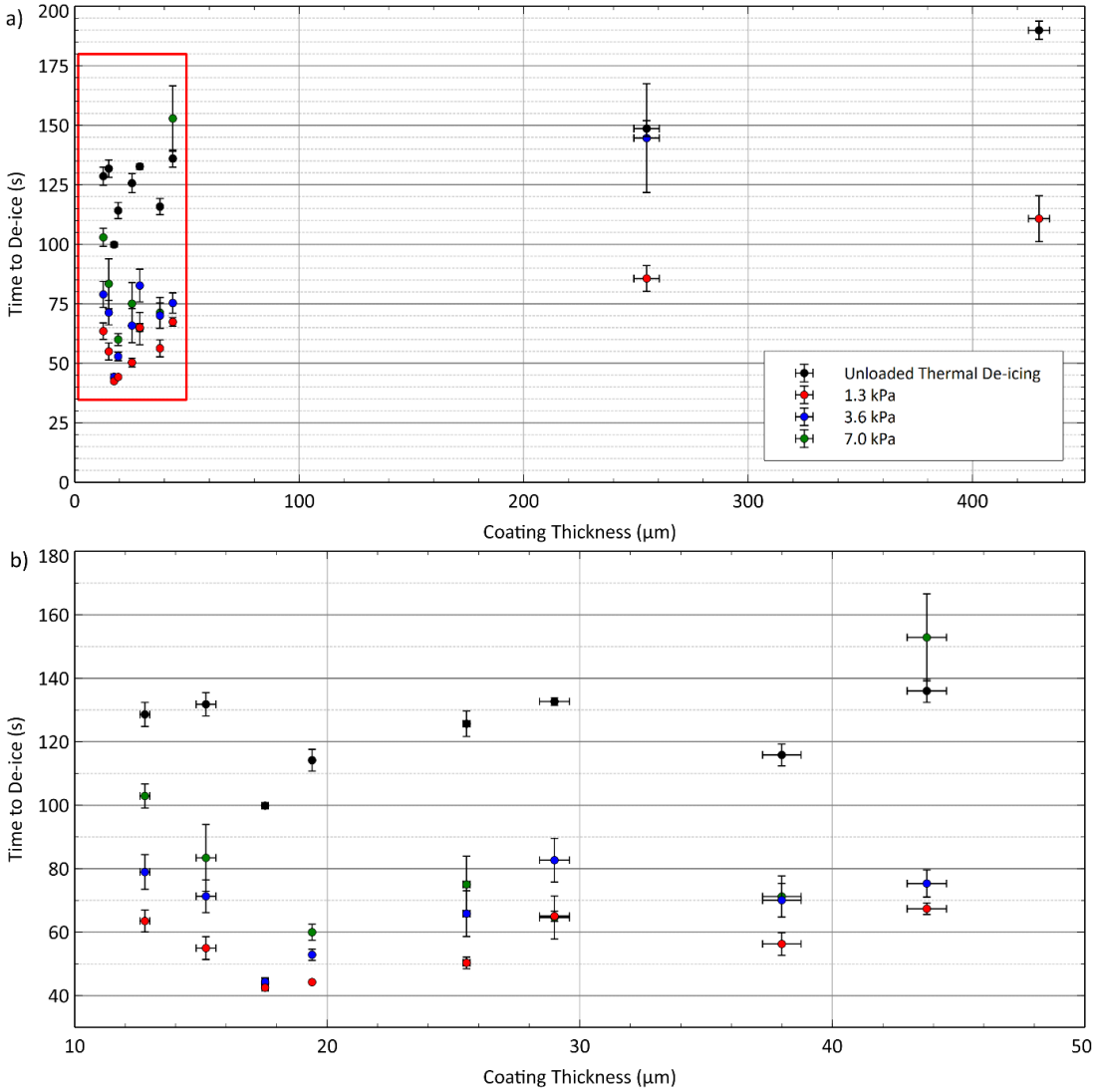

Figure 7.8 Using the data shown in Figure 7.7, only samples with the same substrates were also tested using static electro-thermal de-icing with a 10W supply without any applied load.

Comparing the trends for thermal de-icing and dynamic thermal de-icing for all samples that were evaluated using both experiments to compare general trends are graphed in Figure 7.8. This range of thicknesses shows no clear relationship between coating thickness and the time to de-ice under no load. When comparing samples that took less or more time to de-ice in one test, they had similar relative results to those in the other tests. For example, the time to de-ice decreases as the thickness increases for samples under 20 µm thick as an example of a localised trend that remains consistent. The two tests use a different iced surface area, volume and environmental temperature, so the thermal de-icing result cannot be equivocated to a 0 kPa result for the dynamic testing or at 57 RPM where the centripetal acceleration would be 9.8 m^2/s. The

dynamic testing can not be performed at a rotation equivalent to a centripetal acceleration comparable to gravity of 57 RPM as the ice and mould do not shed, the ice melts in its entirety, and the mould does not move. As the distribution of the data appears consistent across all tests the measured differences are primarily due to the coating and not variance inherent to the experiment.

7.2.3 PDMS containing SiC

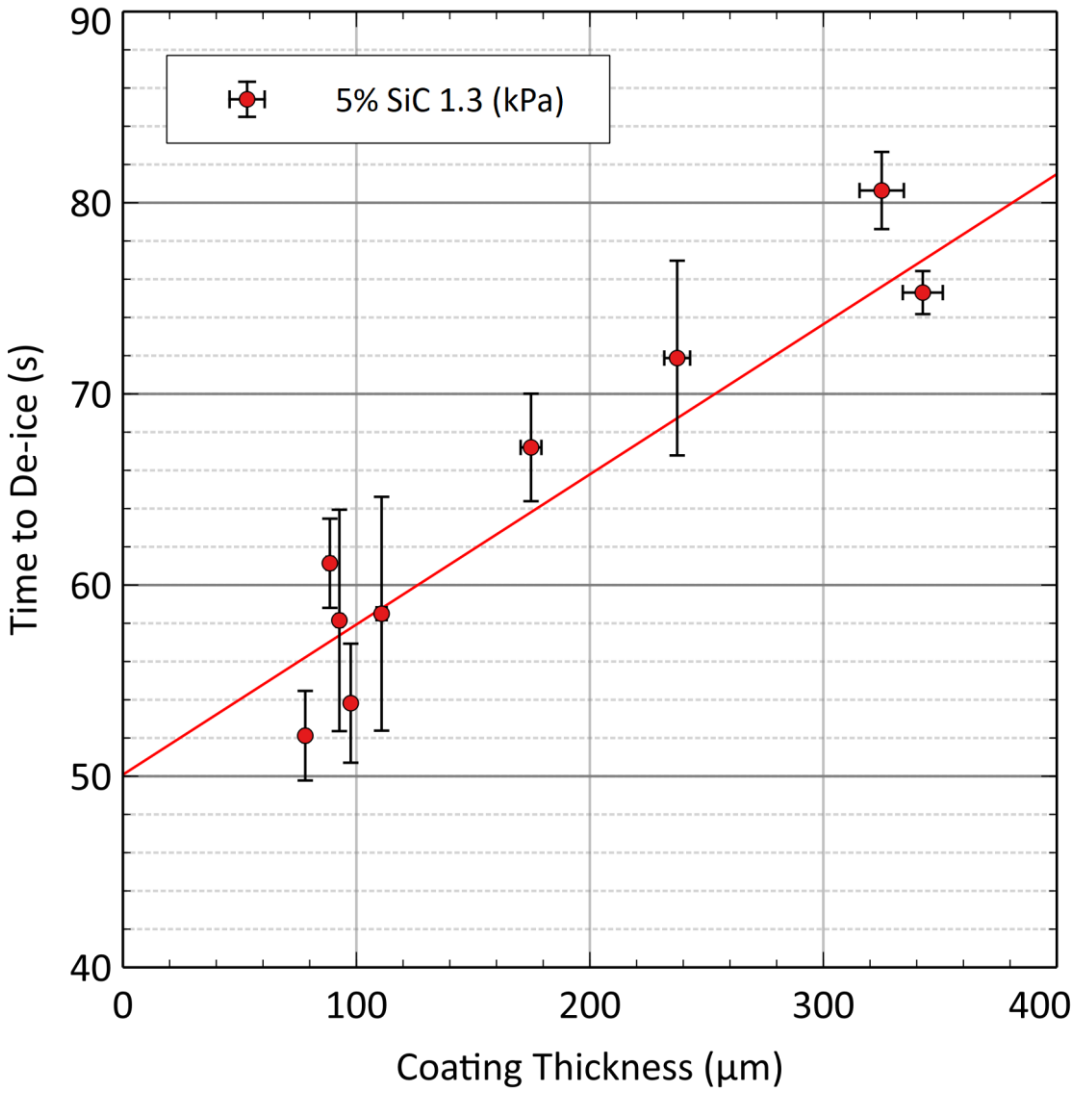

Figure 7.9 Dynamic thermal de-icing of PDMS containing 5% SiC with varying thicknesses tested at a low speed and respective applied stress indicated a linear relationship between thickness and time to de-ice as with the static electro-thermal de-icing tested.

A better distribution of coating thicknesses across the full range tested for PDMS containing 5% SiC than for PDMS as that data concentrated results below 50 µm thick, Figure 7.9. However, none around or below 50 µm which is a comparable length scale to the SiC fibres. The range of performance, despite this, was relatively poor. When comparing the five thinnest samples, a ~100 µm coating could have time to de-ice that varies by over 20%. Increasing the thickness resulted in a linear increase in the time to de-ice when a low shear stress of 1.3 kPa was applied.

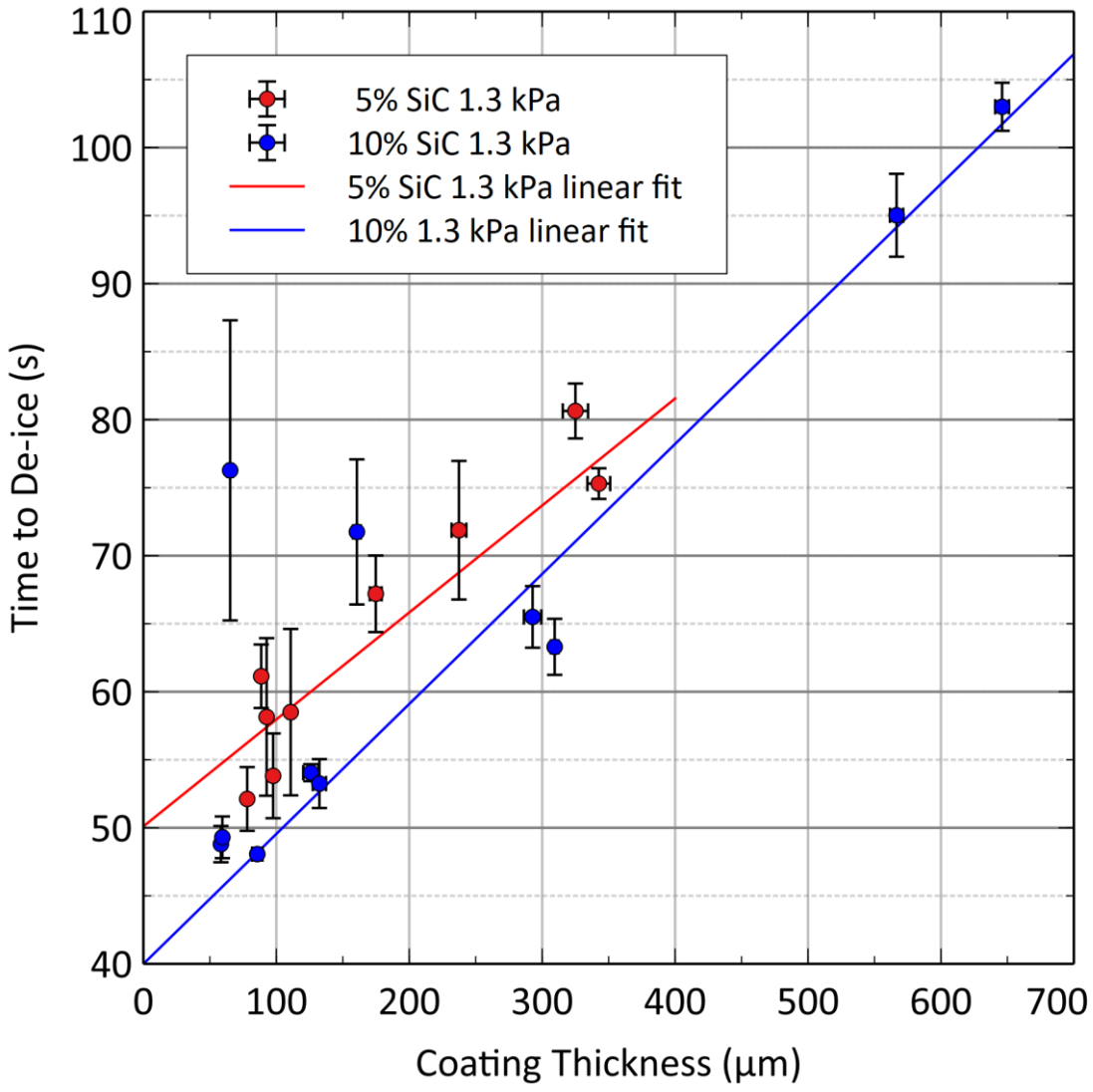

Figure 7.10 Dynamic thermal de-icing of PDMS containing two different filler fractions with an applied shear load of 1.3 kPa.

Increasing the SiC content improves the efficiency of the coating, Figure 7.10, as seen by comparing the y-intercept of the trendlines and that of 10% SiC, which is

20% lower. However, the trend lines converge to a point well past the range of the 5% SiC data as the thickness of the coatings increases. If the material was reliably superior in energy efficiency, the lines of best fit would diverge, and the data does not provide enough clarity to discern the relative importance of the coatings' surface properties and how much they differ. A greater range of coating thicknesses tested would provide better clarity upon the relative performance of the two materials and the difference in cost per additional thickness of coating measured by the gradient and relative benefit of the surface properties inferred from the y-intercept where the coating thickness would be zero.

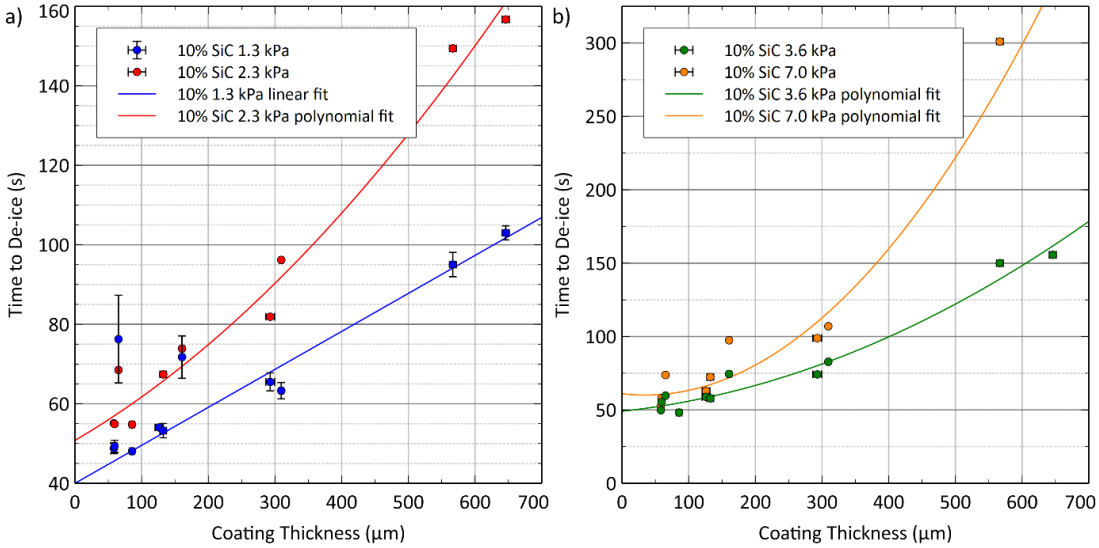

Figure 7.11 Increasing the applied shear stress when de-icing PDMS containing 10% SiC a) 1.3 kPa and 2.3 kPa, b) 3.6 kPa and 7.0 kPa. Results without vertical error bars are a single data point.

Increasing the rotational speed of the test showed a noticeable change in the time required to de-ice, and the relationship between the coating thickness and time to de-ice, Figure 7.11. The 10% SiC coating is more efficient at de-icing than the 10%. As the speed increases, the time to de-ice no longer remains linearly proportional to the coating thickness. The Chi-squared value for the polynomial fit is marginally lower than the linear fit for 2.3 kPa of 10% SiC, which is close to the breakdown of the linear relationship. Increasing the applied stress to 3.6 and 7.0 kPa shows that the relationship becomes less linear as the applied stress increases. The increased energy cost to electro-thermally de-ice thicker coatings became more substantial in this dynamic scenario. As applying a higher shear load increases the relative air velocity, the heat lost to the environment is also higher. This difference is more apparent with thicker coatings, where the length

of the tests was longer and more sensitive to the increased rate of environmental heat loss.

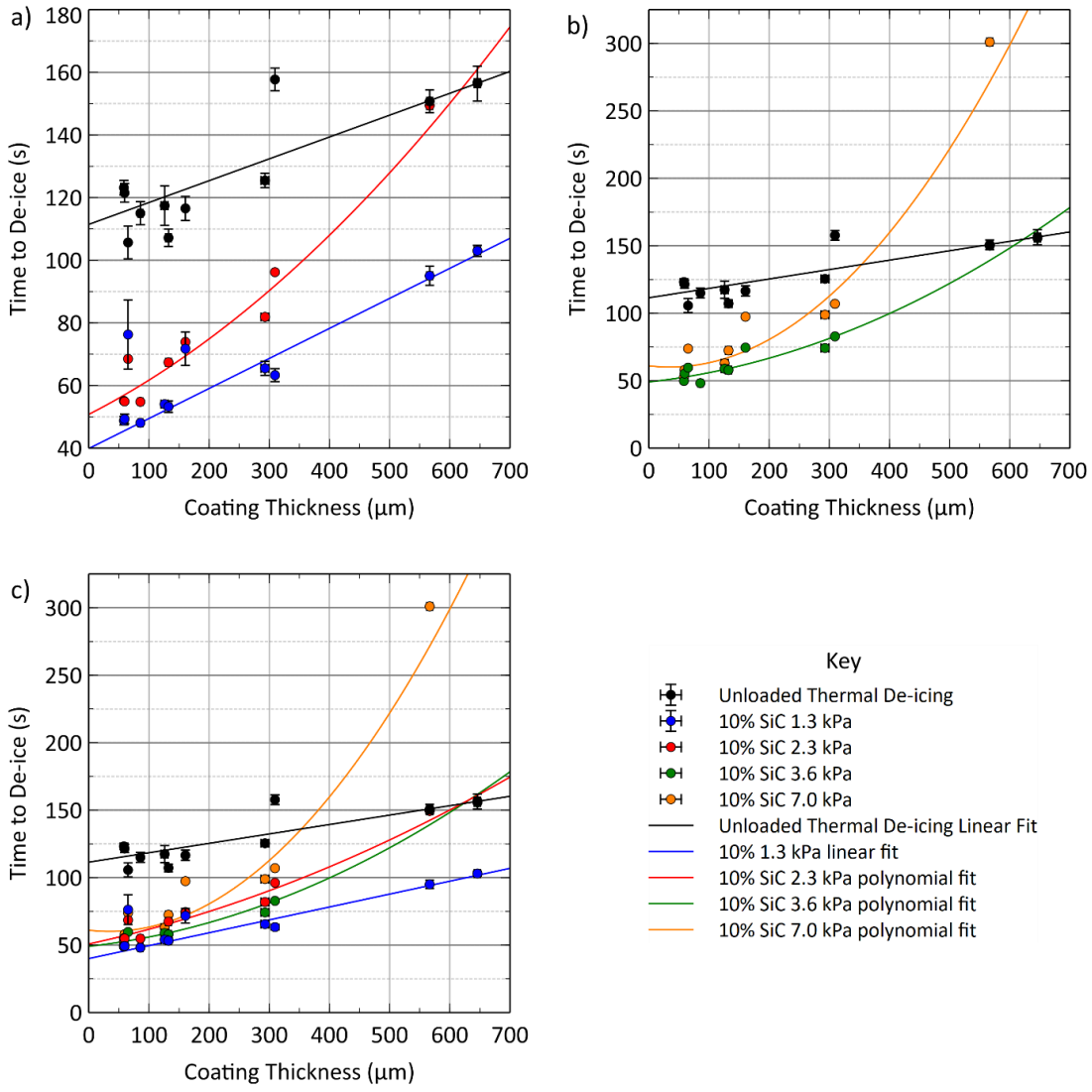

Figure 7.12 a) and b) show the same graphs in Figure 7.11 with the thermal de-icing result overlayed, and c) all results on the same graph. Results without vertical error bars are a single data point.

Overlaying the result for thermal de-icing for each sample shows that its gradient is comparable to the de-icing time when 1.3 kPa is applied in this experiment. The time to de-ice for the two thickest samples with an applied stress of 2.3 kPa and 3.6 kPa, respectively, are almost identical and are similar to those respective results for the static electro-thermal de-icing test, shown in black in Figure 7.12. The unloaded thermal de-icing result is not directly comparable regarding the time to de-ice measured. However, it can be compared for general trend and relative performance from one sample to another. The heater's energy

consumption was also not measured for the dynamic de-icing and was not a consistent input like the unloaded thermal de-icing test.

7.3 Discussion

7.3.1 Ice adhesion strength

Section 7.1 contains the ice adhesion testing where 10% SiC did not perform well, with an insignificant improvement over aluminium. This was tested with ~50 μm thick samples, which poses two reasons why this coating thickness could impede the result. As mentioned above, the thermal de-icing results were poor at this thickness range, suggesting a deterioration or inconsistency of the material's surface properties relative to that of a thicker counterpart. The second is that elastomers utilise interfacial cavitation to reduce the ice adhesion strength, and a thicker coating allows more significant deformation to occur. For the PDMS used in this work, the ice adhesion strength was found to be proportional to $1/\sqrt{t}$ where t is the coating thickness, up to 500 μm [59], so a thicker coating would also likely improve ice adhesion strength; this relationship will likely not be as sensitive due to the filler. The fibres were selected as the geometry would likely aid in improving durability over low aspect ratio filler with higher sphericity. It was also hoped that this would allow anisotropic design where vertically aligned fibres would disproportionally increase the thermal diffusivity in the desired plane and inhibit the Youngs modulus parallel to the substrate. PDMS also benefits from a high Poisson's ratio, which was considered. The plane of alignment may also matter. The alignment of fibres perpendicular or parallel to the shear force on the ice affects its deformation. A significant oversight in vertically aligning the fibres, if possible, is the benefit of peel stress for elastomeric coatings. The fibre alignment was not controlled, but there may have been a radial bias from the spin coating process. As the low Youngs modulus will influence the potential deformation in the horizontal shear plane, the vertical plane where peel stress aids interfacial cavitation significantly, the vertical alignment of fibres may disproportionately diminish the PDMS's potential at reducing ice adhesion strength of the surface Figure 7.13.

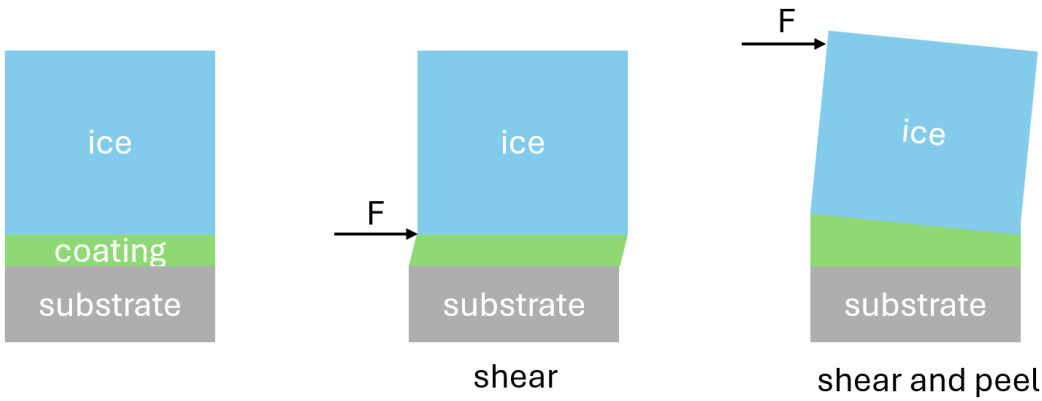

Figure 7.13 How the elasticity of the coating influences the effectiveness of an applied shear force.

This means that the coating's thickness should also be highlighted as an important factor when comparing ice adhesion results. It also follows that when considering a high tolerance application where the safe limit of accretions is low, relying on peel stress for performance should be avoided as the centre of mass of that thin accretion deemed the maximum allowable will be close to the surface. In applications with a higher tolerance, interfacial cavitation coating will perform better as the ice accretion grows larger and the moment around the surface causing peel stress to increase with both the mass of the ice and the moment arm. A doubling of the ice above the surface doubles the applied shear stress and the applied peel stress.

Accounting for the peel stress and the thickness of the coatings when testing for ice adhesion would provide greater clarity and more specific analysis. Isolating for shear stress was attempted in the pull test described in section 4.8.1 by minimising peel stress and applying the force as close to the surface as possible. This ultimately failed as a reliable harness mechanism capable of this could be adequately retrofitted as it would require realigning the hole in the lid that the chord was fed through to be in line with the surface and not above it in line with the ice's centre of mass. The ice moulds used in the CAT were in the shape of an elliptical hemisphere with an internal volume of 1.3 ml, so the centre of mass is skewed lower to the surface by its rounded shape. More empirical analysis can be done by looking at these geometric details from one laboratory to another and reducing the need to rely on aluminium as a reference material. Using a reference like this depends on the alloy and finish being the same, and the results of using different geometries or densities of ice at a given temperature would produce different stresses. To truly assess ice adhesion strength, the shear stress component must be isolated. For the ice used in the CAT, the centre of mass lies

2.6 mm above the iced area of 1.38 cm^2, the true value is closer to 3 mm when accounting for the mould present in the test. If the same volume of ice was in a column with a vertical wall and flat top, the centre of mass would be 4.7 mm above the surface for the same volume of ice.

The CAT was completed with the mould still in place, removing this from calculations and using the result measured for aluminium. The shear force was 13.5 N. Considering the peel stress present, if only the mass of the ice was present at the time of detachment, the moment about the surface could be calculated. Comparing the moment for the two ice geometries described, both with no moulds present and the same volume of ice, the moment about the centre of the adhered area is 0.35 Nm for the tested ice and 0.62 Nm for the hypothetical column.

The diamond-containing coating, which produced the lowest ice adhesion result, would have had equivalent values of 0.20 Nm and 0.35 Nm moments present, respectively. This does not account for the additional peel stress in the perpendicular direction due to drag. It shows that controlling for ice geometry is important and should be standardised. Or, more precisely, analysed to allow meaningful discussion around the influence of the peel stress and the coating thickness on the result. If the field moved to using a spherical hemisphere, the size would be less influential between laboratories, and it would allow better inference of contextual information if it was not supplied. If a shape like this is standardised, the centre of mass can be inferred, a standardised drag coefficient can be applied, and air velocity can be inferred at detachment. Ideally, studies would provide the moments present alongside the measured ice adhesion strength, area iced, coating thickness and true or estimated substrate temperature deviation from the air temperature due to wind chill. This contextual information is vital to provide consistent and qualitative analysis. While this composite has produced a lower ice adhesion strength, this is most likely a result of the coating being multiple times thicker than the PDMS. The filler should increase the Youngs modulus which would also increase the ice adhesion strength, the higher thickness appears to have had a much larger effect and lead to a reduction of ice adhesion strength.

Some of this information is missing from the work presented here, and the experience gained from testing the dynamic thermal de-icing performance has illuminated the difficulty of effectively using a thermocouple on a high-speed rotational application due to the significant capital limitations this would impose upon making equipment capable of this by way of a high-speed slip ring that can operate in freezing temperatures. Fluid flow and heat transfer calculations coupled with a few comprehensive studies would be sufficient to extrapolate the

observed trends across the field with the relationship of coating thickness on ice adhesion strength of PDMS [59] and interfacial toughness [52].

This moment's influence on the apparent ice adhesion strength is also dependent on the area of adhered ice, as a wider accretion will benefit less from a coating's ability to deform away from the substrate. Assuming a fixed maximum strain, the rate of change per unit length of the surface will decrease as the adhered area increases. The pull test that aimed to better analyse the peel stress presented in Figure 7.1 produced significant errors, making surfaces indistinguishable. Fiction of the harness over the elastomer was likely an issue for all coatings, and applying the force at the surface proved highly unstable.

The limitation of elastomers, where interfacial cavitation limits the propagation of a crack, is discussed in the approach of LIT surfaces, where adhesion failure does not result in complete adhesion failure from the crack initiated [53]. It must be noted that this crack is formed on coatings 1 mm thick, so the thickness of the coatings should not limit the performance. It was found that reducing the thickness of a PVC film reduced the interfacial toughness [52].

The measurements in these two studies use a low-velocity force gauge with 74 $\mu m/s$ used in the first study [53] and 50 $\mu m/s$ in the second [52]. Chosen to be below the critical velocity where sudden debonding occurs under high load, where a shear force moves a glass prism over an elastomeric film, the interface cavitates at specific wavelengths depending on its properties and film thickness [68]. With the wavelength or size of the bubbles, the film thickness and the critical speed are proportional to the film thickness. This can be compared to the ice adhesion strength of Sylgard 184, the PDMS used in this work, being inversely proportional to the coating thickness. Considering this information and applying it to high-speed applications such as a helicopter or wind turbine blade, the cavities caused by elastic instability do stop in this low-velocity application, but in a high-velocity environment, this may not be limiting. Ice adhered to a blade, the ice-surface interface is constantly experiencing shear stress due to angular velocity and drag. A cavity in a low strain rate environment may not propagate, but under these conditions, while experiencing structural vibration, the stress at the interface increases proportionally to the decrease in the adhered area produced by the cavity. Causing a runaway adhesion failure of the ice. Additionally LIT toughness surfaces may be impeded by an inconsistent ice accretion, where porosity or cracks in the ice limit the length a crack can travel. The issue would likely lie in creating a crack with such a large accretion.

7.3.2 Targeting complex applications

Looking for an appropriate solution for a helicopter blade, a simplistic, potentially reductively so, surface design requirement would be reducing the critical thickness of ice accretion as much as possible along the blade. The portion of the blade closer to the middle and further out to the tip produces the majority of the lift by virtue of sweeping through more air at a higher velocity. Therefore, it is important to ensure the aerodynamic profile of this section of the blade is impacted the least, requiring the most hydrophobic surface capable of delaying icing as much as possible and reducing the frequency of icing while having the lowest ice adhesion strength possible. Icing would be less frequent and less dangerous when it does occur because the critical thickness before detachment would then be small. However, such a surface will be thermally insulative to delay ice nucleation and suffer from low durability when faced with water and particulate erosion if not addressed in the design. If the blade encounters this during operation, the performance of the surface may degrade and fall outside the required envelope of necessary properties.

An undesirable approach, but with the potential of meagre success, may be to tune an elastomeric coating to sacrifice some ice adhesion strength in this high-velocity portion of the blade in favour of performance elsewhere. Perhaps increasing the filler content to improve durability would work but simultaneously increase the elastomer's Youngs modulus, increasing the ice adhesion strength. This causes the critical thickness of the ice accretion to increase as a cost of improving the coating's durability in this way. With the coatings tested in this work, a similar trade-off can be seen when comparing thermal de-icing performance and ice adhesion strength. At the cost of increasing the ice adhesion strength of the PDMS matrix to be more comparable with aluminium PDMS alone, as seen in Figure 7.2 from the CAT results, the 10% SiC coating had a per-thickness energy cost 59% lower than PDMS alone.

The initial performance of this redesigned coating appears to be worse than the first coating, but if, in the context of the application, the critical thickness of the ice remains within an acceptable tolerance, a successful improvement has been made. As the coating still functions, durability has then been suitably prioritised.

Key metrics such as hydrophobicity and ice adhesion strength have historically been the backbone of icephobic performance by delaying ice accretion and reducing its potential severity. However, reducing the importance of these properties in favour of others may widen what could be considered a viable solution depending on the application of the surface. The effect size of the coatings successfully designed in this way would be smaller but an improvement, nonetheless. LIT coatings highlight that the breadth of

considerations is often not wide enough, with the interfacial toughness of surfaces shown to better estimate performance at larger length scales than ice adhesion strength.

Where successfully designing a passive icephobic solution could be considered like a vaccine or antibiotic, designing a surface to function alongside thermal de-icing systems can be considered a therapeutic remedy that intends to treat the symptoms rather than prevent or cure the disease itself.

Helicopters highlight the potential for this approach due to the variability and extreme nature of where and how a coating would need to perform. If an ill-prepared helipad, or perhaps a desert location, poses the risk of significant damage to the leading edge of a blade to such a degree, repeated operation raises concerns for the lifespan of the titanium erosion shield. Sea spray striking the blade is less extreme; however, it poses similar durability questions for any applied coating. A reasonable assumption would be that any applied coating or surface will not have a longer lifespan than the blade's erosion shield. Suggesting reapplication and the requirement for safe operation without an effective icephobic coating would be necessary or desired. If the coating degrades mid-flight or is not fit for the next flight, it will come at a significant cost or risk to use the vehicle if the coating cannot be reapplied in situ or necessitates immediate grounding by adding a critical point of failure. While a passive solution would be optimal, reliance upon a coating that must operate in extreme environments on different sections of the blade, further diversifying the properties of the environment, may not be possible while maintaining a safe level of reliability. In such cases, the active thermal de-icing systems will remain in place in future vehicle iterations as icephobic research develops. If a passive icephobic solution is not suitable for this application, such a conclusion does not necessarily require all icephobic surfaces not to be applicable. Designing a coating to enhance the thermal de-icing system, rather than replace it, would still be an improvement if viable. An easily appliable surface, such as on an adhesive tape, would provide a sacrificial layer for the erosion shield while reducing the frequency and severity of icing incidents. If this coating or tape is designed to work alongside the thermal de-icing system, the lifetime energy consumption could be reduced while improving flight safety. Where a passive coating would eliminate this sub-optimal approach, a sub-optimal approach may be the only avenue for a viable improvement. Moving towards less extreme applications such as fixed-wing aircraft or wind turbines would allow a blended design approach where the application dictates the importance of all relevant performance metrics, downstream of which, material properties. As with helicopter blades, the root of a wind turbine has a much lower rotational velocity than the tip; designing a coating should be specific to each area to be optimised

for its operation. A wind turbine has a lower tip speed and angular velocity. Therefore, it experiences a lower likelihood or rate of severe erosion, different structural vibrations, and fluid dynamic properties such as Reynolds number that may impact the structure of ice growth.

The specificity of coating design is paramount for a hybrid solution, where a passive solution is not yet viable. An imperfect solution could be more achievable as research progresses towards a passive solution. This chapter delves into experiments designed to test surfaces under mixed-loading scenarios where mechanical loading is present on the surface-ice interface while a heater is in operation to allow consideration of whether this design approach is viable.

A core goal of this research is to produce testing methods that promote application-specific design testing coatings' electro-thermal de-icing performance, allowing analysis of what affects a coating's performance. It does not adequately predict its viability or the weighting of each variable in a given application. As the fluid and solid mechanics affect ice accretion and the ice adhesion requirements change along the length of a blade, so will the performance of a thermal de-icing system. As the drag scales along the leading edge, the interface at the tip will be under compression and tension at the root if the accretion has sufficient cohesive strength not to fracture.

The airflow in freezing conditions will cool the blade as it passes over it, which would reduce the efficiency of the thermal de-icing system. However, the tip may undergo aerodynamic heating for high-speed applications such as a helicopter. Further highlighting the need for specificity in design as considerations regarding the importance of aerodynamics of each blade area, and therefore, maximum tolerance of the ice accretion must use the specific operating conditions to determine the best method to shed the ice. Near the root, the mechanical loading on a given accretion will be less than that at the tip, and the reduction of lift generation will also be less severe.

This increase in maximum accretion may not be a concern as the acceptable tolerance is wider. Considering thermal de-icing, the root may be travelling sufficiently quickly through the air that the thermal de-icing system is heavily impeded by its cooling, and in contrast, the tip is aerodynamically heated by the friction of the flow. Potentially producing a temperature profile along the blade that lies above and below the environmental temperature. Ice adhesion strength increases as temperature decreases, and this has also been shown to be true for interfacial toughness. This phenomenon adds a further dimension to this complex problem that could result in a coating that has been well tested in each metric of performance in great detail and succeeded in achieving the criteria for

use in the desired application, to then not behave as expected in a more complex scenario. Simplified testing provides better analysis and is imperative for meaningful research by isolating factors and describing their value relative to a desired function. An example of this completed in this work is the relative importance of the coating material and its surface when thermal de-icing. The material and surface properties must be analysed with additional context that can be as simple as the thickness of the coating to change the relative importance of each property drastically.

With elastomers utilising interfacial cavitation occurring through elastic instability, changing the coating thickness, the peel stress present, and the environmental temperatures impacting upon its Youngs modulus are necessary contexts for a coating potential to be understood thoroughly. If an elastomeric coating appears to have a low ice adhesion strength and the application requires it to operate at colder temperatures, be thinner, and the maximum ice accretion that is tolerated or the geometry of the application reduces the peel stress that is present, the performance will have been severely overstated. Greater critique must be applied to experimental methodology as this field often lacks consistency between researchers' measured values. There is insufficient standardisation to make comparisons as meaningful as possible due to the inherent error. A primary example is ice adhesion strength, as the measured stress must also be considered with the result of aluminium as a reference material, as the value it achieves varies significantly from laboratory to laboratory. It was hoped that this approach would help reduce the creativity in design by making it more effective and targeted, allowing for more creative solutions to be considered. Rather than creative attempts to produce a coating for a wide range of applications, use a broader range of coatings or design features within one application depending on its complexity.

A key step in testing the viability of a coating that works synergistically with an electro-thermal de-icing system is applying mechanical loading to the ice-surface interface during thermal de-icing tests to simulate a more realistic use case. As ice adhesion changes with temperature tracking, the time to de-ice under a range of applied shear stresses, ideally up to the adhesion strength of that surface, would provide insight into the expected performance of a coating. Considering absolute load in applied shear stress as a proportion of that surface's adhesion strength. Investigating the relationship could show that surfaces using specific mechanisms better utilise a load that is only 25% of their adhesion strength but worse at 75%. The relationship may be simple and consistent, but any apparent differences would present an opportunity for knowledge acquisition. Differences would allow further optimisation by

appreciating a deeper understanding of the mechanisms present and how they interact in more complex scenarios.

For example, testing adhesion strength and thermal de-icing may not sufficiently encapsulate a helicopter blade. As a helicopter flies forward, the drag on the advancing blade is no longer consistently perpendicular to the leading edge, and the relative airflow velocity now has a component based on the vehicle's motion, Figure 7.14.

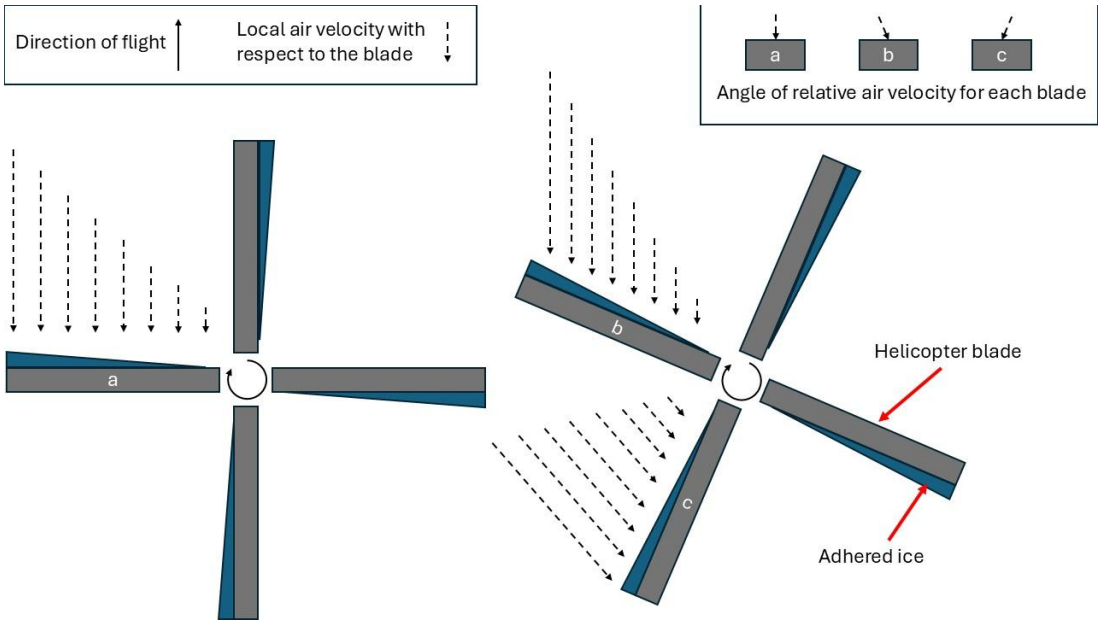

Figure 7.14 Diagram showing the relative air velocity for several blades of a moving vehicle where the velocity component from the angular velocity is far higher than the vehicle's motion.

If the ice is one solid body, the attachment area will also experience oscillating stress that varies down the leading edge from tension to compression as the net compressive forces are asymmetric, creating a moment. As the angle of airflow on the ice also oscillates with the blades' rotation about its axis, coatings that effectively utilise peel stress may perform better than expected and have that benefit compound further down the blades' length towards the tip. As it increases with the present shear stress due to the change in magnitude of the local velocity, the accretion may have grown thicker relative to the root end. The increase in the moment caused by the drag at each position along the leading edge may not be linear as the perpendicular distance from the leading edge of the net force may increase, as well as the surface area and local velocity. LIT

surfaces may suffer when the cohesive strength of the ice is low, and it is prone to partial shedding. Ice fracture could limit its situational potential.

7.3.3 Dynamic electro-thermal de-icing

This test assesses how the applied shear stress altars the energy cost to electro-thermally de-ice the surface. The ice adhesion strength of a surface typically falls as the temperature rises [55] [59]. A more significant applied load would require a thinner melt layer before detachment if the ice adhesion strength does not fall below the applied stress before melting. The magnitude of the difference in melt layer depth would depend on the surface properties if a more hydrophobic surface would require a thinner melt layer than a less hydrophobic surface, as overcoming the Van der Waals forces and capillary pressure should be more readily achieved for a lower surface energy material.

As the harness was unreliable and the CAT experiment is more applicable to rotational applications, a dynamically loaded electro-thermal de-icing test was conceived to represent better de-icing a helicopter or wind turbine blade. As the thermal de-icing must occur in a cold environment with the temperature below, or at best comparable to, the freezing point of water, ΔT may be significant enough to noticeably extend the time to de-ice, as seen in Figure 7.4. However, increasing the relative airspeed also has the potential to noticeably slow the heating of the surface-ice interface. In this experiment, increasing the rotational velocity increases the applied stress and changes the structural vibration present, which could reduce the time to de-ice. However, the increased rotational velocity will also increase the relative airspeed, leading to more significant environmental heat loss.

The environmental temperature was maintained at -15°C and a testing temperature of -10°C throughout. Considering how ice adhesion strength measurements vary between laboratories, this could be highly relevant. Different equipment using different lengths of the spun arm, angular acceleration, and mass of adhered ice may mean 100 kPa represents different time lengths of test and flow speeds. As ice adhesion strength varies with temperature, this could be a source of error as the actual temperature of the interface is lowered from the air temperature by wind chill.

Figure 7.6 showed significant variation in local trends as the applied stress was increased with aluminium and sandblasted aluminium, made using the second blast media, described in section 4.1, with sandblasted aluminium often performing worse than smooth aluminium. This controlled study implies that

other variables are unaccounted for, affecting the results. The airspeed, already mentioned, and the structural vibration present are assumed to be the most influential. An accelerometer on the arm would have provided insight into this, and an additional thermocouple on the counterweight would have allowed analysis of the trend loosely followed by both surfaces with an average error of 6%.

Low speeds were used to test low-thickness coatings to minimise the impact of cooling and vibration. Figure 7.7 illustrates that a higher applied stress increased the time to de-ice, with two thick coatings above 200 μm tested and the rest below 50 μm. The two thick samples impeded the heater such that only the lowest speed tested caused adhesion failure. The 44 μm thick coating displayed a significant uptick in time to de-ice when the applied stress was increased to 7 kPa, with a longer time to de-ice than the 255 and 430 μm thick coating results for 1.3 kPa of applied load. If this was caused by an exponential trend dominating where the airflow cooling out-competed the heater, then it is reasonable that the two thick samples did not de-ice for 3.6 and 7.0 kPa. The trend can be compared by comparing the samples to the unloaded electro-thermal de-icing results, but not the values. The trend from sample to sample is generally comparable in Figure 7.8.

5% SiC showed a linear relationship between the time to ice and thickness at 1.3 kPa, suggesting that the cooling due to the airflow is insignificant at this speed. Comparing it to the performance of 10% SiC, the latter is marginally faster to de-ice as with the unloaded tests in the previous chapter, but the results are more comparable in this test at higher thicknesses. This is likely because the time to de-ice in this test is shorter, and the need for a higher-powered heater suggests that the energy cost associated with the equipment is a higher proportion of the energy expenditure, narrowing the measured difference between materials.

Nearly all 10% SiC samples produced results at all applied loads, with the thickest at 646 μm unable to shed at 7.0 kPa and 567 μm shedding after 5 minutes. This material showed an apparent deviation from a linear relationship between the time to de-ice and the thickness of the coating as the applied stress was increased. The inability of PDMS to produce results at much lower thicknesses implies that its lower thermal diffusivity makes it much more sensitive to the cooling of the airflow. Again, comparing the unloaded results, the sample-to-sample deviations within the trend appear consistent between the two tests. This is promising as it implies that the deviation from the linear fit is more dependent on the sample than the data collection method and that, as expected at these low applied stresses, the thermal de-icing performance is the dominant factor, Figure 7.12.

Clearly, to have broader applicability, this experiment needs further improvement. A more powerful heating system with insulated sample holders would allow testing over a larger range of applied stresses closer to each material's ice adhesion strength. The data in the aluminium and sandblasted aluminium over a greater range of speeds than that used for the coatings demonstrated the need for an accelerometer and a method to measure the wind chill on the counterweight. This may require changing the environmental temperature to the start temperature of -10°C from -15°C. Comparing the results for 10% and SiC and PDMS in this experiment, the benefits of increasing the thermal diffusivity are clear. Eventually, PDMS will be better at higher applied stresses as the adhesion strength is noticeably lower, and so would shed at 0 s when 10% SiC may never be if the airflow cooling is significant.

LIT surfaces have been tested alongside active systems that caused detachment below 0°C and were used to heat only a portion of the coating, and not the interface, to reduce the interfacial toughness, which was shown to increase, as with ice adhesion strength, as the temperature decreases [55]. An intriguing prospect would be applying an elastomeric coating that is thick near the blade's root and thin along the middle and tip portion to promote cavitation where the interface is under less stress and a lower interfacial toughness material where the applied stress is higher.

7.4 Summary

The dynamic electro-thermal de-icing experiment has further emphasised the findings from the static electro-thermal de-icing experiment in the previous chapter. The thickness and thermal diffusivity of an icephobic coating employed alongside an active de-icing system could critically hinder its performance if not considered adequately before its implementation. In a low airflow environment, increasing the coating's thickness linearly increases the time required to de-ice using an electro-thermal system. In section 7.1.2, The ice adhesion of PDMS was reduced with the addition of SiC submicron fibres and nanodiamond powder, despite the addition of filler material that should increase the Youngs modulus, and so the ice adhesion strength. This was not found as the composite coating was over three times as thick. In this case, if a PDMS coating that had the same thickness as the SiC and diamond composite was tested, it would likely outperform it and have a lower ice adhesion strength. Coupled with the measured efficiency improvements for electro-thermal de-icing of PDMS by adding thermally conductive fillers, a window of opportunity may present itself in icephobic research, where increasing the thickness of a composite coating could be used to counter the increase in stiffness due to the presence of a filler

material. In both static electro-thermal de-icing tests in the previous chapter and its dynamic counterpart in this chapter, the addition of SiC improved the active de-icing efficiency of PDMS. This was important when operating in the presence of a higher airflow, actively cooling the surface with thicker coatings, which are much more susceptible to performance inhibition.

If an icephobic application requires adding filler material and a minimum coating thickness to have sufficient durability while maintaining a low ice adhesion strength, ensuring those fillers increase the thermal conductivity would be highly beneficial if the coating is employed with an active ice protection system. Increasing the thickness does not cause a linear reduction in ice adhesion strength but linearly increases the energy cost to de-ice electro-thermally. In the dynamic test, it is much worse where an increase in thickness can effectively insulate the ice from the heater and a non-linear relationship was observed with the thickest sample of 10% SiC not being de-iced by the heater at the highest speed, applying 7 kPa of shear stress. This is a significant safety concern when considering the early adoption of icephobic coatings. This research presents a window of opportunity for balancing material properties to prioritise performance across various metrics for a specific application, which could provide a viable solution.

The lack of standardisation within icephobic testing limits the comparability of research and, thereby, the field's progress rate. This work aimed to highlight the need for electro-thermal de-icing testing and key factors required for consideration when designing both coatings and testing methodologies, specifically, to dictate the parameters of success of a coating rather than an improvement in individual metrics at the cost of another when to goal application is dynamic and varied.

Chapter 8: Conclusions and future work

8.1 Conclusions

To date, the primary aim of coatings research for anti-icing or de-icing applications has been developing a passive solution: a coating that prevents or mitigates ice formation on a structure. However, helicopters offer a strong argument for a hybrid solution, where a passive coating works in conjunction with electro-thermal de-icing systems. This is because of the extreme, abrasive environment any coating would be subject to, which would quickly destroy any passive coating. In less harsh environments, any successful passive solution would be retroactively applied to vehicles likely equipped with an electro-thermal de-icing system. Hence, understanding the interplay between coating and electro-thermal de-icing remains critical for viable long-term solutions.

This work is centred on understanding how the presence of electro-thermal de-icing systems affects coating design choices. Testing protocols for icephobic coatings, which are highly variable in a simple passive system, have been developed to allow for understanding their implementation in a hybrid system.

PDMS was selected as an example material over a range of thicknesses with the inclusion of thermally conductive fillers to assess how a coating should be designed for a hybrid application. A coating's surface and thermal properties affect the spreading of impinging droplets and solidification behaviour, leading to changes in the location, type and form of ice accreted.

This process was explored through the ice accretion on a spinning coated aluminium disc due to impinging supercooled droplets striking the stagnation point at the centre and accelerating radially. This highlighted this interplay between ice formation and the disc surface properties within a controlled environment with simplified geometry. The experiment demonstrated how the Stokes number of the droplets and Stefan number are fundamental to the ice growth regime that is present and are essential to understanding why different structures form.

The results of this simplified experiment were informative when designing and interpreting the data from an experiment with more realistic geometry. This study investigated ice accretion on rotating blades in a simulated cloud environment. Changing the rotation and cloud conditions produced discernible differences in the ice geometry at the tip in rime conditions and the formation of ripples within the ice along the leading edge. In wetter growth accretions, these factors also controlled the ice distribution along the blade, which requires a more complex

analysis than for the mass distribution in a rime accretion. The blade icing experiment has significant potential to inform modelling techniques and predict changes a candidate icephobic coating would have on ice accretions if the environmental and operational conditions are known. This has the potential to accelerate the design process and reduce potential unseen hazards, such as the coating changing the ice accretion's structure to one for which its de-icing capabilities are no longer optimised.

The thickness of elastomeric coatings is known to impact the adhesion strength of accreted ice and interfacial toughness. Both are fundamentally important properties when designing a passive coating solution. As enhancing electro-thermal de-icing systems is not well studied, this simple parameter was the first studied alongside surface topography and water contact angle. The power required to de-ice a surface with an electro-thermal system was used to quantify the relative performance of each surface and coating. The thickness of each coating was measured using QNix 8500 coating thickness gauge, which detects changes in the magnetic field to measure the distance between the surface and substrate, the topography was characterised using an optical profilometer and the water contact angle was measured with a sessile droplet technique. As expected in a static scenario, increasing a coating's thickness linearly increases the energy required to de-ice its surface. The surface properties of the coatings tested and uncoated aluminium highlighted that their relative impact was diminished when the coating was in the region of 100 μm or more for the materials tested here. Electro-thermal de-icing performance is much more sensitive to thinner coatings' surface properties, and thicker coatings have their performance primarily dictated by their thermal diffusivity. This was shown by including SiC in PDMS to reduce the per-thickness cost by 59%. Using reference materials, a range of coating thicknesses and environmental temperatures have been tested and can be used to normalise differences in results obtained at a different laboratory with a similarly designed experiment.

As this approach of using a hybrid coating with some passive capability while also working with an active system, the ice adhesion strength is still very relevant and was tested with two different methods. Using a pull test and a centrifuge method, the latter being much more reliable due to the relative ease of consistent operation and smaller standard error of the mean at 3%, roughly a third of the pull test. The ice adhesion strength and static electro-thermal de-icing performance of a coating may not provide a holistic representation of dynamic thermal de-icing performance. If a coating type was more effective at utilising structural vibration, it could be overlooked as inferior if testing of this sort is not performed. A rotating arm was used to apply shear stress at the surface-ice interface during electro-thermal de-icing. In this experiment, increasing the

coating thickness did not produce a linear increase in the time required to de-ice when the rotation velocity was sufficiently high, as the environmental heat loss to the airflow became more significant, extending the time to de-ice further. Some samples failed to de-ice, highlighting the importance of testing coatings in this way to avoid catastrophic failures. Considering the potential benefit of including thermally conductive fillers, despite their significant drawbacks, it could be a benefit of much greater magnitude and be used to increase the durability of the coating. The interplay of properties and different performance metrics could provide a window of opportunity to produce a viable coating tailored to a specific application's needs.

One significant problem within this field is laboratory discrepancies resulting from a lack of standardised testing. It has been mentioned throughout this thesis that providing all contextual information about the testing is necessary for comparisons to be meaningful. A coating's thickness could be increased to reduce its ice adhesion strength and potential to withstand wear. Reducing its thickness reduces its interfacial toughness and the energy cost to de-ice it using an electro-thermal system. Furthermore, changing the geometry of the adhered ice during testing will alter the forces applied to the ice, potentially changing the dominant modes of adhesion failure. It is imperative to characterise the performance of a coating sufficiently, where producing measured improvements can be reductively simple by changing a coating's thickness or using a more favourable testing methodology without analysis of peel stress, for example.

The search for an ultimate passive, icephobic coating remains enticing. However, this thesis underlines the overriding importance of context when selecting design criteria. We have focussed on coupling coatings with electro-thermal strategies, which shows that competing mechanisms can easily lead to contradictory design choices that question what ultimately that coating should achieve. Performance could outstrip the need to consider electro-thermal de-icing alongside coatings or durability concerns, and inconsistencies between different laboratories' testing methods may be dwarfed by the continued progress of making a viable passive solution.

Most vehicles that could utilise a passive solution will not be retired when a suitable coating is verified. Any coating would be retroactively applied, with lifespans of several decades for commercial fixed-wing aircraft. If this is the case, a coating that works alongside electro-thermal de-icing systems could provide a more straightforward goal as work progresses towards a passive solution. If a solution cannot be found with this hybrid approach, then the tests described in this research could form the basis for safety testing during the inevitable trial period before sufficient confidence in a passive solution is obtained.

8.2 Future work

- Expanding the analysis of the blade ice accretion experiments to greater time lengths will provide more clarity on the tip growth mechanisms identified. These should focus on the frequency of nucleation with improved image capture and expanding the testing to blades coated in an icephobic coating to reassess the wet growth analysis used in this work. The use of additional blades with a larger chord length is also necessary to improve the applicability of the results by increasing the Reynolds number. A deeper analysis of the cloud structure to provide more accurate impinging Reynolds numbers would enhance the data obtained, and modelling droplets' motion over the aerofoil's surface in a wet growth regime alongside the disc experiment could provide more granular predictions of the structure of the accretion.

- The disc analysis could be very fruitful if higher Reynolds numbers can be studied. This experiment could be instrumental as a preliminary ice accretion test for icephobic coatings and analysis of their impact on the Weber number to relate the results better to glaze ice accretion on an aerofoil.

- The use of PDMS was a source of several issues, as its transparency limited the characterisation of the surface roughness. However, it is a widely used material, so ideal for comparison. Using a range of matrix materials and fillers would better identify the limitations of the equipment and the relationships identified. SiC or diamond low aspect ratio powder would have been a better choice and should be explored. To provide more precise relationships where the fillers' morphology is less prone to damage, anisotropy or alterations to the surface properties for thinner samples. After more apparent relationships have been identified at thicknesses below 50 μm then work considering the potential anisotropy or durability benefits fibres may offer would be useful. Durability testing would better round out the considerations of this design approach, valuing practicality and specificity as a means to success over a holistic solution.

- Detailed analysis of the relevance of peel stress in the measured ice adhesion strength and the relative impact of peel stress depending on the mechanisms and properties the coating utilises, such as an FEA study for the testing equipment being used that can be referenced. This would include calculating the impact of drag on the applied force and cooling of the testing sample to identify the sources of error across different testing methodologies to provide more representative results of properties like ice adhesion strength and to what extent a coating benefits from peel

stress for overcoming ice adhesion. Both the CAT and dynamic electro-thermal de-icing experiments would benefit from vibrational studies.

- The thermal diffusivity data obtained was of low quality, and broadening the range of coatings tested would provide much more substance to the relationships this work attempted to identify. This would also allow more precise characterisation of the importance of surface properties for thermal de-icing. Balancing this benefit with its potential impact when designing a coating of known thickness can better dictate the design direction. The dynamic thermal de-icing experiment needs significant improvements from this initial version to be more representative. Once it is, it can provide considerable insight into the potential performance or safety limitations of icephobic coatings when employed alongside a thermal de-icing system.

References

[1] P. Collins, S. Gateway, H. O. Centre, D. Equipment, C. Moore, and M. Engineer, “Solutions to helicopter blade erosions~improving aircraft availability and reducing costs,” *Eur. Rotorcr. Forum*, vol. 40, p. Paper No 009, 2014.

[2] R. Rozelle, A. Sanfelici, A. Alvis, and S. Mitchell, “Inflight Icing and the Helicopter,” *Flight Saftey Found. Helicopter Saftey*, vol. 16, no. 6, pp. 1–4, 1990.

[3] L. Gao, Y. Liu, W. Zhou, and H. Hu, “An experimental study on the aerodynamic performance degradation of a wind turbine blade model induced by ice accretion process,” *Renew. Energy*, vol. 133, pp. 663–675, 2019.

[4] A. P. Broeren, M. G. Potapczuk, S. Lee, A. M. Malone, B. P. Paul, and B. S. Woodard, “Ice-accretion test results for three large-scale swept-wing models in the NASA icing research tunnel,” in *8th AIAA Atmospheric and Space Environments Conference*, 2016, no. September 2016, pp. 1–34.

[5] O. Fakorede, Z. Feger, H. Ibrahim, A. Ilinca, J. Perron, and C. Masson, “Ice protection systems for wind turbines in cold climate: characteristics, comparisons and analysis,” *Renew. Sustain. Energy Rev.*, vol. 65, pp. 662–675, 2016.

[6] Y. Cao, W. Tan, and Z. Wu, “Aircraft icing: An ongoing threat to aviation safety,” *Aerosp. Sci. Technol.*, vol. 75, pp. 353–385, Apr. 2018.

[7] S. Tarquini, C. Antonini, A. Amirfazli, M. Marengo, and J. Palacios, “Investigation of ice shedding properties of superhydrophobic coatings on helicopter blades,” *Cold Reg. Sci. Technol.*, vol. 100, pp. 50–58, 2014.

[8] J. Hansson, J. Lindvall, and Ø. Byrkjedal, “Quantification of icing losses in wind farms,” vol. 299, pp. 1–69, 2016.

[9] L. Shu *et al.*, “Study of ice accretion feature and power characteristics of wind turbines at natural icing environment,” *Cold Reg. Sci. Technol.*, vol. 147, no. January, pp. 45–54, 2018.

[10] P. Frohboese and A. Anders, “Effects of icing on wind turbine fatigue loads,” *J. Phys. Conf. Ser.*, vol. 75, no. 1, pp. 1–13, 2007.

[11] Q. Li and Z. Guo, “Fundamentals of icing and common strategies for designing biomimetic anti-icing surfaces,” *J. Mater. Chem. A*, vol. 6, no. 28, pp. 13549–13581, 2018.

[12] X. Huang *et al.*, “A survey of icephobic coatings and their potential use in a hybrid coating/active ice protection system for aerospace applications,” *Prog. Aerosp. Sci.*, vol. 105, no. January, pp. 74–97, 2019.

[13] Y. Liu, Q. Wang, X. Yi, N. Chen, J. Ren, and W. Li, “An anti-icing scaling

method for wind tunnel tests of aircraft thermal ice protection system," *Chinese J. Aeronaut.*, vol. 37, no. 6, pp. 1–6, 2024.

[14] Ethiopian Standards Agency, "Es Iso 12494:2012, Ics: 91.080.01," vol. 12494, 2001.

[15] Z. A. Janjua, B. Turnbull, S. Hibberd, and K. S. Choi, "Mixed ice accretion on aircraft wings," *Phys. Fluids*, vol. 30, no. 2, p. 27101, 2018.

[16] X. Zhang, J. Min, and X. Wu, "Model for aircraft icing with consideration of property-variable rime ice," *Int. J. Heat Mass Transf.*, vol. 97, no. June, pp. 185–190, 2016.

[17] A. S. Van Dyke, D. Collard, M. M. Derby, and A. R. Betz, "Droplet coalescence and freezing on hydrophilic, hydrophobic, and biphilic surfaces," *Appl. Phys. Lett.*, vol. 107, no. 14, pp. 1–5, 2015.

[18] M. Nosonovsky and B. Bhushan, "Roughness optimization for biomimetic superhydrophobic surfaces," *Microsyst. Technol.*, vol. 11, no. 7, pp. 535–549, 2005.

[19] C. Zhu, S. Liu, Y. Shen, J. Tao, G. Wang, and L. Pan, "Verifying the deicing capacity of superhydrophobic anti-icing surfaces based on wind and thermal fields," *Surf. Coatings Technol.*, vol. 309, pp. 703–708, 2017.

[20] K. R. Khedir, G. K. Kannarpady, C. Ryerson, and A. S. Biris, "An outlook on tunable superhydrophobic nanostructural surfaces and their possible impact on ice mitigation," *Prog. Org. Coatings*, vol. 112, no. January, pp. 304–318, 2017.

[21] J. Chen *et al.*, "Superhydrophobic surfaces cannot reduce ice adhesion," *Appl. Phys. Lett.*, vol. 101, no. 11, pp. 18–21, 2012.

[22] H. Y. Zhang, Y. L. Yang, J. F. Pan, H. Long, L. S. Huang, and X. K. Zhang, "Compare study between icephobicity and superhydrophobicity," *Phys. B Condens. Matter*, vol. 556, no. August 2018, pp. 118–130, 2019.

[23] NASA, "Online Pilots guide to De-icing," 2017. [Online]. Available: https://aircrafticing.grc.nasa.gov/2_4_5_1.html. [Accessed: 25-Jun-2019].

[24] A. I. Freeman, B. W. J. Surridge, M. Matthews, M. Stewart, and P. M. Haygarth, "Understanding and managing de-icer contamination of airport surface waters: A synthesis and future perspectives," *Environ. Technol. Innov.*, vol. 3, pp. 46–62, Apr. 2015.

[25] D. Bowden, "Effect of pneumatic de-icers and ice formations on aerodynamic characteristics of an arfoil," *Natl. Advis. Comm. Aeronaughtics*, vol. 16, no. 6, pp. 1–59, 1956.

[26] P. Wheeler and S. Bozhko, "The more electric aircraft: Technology and challenges," *IEEE Electrif. Mag.*, vol. 2, no. 4, pp. 6–12, 2014.

[27] Z. Zhao, H. Chen, X. Liu, H. Liu, and D. Zhang, “Development of high-efficient synthetic electric heating coating for anti-icing/de-icing,” *Surf. Coatings Technol.*, vol. 349, no. June, pp. 340–346, 2018.

[28] A. J. NEGRETTE, “Helicopter Icing Hazards Proficiency and the Private Pilot Great Expectations •,” *Flying Saftey*, no. April, pp. 1–31, 1981.

[29] M. J. Kreder, J. Alvarenga, P. Kim, and J. Aizenberg, “Design of anti-icing surfaces: Smooth, textured or slippery?,” *Nat. Rev. Mater.*, vol. 1, no. 1, pp. 1–15, 2016.

[30] D. Quéré, “Non-sticking drops,” *Reports Prog. Phys.*, vol. 68, no. 11, pp. 2495–2532, 2005.

[31] S. A. Kulinich and M. Farzaneh, “Ice adhesion on super-hydrophobic surfaces,” *Appl. Surf. Sci.*, vol. 255, no. 18, pp. 8153–8157, 2009.

[32] T. Bharathidasan, T. N. Narayanan, S. Sathyanaryanan, and S. S. Sreejakumari, “Above 170° water contact angle and oleophobicity of fluorinated graphene oxide based transparent polymeric films,” *Carbon N. Y.*, vol. 84, no. 1, pp. 207–213, 2015.

[33] N. Wang, L. Tang, W. Tong, and D. Xiong, “Fabrication of robust and scalable superhydrophobic surfaces and investigation of their anti-icing properties,” *Mater. Des.*, vol. 156, pp. 320–328, 2018.

[34] H. Yu *et al.*, “Superhydrophobic carbon nanotube/silicon carbide nanowire nanocomposites,” *Mater. Des.*, vol. 87, pp. 198–204, 2015.

[35] A. Mohammad Karim, J. P. Rothstein, and H. P. Kavehpour, “Experimental study of dynamic contact angles on rough hydrophobic surfaces,” *J. Colloid Interface Sci.*, vol. 513, pp. 658–665, 2018.

[36] T. Liu and C.-J. Kim, “Turning a surface superrepellent even to completely wetting liquids,” *Science (80-.).*, vol. 346, no. 6213, pp. 1096–1099, 2019.

[37] S. Lei, F. Wang, X. Fang, J. Ou, and W. Li, “Icing behavior of water droplets impinging on cold superhydrophobic surface,” *Surf. Coatings Technol.*, vol. 363, no. February, pp. 362–368, 2019.

[38] L. B. Boinovich, A. M. Emelyanenko, K. A. Emelyanenko, and E. B. Modin, “Modus Operandi of Protective and Anti-icing Mechanisms Underlying the Design of Longstanding Outdoor Icephobic Coatings,” *ACS Nano*, vol. 13, pp. 4335–4346, 2019.

[39] M. H. Kim, H. Kim, K. S. Lee, and D. R. Kim, “Frosting characteristics on hydrophobic and superhydrophobic surfaces: A review,” *Energy Convers. Manag.*, vol. 138, pp. 1–11, 2017.

[40] K. Golovin, S. P. R. Kobaku, D. H. Lee, E. T. DiLoreto, J. M. Mabry, and A. Tuteja, “Designing durable icephobic surfaces,” *Sci. Adv.*, vol. 2, no. 3, pp. 1–12, 2016.

[41] N. Li *et al.*, “Ballistic Jumping Drops on Superhydrophobic Surfaces via Electrostatic Manipulation,” *Adv. Mater.*, vol. 30, no. 8, pp. 1–7, 2018.

[42] S. Ozbay, C. Yuceel, and H. Y. Erbil, “Improved Icephobic Properties on Surfaces with a Hydrophilic Lubricating Liquid,” *ACS Appl. Mater. Interfaces*, vol. 7, no. 39, pp. 22067–22077, 2015.

[43] V. Palanque, E. Villeneuve, M. Budinger, V. Pommier-Budinger, and G. Momen, “Experimental measurement and expression of atmospheric ice Young’s modulus according to its density,” *Cold Reg. Sci. Technol.*, vol. 212, no. May, p. 103890, 2023.

[44] Q. Luo and L. Tong, “Linear and higher order displacement theories for adhesively bonded lap joints,” *Int. J. Solids Struct.*, vol. 41, no. 22–23, pp. 6351–6381, 2004.

[45] M. Schulz and M. Sinapius, “Evaluation of Different Ice Adhesion Tests for Mechanical Deicing Systems Methods of Ice Adhesion Strength Measurement,” *SAE Int.*, no. June, pp. 1–9, 2015.

[46] Z. A. Janjua, “The influence of freezing and ambient temperature on the adhesion strength of ice,” *Cold Reg. Sci. Technol.*, vol. 140, no. October 2016, pp. 14–19, 2017.

[47] L. Li, Y. Liu, Z. Zhang, and H. Hu, “Effects of thermal conductivity of airframe substrate on the dynamic ice accretion process pertinent to UAS inflight icing phenomena,” *Int. J. Heat Mass Transf.*, vol. 131, pp. 1184–1195, 2019.

[48] Y. Li *et al.*, “Submicron/nano-structured icephobic surfaces made from fluorinated polymethylsiloxane and octavinyl-POSS,” *Appl. Surf. Sci.*, vol. 360, pp. 113–120, 2016.

[49] H. Memon, J. Liu, D. S. A. De Focatiis, K. so Choi, and X. Hou, “Intrinsic dependence of ice adhesion strength on surface roughness,” *Surf. Coatings Technol.*, vol. 385, no. October 2019, p. 125382, 2020.

[50] Z. He, S. Xiao, H. Gao, J. He, and Z. Zhang, “Multiscale crack initiator promoted super-low ice adhesion surfaces,” *Soft Matter*, vol. 13, no. 37, pp. 6562–6568, 2017.

[51] P. Irajizad *et al.*, “Stress-localized durable icephobic surfaces,” *Mater. Horizons*, vol. 6, no. 4, pp. 758–766, 2019.

[52] K. Golovin, A. Dhyani, M. D. Thouless, and A. Tuteja, “Low-interfacial toughness materials for effective large-scale deicing,” *Science (80-.).*, vol. 364, no. 6438, pp. 371–375, 2019.

[53] M. Mohseni, Z. A. Dijvejin, and K. Golovin, “Designing scalable elastomeric anti-fouling coatings : Shear strain dissipation via interfacial cavitation,” *J. Colloid Interface Sci.*, vol. 589, pp. 556–567, 2021.

[54] K. Alasvand Zarasvand, D. Orchard, C. Clark, and K. Golovin, “Effect of

curvature on durable ice-phobic surfaces based on buckling metallic plates," *Mater. Des.*, vol. 220, p. 110884, 2022.

[55] Z. Azimi Dijvejin, M. C. Jain, R. Kozak, M. H. Zarifi, and K. Golovin, "Smart low interfacial toughness coatings for on-demand de-icing without melting," *Nat. Commun.*, vol. 13, no. 1, p. 5119, 2022.

[56] L. Ding, S. Chang, X. Yi, and M. Song, "Coupled thermo-mechanical analysis of stresses generated in impact ice during in-flight de-icing," *Appl. Therm. Eng.*, vol. 181, no. April, p. 115681, 2020.

[57] F. Wang, B. Yang, Z. Zhang, Q. He, and Y. Zhang, "Synergistic effect of hybrid fillers on electro-thermal behavior of nanocomposite for active de-icing application," *Compos. Commun.*, vol. 25, no. March, p. 100746, 2021.

[58] Y. Zheng, J. Wang, J. Liu, K. S. Choi, and X. Hou, "Energy saving strategy for the development of icephobic coatings and surfaces," *Thin Solid Films*, vol. 687, no. April, p. 137458, 2019.

[59] C. Wang, T. Fuller, W. Zhang, and K. J. Wynne, "Thickness dependence of ice removal stress for a polydimethylsiloxane nanocomposite: Sylgard 184," *Langmuir*, vol. 30, no. 43, pp. 12819–12826, 2014.

[60] M. G. Worster, *Solidification of fluids*. 2000.

[61] J. K. Hunter, "Dimensional Analysis, Scaling, and Similarity," in *Lecture Notes on Applied Mathematics*, 2009, pp. 11–42.

[62] M. Susoff, K. Siegmann, C. Pfaffenroth, and M. Hirayama, "Evaluation of icephobic coatings - Screening of different coatings and influence of roughness," *Appl. Surf. Sci.*, vol. 282, pp. 870–879, 2013.

[63] T. Zhu *et al.*, "A polydimethylsiloxane coating with excellent large-scale deicing property and durability," *J. Ind. Eng. Chem.*, vol. 139, no. April, pp. 492–501, 2024.

[64] S. Dogru, B. Aksoy, H. Bayraktar, and B. E. Alaca, "Poisson's ratio of PDMS thin films," *Polym. Test.*, vol. 69, no. April, pp. 375–384, 2018.

[65] A. Work and Y. Lian, "A critical review of the measurement of ice adhesion to solid substrates," *Prog. Aerosp. Sci.*, vol. 98, no. March, pp. 1–26, 2018.

[66] Z. Wang, "Recent progress on ultrasonic de-icing technique used for wind power generation, high-voltage transmission line and aircraft," *Energy Build.*, vol. 140, pp. 42–49, 2017.

[67] C. Laforte and A. Beisswenger, "Icephobic Materials Centrifuge Adhesion Test," 2018, no. January 2005, pp. 1–5.

[68] M. K. Chaudhury and K. H. Kim, "Shear-induced adhesive failure of a rigid slab in contact with a thin confined film," *Eur. Phys. J. E*, vol. 23, no. 2, pp. 175–183, 2007.

[69] J. Liu *et al.*, “Hydrophobic/icephobic coatings based on thermal sprayed metallic layers with subsequent surface functionalization,” *Surf. Coatings Technol.*, vol. 357, no. October 2018, pp. 267–272, 2019.

[70] J. Liu *et al.*, “Super-hydrophobic/icephobic coatings based on silica nanoparticles modified by self-assembled monolayers,” *Nanomaterials*, vol. 6, no. 12, p. 232, 2016.

[71] H. Memon, D. S. A. De Focatiis, K. S. Choi, and X. Hou, “Durability enhancement of low ice adhesion polymeric coatings,” *Prog. Org. Coatings*, vol. 151, no. November 2020, p. 106033, 2021.

[72] J. Liu *et al.*, “Development and evaluation of poly(dimethylsiloxane) based composite coatings for icephobic applications,” *Surf. Coatings Technol.*, vol. 349, no. April, pp. 980–985, 2018.

[73] J. Li *et al.*, “Durable one-component polyurea icephobic coatings with energy-saving performance in electrical heating de-icing,” *Chem. Eng. J.*, vol. 498, no. June, p. 155793, 2024.

[74] T. Ren and J. He, “Substrate-versatile approach to robust antireflective and superhydrophobic coatings with excellent self-cleaning property in varied environments,” *ACS Appl. Mater. Interfaces*, vol. 9, no. 39, pp. 34367–34376, 2017.

[75] Z. Zhang *et al.*, “A novel thermo-mechanical anti-icing/de-icing system using bi-stable laminate composite structures with superhydrophobic surface,” *Compos. Struct.*, vol. 180, pp. 933–943, 2017.

[76] X. Wang, X. Huang, Z. Ji, W. Hu, H. Sheng, and X. Li, “Self-healing icephobic coating with UV shielding and removability based on biobased epoxy and reversible disulfide bonds,” *Polymer (Guildf).*, vol. 283, no. August, p. 126274, 2023.

[77] O. Redondo, S. G. Prolongo, M. Campo, C. Sbarufatti, and M. Giglio, “Anti-icing and de-icing coatings based Joule’s heating of graphene nanoplatelets,” *Compos. Sci. Technol.*, vol. 164, no. February, pp. 65–73, 2018.

[78] X. Liu, H. Chen, Z. Zhao, Y. Yan, and D. Zhang, “Slippery liquid-infused porous electric heating coating for anti-icing and de-icing applications,” *Surf. Coatings Technol.*, vol. 374, pp. 889–896, 2019.

[79] S. Dash, J. de Ruiter, and K. K. Varanasi, “Photothermal trap utilizing solar illumination for ice mitigation,” *Sci. Adv.*, vol. 4, no. 8, pp. 1–7, 2018.

[80] J. Soltis, J. Palacios, T. Eden, and D. Wolfe, “Evaluation of Ice-Adhesion Strength on Erosion-Resistant Materials,” *AIAA J.*, vol. 53, no. 7, pp. 1825–1835, 2014.

[81] Y. Han, J. Palacios, and S. Schmitz, “Scaled ice accretion experiments on a rotating wind turbine blade,” *J. Wind Eng. Ind. Aerodyn.*, vol. 109, pp. 55–67, 2012.

[82] H. Sun *et al.*, “Experimental investigation of surface wettability induced anti-icing characteristics in an ice wind tunnel,” *Renew. Energy*, vol. 179, pp. 1179–1190, 2021.

[83] M. Vargas and E. Reshotko, “Parametric experimental study of the formation of glaze ice shapes on swept wings,” in *37th Aerospace Sciences Meeting and Exhibit*, 1999, no. June 1999, p. 208900.

[84] A. Elzaabalawy and S. A. Meguid, “Development of novel icephobic surfaces using siloxane-modified epoxy nanocomposites,” *Chem. Eng. J.*, vol. 433, no. P3, p. 133637, 2022.

[85] Y. Li, C. Sun, Y. Jiang, X. Yi, Z. Xu, and W. Guo, “Temperature effect on icing distribution near blade tip of large-scale horizontal-axis wind turbine by numerical simulation,” *Adv. Mech. Eng.*, vol. 10, no. 11, pp. 1–13, 2018.

[86] G. M. Ibrahim, K. Pope, and Y. S. Muzychka, “Transient atmospheric ice accretion on wind turbine blades,” *Wind Eng.*, vol. 42, no. 6, pp. 596–606, 2018.

[87] H. Li, X. Li, C. Luo, Y. Zhao, and X. Yuan, “Icephobicity of polydimethylsiloxane-b-poly(fluorinated acrylate),” *Thin Solid Films*, vol. 573, pp. 67–73, 2014.

[88] L. C. S. Nunes, “Mechanical characterization of hyperelastic polydimethylsiloxane by simple shear test,” *Mater. Sci. Eng. A*, vol. 528, no. 3, pp. 1799–1804, 2011.

[89] I. D. Johnston, D. K. McCluskey, C. K. L. Tan, and M. C. Tracey, “Mechanical characterization of bulk Sylgard 184 for microfluidics and microengineering,” *J. Micromechanics Microengineering*, vol. 24, no. 3, 2014.

[90] Y. S. Touloukian and C. Y. Ho, *Thermophysical Properties of Matter*, vol. 4. 1970.

[91] Siemens Wind Power, “Siemens Wind Turbine SWT-2.3-108,” *Siemens*, pp. 1–8, 2011.

[92] R. M. Stringer, A. J. Hillis, and J. Zang, “Numerical investigation of laboratory tested cross-flow tidal turbines and Reynolds number scaling,” *Renew. Energy*, vol. 85, pp. 1316–1327, 2016.

[93] Omron, *NE-U17 Instruction Manual*. 2014.

[94] “ISO 12494:2017, Atmospheric Icing of Structures, Mar. 2017.”

[95] J. Y. Jin and M. S. Virk, “Study of ice accretion and icing effects on aerodynamic characteristics of DU96 wind turbine blade profile,” *Cold Reg. Sci. Technol.*, vol. 160, no. January, pp. 119–127, 2019.

[96] D. Olejniczak and M. Nowacki, “Evaluation of the Influence of Icing on Wings on Aircraft Flight Parameters,” *Transp. Res. Procedia*, vol. 35, pp.

100–109, 2018.

[97] E. B. Lebatto, M. Farzaneh, and E. P. Lozowski, “Conductor icing: Comparison of a glaze icing model with experiments under severe laboratory conditions with moderate wind speed,” *Cold Reg. Sci. Technol.*, vol. 113, pp. 20–30, 2015.

[98] A. Zanon, M. De Gennaro, and H. Kühnelt, “Wind energy harnessing of the NREL 5 MW reference wind turbine in icing conditions under different operational strategies,” *Renew. Energy*, vol. 115, pp. 760–772, 2018.

[99] W. Lian, L. Zhao, Y. Xuan, and J. Shen, “A modified spongy icing model considering the effect of droplets retention on the ice accretion process,” *Appl. Therm. Eng.*, vol. 134, no. August 2017, pp. 54–61, 2018.

[100] S. Tarquini, C. Antonini, A. Amirfazli, M. Marengo, and J. Palacios, “Investigation of ice shedding properties of superhydrophobic coatings on helicopter blades,” *Cold Reg. Sci. Technol.*, vol. 100, pp. 50–58, Apr. 2014.

[101] W. K. Du, Y. S. Zhao, H. Liu, and Y. P. He, “Analysis of the critical reynolds number for floating wind turbine blades,” *Proc. 11th Pacific/Asia Offshore Mech. Symp. PACOMS 2014*, no. October, pp. 7–12, 2014.

[102] K. Yousefi and A. Razeghi, “Determination of the critical reynolds number for flow over symmetric NACA airfoils,” *AIAA Aerosp. Sci. Meet. 2018*, no. January, pp. 1–11, 2018.

[103] R. J. MacLoughlin, B. D. Higgins, J. G. Laffey, and T. O’Brien, “Optimized aerosol delivery to a mechanically ventilated rodent,” *J. Aerosol Med. Pulm. Drug Deliv.*, vol. 22, no. 4, pp. 323–332, 2009.

[104] D. Anderson, “Further evaluation of traditional icing scaling methods,” *34th Aerosp. Sci. Meet. Exhib.*, vol. 34, p. 107140, Jan. 1996.

[105] D. Liao, M. He, and H. Qiu, “High-performance icephobic droplet rebound surface with nanoscale doubly reentrant structure,” *Int. J. Heat Mass Transf.*, vol. 133, pp. 341–351, 2019.

[106] D. Anderson, “Evaluation of constant-Weber-number scaling for icing tests,” *34th Aerosp. Sci. Meet. Exhib.*, vol. 34, p. 107141, Jan. 1996.

[107] D. Anderson and A. Feo, “Ice-accretion scaling using water-film thickness parameters,” in *40th AIAA Aerospace Sciences Meeting & Exhibit*, 2002, no. June 2003, p. 211826.

[108] J. Wang and M. Wu, “Surface & Coatings Technology Study on durable icephobic surfaces modified with phase change oil impregnation,” *Surf. Coat. Technol.*, vol. 481, no. November 2023, p. 130646, 2024.

[109] B. H. Lau, A. W. Louie, N. Griffiths, and C. P. Sotiriou, “Performance and rotor loads measurements of the Lynx XZ170 helicopter with rectangular blades,” *NASA Tech. Memo. 104000*, vol. may, no. 1, p. 362, 1993.

Appendix

Blade icing

Table F Property fields for the large, 215 mm, blade for testing at -10°C where the environmental conditions provide the largest Reynolds and Stokes numbers for the tested speed. Showing the Reynolds number, Stokes number and the product of the two, ReSt. Percentile values represent positions along the leading edge with 0 at the root and 100 at the tip.

Key	Stokes number	Reynolds number	ReSt
	St<0.1	$Re<10^3$	$ReSt<10^3$
	$0.1 \leq St < 0.8$	$10^3 \leq Re < 10^4$	$10^3 \leq ReSt < 10^4$
	$0.8 \leq St < 1.2$	$10^4 \leq Re < 10^5$	$10^4 \leq ReSt < 10^5$
	$1.2 \leq St$	$10^5 \leq Re$	$10^5 \leq ReSt$

RPM	Tip speed (m/s)	Reynolds number at each percentile 20th	40th	60th	80th	100th
500	12.04	5.50E+03	9.58E+03	1.03E+04	9.46E+03	8.73E+03
1000	24.09	1.10E+04	1.92E+04	2.06E+04	1.89E+04	1.75E+04
1500	36.13	1.65E+04	2.87E+04	3.10E+04	2.84E+04	2.62E+04
2000	48.17	2.20E+04	3.83E+04	4.13E+04	3.78E+04	3.49E+04
2500	60.21	2.75E+04	4.79E+04	5.16E+04	4.73E+04	4.36E+04
3000	72.26	3.30E+04	5.75E+04	6.19E+04	5.68E+04	5.24E+04

RPM	Tip speed (m/s)	Stokes number at each percentile, 2µm -10°C 20th	40th	60th	80th	100th
500	12.04	0.002	0.003	0.006	0.011	0.018
1000	24.09	0.004	0.006	0.012	0.022	0.036
1500	36.13	0.005	0.009	0.018	0.033	0.053
2000	48.17	0.007	0.013	0.024	0.043	0.071
2500	60.21	0.009	0.016	0.030	0.054	0.089
3000	72.26	0.011	0.019	0.035	0.065	0.107

RPM	Tip speed (m/s)	ReSt at each percentile, 2µm -10°C 20th	40th	60th	80th	100th
500	12.04	9.89E+00	3.00E+01	6.10E+01	1.03E+02	1.56E+02
1000	24.09	3.96E+01	1.20E+02	2.44E+02	4.11E+02	6.22E+02
1500	36.13	8.90E+01	2.70E+02	5.49E+02	9.25E+02	1.40E+03
2000	48.17	1.58E+02	4.80E+02	9.75E+02	1.65E+03	2.49E+03
2500	60.21	2.47E+02	7.50E+02	1.52E+03	2.57E+03	3.89E+03
3000	72.26	3.56E+02	1.08E+03	2.19E+03	3.70E+03	5.60E+03

RPM	Tip speed (m/s)	Stokes number at each percentile, 4.6µm -10°C 20th	40th	60th	80th	100th
500	12.04	0.010	0.017	0.031	0.057	0.094
1000	24.09	0.019	0.033	0.062	0.115	0.189
1500	36.13	0.029	0.050	0.094	0.172	0.283
2000	48.17	0.038	0.066	0.125	0.230	0.377
2500	60.21	0.048	0.083	0.156	0.287	0.471
3000	72.26	0.057	0.099	0.187	0.345	0.566

RPM	Tip speed (m/s)	percentile, 20th	0 40th	0 60th	0 80th	0 100th
500	12.04	5.23E+01	1.59E+02	3.23E+02	5.44E+02	8.23E+02
1000	24.09	2.09E+02	6.35E+02	1.29E+03	2.18E+03	3.29E+03
1500	36.13	4.71E+02	1.43E+03	2.90E+03	4.90E+03	7.41E+03
2000	48.17	8.37E+02	2.54E+03	5.16E+03	8.70E+03	1.32E+04
2500	60.21	1.31E+03	3.97E+03	8.06E+03	1.36E+04	2.06E+04
3000	72.26	1.88E+03	5.71E+03	1.16E+04	1.96E+04	2.96E+04

RPM	Tip speed (m/s)	Stokes number at each percentile, 10µm -10°C 20th	40th	60th	80th	100th
500	12.04	0.045	0.078	0.148	0.272	0.446
1000	24.09	0.090	0.157	0.295	0.543	0.891
1500	36.13	0.135	0.235	0.443	0.815	1.337
2000	48.17	0.180	0.313	0.591	1.087	1.782
2500	60.21	0.225	0.391	0.738	1.358	2.228
3000	72.26	0.270	0.470	0.886	1.630	2.673

RPM	Tip speed (m/s)	ReSt at each percentile, 10µm -10°C 20th	40th	60th	80th	100th
500	12.04	2.47E+02	7.50E+02	1.52E+03	2.57E+03	3.89E+03
1000	24.09	9.89E+02	3.00E+03	6.10E+03	1.03E+04	1.56E+04
1500	36.13	2.23E+03	6.75E+03	1.37E+04	2.31E+04	3.50E+04
2000	48.17	3.96E+03	1.20E+04	2.44E+04	4.11E+04	6.22E+04
2500	60.21	6.18E+03	1.87E+04	3.81E+04	6.43E+04	9.72E+04
3000	72.26	8.90E+03	2.70E+04	5.49E+04	9.25E+04	1.40E+05

Table G Property fields for the small, 146 mm, blade for testing at -10°C where the environmental conditions provide the largest Reynolds and Stokes numbers for the tested speed. Showing the Reynolds number, Stokes number and the product of the two, ReSt. Percentile values represent positions along the leading edge, with 0 at the root and 100 at the tip.

Key	Stokes number	Reynolds number	ReSt
	St<0.1	$Re<10^3$	$ReSt<10^3$
	$0.1 \le St < 0.8$	$10^3 \le Re < 10^4$	$10^3 \le ReSt < 10^4$
	$0.8 \le St < 1.2$	$10^4 \le Re < 10^5$	$10^4 \le ReSt < 10^5$
	$1.2 \le St$	$10^5 \le Re$	$10^5 \le ReSt$

RPM	Tip speed (m/s)	Reynolds number at each percentile				
		20th	40th	60th	80th	100th
500	8.43	1.42E+03	3.45E+03	4.49E+03	4.97E+03	6.79E+04
1000	16.86	2.85E+03	6.90E+03	8.98E+03	9.95E+03	1.36E+05
1500	25.29	4.27E+03	1.03E+04	1.35E+04	1.49E+04	2.04E+05
2000	33.72	5.69E+03	1.38E+04	1.80E+04	1.99E+04	2.72E+05
2500	42.15	7.12E+03	1.72E+04	2.24E+04	2.49E+04	3.39E+05
3000	50.58	8.54E+03	2.07E+04	2.69E+04	2.98E+04	4.07E+05

RPM	Tip speed (m/s)	Stokes number at each percentile, 2µm -10°C				
		20th	40th	60th	80th	100th
500	8.43	0.001	0.003	0.005	0.008	0.001
1000	16.86	0.003	0.006	0.010	0.016	0.002
1500	25.29	0.004	0.008	0.015	0.024	0.003
2000	33.72	0.005	0.011	0.020	0.032	0.004
2500	42.15	0.007	0.014	0.025	0.040	0.006
3000	50.58	0.008	0.017	0.030	0.048	0.007

RPM	Tip speed (m/s)	ReSt at each percentile, 2µm -10°C				
		20th	40th	60th	80th	100th
500	8.43	1.95E+00	9.54E+00	2.21E+01	3.98E+01	7.62E+01
1000	16.86	7.80E+00	3.82E+01	8.86E+01	1.59E+02	3.05E+02
1500	25.29	1.75E+01	8.58E+01	1.99E+02	3.58E+02	6.86E+02
2000	33.72	3.12E+01	1.53E+02	3.54E+02	6.36E+02	1.22E+03
2500	42.15	4.87E+01	2.38E+02	5.54E+02	9.94E+02	1.91E+03
3000	50.58	7.02E+01	3.43E+02	7.97E+02	1.43E+03	2.74E+03

RPM	Tip speed (m/s)	Stokes number at each percentile, 4.6µm -10°C				
		20th	40th	60th	80th	100th
500	8.43	0.007	0.015	0.026	0.042	0.006
1000	16.86	0.014	0.029	0.052	0.085	0.012
1500	25.29	0.022	0.044	0.078	0.127	0.018
2000	33.72	0.029	0.059	0.104	0.169	0.024
2500	42.15	0.036	0.073	0.131	0.211	0.030
3000	50.58	0.043	0.088	0.157	0.254	0.036

RPM	Tip speed (m/s)	ReSt at each percentile, 4.6µm -10°C				
		20th	40th	60th	80th	100th
500	8.43	1.03E+01	5.05E+01	1.17E+02	2.10E+02	4.03E+02
1000	16.86	4.12E+01	2.02E+02	4.69E+02	8.41E+02	1.61E+03
1500	25.29	9.28E+01	4.54E+02	1.05E+03	1.89E+03	3.63E+03
2000	33.72	1.65E+02	8.07E+02	1.87E+03	3.37E+03	6.45E+03
2500	42.15	2.58E+02	1.26E+03	2.93E+03	5.26E+03	1.01E+04
3000	50.58	3.71E+02	1.82E+03	4.22E+03	7.57E+03	1.45E+04

RPM	Tip speed (m/s)	Stokes number at each percentile, 10µm -10°C				
		20th	40th	60th	80th	100th
500	8.43	0.034	0.069	0.123	0.200	0.028
1000	16.86	0.068	0.138	0.247	0.400	0.056
1500	25.29	0.103	0.207	0.370	0.599	0.084
2000	33.72	0.137	0.277	0.493	0.799	0.112
2500	42.15	0.171	0.346	0.617	0.999	0.140
3000	50.58	0.205	0.415	0.740	1.199	0.168

RPM	Tip speed (m/s)	ReSt at each percentile, 10µm -10°C				
		20th	40th	60th	80th	100th
500	8.43	4.87E+01	2.38E+02	5.54E+02	9.94E+02	1.91E+03
1000	16.86	1.95E+02	9.54E+02	2.21E+03	3.98E+03	7.62E+03
1500	25.29	4.39E+02	2.15E+03	4.98E+03	8.95E+03	1.71E+04
2000	33.72	7.80E+02	3.82E+03	8.86E+03	1.59E+04	3.05E+04
2500	42.15	1.22E+03	5.96E+03	1.38E+04	2.48E+04	4.76E+04
3000	50.58	1.75E+03	8.58E+03	1.99E+04	3.58E+04	6.86E+04

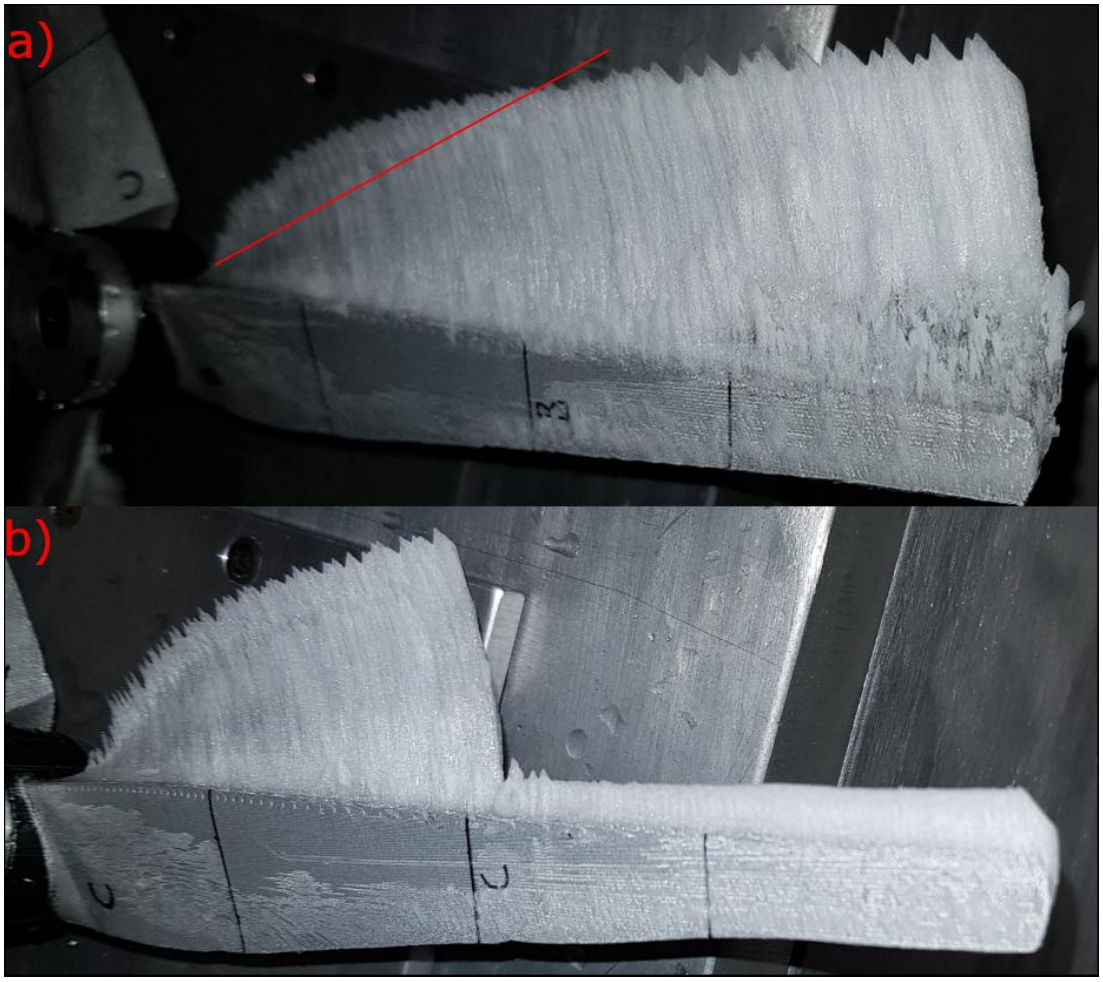

Figure O Extreme accretion after 30 minutes at 500 rpm in a -4°C environment with the line extending from the rime angle a). Highlighting the limitations of extrapolating this feature. b) shows a better view of this angle on a blade that experienced shedding.

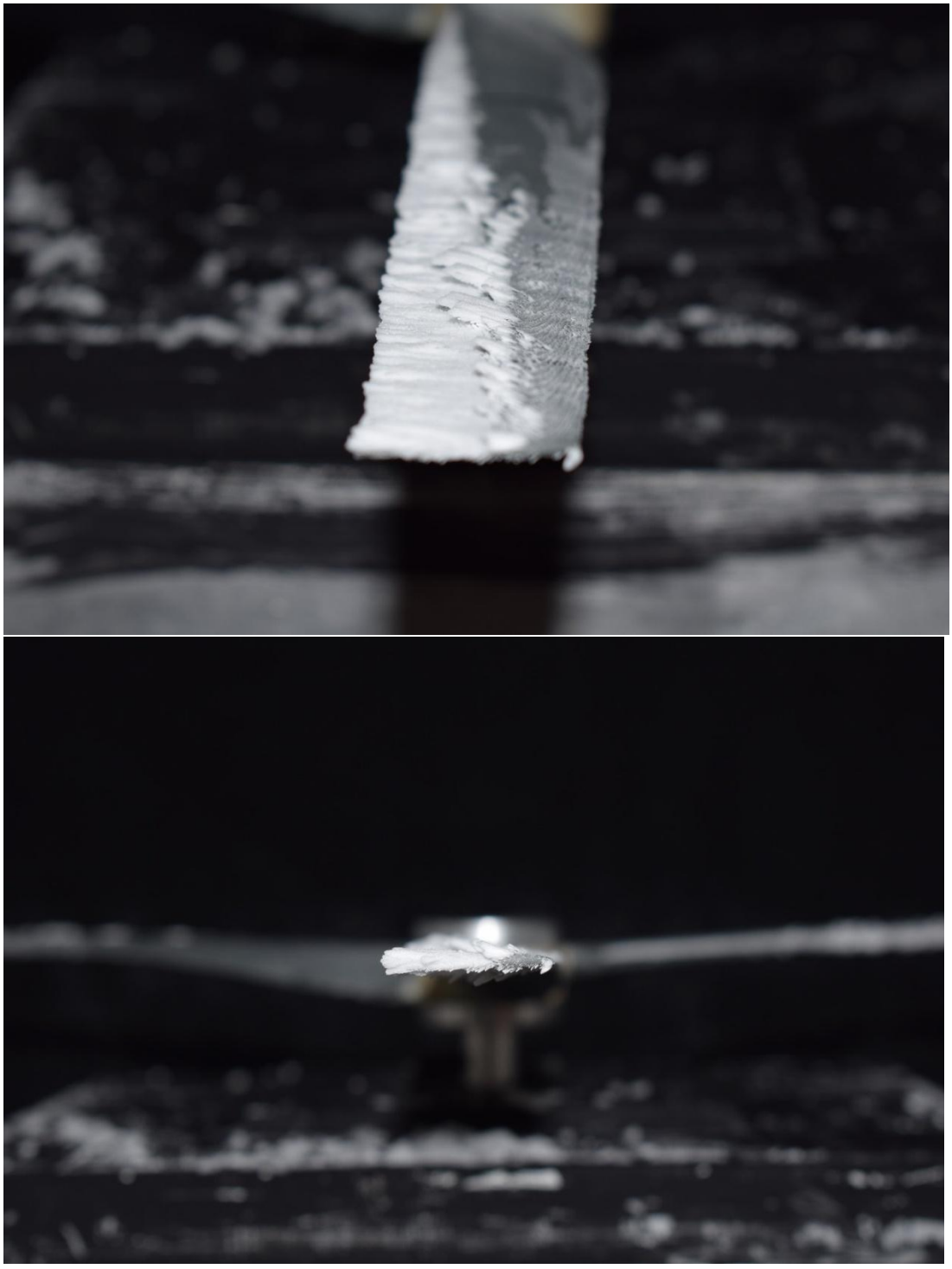

Figure P tip image used for the 10-minute, 500 rpm analysis for -10°C with an additional view above displaying horn structures.

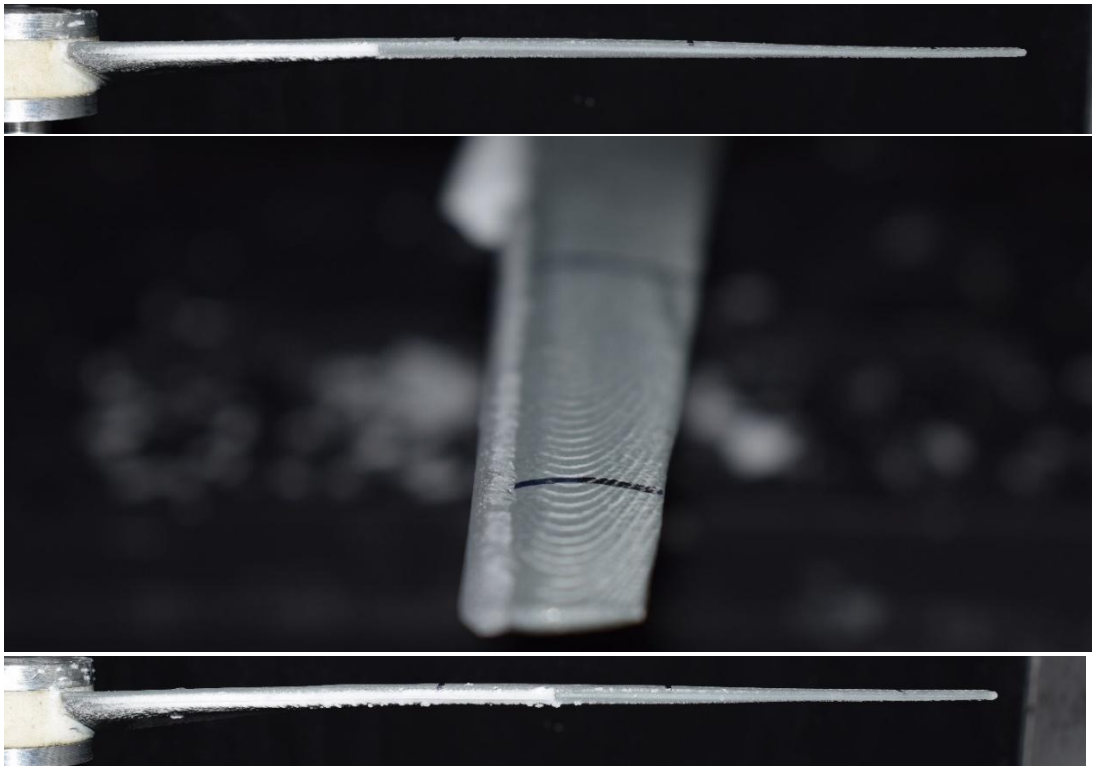

Figure Q Additional images of the shedding captured after 10 minutes at 2500 rpm in a -6°C cloud with two blades shedding at different positions along the leading edge.

Disc icing

Additional properties of the ice were present that could not be adequately quantified. Figure R shows the PDMS disc with no ice accretion at the centre in an irregular shape, indicating the coating may have delayed freezing to occur away from the stagnation point.

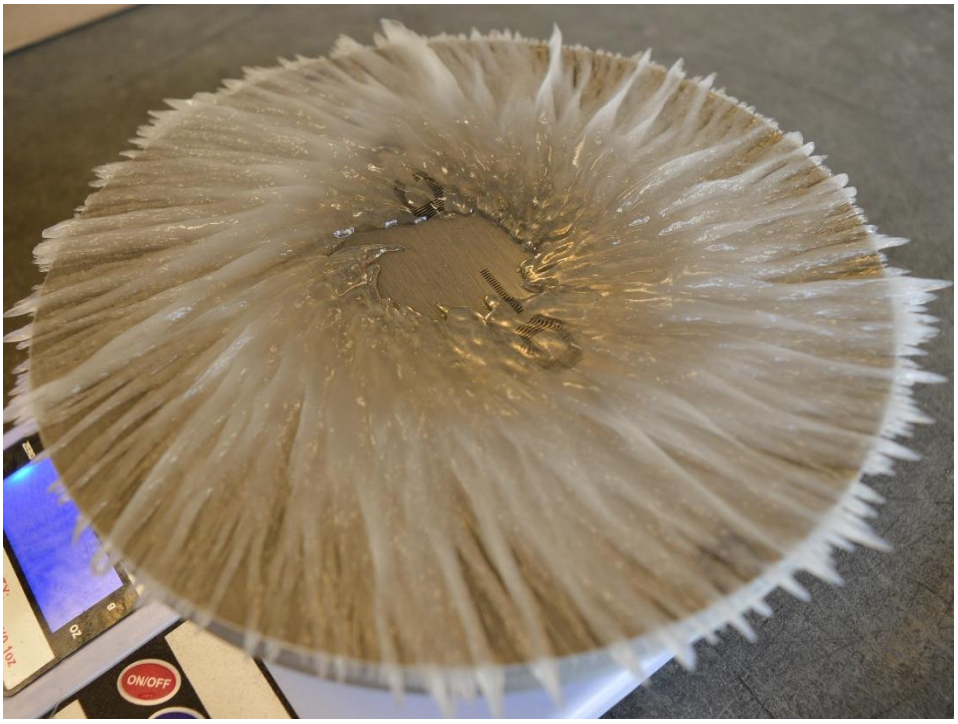

Figure R PDMS coated disc with no accretion forming at the centre.

A second run, Figure S, shows clearly that consistency between tests was not adequate. This result shows adhered ice at the centre. Features that could not be accurately analysed include the proportion of volume above the glazed area, which is air, the maximum height reached at the transition point and ripples visible on the glaze accretion with a higher wave number than the protrusions.

Figure S PDMS disc, from two perspectives, with the centre covered with glaze ice that is much thinner than at the transition point containing ripples with a much smaller wavelength than the protrusions.

Identical issues were found with the PDMS 5% SiC data collection Figure T, displaying a different structure to that seen in Figure S with no qualitative difference measured.

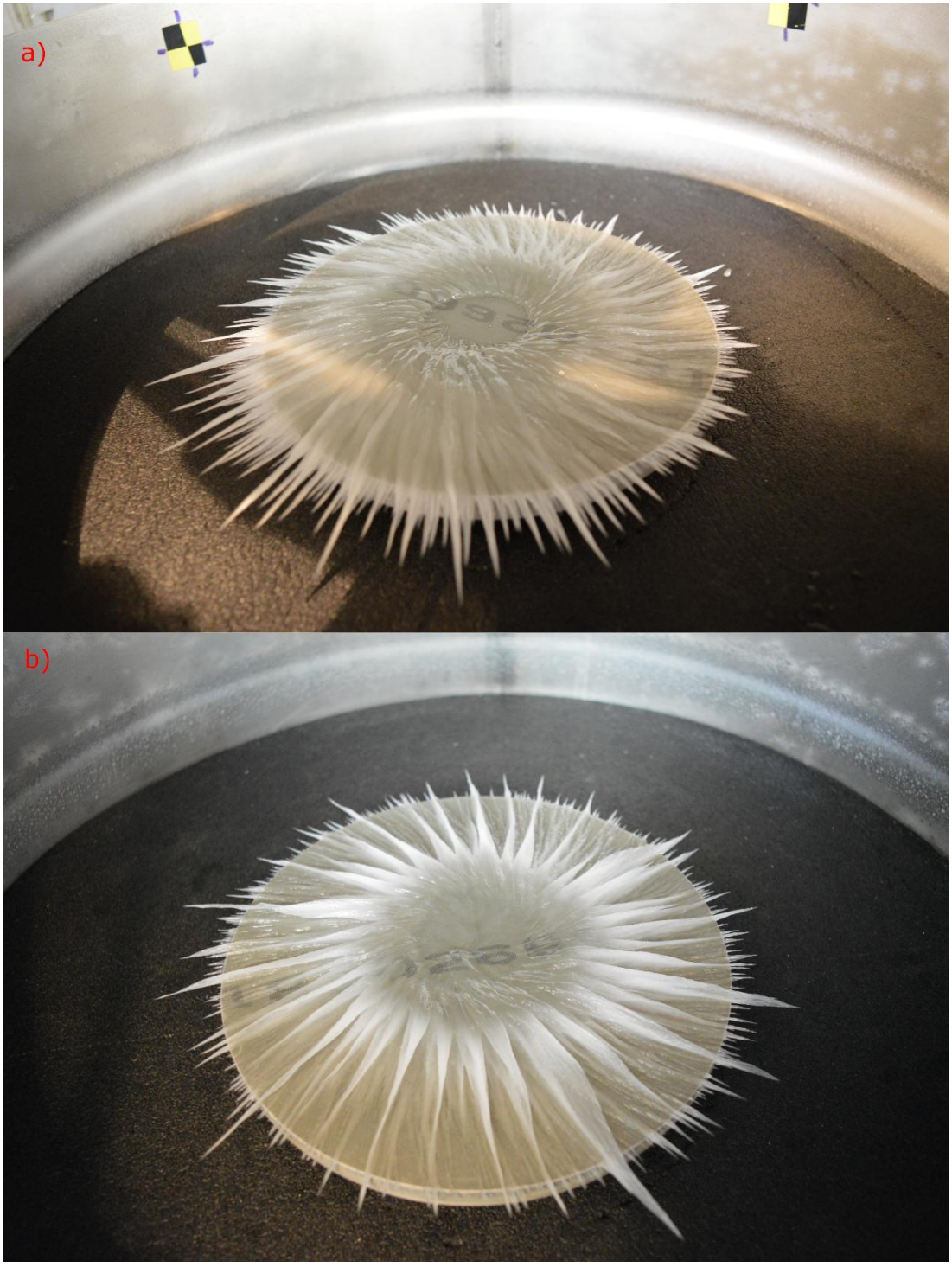

Figure T a) PDMS 5% SiC disc showing no accretion in the centre and significant accretion on the drum wall and b) an irregular geometry on the surface of the glaze ice in the centre with a larger overall accretion and less on the drum wall.

The strip disc produced mixed ice over the uncoated strips, and the glaze ice above them was thicker than the neighbouring uncoated radius chord, with a small area at the centre with no accretion present.

Figure U Example of accretion on the strip disc.

The sand-blasted disc produced mixed ice at the transition point where the accretion pattern changes from a glaze ice radius to protrusions, but then the protrusions turn back to glaze ice as the radius increases, Figure V.

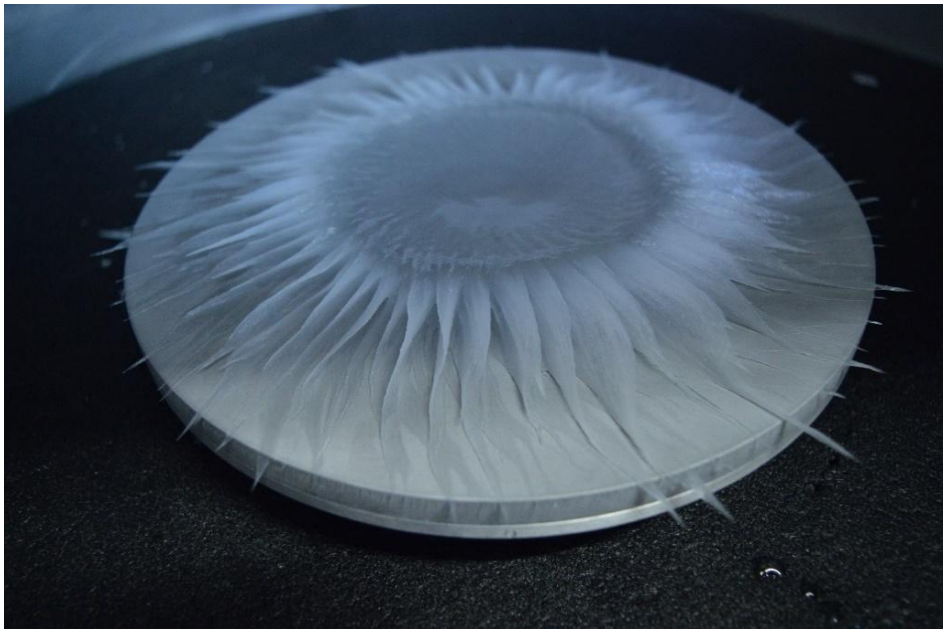

Figure V Accretion on the sandblasted disc.

The cross disc exhibited an increase in ice opacity as with the strip disc but was not as significant Figure W.

Figure W Cross disc accretion.

The petal disc changed the glaze ice radius such that it was less consistent depending on the angle measured Figure X. When comparing this disc, which has two directions of curvature of uncoated strips, both the wavenumber and its error did not appear to be affected by this when compared to both patterned and unpatterned surfaces.

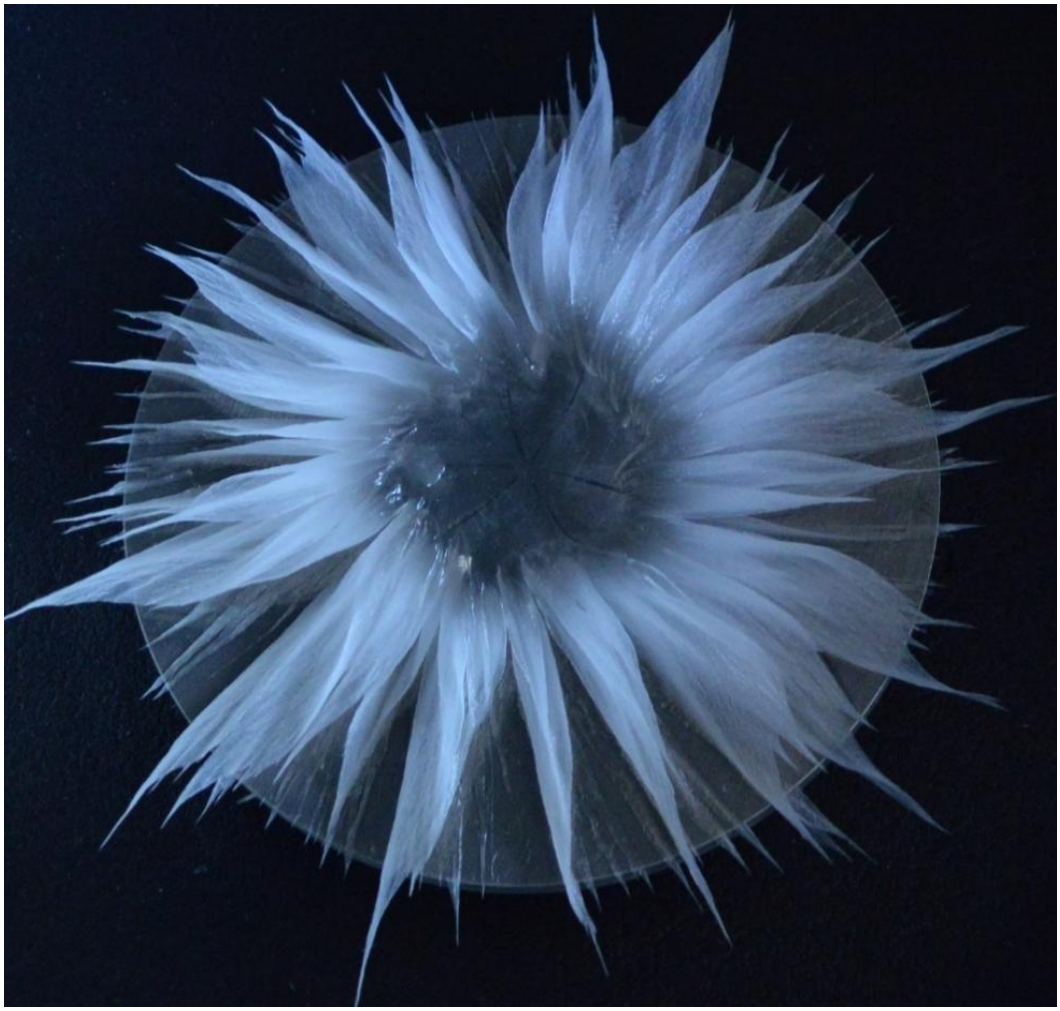

Figure X Petal disc accretion.

POTS functionalised aluminium

Preliminary testing of as-received and grit-blasted aluminium functionalised with POTS, a highly fluorinated self-assembling monolayer. Considering only the first de-icing result for the POTS surfaces produces a reduction in energy consumption of roughly 10%, Figure Y and Figure Z.

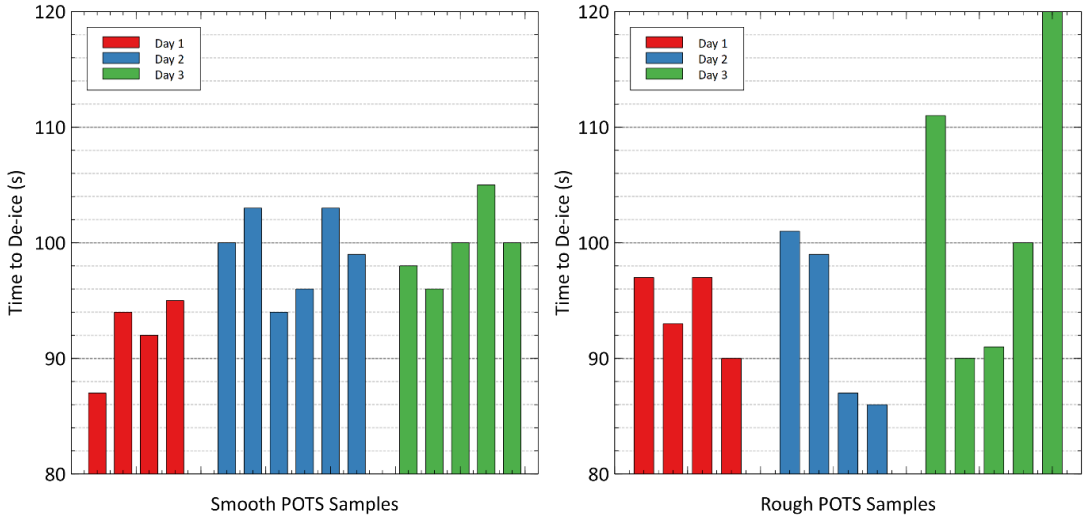

Figure Y Freezing cycle change in performance of POTS functionalised surfaces. Each bar represents a single data point from one sample. The disparity in the number of results per day is due to spilt ice overflowing from the mould or supercooling, causing no freezing to occur.

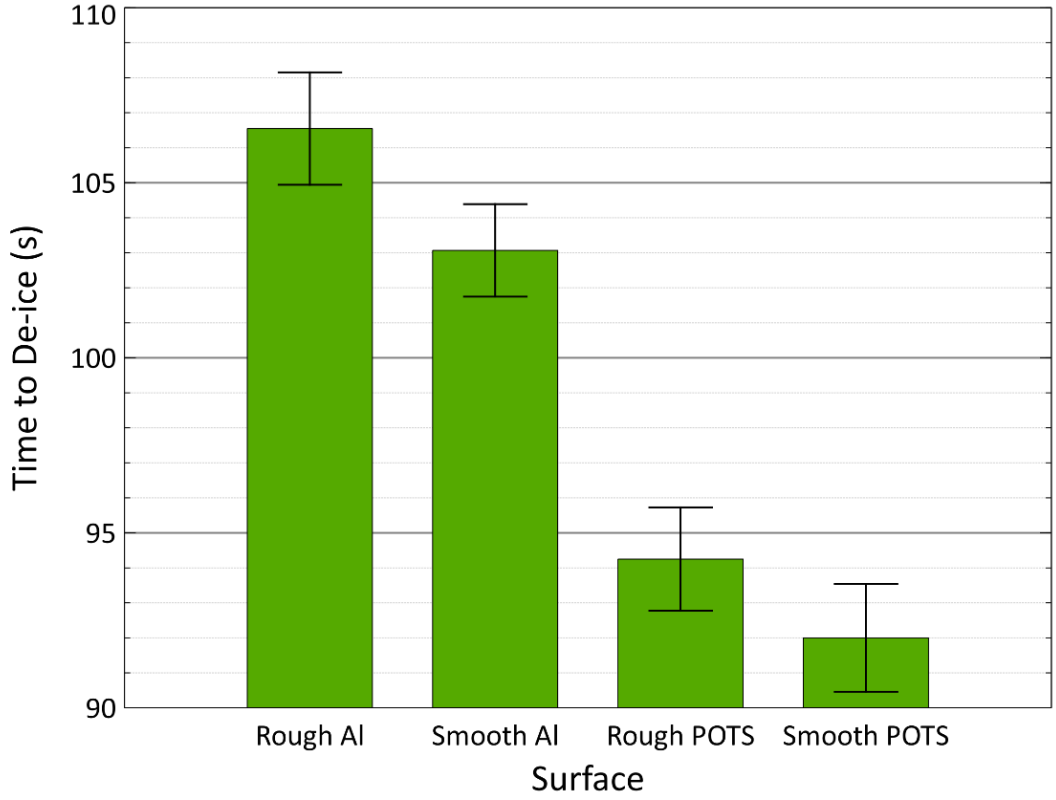

Figure Z Static de-icing of aluminium with two different topographies, functionalised and unfunctionalised with POTS.

Surface roughness

Table H Mean roughness values for tested aluminium surfaces compared to equivalent carbon coated surfaces shown with their respective standard deviation, CC denotes surfaces that have a carbon coating.

Surface	Ra (µm)	Rq (µm)	Rt (µm)	Rz (µm)	Rmax (µm)	Rp (µm)	Rv (µm)	Rc (µm)	Rsm (µm)	Rsk	Rku	Rdq	Rt/Rz
Aluminium	1.00 ± 0.09	1.29 ± 0.13	8.41 ± 1.41	6.15 ± 0.70	7.92 ± 1.36	4.17 ± 0.95	4.25 ± 0.90	4.04 ± 0.48	100.25 ± 13.07	-0.06 ± 0.29	3.70 ± 0.87	0.13 ± 0.01	1.36 ± 0.13
Rough Al	1.41 ± 0.13	1.76 ± 0.16	9.72 ± 1.28	7.45 ± 0.68	9.30 ± 1.30	5.01 ± 0.92	4.71 ± 0.73	5.25 ± 0.53	125.01 ± 13.15	0.05 ± 0.21	2.92 ± 0.45	0.13 ± 0.01	1.30 ± 0.11
Aged Rough Al	0.77 ± 0.12	1.03 ± 0.21	7.13 ± 2.40	4.72 ± 0.98	6.89 ± 2.42	3.14 ± 1.11	3.99 ± 1.57	3.24 ± 1.00	120.23 ± 49.31	-0.31 ± 0.48	4.77 ± 2.43	0.10 ± 0.01	1.47 ± 0.23
CC Aluminium	1.21 ± 0.11	1.55 ± 0.16	9.82 ± 2.01	7.13 ± 0.84	9.23 ± 1.94	4.97 ± 1.19	4.85 ± 1.26	4.83 ± 0.64	115.10 ± 18.12	0.07 ± 0.31	3.59 ± 0.98	0.15 ± 0.01	1.37 ± 0.16
CC Rough Al	1.26 ± 0.12	1.59 ± 0.17	9.56 ± 1.88	7.06 ± 0.77	9.08 ± 1.89	4.68 ± 1.47	4.88 ± 0.95	4.89 ± 0.65	119.91 ± 21.38	-0.06 ± 0.37	3.33 ± 1.43	0.13 ± 0.01	1.35 ± 0.15

Table I Surface areal roughness parameters for the tested Aluminium surfaces shown with their respective standard deviation, CC denoted surfaces have a carbon coating.

Surface	Sa (µm)	Sq (µm)	Sp (µm)	Sv (µm)	Sz (µm)	S10z (µm)	Ssk	Sku	Sdq	Sdr (%)	FLTt (µm)
Aluminium	1.25	1.62	11.88	10.65	22.53	18.87	-0.04	4.08	0.18	1.61	22.53
Rough Al	1.99	2.50	15.67	11.77	27.44	23.61	-0.01	3.13	0.19	1.83	27.44
Aged Rough Al	0.96	1.33	11.89	13.34	25.23	21.28	-0.64	9.66	0.14	0.97	25.23
CC Aluminium	1.69	2.18	15.44	16.58	32.02	26.67	0.14	3.92	0.26	3.24	32.02
CC Rough Al	1.83	2.32	25.06	11.54	36.60	34.07	0.07	4.38	0.20	2.04	36.60

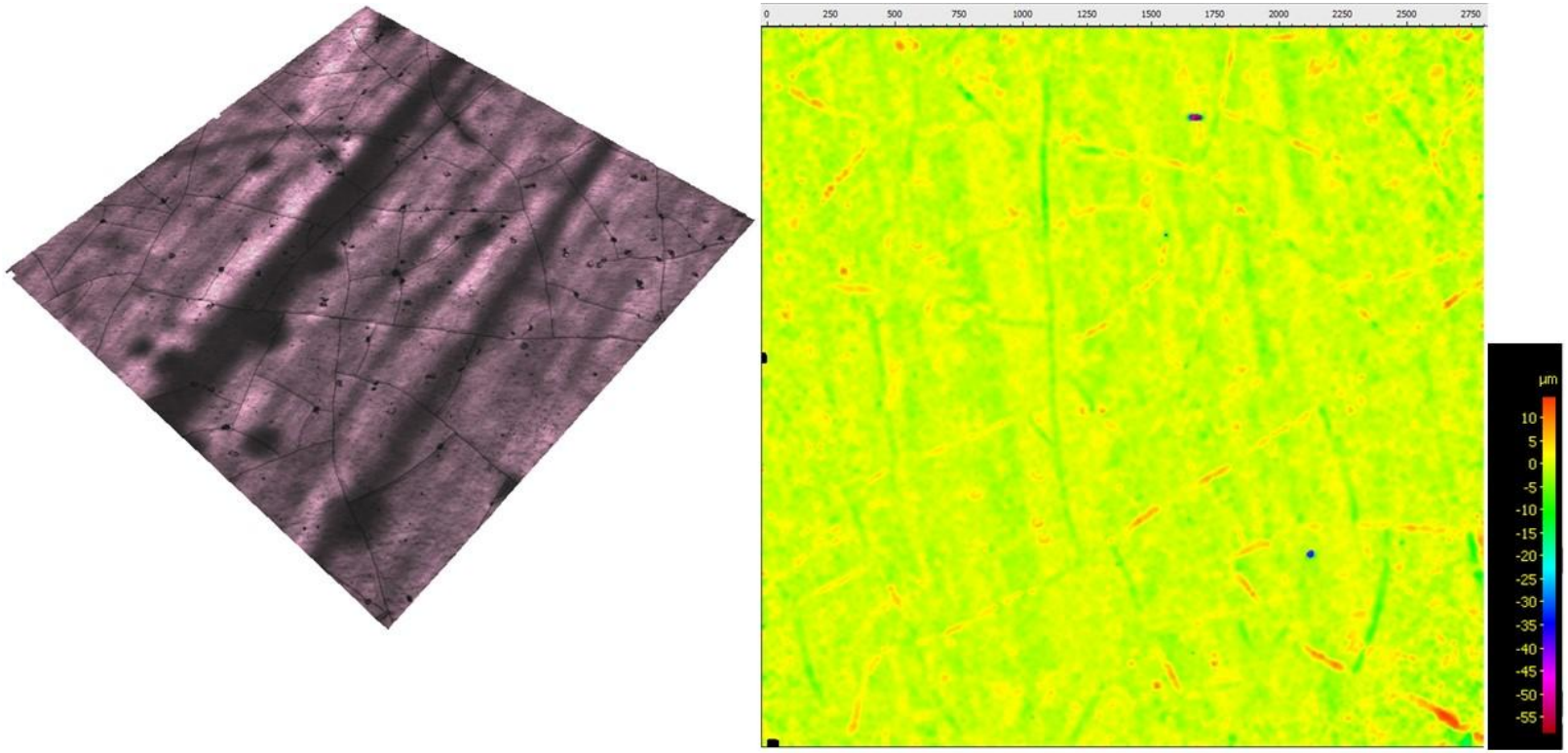

Figure AA Carbon coated 115 µm thick PDMS coating with a well-mapped surface and visible ridges formed by the deposited carbon that are visible in the filtered dataset, implying an impact on the measurements.

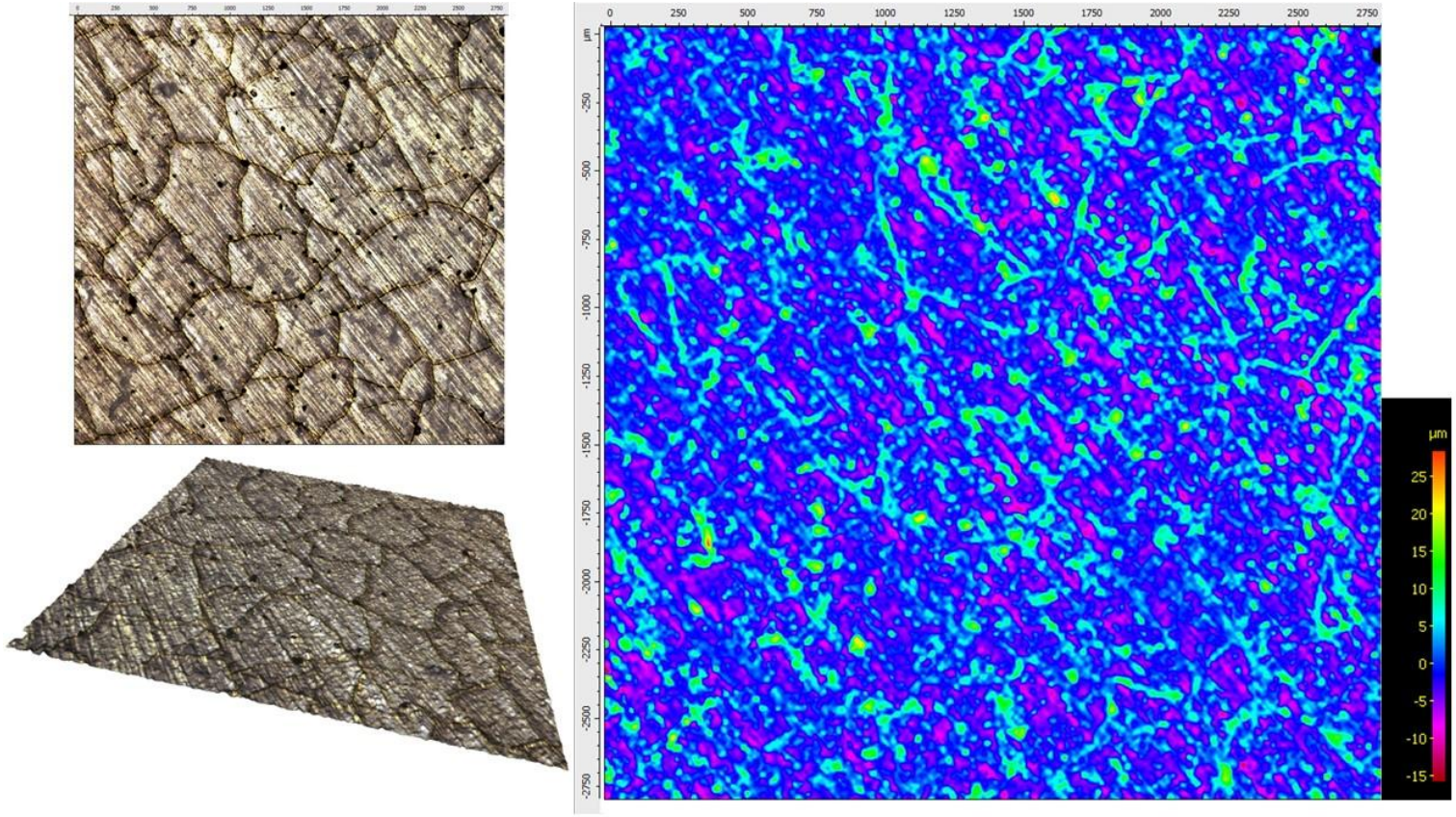

Figure BB Heavy carbon coating on a 23 µm PDMS sample showing significant surface defects caused by the carbon forming ridges upon cooling.

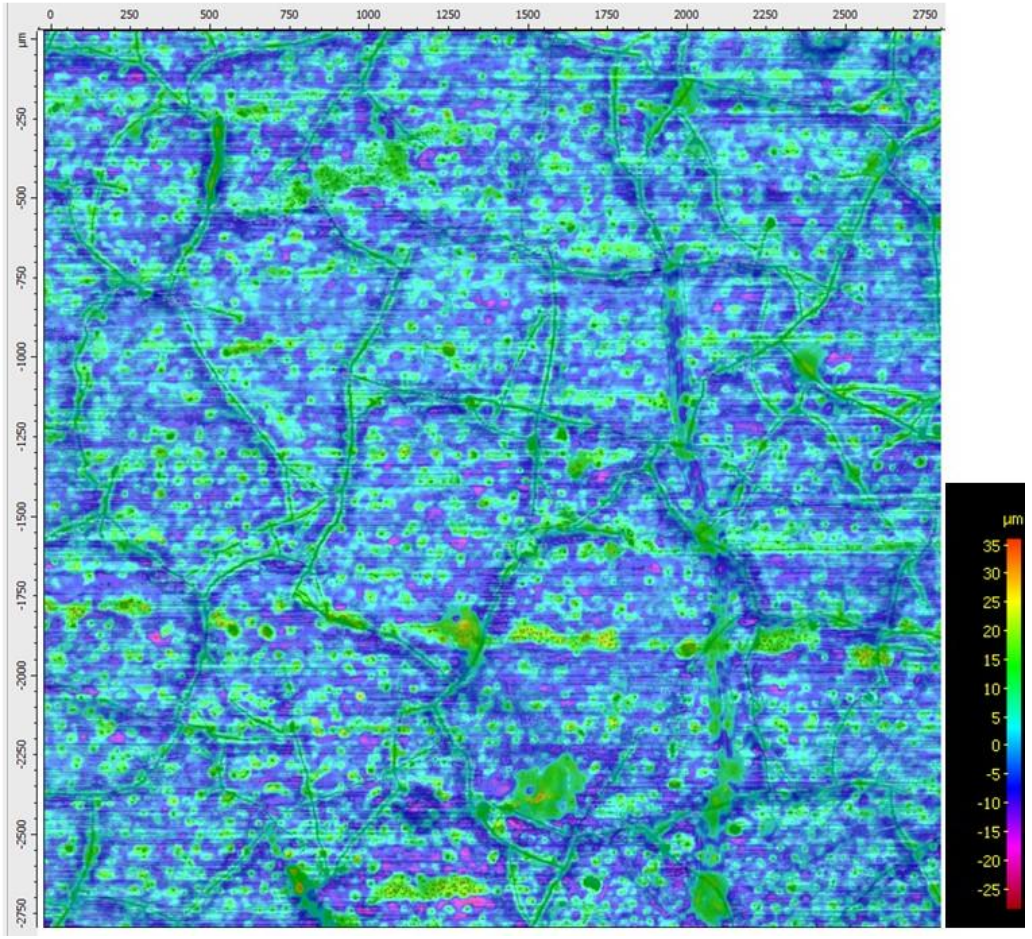

Figure CC Heavy carbon deposition and crack formation atop a PDMS coating that is 22µm thick visible optically and with a filtered overlay of the topographical height heatmap.

Table J Mean surface roughness of PDMS coatings shown with their respective standard deviation.

Surface	Ra (µm)	Rq (µm)	Rt (µm)	Rz (µm)	Rmax (µm)	Rp (µm)	Rv (µm)	Rc (µm)	Rsm (µm)	Rsk	Rku	Rdq	Rt/Rz
CC PDMS (13.8 µm)	1.09 ± 0.12	1.41 ± 0.16	9.09 ± 1.75	6.49 ± 0.80	8.68 ± 1.70	4.90 ± 1.35	4.19 ± 0.93	4.39 ± 0.62	114.45 ± 18.52	0.23 ± 0.38	3.87 ± 1.38	0.13 ± 0.01	1.40 ± 0.16
CC PDMS (115 µm)	0.86 ± 0.13	1.16 ± 0.36	8.79 ± 5.10	5.55 ± 1.46	8.25 ± 5.11	4.04 ± 1.68	4.75 ± 4.22	4.27 ± 4.86	146.23 ± 174.55	-0.20 ± 1.08	6.18 ± 10.08	0.12 ± 0.04	1.53 ± 0.30
PDMS (430 µm)	1.10 ± 0.11	1.42 ± 0.14	9.31 ± 1.52	6.78 ± 0.75	8.77 ± 1.46	4.40 ± 0.99	4.91 ± 1.04	4.48 ± 0.51	103.95 ± 13.15	-0.19 ± 0.29	3.72 ± 0.80	0.14 ± 0.01	1.37 ± 0.14

Table K Surface areal roughness properties of PDMS coatings.

Surface	Sa (µm)	Sq (µm)	Sp (µm)	Sv (µm)	Sz (µm)	S10z (µm)	Ssk	Sku	Sdq	Sdr (%)	FLTt (µm)
CC PDMS (13.8 µm)	1.70	2.19	17.76	12.51	30.27	24.17	0.33	3.90	0.23	2.67	30.27
CC PDMS (115 µm)	1.19	1.68	28.15	53.45	81.60	67.88	-2.06	72.06	0.20	1.96	81.60
PDMS (430 µm)	1.36	1.78	12.10	15.31	27.42	22.60	-0.23	4.13	0.21	2.18	27.42

Table L Mean roughness parameters of 5% SiC coatings shown with their respective standard deviation.

Surface	Ra (µm)	Rq (µm)	Rt (µm)	Rz (µm)	Rmax (µm)	Rp (µm)	Rv (µm)	Rc (µm)	Rsm (µm)	Rsk	Rku	Rdq	Rt/Rz
cc 5% (40 µm)	0.71 ± 0.11	0.95 ± 0.30	7.16 ± 4.90	4.58 ± 1.25	6.83 ± 4.89	3.40 ± 1.16	3.76 ± 4.05	3.44 ± 3.73	122.15 ± 116.11	0.03 ± 0.89	5.49 ± 7.77	0.12 ± 0.04	1.49 ± 0.35
cc 5% (174 µm)	0.82 ± 0.12	1.11 ± 0.26	8.81 ± 4.42	5.50 ± 1.52	8.33 ± 4.45	5.18 ± 3.76	3.63 ± 1.20	3.94 ± 2.57	140.53 ± 124.20	0.62 ± 1.04	6.97 ± 9.85	0.12 ± 0.03	1.55 ± 0.30
cc 5% (325 µm)	1.14 ± 0.11	1.49 ± 0.17	10.61 ± 2.60	7.21 ± 0.97	10.06 ± 2.63	5.16 ± 1.45	5.45 ± 1.73	4.87 ± 0.97	107.51 ± 23.03	0.02 ± 0.42	4.39 ± 1.84	0.17 ± 0.02	1.45 ± 0.20

Table M Surface areal roughness properties of 5% SiC coatings.

Surface	Sa (µm)	Sq (µm)	Sp (µm)	Sv (µm)	Sz (µm)	S10z (µm)	Ssk	Sku	Sdq	Sdr (%)	FLTt (µm)
cc 5% (40 µm)	1.01	1.40	13.56	57.48	71.05	55.81	-1.35	63.35	0.18	1.61	71.05
cc 5% (174 µm)	1.07	1.51	53.66	15.45	69.11	42.77	2.02	39.57	0.19	1.68	69.11
cc 5% (325 µm)	1.46	1.93	15.35	22.09	37.44	33.72	-0.08	5.93	0.24	2.95	37.44

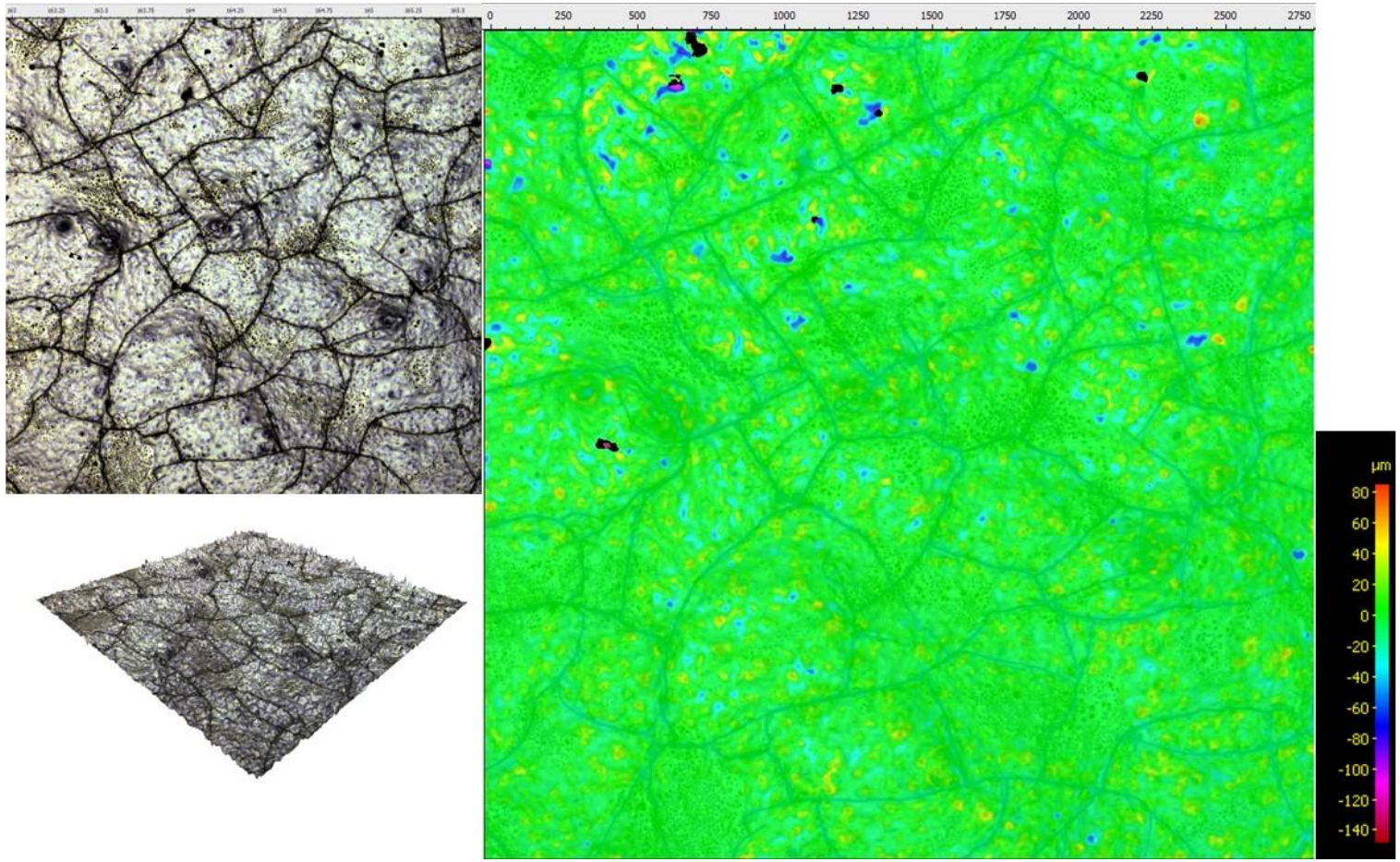

Figure DD 56 µm thick 10% SiC coating with significant cracking of the carbon coating.

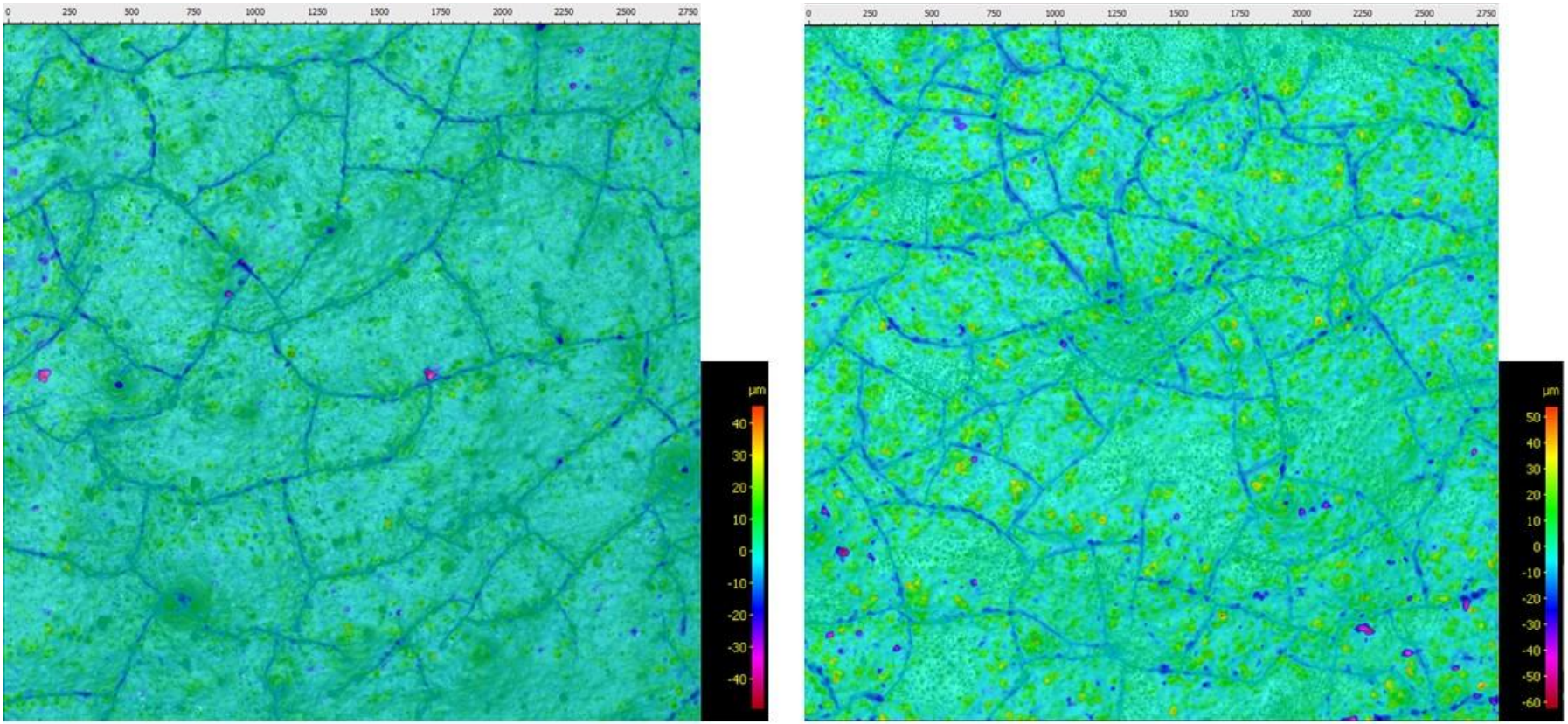

Figure EE Results least compromised by the heavy carbon coating for a 56 µm thick 10% coating with a faded overlay of the filtered data.

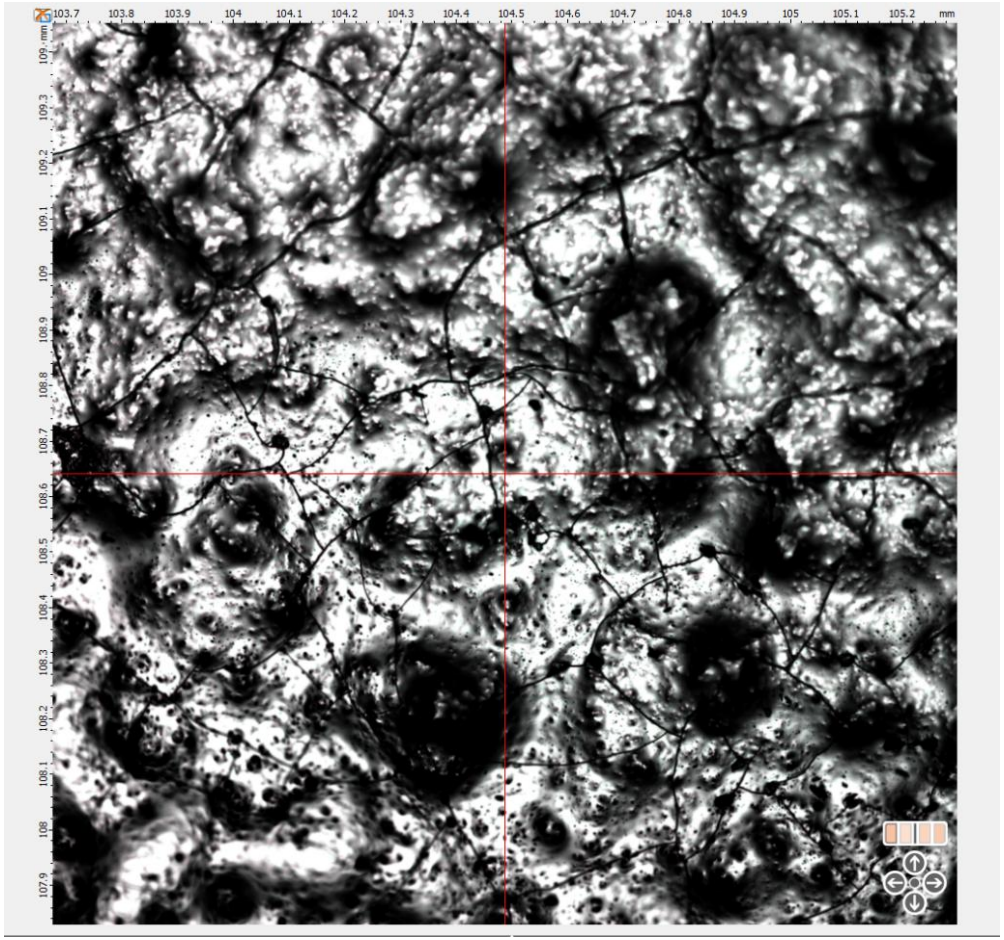

Figure FF Image of 20% SiC with two layers of carbon coating, taken using the 20x optical zoom as opposed to the 5x in other images, displaying cracking of the carbon layer and porosity of the surface.

Table N Mean surface roughness parameters for higher SiC fraction PDMS coatings.

Surface	Ra (µm)	Rq (µm)	Rt (µm)	Rz (µm)	Rmax (µm)	Rp (µm)	Rv (µm)	Rc (µm)	Rsm (µm)	Rsk	Rku	Rdq	Rt/Rz
light CC 10% (60 µm)	2.58 ± 0.47	3.35 ± 0.64	23.72 ± 7.88	15.95 ± 3.49	22.66 ± 7.84	14.33 ± 6.00	9.39 ± 2.91	10.76 ± 2.58	107.89 ± 25.64	0.58 ± 0.48	4.78 ± 3.17	0.37 ± 0.09	1.47 ± 0.23
double CC 10% (126 µm)	3.38 ± 0.44	4.45 ± 0.67	32.00 ± 9.01	21.17 ± 3.82	30.92 ± 9.10	21.02 ± 7.51	10.97 ± 2.44	14.47 ± 2.94	115.70 ± 26.82	0.81 ± 0.50	5.51 ± 3.11	0.51 ± 0.11	1.49 ± 0.22
heavy CC 10% (56 µm)	1.64 ± 0.29	2.37 ± 0.51	20.87 ± 6.85	12.41 ± 2.75	19.23 ± 6.69	11.50 ± 4.43	9.38 ± 4.52	9.50 ± 3.32	178.60 ± 78.21	0.54 ± 1.02	8.31 ± 5.92	0.24 ± 0.05	1.67 ± 0.29
heavy CC 10% (215 µm)	3.45 ± 0.47	4.77 ± 0.66	34.70 ± 8.64	23.13 ± 3.65	32.76 ± 8.44	18.86 ± 5.51	15.84 ± 5.21	16.09 ± 3.25	123.92 ± 30.27	0.49 ± 0.45	5.06 ± 1.79	0.53 ± 0.08	1.49 ± 0.19
CC 20% (60 µm)	3.15 ± 0.38	4.23 ± 0.59	31.54 ± 8.24	20.71 ± 3.54	30.27 ± 8.28	20.41 ± 6.98	11.13 ± 2.26	14.29 ± 2.77	130.88 ± 32.13	0.83 ± 0.54	5.98 ± 3.18	0.45 ± 0.08	1.51 ± 0.23

Table O Surface areal roughness properties of higher SiC fraction PDMS coatings.

Surface	Sa (µm)	Sq (µm)	Sp (µm)	Sv (µm)	Sz (µm)	S10z (µm)	Ssk	Sku	Sdq	Sdr (%)	FLTt (µm)
light CC 10% (60 µm)	3.34	4.36	47.94	27.33	75.27	68.43	0.75	5.72	0.57	14.63	75.27
double CC 10% (126 µm)	4.28	5.62	50.39	22.26	72.65	68.76	0.93	6.08	0.74	23.33	72.65
heavy CC 10% (56 µm)	2.29	3.37	45.30	49.56	94.86	83.81	0.19	14.42	0.40	72.01	94.86
heavy CC 10% (215 µm)	4.19	5.69	49.32	45.16	94.48	86.83	0.57	5.74	0.75	24.79	94.48
CC 20% (60 µm)	4.40	5.87	54.17	34.90	89.06	73.74	0.88	6.35	0.69	20.49	89.06